CIVIL ENGINEERING JOURNAL

číslo 4/2021

Obsah:

CIVIL ENGINEERING JOURNAL

Article no. 60

THE CIVIL ENGINEERING JOURNAL 4-2021

EFFECTS OF SHEAR WALLS ON A TYPICAL FOUR-STORY REINFORCED CONCRETE STRUCTURE SUBJECTED TO SEVERE EARTHQUAKE EVENTS

Nader Zad and Hani Melhem

Kansas State University, Ph.D., Department of Civil Engineering, Manhattan, Kansas, United States of America; naderzad@k-state.edu, melhem@k-state.edu

ABSTRACT

Various seismic-resistant design methods are used to ensure the stability of multi-story buildings against lateral forces caused by earthquakes. Utilization of reinforced concrete shear walls is one of the most reliable methods of design and construction of earthquake-resistant buildings because it increases structural resistance to lateral loads and stiffens and strengthens the structure, thereby minimizing earthquake-induced damages. This paper investigates the beneficial effects of using shear walls in the structural design of a typical low-rise building to improve its resistance to earthquake events. To this end, a four-story reinforced concrete structure is modeled first without any shear walls, then with the addition to shear walls. The 2002 Denali Alaska earthquake is used as an example of a severe seismic excitation because it is considered the most massive strike-slip earthquake in North America in almost 150 year. SAP2000 is used to perform the dynamic analysis. In order to obtain an accurate representation of the structure's behavior, response modal nonlinear time-history dynamic analysis is utilized to analyze and compare the response of the building with and without shear walls. Study results showed that shear walls are very effective in achieving compliance with seismic design codes. In addition, the use of shear walls significantly reduces the shear stresses, bending moments, and displacements of the various members of the structure.

KEYWORDS

Modal, Nonlinear, Time history, Dynamic analysis, Denali, Reinforced concrete structure, Shear walls, SAP2000

NTRODUCTION

General Excitation of an SDOF System

The impulse response approach is used to solve for the response of an SDOF system to an arbitrary loading sequence, *F(t)*:

$$F(t) = m\ddot{x} + c\dot{x} + kx \quad (1)$$

$$F(t) = P_0 \sin(\Omega t) \quad (2)$$

$$F(t) = P_0 \sin(\Omega t + \phi) \quad (3)$$

kx	restoring pull of the spring
$c\dot{x}$	damping force in the direction opposite to the direction of motion
$m\ddot{x}$	intertidal force acting through the center of mass
$\dot{x}$	velocity
$\ddot{x}$	acceleration
t	time

Ω frequency
P_0 amplitude or maximum value of the force
ϕ phase angle or phase lag

which represent the most general form of excitation. Such an arbitrary loading sequence can be approximated as a series of impacts [1].

Excitation by Rigid Base Translation

Base translation of the SDOF system is defined by the displacement *y(t)*, and the corresponding base acceleration is denoted by $\ddot{y}(t)$. The equilibrium equation for a damped SDOF system with rigid base translation *y(t)* can be expressed as [1]

$$m(\ddot{x}+\ddot{y})+c\dot{x}+kx=0 \quad (4)$$

Building Components and Numerical Modeling

When building a numerical model of a structure slabs are typically modeled using shell elements while shear walls are modeled using plate elements since out-of-plane bending is insignificant for walls. Interior walls may be non-load-bearing partition walls or load-bearing walls that must carry the floor loads and act as shear walls to resist lateral forces [2].

Load-Bearing Walls

Bearing walls potentially act as shear walls as they carry roof and floor loads as well as the weight of overhead walls. As exterior walls, load-bearing walls also must perform as curtain walls to resist lateral wind pressure in slab action.

Vertical structural planes in a building are connected by horizontal floor planes, and external and internal lateral forces are distributed along the floor structures, which act as deep horizontal beams, to the vertical shear walls. The shear walls, which can be arranged in a variety of ways, carry lateral loads to the foundation and to the ground. Common bearing wall structures include the following [2]:

- Plain or reinforced masonry walls (e.g., brick, concrete block)
- Cast-in-place concrete walls
- Precast concrete walls
- Framed walls (e.g., stud walls, tubular structures)
- Trussed walls (e.g., traditional half-timber construction in Europe, brace-framed tubes, latticed tubes)

Wall Proportion and Shear Wall Behavior

The wall proportion, height/width (H/W) ratio, of rectangular shear walls ranges from low-rise (low/long) walls to slender high-rise (tall) walls. Tall shear walls typically deform in the bending mode, allowing shear deformation to be ignored. However, shear deformations control low shear walls with approximately H/B < 1. The wall proportion significantly influences shear wall behavior in the following ways:

- Long shear walls with lengths at least approximately three times longer than their heights, H/B ≤ 0.33, represent shear panels controlled by shear deflections; in other words, shear panels wrack linearly with distortion similar to a parallelogram.
- Slender shear walls with heights at least approximately three times higher than their widths, H/B ≥ 3, exhibit shallow beam behavior similar to vertical cantilever beams controlled primarily by flexural deflections.

- Intermediate shear walls, approximately 3 > H/B > 0.33, represent deep beam behavior, with a transition stage from the long to the slender wall or from the shear cantilever to the flexural cantilever.

In low-rise buildings, openings may penetrate walls, causing slender piers to act as flexural cantilevers under lateral shear wracking.

Long and intermediate concrete walls usually have relatively light reinforcement, with the exception of additional vertical bars at wall boundaries and around openings and additional horizontal bars at the floor levels.

Although the walls in bearing-wall structures are typically load-bearing to support floor loads, they can also act as shear walls to resist lateral forces due to wind and earthquakes. Shear walls in masonry buildings usually intersect with other walls, resulting in single or double returns at the ends of the walls. With respect to lateral force action, shear walls can act as vertical cantilever plate girders over the full building height, with walls representing a web, floors representing web stiffeners, and end returns representing flanges. The flanges are assumed to carry only axial forces due to cantilever bending, and the web is expected to carry all the shear [2].

Openings in Shear Walls

Small openings do not influence behavior of a shear wall, but a wall with larger openings is modeled as a pier/spandrel system. A wall with very large openings, however, converts to a frame, thereby exhibiting frame behavior [2].

Modeling Walls with Frame Elements

Since walls behave similarly to trusses, a truss model may be used to visualize force flow in concrete and masonry shear walls. The truss model can approximate the behavior of a shear wall because it assumes that the vertical elements provide axial-flexural resistance and the diagonal members provide shear resistance [2].

Shear Wall-Frame Interaction

Shear walls and frames typically interact in braced skeleton buildings. Interaction may include the following:

- Shear walls that resist all lateral forces stabilize hinged frames that carry only gravity loads.
- Similar to compressive struts, infill panels brace rigid frames. Beams, columns, and walls in the frame provide maximum stiffness to the system
- Rigid frames are hinged to or continuously connected to shear walls so that shear walls and frames both resist lateral forces.

Interactive behavior of the rigid frame-shear wall structure depends on the relative stiffness of the frame and the stiffness of the shear walls. For example, shear walls in a tower structure with a large central core and widely spaced perimeter columns may provide 90% of the lateral stiffness. In general, however, shear walls provide most lateral resistance only for buildings of moderate height or the bottom portion of tall buildings. In addition, resulting stiffness of the combined structure of frames and shear walls is considerably higher than the sum of its components. Frame shear deformation and bending deflection of the wall in tall buildings results in a flat S-curve, as if a shear-frame building sits on top of a flexural cantilever structure.

In this study, membrane elements are utilized to model shear walls when the beams are hinged to the shear wall and when the shear walls are fill-in panels that provide full continuity with beams and columns. Shell elements are used when moment continuity with beams is required [2].

Vertical Lateral Force-Resisting Structures

Although wind pressure and seismic excitation cause primary lateral loads, lateral soil and liquid pressures as well as gravity loads in cantilevering structures and irregular structures can cause

lateral loads. Vertical lateral force-resisting structures such as moment-resisting frames, braced frames, shear walls, and dual systems (e.g., shear wall and frames) typically resist these loads.

A frame braced by trussing or shear walls is relatively stiffer than only a frame in which lateral deflection depends on the rigidity of beam-column and slab joints [2].

Bearing Wall Systems

Examples of bearing wall systems include load-bearing shear walls, such as reinforced or plain concrete shear walls (ordinary, special) and reinforced or plain masonry shear walls (ordinary, special), and light frame walls with shear panels [2].

Tall buildings respond to lateral load action as flexural cantilevers if the resisting structure consists of shear walls or a braced frame, whereas rigid frame structures and massive buildings respond as shear cantilevers. The combined action of different structure systems for tall buildings, such as rigid frame shear wall interaction, may have the appearance of a flat S-curve [2].

SUMMARY OF COMPARABLE RESEARCH LITERATURE

Bhat et al. used STAAD Pro to compare earthquake responses of buildings with and without shear walls [3]. Chandurkar et al. determined the optimal location for shear walls in a multi-storied building and studied shear wall effectiveness using four models [4]. Kurma et al. conducted pushover analysis on two multi-storied Reinforced Concrete (R.C.) frame buildings: one building had 10 stories with five bays in *X* direction and five bays in *Y* direction, and the second building contained 15 stories. The shear wall was used to study their resisting lateral forces, and the paper highlighted the effect of a shear wall on the building when a wall was located along the long as well as the short sides of the building [5]. Tidke et al. used five models to study the effect of seismic loading relative to shear wall placement in various locations in a building [6]. Sanjeev et al. considered a spatial configuration of a 20-storied structure with a maximum 70 m height, and each story height of 3.5 m with a shear wall and bracing at various locations in the building [7].

EXPERIMENTAL STUDY

Seismic Excitation

The novelty of this paper and research is a realistic application that considers an actual seismic excitation record (2002 Denali Alaska earthquake) that was the strongest ever recorded in the interior of Alaska happened in the United States of America. The authors consider this to be a meaningful contribution to the state of knowledge. The Denali fault event was felt as far as Washington and caused seiches in pools and lakes as far as Texas and Louisiana. “The earthquake was associated with 340 kilometers of surface rupture and was the most massive strike-slip earthquake in North America in almost 150 years” [8]. The other scholars and researchers reviewed referenced in the literature review section of the paper did not consider an actual seismic record for their analysis, especially earthquakes that happened in the United States. Updates and enhancement of the building codes normally consider results of this nature to modify the design requirements and recommendations.

“The estimated magnitude of this earthquake ranges from the body wave magnitude of 7.0 to the moment magnitude (MW) of 7.9 to the surface wave magnitude of 8.5. While the fault rupture lasted for about 100 seconds from its initiation to the arrest, its distal effects were felt for many days. There were reports of triggered seismicity in volcanic and geothermal centers in Washington and California and regional seismicity in Utah” [9].

Building Description

The building in this study was a four-storied concrete shear wall building with concrete flat slabs supported by concrete columns. Figure 1 shows the floor and roof plan.

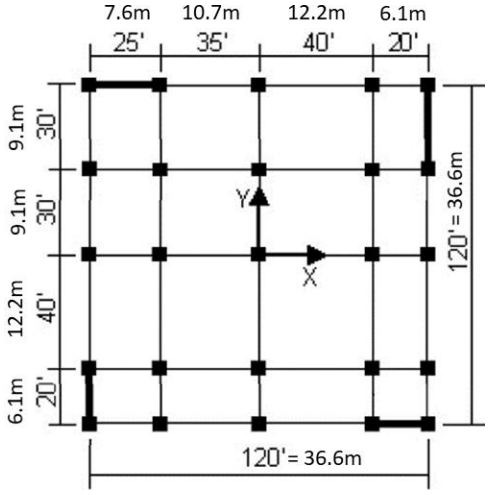

Fig. 1 - Building Floor and Roof Plan

Based on Zad et al. research paper, one of the best locations of shear walls is on the structure's perimeter at the left of each of the four building faces. They showed in their research that using shear walls on those locations will significantly improve structural behavior [10]. The authors had investigated the effects of shear wall locations in a different published paper [10].

The steel properties used in this study were as follows:

- E = 29,000 ksi = 199947961.12 KN/m^2
- Poisson's ratio = 0.3

The concrete properties were as follows:

- E = 3600 ksi = 24821126.208 KN/m^2
- Poisson's ratio = 0.2
- Weight per unit volume is 0.15 kip/ft^3 = 23.56 N/m^3

The members geometric properties were as follows:

- Walls are 12 in. (30.48 cm) thick.
- Columns are 20 in. ×20 in. (50.8×50.8 cm)
- Size of beams is 12 in. × 18 in. (30.48×45.72 cm)
- Floors and roof are 10 in. (25.4 cm) thick flat slabs.

The assumptions used here are that the diaphragms are rigid in plane, and the columns are fixed base. Figure 2 shows a three-dimensional (3-D) perspective of the building model.

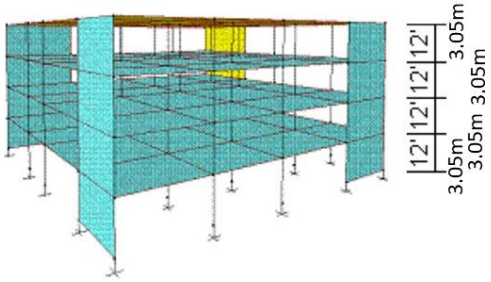

Fig. 2 - 3D Perspective

The roof and floors are shell-thin members. Figure 3 shows the reinforced concrete sections for the columns.

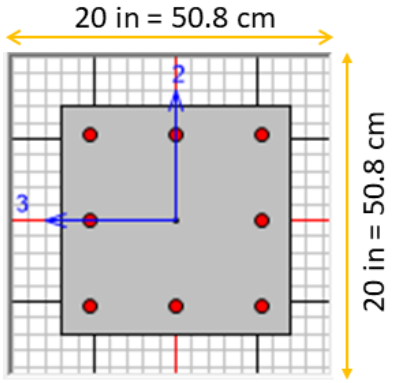

Fig. 3 - Columns' sections

The time history files Anchorage-1 (earthquake station) in the *X* direction and Anchorage-2 (earthquake station) in the *Y* direction were applied to the structure. Each time history was given in units of g, with 34,400 time steps at equal spacings of 0.005 second for a total of 172 seconds. Each line in the time history files contained five accelerations points.

Figure 4 shows the unscaled response spectra.

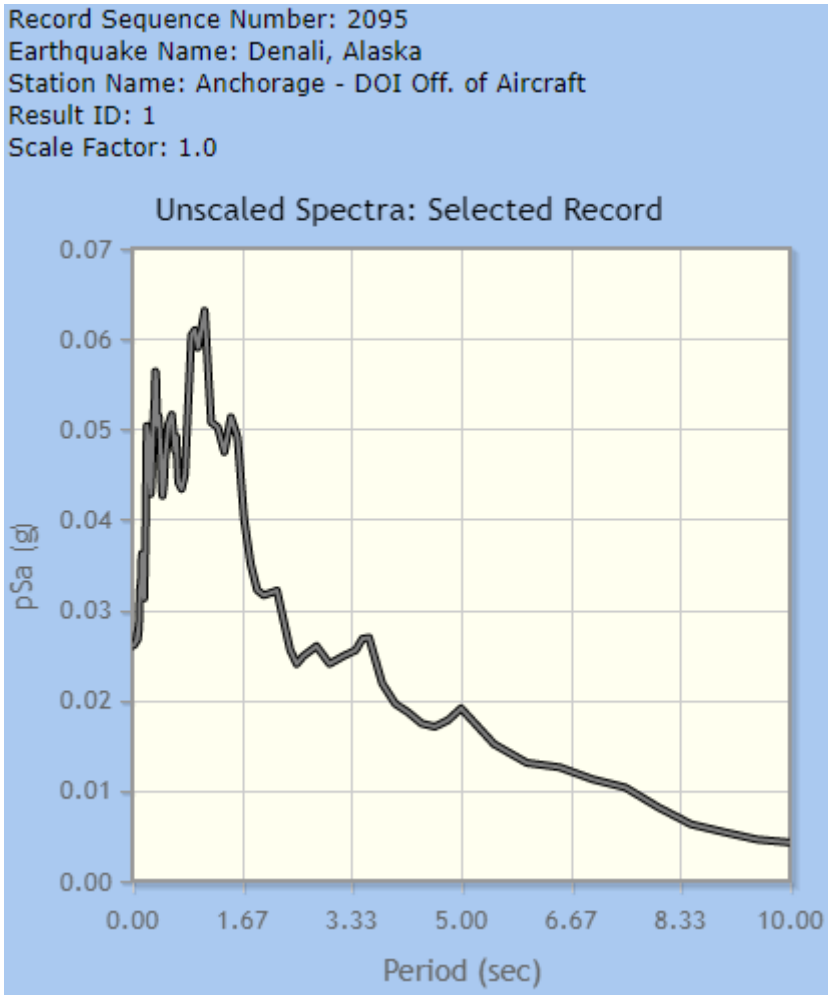

Fig. 4 - Unscaled Response Spectra

In general, an accelerogram that measures peak ground acceleration, duration, and frequency content of an earthquake can be integrated to obtain time variations of ground velocity and ground displacement [10].

NUMERICAL COMPARISON

Figure 5 demonstrates the unscaled time series of the Denali earthquake record (Horizontal-1 Component).

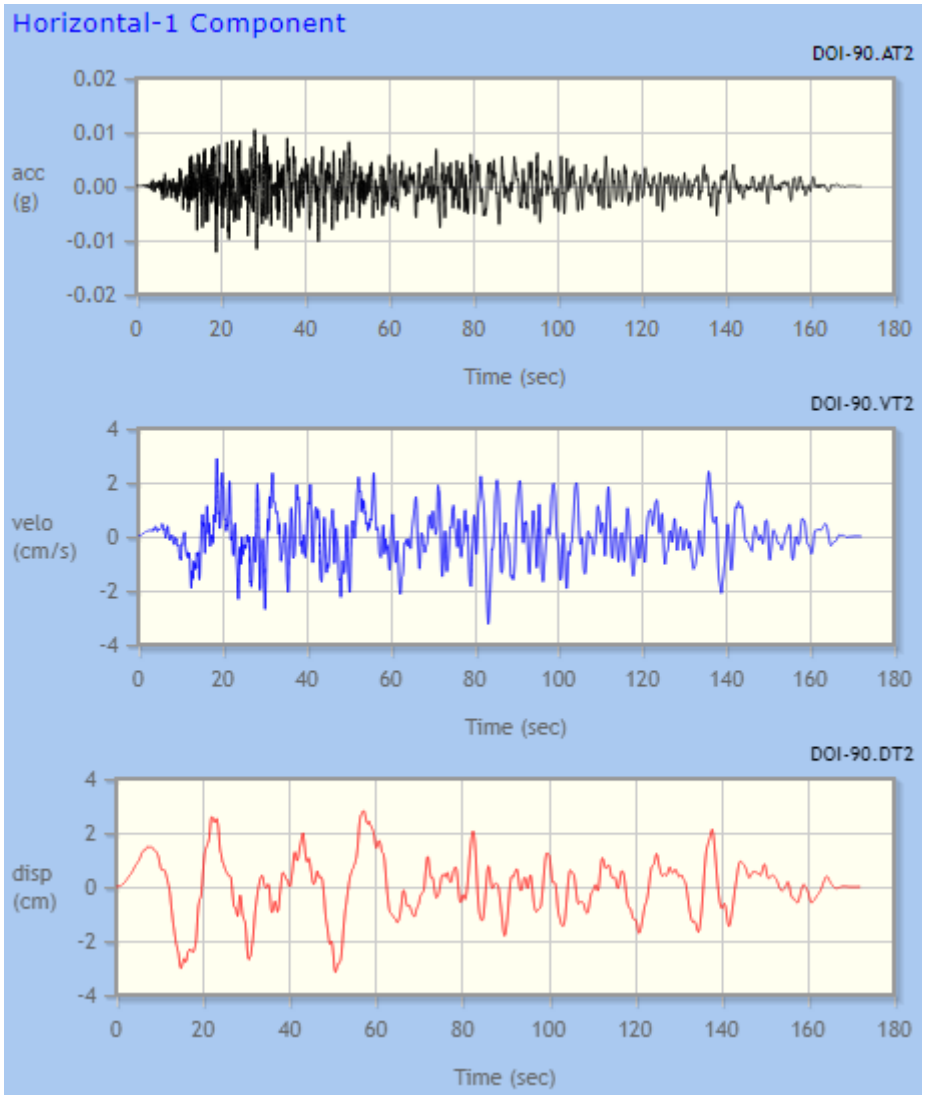

*Fig. 5 - Acceleration–Time, Velocity–Time, and Displacement–Time Graphs ("Anchorage - DOI Off. of Aircraft" Record of 3 November 2002, Denali Earthquake) (Horizontal-1 Component) (*90°)

Figure 6 demonstrates the unscaled time series of the Denali earthquake record (Horizontal-2 Component).

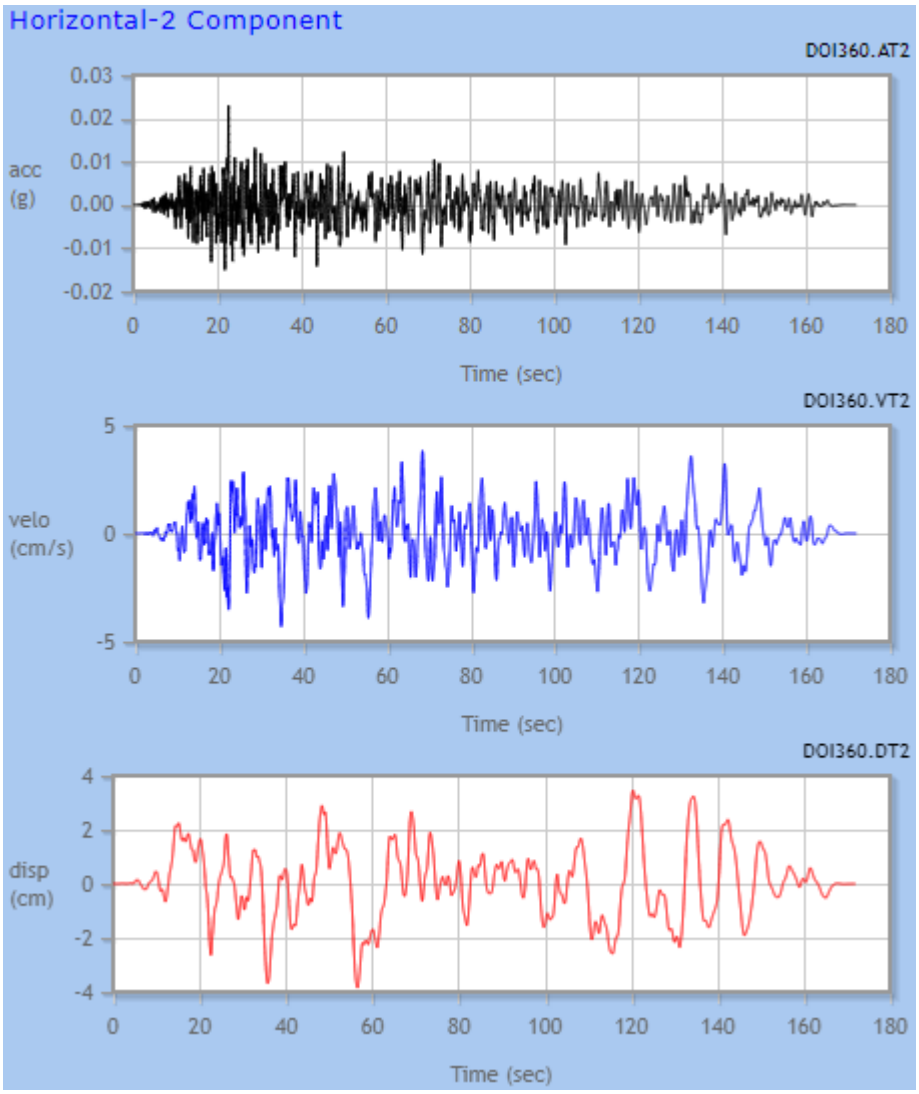

*Fig. 6 - Acceleration–Time, Velocity–Time, and Displacement–Time Graphs ("Anchorage - DOI Off. of Aircraft" Record of 3 November 2002, Denali Earthquake) (Horizontal-2 Component) (*360°)

Figure 7 demonstrates the unscaled time series of the Denali earthquake record (Vertical Component).

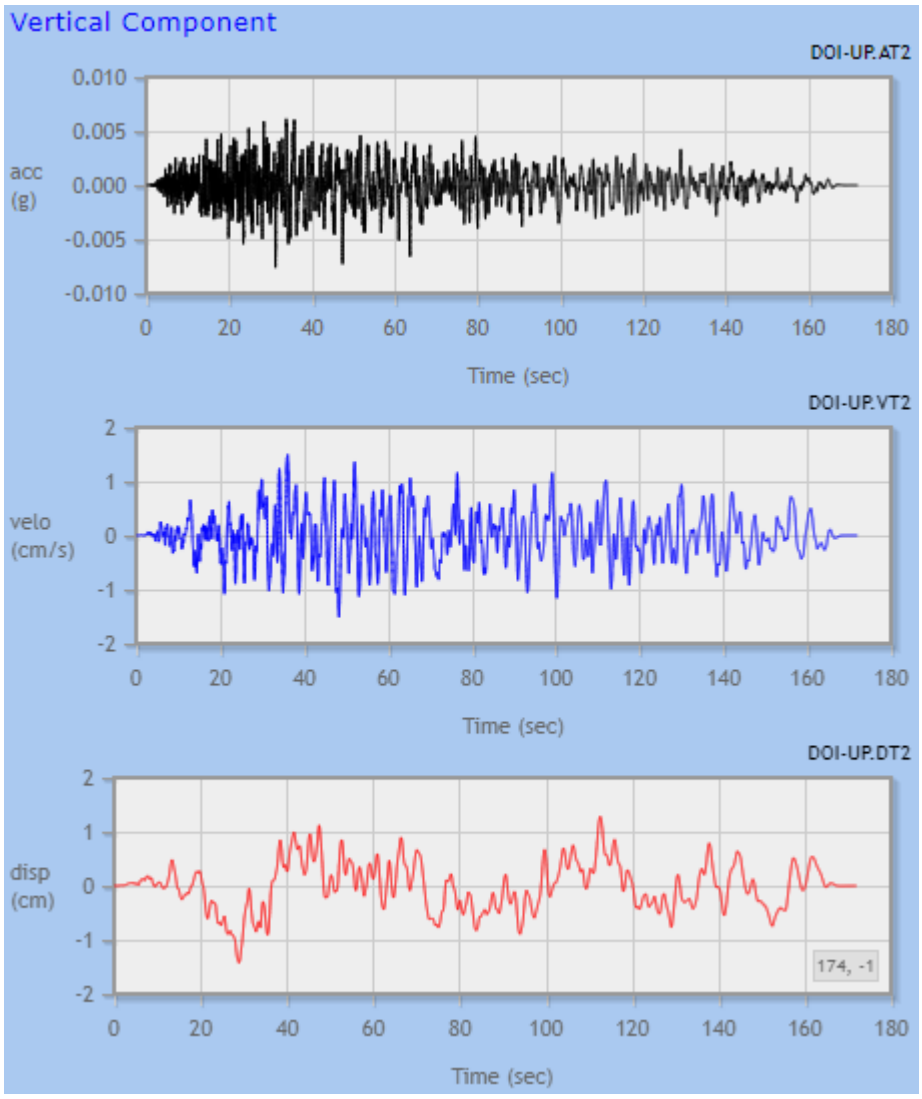

Fig. 7 - Acceleration–Time, Velocity–Time, and Displacement–Time Graphs ("Anchorage - DOI Off. of Aircraft" Record of 3 November 2002, Denali Earthquake) (Vertical Component)

Figures 8 and 9 show load time histories (function graphs in the *X* and *Y* direction) of Anchorage-1.TH and Anchorage-2.TH, respectively.

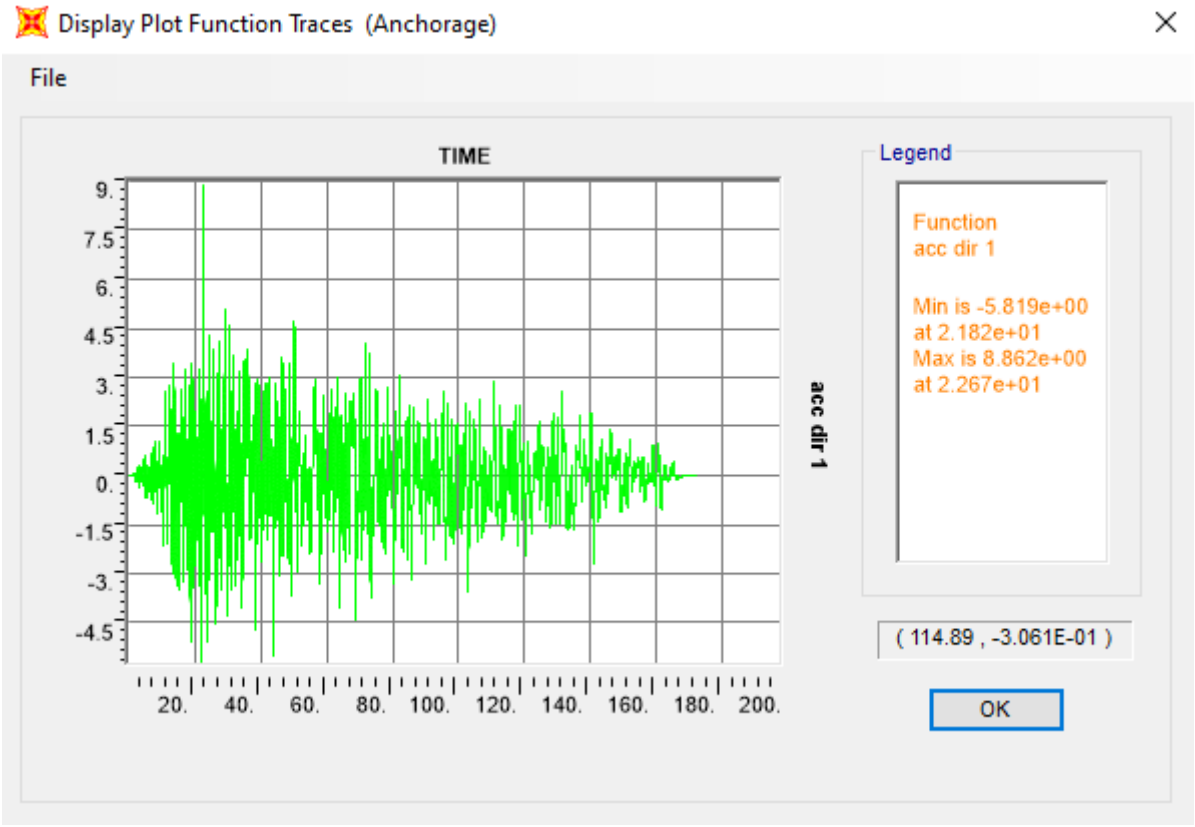

Fig. 8 - Time History Function Graph, X Direction

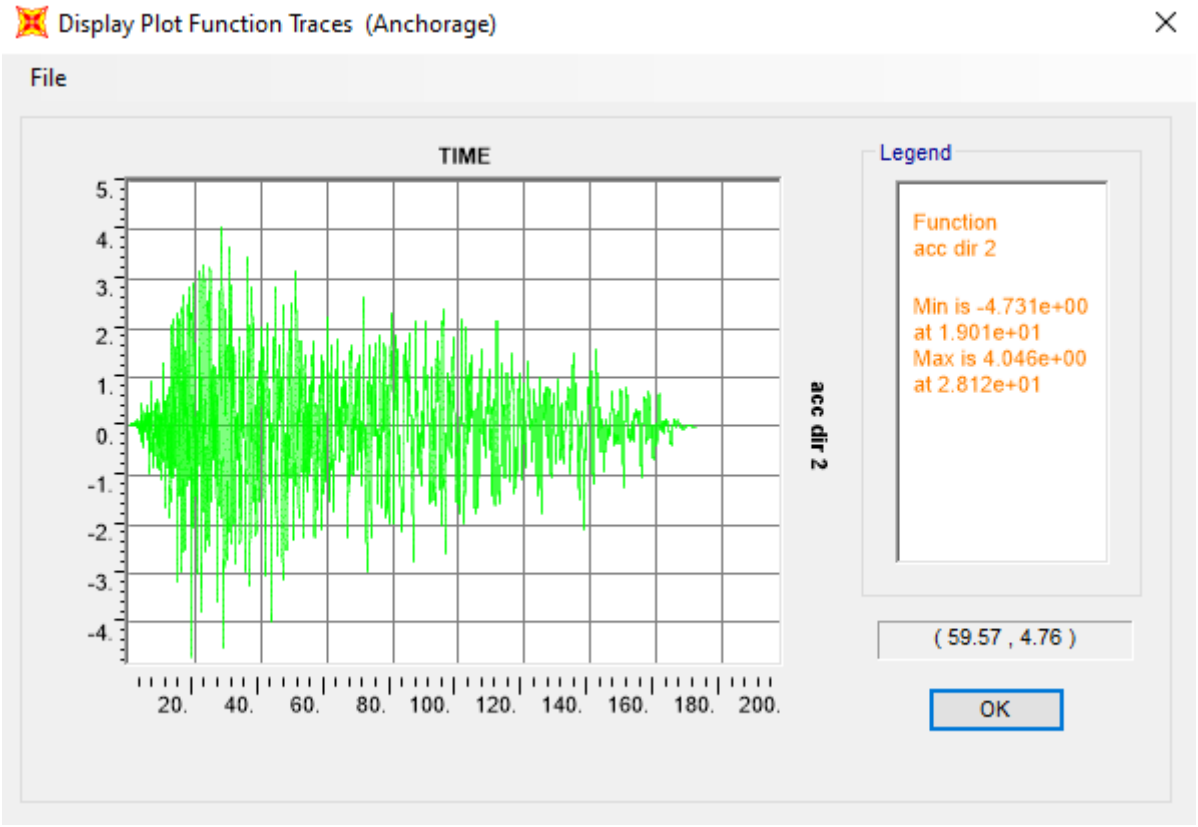

Fig. 9 - Time History Function Graph, Y Direction

RESULTS

Figure 10 depicts the isometric (3-D) and the two-dimensional (2-D) views of the structure withoutany shear walls, and Figure 11 shows the deformed shape of this study's building without any shear walls.

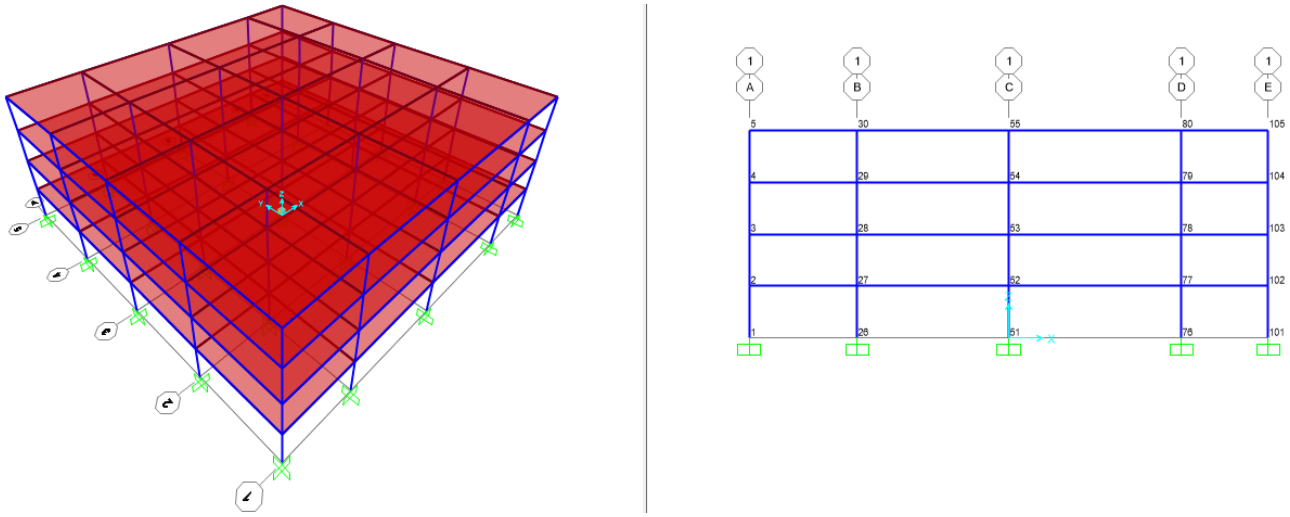

Figure 10 - 3-D and 2-D Views without any Shear Walls

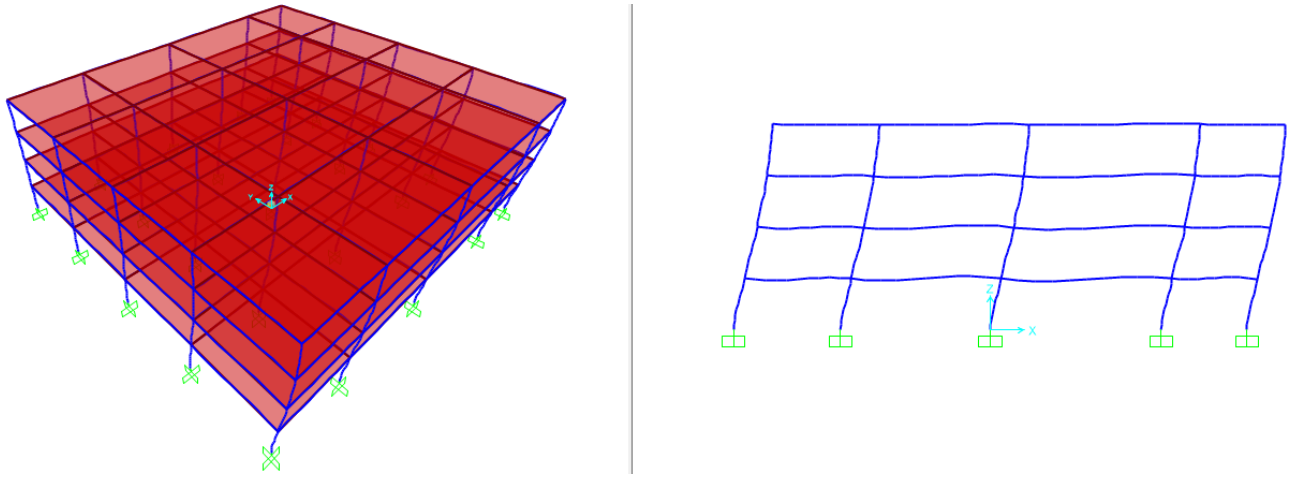

Fig. 11 - Deformed Shape of Building without any Shear Walls

Figure 12 depicts the isometric (3-D) and the two-dimensional (2-D) views of the structure with shear walls, and Figure 13 shows the deformed shape of this study's building with shear walls.

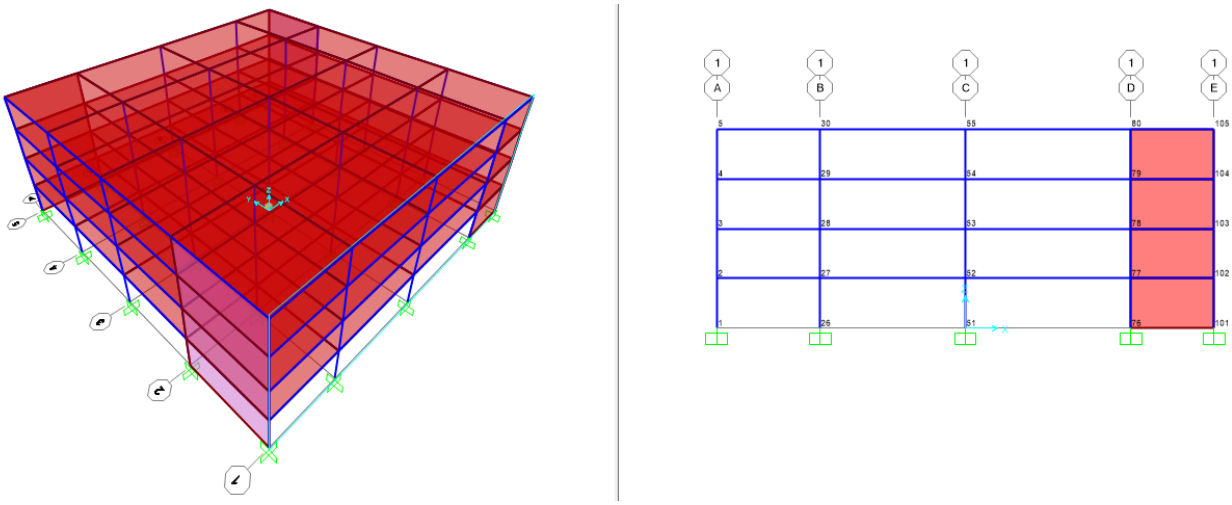

Figure 12 - 3-D and 2-D views with shear walls

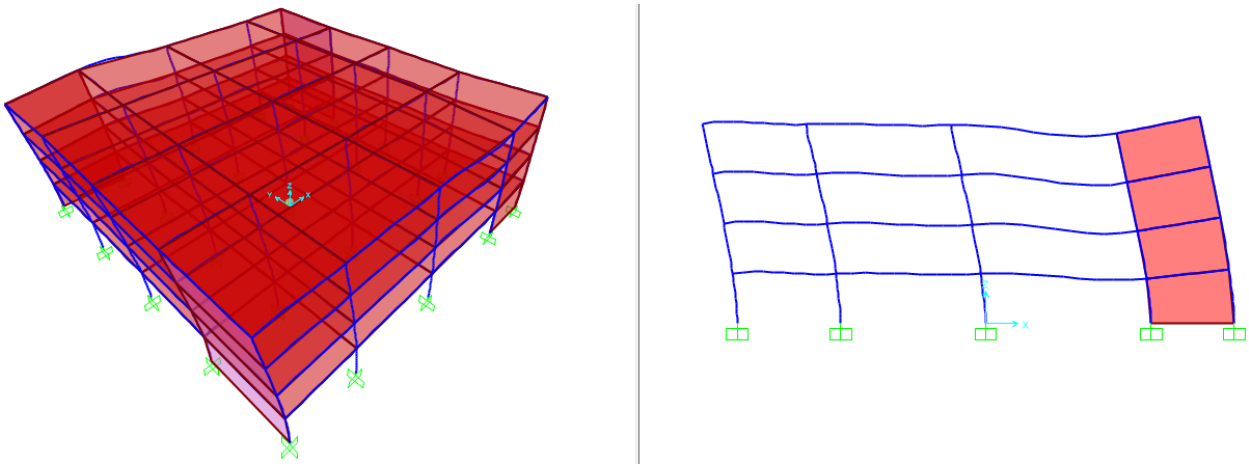

Fig. 13 - Deformed Shape of Building with Shear Walls

Tables 1 through 7 compare the data and results of nonlinear time history analysis of the structure without shear versus those of the structure with shear walls.

Tab. 1 - Structural time period for nonlinear time history analysis without and with shear walls

	Without shear walls	With shear walls	Effect of shear walls
Mode 1	0.90432 s	0.32854 s	63.67% decrease
Mode 2	0.88607 s	0.25011 s	71.77% decrease
Mode 3	0.82213 s	0.18912 s	84.29% decrease
Mode 4	0.29430 s	0.11885 s	59.61% decrease
Mode 5	0.28930 s	0.11685 s	59.6% decrease

Tab. 2 - Structural frequency for nonlinear time history analysis without and with shear walls

	Without shear walls	With shear walls	Effect of shear walls
Mode 1	1.10580 Hz	3.04376 Hz	175.25% increase
Mode 2	1.12857 Hz	3.99809 Hz	254.26% increase
Mode 3	1.21634 Hz	5.28750 Hz	334.70 % increase
Mode 4	3.39780 Hz	8.41340 Hz	147.61% increase
Mode 5	3.45652 Hz	8.55775 Hz	147.58% increase

Tab. 3 - Design base shear for nonlinear time history analysis without and with shear walls

	Without shear walls	With shear walls	Effect of shear walls
in *X* direction	703.747 Kip = 3130.42 KN	1022.912 Kip = 4550.14 KN	45.35% increase
in *Y* direction	595.104 Kip = 2647.15 KN	795.795 Kip = 3539.87 KN	33.72% increase

Tab. 4 - Base moment for nonlinear time history analysis without and with shear walls

	Without shear walls	With shear walls	Effect of shear walls
in *X* direction	19879.1282 Kip-ft = 26952.5 KN-m	30284.2814 Kip-ft = 41059.9618 KN-m	52.34% increase
in *Y* direction	-23330.7542 Kip-ft = -31632.2472 KN-m	-38160.8949 Kip-ft = -51739.2131 KN-m	63.56% increase

Tab. 5 - Maximum displacements for nonlinear time history analysis without and with shear walls

	Without shear walls	With shear walls	Effect of shear walls
Max *UX* for Joint 52	-1.62891 in. = -4.13743 cm	-1.52704 in. = -3.87868 cm	6.25% decrease
Max *UY* for Joint 52	-1.28192 in. = -3.25607 cm	-1.24967 in. = -3.17416 cm	2.51% decrease
Max *UX* for Joint 53	-1.88686 in. = -4.79262 cm	-1.57223 in. = -3.99346 cm	16.67% decrease
Max *UY* for Joint 53	-1.32037 in. = -3.35373 cm	-1.25751 in. = -3.19407 cm	4.76% decrease

Max *UX* for Joint 54	-2.08840 in. = -5.304536 cm	-1.62858 in. = -4.13659 cm	22.01% decrease
Max *UY* for Joint 54	1.43210 in. = 3.63753 cm	-1.2662 in. = -3.2161 cm	11.58% decrease
Max *UX* for Joint 65	-2.22948 in. = -5.66287 cm	-1.65246 in. = -4.19724 cm	25.88% decrease
Max *UY* for Joint 65	1.49782 in. = 3.80446 cm	-1.27455 in. = -3.23735 cm	14.9% decrease

Note: Joints 52, 53, 54, and 65 are the center joints on the first, second, third, and forth floor, respectively

Tab. 6 - Drifts for nonlinear time history analysis without and with shear walls

	Without shear walls	With shear walls	Effect of shear walls
1st Floor - *X* direction	0.01131 in. = 0.287274 mm	0.0106 in. = 0.2692 mm	6.25% decrease
1st Floor - *Y* direction	0.0089 in.= 0.226 mm	0.00867 in. = 0.22021 mm	2.51% decrease
2nd Floor - *X* direction	0.00179 in. = 0.04546 mm	0.00031 in. = 0.00787 mm	82.52% decrease
2nd Floor - *Y* direction	0.00026 in. = 0.0066 mm	0.00005 in. = 0.00127 mm	79.69% decrease
3rd Floor - *X* direction	0.00139 in. = 0.0353 mm	0.00039 in. = 0.0099 mm	72.05% decrease
3rd Floor - *Y* direction	0.00077 in. = 0.01955 mm	0.00006 in. = 0.00152 mm	92.25% decrease
4th Floor - *X* direction	0.00097 in. = 0.02463 mm	0.00016 in. = 0.00406 mm	83.14% decrease
4th Floor - *Y* direction	0.00045 in. = 0.01143 mm	0.00005 in. = 0.00127 mm	87.28% decrease
Total drift - *X* direction	0.00387 in. = 0.09829 mm	0.00286 in. = 0.07264 mm	25.89% decrease
Total drift- *Y* direction	0.0026 in. = 0.066 mm	0.00221 in. = 0.05613 mm	14.92% decrease

Tab. 7 - Total weight of building for nonlinear time history analysis without and with shear walls

	Without shear walls	With shear walls	Effect of hear walls
Total weight of building	9700 Kip = 43147.74 KN	10456 Kip = 46510.605 KN	7.79% increase

Interpretation of the Results

Tables 1 and 2 indicate that adding shear walls to the structure leads to a decrease of the structural time period ranging between nearly 59.6% and 84.3%, corresponding to an increase of the structure frequency ranging between approximately 148% and 255%.

As shown in Tables 3 and 4, shear walls result in the increase of the design base shear (45.35% in the *X* direction and 33.72% in the *Y* direction), and the base moment (52.34% in the *X* direction and 63.56% in the *Y* direction). Such increases will lead to a safer and more conservative design.

As it can be seen in Tables 5 and 6, the horizontal displacements and the inter-story drifts are significantly decreased when the shear walls are added. This data comparison is better represented in Figure 14 which charts in a bar graph to provide a clear understanding of the displacement of each floor in *X* and *Y* directions with and without any shear walls, and in Figure 15 which charts the drifts of various stories of the building. The addition of the shear walls causes a decrease in the joints maximum horizontal displacement in the *X* direction that ranges between 6.25% and 25.88%, and a decrease in joint maximum horizontal displacement in the *Y* direction ranging from 2.51% to 14.9%. Also, the decrease in floor drifts of the structure in the *X* direction ranges from 6.25% to 83.14%, and in the *Y* direction from 2.51% to 92.25%. These are considered significant improvements to the structure performance during such a powerful earthquake.

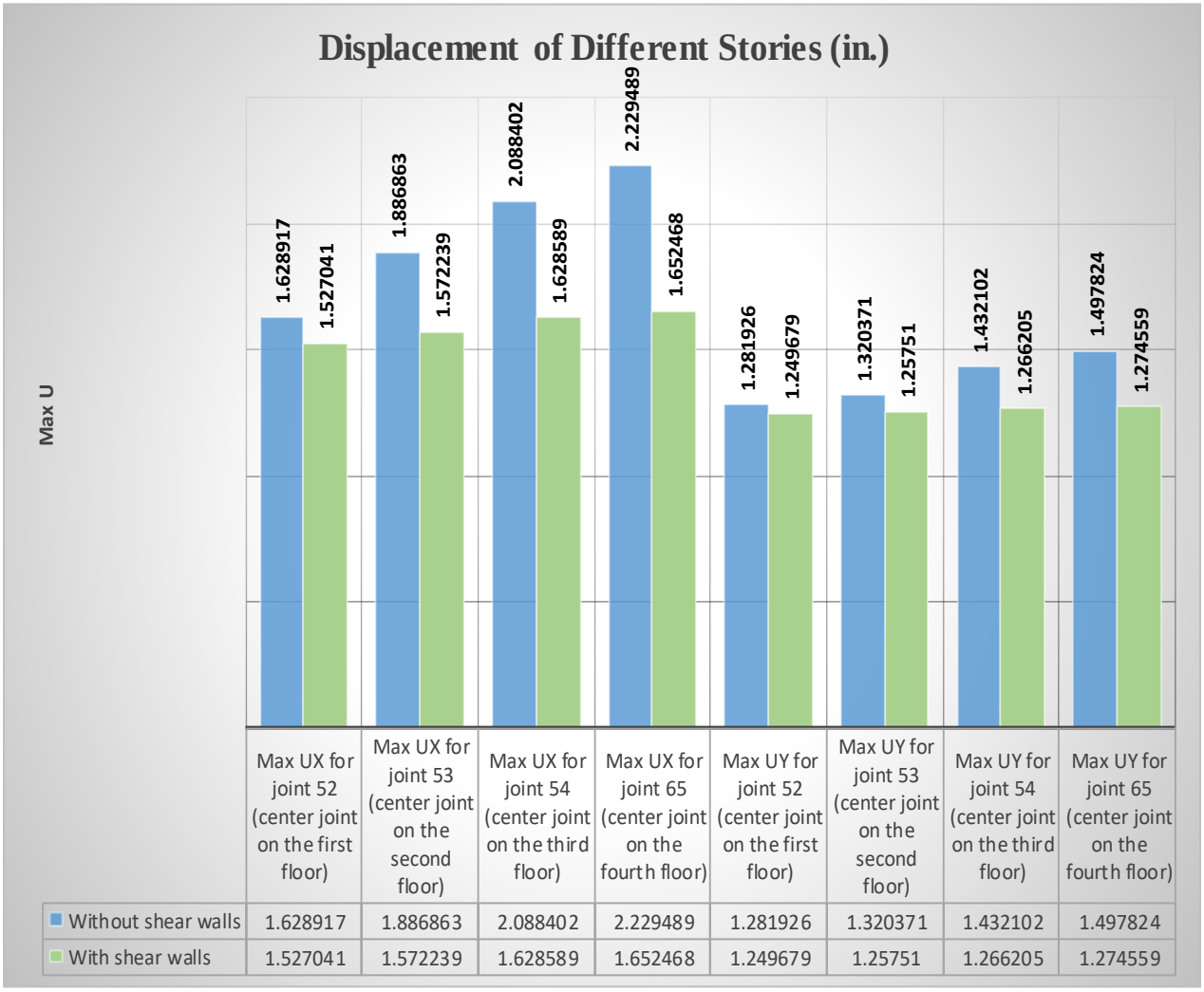

Fig. 14 - Story Displacements

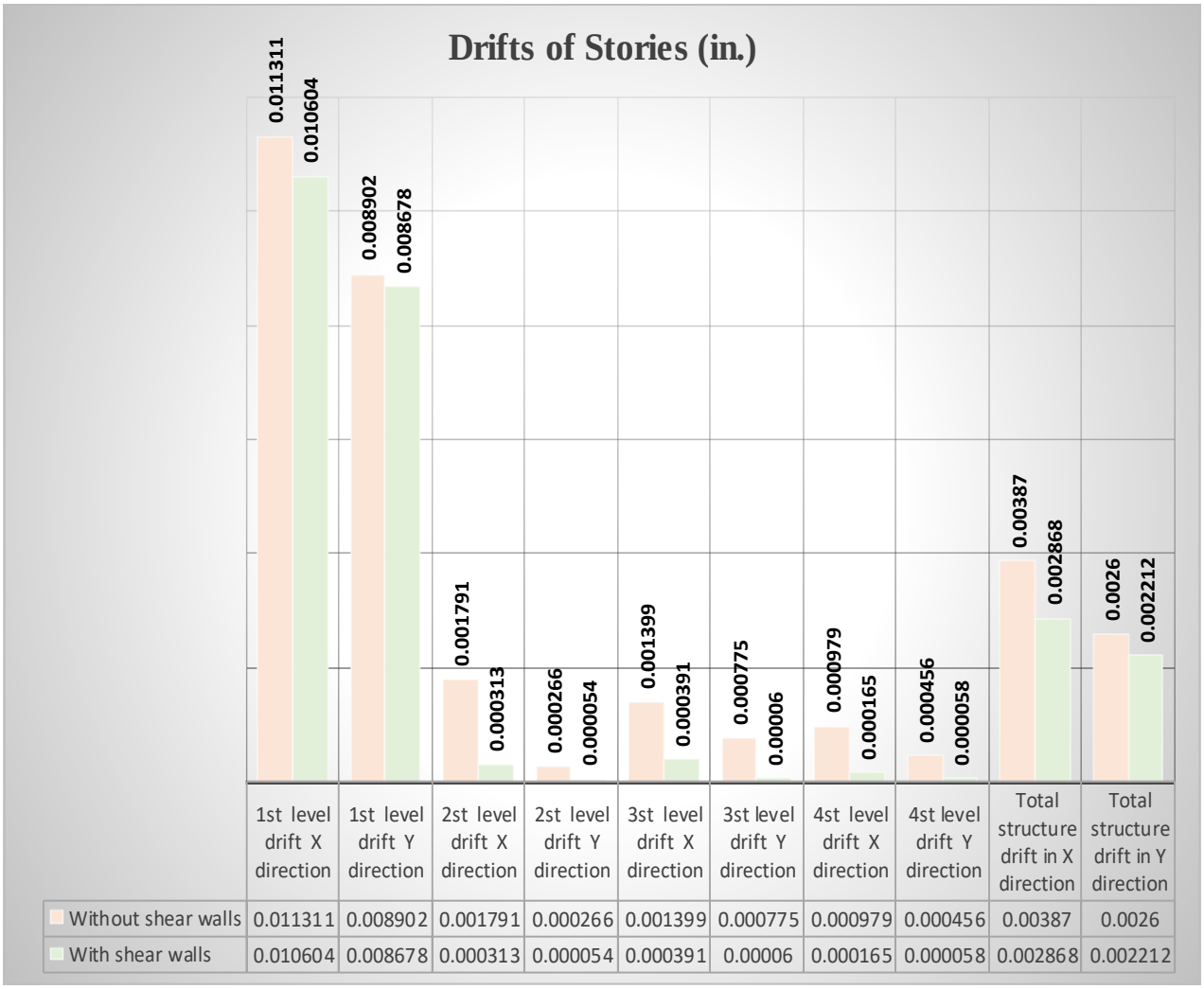

Fig. 15 - Story Drifts

It is clear from the above results that the improvements in the structure seismic resistance and performance are quite beneficial in exchange for the slight increase in the building weight (7.79% as shown in Table 7) when the shear walls are added.

CONCLUSION

This study analyzed a structure with and without any shear walls to determine the effects of shear walls on a building's response to a major earthquake event, the 2002 earthquake in Denali, Alaska. The structural frequency for various modes, design base shear, base moment, and the total weight of the building increased with shear walls, while structural time periods for various modes, maximum story displacements, and story drifts decreased significantly with shear walls. Response modal nonlinear time history analysis most accurately depicted structural behavior.

The results of this study showed that shear walls are necessary to resist lateral loads in a structure. In addition, the use of shear walls significantly reduces the horizontal displacements and drifts.

Nonlinear modal time history analysis, also called Fast Nonlinear Analysis (FNA), is more meticulous and effective than direct integration time history analysis. Numerical values and percent

of increase and decrease have been reported in the paper. Results also showed that shear walls significantly affect individual framing members and lead to an increase in column base shear force (up to 45.35%) and column base moments (up to 63.56%), as well as a decrease in horizontal displacements (up to 25.88%) and story drifts (up to 92.25%). It should be noted that maximum story drifts often govern the design according to most building codes.

REFERENCES

[1] Felber, Andreas J. 2017. Applied Time History Processing and Interpretation: Strong Motion Record Manipulation for Dynamic Analysis with Tips and Tricks for Data Evaluation. Vancouver, British Columbia: EDI Experimental Dynamic Investigations, Ltd.

[2] Schueller, Wolfgang. 2009. Building Support Structures: Analysis and Design Using SAP2000 Software. Berkeley, CA: Computer and Structures, Inc.

[3] Bhat M, Shyam, N.A.Premanand Shenoy, and Asha U Rao. 2014. "EARTHQUAKE BEHAVIOUR OF BUILDINGS WITH AND WITHOUT SHEAR WALLS." IOSR Journal of Mechanical and Civil Engineering (IOSR-JMCE) 3: 20–25. https://www.iosrjournals.org/iosr-jmce/papers/ICICE-2014/Volume-3/27.%20147%20S.pdf.

[4] Chandurkar, P. P., and P. S. Pajgade. 2013. "Seismic Analysis of RCC Building with and Without Shear Wall." International Journal of Modern Engineering Research (IJMER) 3 (3): 1805–10. http://www.ijmer.com/papers/Vol3_Issue3/DT3318051810.pdf.

[5] Chandana. Kurma, G. S. Vignan, and T. Sai Krishna Teja. 2018. "Non Linear Analysis of Multistoreyed Building with and without Shear Wall." International Journal of Engineering Research And V7 (01). https://doi.org/10.17577/ijertv7is010009.

[6] Tidke, Kiran, Rahul Patil, and G. R. Gandhe. 2016. "Seismic Analysis of Building with and Without Shear Wall." International Journal of Innovative Research in Science, Engineering and Technology 5 (10): 17852–58. https://doi.org/10.15680/IJIRSET.2016.0510080.

[7] Sanjeev, Lokesh. G, Sahebgouda Patil, and Lingaraj Shastri. 2017. "Dynamic Analysis of Multi Storied Building with and without Shear Wall and Bracing." GRD Journals- Global Research and Development Journal for Engineering 2 (9): 44–51. https://www.grdjournals.com/uploads/article/GRDJE/V02/I09/0034/GRDJEV02I090034.pdf.

[8] Eberhart-Phillips, D. 2003. "The 2002 Denali Fault Earthquake, Alaska: A Large Magnitude, Slip-Partitioned Event." Science 300 (5622): 1113–18. https://doi.org/10.1126/science.1082703.

[9] "2002 M7.9 Denali Fault Earthquake: Alaska Earthquake Center." n.d. 2002 M7.9 Denali Fault Earthquake | Alaska Earthquake Center. Accessed September 29, 2021. https://earthquake.alaska.edu/earthquakes/notable/2002-m79-denali-fault-earthquake.

[10] Zad, Nader, and Hani Melhem. 2021. "A Parametric Study on the Effects of Shear Wall Locations in a Typical Five-Story Reinforced Concrete Structure Subjected to a Severe Earthquake." Current Trends in Civil & Structural Engineering 7 (5): 1–15. https://doi.org/10.33552/CTCSE.2021.07.000675.

CIVIL ENGINEERING JOURNAL

Article no. 61

THE CIVIL ENGINEERING JOURNAL 4-2021

CRACK ANALYSIS OF RC BEAMS STRENGTHENED WITH CFRP STRIPS UNDER SECONDARY LOADING

Liu Jin-liang[1], Wang Jia-wei[2] and Jia Yan-min[1]

1. *Northeast Forestry University, School of civil engineering, Harbin, 150040, China; jinliangliu_2015@126.com*
2. *Liaoning communication planning and Design Institute Co., Ltd, Shenyang, 110166, China;18809859622@163.com*

ABSTRACT

The paper established the calculation formulas on the average crack spacing and the maximum crack width of CFRP（Carbon Fiber Reinforced Polymer）reinforced concrete beam under the secondary loading. Conversion of CFRP plate area into the reinforcement ratio of the reinforced beam, the calculation formula on the average crack spacing of CFRP reinforced concrete beam under the secondary loading was established. Based on calculation formula of the maximum crack width for concrete beam, the calculation formula on the maximum crack width of CFRP reinforced concrete beam under the secondary loading was established. The average crack spacing and the maximum crack width calculated by the formulas in the paper were compared with the test results, which verified that the formula is correct.

KEYWORDS

Carbon fiber reinforced polymer plates, Reinforced concrete beam, Secondary loading, Average crack spacing, Maximum crack width

INTRODUCTION

Strengthening with CFRP plate is a kind of new structure strengthening technology with fast research, application and development in the recent years. Compared with traditional reinforced methods, the method has such advantage as high strength, high efficiency, simple construction and excellent durability [1]. Due to the concrete structure has been subjected to load before reinforcement, there is a "stress hysteresis" phenomenon between the reinforcement material attached to the structural surface during the later loading process. Therefore, it is of great significance to the analysis of the structural characteristics of CFRP reinforced concrete beams under secondary loads. When a bridge structure is reinforced, besides bearing its own weight and the constant load of the superstructure, it may also bears vehicle load; for the structures such as beam and plate of a house building, when bearing their own weights, they may bear some loads hard to unload (such as plate decoration layer and fixed equipment, etc.). China Association for Engineering Construction Standardization points out that [2], when the initial bending moment is less than 20% of the bending bearing force of the unreinforced section, the effect of the "stress hysteresis" on the bearing force is negligible; while ACI440 committee and FIB consider the effect of the "stress hysteresis" on the bearing force when calculating bearing force in the relevant specifications [3,4].

As for the destruction theory of the reinforced structure under the secondary loading, the scholars conducted a lot of tests and finite element analyses, researched the stress characteristics of the reinforced structure under the secondary loading and the calculation model on bearing capacity, and the structural safety of the CFRP reinforced beam under secondary loading was guaranteed [5-8]. However, the analysis and calculation of the crack width of the reinforced beam

under the secondary loading were seldom studied. Zhuang et al. [9] carried out a research for the calculation method of crack width of CFRP reinforced concrete beam, and on basis of the *Design Code for Concrete Structure* [10], they proposed the calculation formulas on the average crack spacing and crack width that similar to ordinary reinforced concrete beam crack calculation method; Tan et al. [11] deduced the calculation formulas on the average crack spacing and width of CFRP reinforced concrete beam on basis of the bonding-slippage theory, proposed a theoretical analysis method applicable for calculating the crack width of the CFRP reinforced concrete beam. However, the above scholars failed to consider the effect of the "strain hysteresis" in the calculation on the average crack spacing and the crack width of the reinforced beam. The paper will consider the effect of "strain hysteresis" on the reinforced beam, establish a calculation model on the average crack spacing and maximum crack width of CFRP reinforced concrete beam under the secondary loading.

TEST ON BEARING CAPACITY OF CFRP REINFORCED BEAM

The loading test of CFRP reinforced beam

In order to research the effect of CFRP plates on structural stress characteristics and crack development under the secondary loading of CFRP reinforced concrete beam. The authors of this paper takes two pieces of 16 m pre-stressed hollow slab beams removed from a highway in Shenyang of China. The two pieces of old beam had served for 20 years, the parameters of the reinforced beams are approximate to the actual bridge beams and the test results are more applicable. The test beam adopts C40 concrete, the longitudinal reinforcement adopts HRB335, with a diameter of 12 mm; the stirrup adopts R235, with a diameter of 8 mm; and the pre-stressed reinforcement of the test beam applies ϕ_j15.24（7ϕ5）type, the standard strength is 1,860MPa and the tensioning control stress is 1,395Mpa, the elasticity of reinforcements are 200 GPa. The width of the hollow slab was 99 cm and the height was 70 cm. The center hollow section was a circle with a diameter of 50 cm; the thickness of the top plate was 8 cm and the thickness of the floor was 12 cm. The longitudinal design construction length was 1596 cm; the distance from the centerline of bearing to the end was 18 cm.

In order to simulate the load that is hard to unload in bridge, the concrete with 10 cm thick was poured on the test beams and linked with the beam by bonded reinforcements. Two 0.111x200 mm CFRP plates were pasted on the bottom of the test beam to improve the bearing capacity of the test beam, the elasticity of CFRP plates are165 GPa, the test beam was named as "CFRP beam". In order to contrast the CFRP reinforced effect, one piece of unreinforced test beam, which was named as "non CFRP beam", was taken as the contrast beam. Bending destruction test was conducted for two pieces of test beam. The test of bending failure was carried out to obtain the stress characteristics and crack development of the two test beams under the secondary load. Reinforcement design of test beams and test loading layout are shown in Figure. 1 and Figure 2.

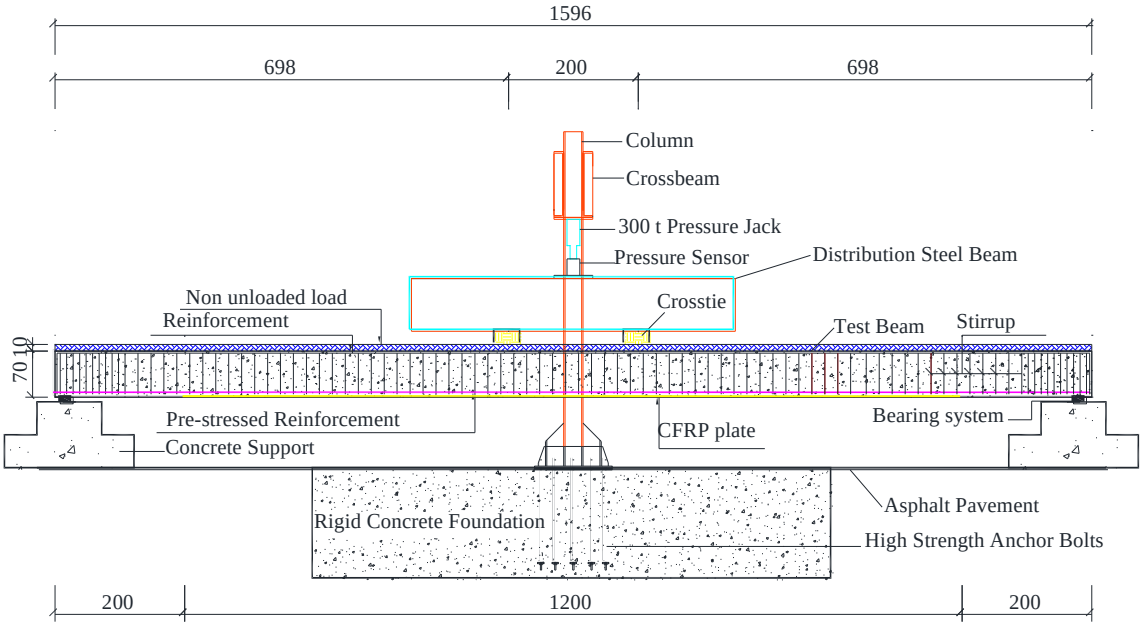

Fig. 1 - Test set-up of the test beam (unit: cm)

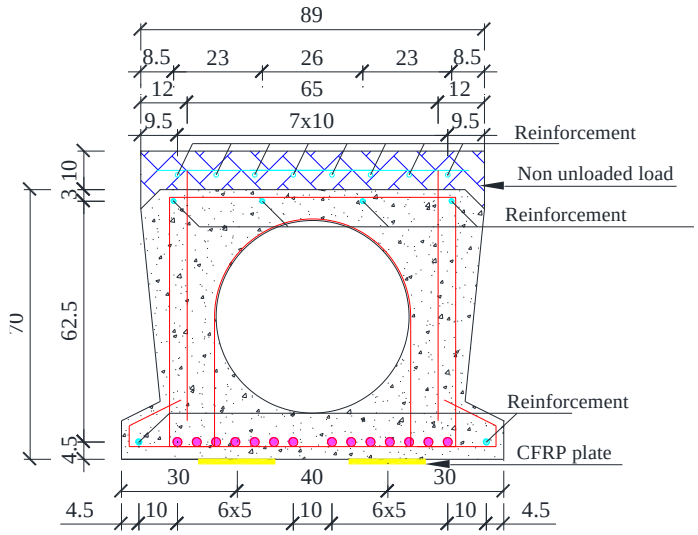

Fig. 2 - Cross section for the test beam (unit: cm)

The results analysis on CFRP reinforced beam under secondary loading test

In order to research the effect of CFRP plates on structural stress characteristics and crack development under the secondary loading of CFRP reinforced concrete beam, a pressure sensor was adopted to record the test load in the loading process of two pieces of beam, the strain of reinforcement and pre-stressed reinforcement at the mid span section was recorded by the reinforcement strain gauge, concrete strain gauges were stuck on the surface of the mid span section to record the strain of concrete, the displacement of the mid span was recorded by the displacement sensor arranged at the mid span section; the surface observation method was adopted to observe the crack development and a crack width gauge was used to measure the maximum crack width of the test beam under all levels of load.

The test beams were loaded for bending test. When the load reached 213 kN, the non CFRP beam cracked, following the continual increase of test load, new crack constantly appeared, and the crack width quickly increased. The concrete strain at the top edge of the mid span section, the strain of reinforcement & pre-stressed reinforcement and displacement changed from linear increase to nonlinear development. For CFRP beam, when the test load reached 308 kN, a crack appeared at the bending position. After a crack appeared, the linear development of the concrete strain at the top edge of the mid span section, the strain of reinforcement & pre-stressed reinforcement and displacement were destroyed, however, the development speed was lower than that of the non CFRP beam. The CFRP plate debonded occurred at the bottom of CFRP beam when the test load reached 480 kN, as shown in Figure 3. After the bond of CFRP plates were damaged, the growth of the crack width and the stress characteristics of structure quickly increased, finally, the destruction loads of the two pieces of beam became basically same. Therefore, the effect of CFRP plates on structural stress characteristics and crack development of the reinforced beam under the secondary loading within the scope of 480 kN will be discussed. Figure 4 gives the contrast of the two pieces of test beams on the stress characteristics and the development of crack width under the secondary load.

Fig. 3 - Photograph of the test in progress

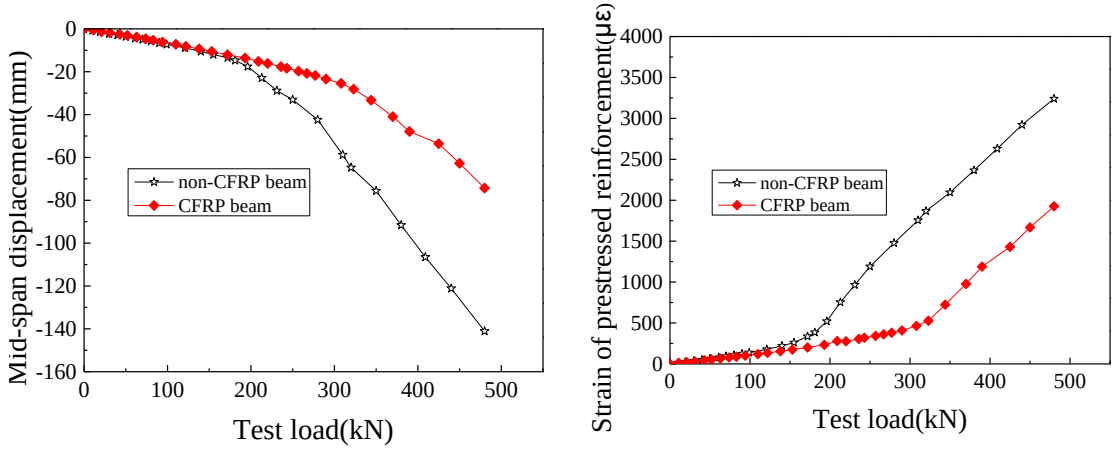

(a) Mid-span displacement *(b) Strain of pre-stressed reinforcement*

Fig. 4 - Comparison of non-CFRP and CFRP beam on stress characteristics and width of crack

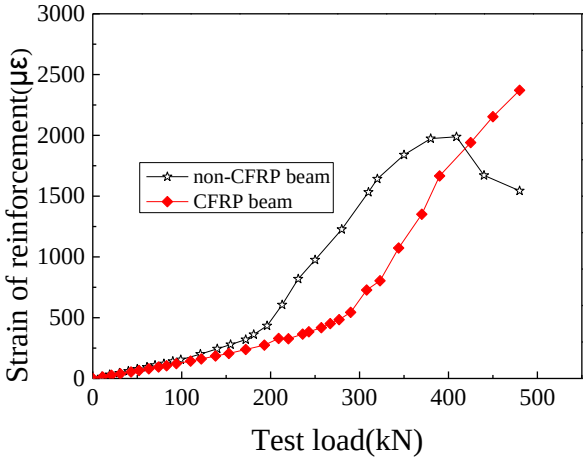

(c) Strain of reinforcement

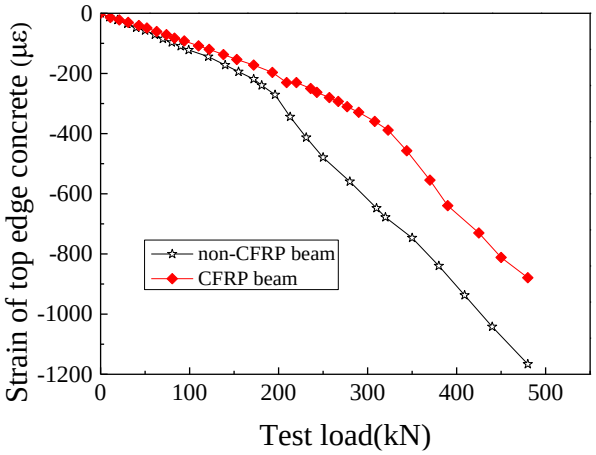

(d) Strain of top edge concrete

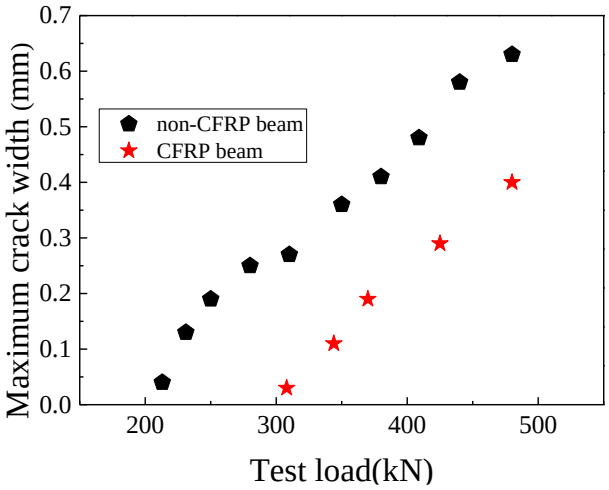

(e) Maximum crack width

Fig. 4 - Comparison of non-CFRP and CFRP beam on stress characteristics and width of crack

In Figure 4, before the cracking load was reached, the stress characteristics of the test beam developed linearly, and value of the stress characteristics for the non-CFRP and the CFRP beam were same. Following continual increase of load, the non-CFRP beam cracked firstly, this shows that CFRP plate strengthening can increase the cracking load of the reinforced beam. After the test beam cracked, the development speed of the stress characteristics of the non-CFRP beam was apparently higher than that of the CFRP beam, this shows that CFRP plate can effectively increase the stress characteristics of the cracked concrete beam. As for the crack width of the test beam, the development speed of the maximum crack width of CFRP beam was less than the non-CFRP beam after structure cracked, this shows that CFRP plate can restrict the development of the crack width of the reinforced beam. As for the average crack spacing of the test beams, the measured average crack spacing of the non-CFRP beam was 197 mm, while the CFRP beam was 184 mm, this shows that CFRP plate can deduce the average crack spacing and crack width on the surface of the reinforced beam.

Form the results of the test, CFRP plate can reduce the stress characteristics and development of the crack of the reinforced beams under the secondary loading. Therefore, it is significance to research the crack of CFRP reinforced concrete beam under the secondary loading, which can provide experience for the design of CFRP reinforced beams. In order to establish and verify the calculation formula on the crack spacing and width of crack under the secondary loading,

the crack data of CFRP reinforced beams under secondary load were collected in this paper [12-14]. The parameters of the CFRP reinforced beams are shown in Table 1.

Tab. 1 - Parameters of beams

Test	Name of Beam	f_{cu} (MPa)	f_{ct} (MPa)	A_f (mm^2)	E_f (GPa)	f_{fu} (MPa)
Li	L1-1-1a	34.4	2.20	11.1	212	3500
	L1-1-2a	34.4	2.20	11.1	212	3500
	L1-2-1b	34.4	2.20	11.1	212	3500
	L1-2-2b	34.4	2.20	11.1	212	3500
	L1-2-3b	34.4	2.20	11.1	212	3500
	L2-2-2c	34.4	2.20	11.1	212	3500
	L2-2-3c	34.4	2.20	11.1	212	3500
Huang	LB-2-2	36.1	2.26	33.4	220	3500
	LB-3-2	36.1	2.26	33.4	220	3500
Bu	RCFP-2	23.4	1.78	200	165	2800
	RCFP-3	24.4	1.82	200	165	2800
	RCFP-4	25.4	1.86	200	165	2800
This paper	CFRP beam	26.8	1.92	400	165	2800

Notes: f_{cu} is the ultimate compressive strength of concrete; f_{ct} is the ultimate tensile strength of concrete; A_f is the area of CFRP section; E_f is the elasticity modulus of CFRP; f_{fu} is the ultimate tensile strength of CFRP.

ANALYSIS ON AVERAGE CRACK SPACING

The existing research shows that the average crack spacing is only related to the ratio of reinforcement, area of CFRP section and the thickness of concrete protection layer [12]. Therefore, the effect of "stress hysteresis" is not considered when establishing the calculation formula for the crack spacing of CFRP reinforced beams under secondary loading. Suppose that the stress of reinforcement and CFRP plate at the section of the first crack are respectively σ_{s1} and σ_{f1}. The stress of concrete, reinforcement and CFRP plate at the other section where a crack will appear are respectively f_t, σ_{s2} and σ_{f2}. The bond stress between reinforcement and concrete, CFRP plate and concrete are respectively τ_s and τ_f. The second crack will appear within the average bond transfer length l_{mf}. Figure 5 shown the calculation model on average crack spacing, and the balance condition between the existing crack and the section where a crack will appear as follows:

$$\sigma_{s1}A_s + \sigma_{f1}A_f = \sigma_{s2}A_s + \sigma_{f2}A_f + f_tA_c. \quad (1)$$

For the reinforcement isolator as shown in Figure 5(b),

$$(\sigma_{s1} - \sigma_{s2})A_s = \tau_s C l_{mf}. \quad (2)$$

For the CFRP isolator as shown in Figure 5(c),

$$(\sigma_{f1} - \sigma_{f2})A_f = \tau_f b_f l_{mf}. \quad (3)$$

In the formula, C is the perimeter of reinforcement; b_f is the sticking width of CFRP plate.

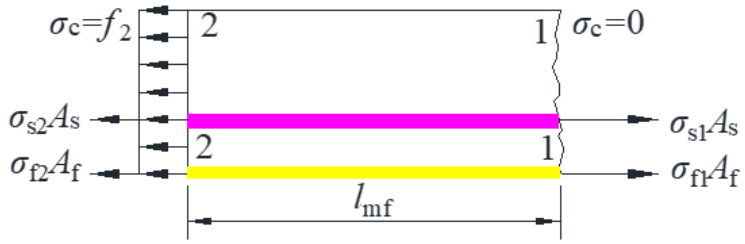

(a) Stress balance between cracks

(b) Stress balance of reinforcement between cracks

(c) Stress balance of reinforcement CFRP plate between cracks

Figure 5 Calculation model on average crack spacing

From Formula (1) to (3), it can be gotten that:

$$f_t A_c = 4\tau_s \frac{A_s + A_f}{d} l_{mf} \left[1 + \frac{A_f}{A_s + A_f} \frac{\tau_f d / (4t_f) - \tau_s}{\tau_s} \right]. \tag{4}$$

Suppose $l_m = \left[1 + \frac{A_f}{A_s + A_f} \frac{\tau_f d / (4t_f) - \tau_s}{\tau_s} \right] l_{mf}$, then,

$$l_m = \frac{f_t A_c}{4\tau_s (A_s + A_f)/d} = \frac{1}{4} \frac{f_t}{\tau_s} \frac{A_c d}{A_s + A_f} = \frac{1}{4} \frac{f_t}{\tau_s} \frac{d}{\rho_f}. \tag{5}$$

In the formula, ρ_f is comprehensive effective reinforcement ratio, $\rho_f = (A_s + A_f)/A_c$; d is the diameter of reinforcement; t_f is thickness of CFRP plate.

The expression of the average crack spacing of the reinforced concrete beams in the Formula (5) is same as *Concrete Structure Design Specification GB 50010-2015*, the expression of average crack spacing of the concrete beam is shown as follows:

$$l_m = 1.9c + 0.08 \frac{d}{\rho_{te}}. \tag{6}$$

In the formula, c is the thickness of the protective layer of reinforcement (mm); for reinforced concrete beam, ρ_{te} is the effective reinforcement ratio of the reinforcement.

For CFRP reinforced beam, the effect of CFRP in the tensile zone should be considered. Calculation of effective reinforcement ratio of CFRP plate according to the principle of effective reinforcement ratio of reinforcement. Thus, the calculation formula of ρ_{te} after strengthening is shown as follows:

$$\rho_{te} = \rho_{ste} + \rho_{fte}. \tag{7}$$

$$\rho_{ste} = \frac{A_s}{0.5bh + (b_f - b)h_f}. \tag{8}$$

$$\rho_{fte} = \frac{A_f}{0.5bh + (b_f - b)h_f}. \tag{9}$$

In the formula, ρ_{ste} is the effective reinforcement ratio of reinforcement in the reinforced beam; ρ_{fte} is the effective reinforcement ratio of CFRP plate in the reinforced beam; h is the height of section; b is the width of section; b_f is width of the tensile flange; h_f is the height of the tensile flange.

According to the research achievements of the Ref. [15], the bond strength τ_f of CFRP and concrete is proportional to the tensile strength f_t of concrete, thus the strengthening influence coefficient β is introduced:

$$\beta=\frac{A_f}{A_s+A_f}\left(\frac{\tau_f d/(4t_f)-\tau_s}{\tau_s}\right)=\frac{A_f}{A_s+A_f}\left(k_f\frac{d}{t_f}-1\right). \quad (10)$$

In the formula, $k_f=\tau_f/(4\tau_s)$ is the coefficient of bonding action between CFRP plate and concrete. By the above analysis, the relationship between the average crack spacing l_{mf} of the CFRP reinforced concrete beam and the average crack spacing l_m of the unreinforced concrete beam is shown as follows:

$$l_{mf}=\frac{l_m}{1+\beta}. \quad (11)$$

According to Formula (10), β is relevant to the tensile strength of concrete and the area ratio of CFRP plate and reinforcement. By the comparison between the actually measured average crack spacing l_{mf} of CFRP plate reinforced concrete beam and the calculation value l_m in Formula (6), β value can be attained. Then, by utilizing Formula (10), the value of k_f can be solved. The calculation result is shown in Table 2.

Tab. 2 - Calculation results of average spacing of test beam cracks

Name of Test Beams	l_{mf} (mm)	c (mm)	d (mm)	ρ_{ste}	ρ_{fte}	A_f (mm²)	A_s (mm²)	A_f/A_s	l_m (mm)	k_f
L1-1-1a	112	20	12	1.21%	0.06%	11.1	226	0.049	113.92	0.0126
L1-1-2a	111	20	12	1.21%	0.06%	11.1	226	0.049	113.92	0.0144
L1-2-1b	105	20	12	1.21%	0.06%	22.2	226	0.098	110.52	0.0294
L1-2-2b	103	20	12	1.21%	0.06%	22.2	226	0.098	110.52	0.0336
L1-2-3b	107	20	12	1.21%	0.06%	22.2	226	0.098	110.52	0.0253
L2-2-2c	79	20	12	1.21%	0.06%	22.2	402	0.055	80.43	0.0187
L2-2-3c	80	20	12	1.21%	0.06%	22.2	402	0.055	80.43	0.0153
LB-2-2	95	25	12	1.70%	0.17%	33.4	339	0.099	99.06	0.0273
LB-3-2	93	25	12	1.70%	0.17%	33.4	339	0.099	99.06	0.0319
RCFP-2	157	30	22	1.22%	0.27%	200	917	0.218	175.17	0.0748
RCFP-3	163	30	22	1.22%	0.27%	200	917	0.218	175.17	0.0644
RCFP-4	161	30	22	1.22%	0.27%	200	917	0.218	175.17	0.0678
CFRP beam	184	35	15.2	0.84%	0.17%	400	1960	0.204	187.33	0.0986

Note: l_{mf} is the average crack spacing of the test beam; l_m is the average crack spacing calculated as Formula (6).

The bonding strength of CFRP plate and concrete is directly proportional to the tensile strength of concrete, therefore, k_f should be a constant. However, there are many factors affecting the bonding strength between CFRP plate and concrete, such as reinforcement and CFRP plate

slippage, etc. In addition, A_f / A_s also affect the bonding strength. By the linear fitting for the data of test beams, as shown in Figure 6, the relationship between k_f and A_f / A_s is shown as follows:

$$k_f = 0.337 A_f / A_s . \quad (12)$$

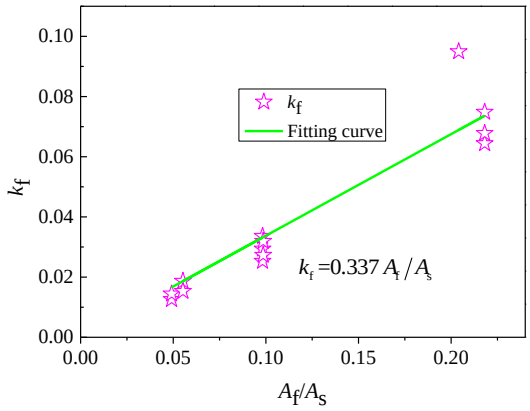

Fig. 6 - Linear fitting graph of k_f and A_f / A_s

As the relationship between k_f and A_f / A_s is obtained, and the β can be calculated by Formula (10), so the average crack spacing of the CFRP plate reinforced concrete beam l'_{mf} could be gotten by Formula (11), which used with the newly calculated β. The l'_{mf} is compared with the test result, as shown in Tab. 3. In the Tab. 3, the average ratio between the calculation value and the test results is 0.995, the average square error is 0.222, the calculation value is quite in agreement with the test results.

Tab. 3 - Comparison of average crack spacing between calculation value and test result

Test	Name of test beams	l_{mf} (mm)	l_m (mm)	l'_{mf} (mm)	l'_{mf} / l_{mf}
Li	L1-1-1a	112	113.917	110.108	0.983
	L1-1-2a	111	113.917	110.108	0.992
	L1-2-1b	105	110.522	103.671	0.987
	L1-2-2b	103	110.522	103.671	1.007
	L1-2-3b	107	110.522	103.671	0.969
Huang	L2-2-2c	79	80.433	79.175	1.002
	L2-2-3c	80	80.433	79.175	0.990
	LB-2-2	95	99.057	92.860	0.977
	LB-3-2	93	99.057	92.860	0.998
Bu	RCFP-2	157	175.174	158.915	1.012
	RCFP-3	163	175.174	158.915	0.975
	RCFP-4	161	175.174	158.915	0.987
This paper	CFRP beam	183	187.327	193.831	1.059

ANALYSIS ON CRACK WIDTH

Deformation relationship of section

Figure 7 shown the deformation relationship of section under the secondary loading. Before strengthening, under the action of the initial bending moment M_i, the compressive strain at the compressive edge of section is ε_{ci}, the strain of the tensile reinforcement is ε_{si}, the initial strain of the concrete at the tensile edge of section and also the hysteresis strain of the CFRP plate ε_i are calculated as follows [2]:

$$\varepsilon_i = \frac{h}{h_0}(\varepsilon_{ci} + \varepsilon_{si}) - \varepsilon_{ci}. \tag{13}$$

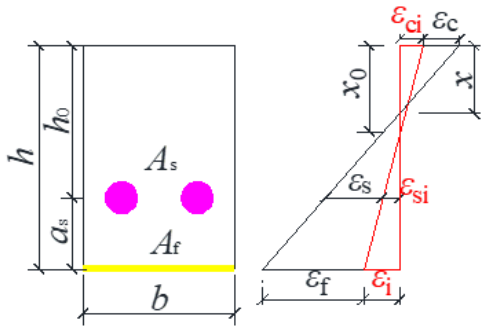

Fig. 7 - Deformation relationship of section under the secondary loading

After structure strengthening, under the action of the secondary bending moment M, the compressive strain at the compressive edge of section is ε_c, the strain of the tensile reinforcement is ε_s, the tensile strain of the CFRP plate is ε_f.

Stress of reinforcement at section

Figure 8 presents the stress distribution between cracks. As shown in Figure 8 (a), under the action of the bending moment M_k, the reinforcement stress is σ_{sk} and the CFRP plate stress is σ_{fk} at the cracked section. Between two cracks, the reinforcement stress is σ_s and the CFRP plate stress is σ_f. Fig.8 (b), (c) and (d) show the distribution of the stress of reinforcement and the compressive stress of concrete between the cracks of the reinforced beam.

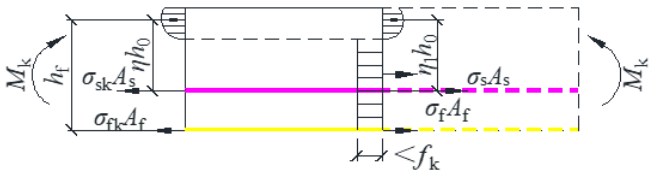

(a) Section stress

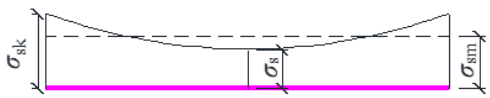

(b) Reinforcement stress

Fig. 8 - Stress distribution between cracks

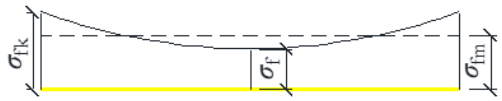

(c) Stress of CFRP plate

(d) Stress of concrete

Fig. 8 - Stress distribution between cracks

Suppose that the mean stress σ_{sm} of the reinforcement between the cracks of the reinforced beam is:

$$\sigma_{sm} = \psi_s \sigma_{sk}. \tag{14}$$

In the formula, ψ_s is the nonuniformity coefficient of the strain of the tensile reinforcement.

According to the past test researches [9], the relationship between the mean stress of reinforcement between cracks and the reinforcement stress at the middle section of crack is shown as follows:

$$\sigma_{sm} = 1.1\sigma_s. \tag{15}$$

According to Figure 8(a), the tensile stress of the section is supported by reinforcement, CFRP plate and concrete. If the resistance moment of reinforcement at this section is $M_s = A_s \sigma_s \eta_1 h_0$, the resistance moment of the concrete is M_{ct}, the resistance moment of CFRP plate is $M_f = A_f \sigma_f \left(\eta_1 h_0 + a_s\right)$, the nonuniformity coefficient of the strain of the tensile reinforcement is shown as follows:

$$\psi_s = 1.1\frac{\sigma_s}{\sigma_{sk}} = 1.1\left(\frac{M_k - M_{ct} - M_f}{A_s \eta_1 h_0 \sigma_{sk}}\right). \tag{16}$$

By taking $\eta = \eta_1 = 0.87$ [2], after simplified, the formula becomes:

$$\psi_s = 1.1 - \frac{0.65 f_{ct}}{\sigma_{sk}\rho_{ste} + \sigma_{fk}\rho_{fte}} = 1.1 - \frac{0.65 f_{ct}}{\sigma_{sk}\left(\rho_{ste} + \rho_{fte}\frac{E_f}{E_s}\right) + E_f \varepsilon_i \rho_{fte}}. \tag{17}$$

In order to attain the stress of reinforcement at the crack section for the reinforced beam, according to the deformation harmonization relationship between reinforcement and concrete shown in Figure 4, the moment of the sum of the concrete stress in the compressive zone can be attained and shown as follows:

$$M_k = A_s \sigma_{sk} \eta h_0 + A_f \sigma_{fk} \left(\eta h_0 + a_s\right). \tag{18}$$

Formula (13) and Formula (18) can be simplified according to the deformation relationship of the structure under the initial loading and the secondary loading shown in Figure 8, the stress of reinforcement at crack section is shown as follows:

$$\sigma_{sk} = \left(\frac{M_k}{A_s \eta h_0} + E_s \varepsilon_i\right)\left(\frac{1}{1 + \frac{A_f}{A_s}\frac{E_f}{E_s}}\right). \tag{19}$$

Calculation on the maximum crack of the reinforced beam

According to the calculation formula on the maximum crack width of the concrete beam in *Design Code for Concrete Structure* [10], the calculation formula of the maximum crack width of the CFRP plate reinforced beam can be attained as follows:

$$\omega_{\max} = 1.9\psi_s \frac{\sigma_{sk}}{E_s} l_{mf}. \quad (20)$$

In the above formula, ψ_s, σ_{sk} and l_{mf} are respectively calculated by Formula (17), (19) and (11), the calculated crack width and the crack width measured in test under the behaviors of different bending moment loads were compared in the Table 4.

Tab. 4 - Comparison between calculated and test value of maximum crack width

Test	Name of Test Beams	M_k ($kN \cdot m$)	ε_i	$\omega'_{\max}$ (mm)	$\omega_{\max}$ (mm)	$\omega'_{\max} / \omega_{\max}$
Li	L1-1-1a	57	0.000215	1.36	2.00	0.68
Huang	LB-2-2	15	0.000287	0.08	0.07	1.15
		20	0.000287	0.11	0.10	1.09
		25	0.000287	0.13	0.12	1.12
		30	0.000287	0.16	0.19	0.85
		40	0.000287	0.22	0.21	1.03
		50	0.000287	0.27	0.21	1.29
		55	0.000287	0.30	0.23	1.28
		60	0.000287	0.33	0.29	1.12
		65	0.000287	0.35	0.31	1.14
		70	0.000287	0.38	0.31	1.22
		75	0.000287	0.41	0.33	1.23
		80	0.000287	0.43	0.36	1.20
	LB-3-2	15	0.000338	0.09	0.07	1.26
		20	0.000338	0.12	0.10	1.19
		25	0.000338	0.15	0.12	1.25
		30	0.000338	0.18	0.19	0.95
		40	0.000338	0.24	0.26	0.93
		50	0.000338	0.30	0.26	1.17
		55	0.000338	0.33	0.27	1.24
		60	0.000338	0.36	0.29	1.25
		65	0.000338	0.40	0.32	1.23
		70	0.000338	0.43	0.34	1.25
		75	0.000338	0.46	0.37	1.23
		80	0.000338	0.49	0.39	1.25
Bu	RCFP-2	117	0.000177	0.12	0.13	0.93

		135	0.000177	0.14	0.15	0.93
		150	0.000177	0.16	0.18	0.87
		165	0.000177	0.17	0.35	0.49
	RCFP-3	117	0.000753	0.12	0.11	1.13
		135	0.000753	0.15	0.12	1.21
		150	0.000753	0.16	0.16	1.02
		165	0.000753	0.18	0.25	0.72
	RCFP-4	117	0.001615	0.13	0.10	1.25
		135	0.001615	0.14	0.11	1.31
		150	0.001615	0.16	0.14	1.15
		165	0.001615	0.18	0.16	1.10
This test	CFRP beam	308	0.001577	0.03	0.03	1.00
		344	0.001577	0.09	0.11	0.82
		370	0.001577	0.17	0.19	0.89
		425	0.001577	0.28	0.29	0.97
		480	0.001577	0.39	0.4	0.98

By the comparison of the results, the mean ratio of the calculation value and test results was 1.080, the mean square error is 0.186. Therefore, it can be known that the crack calculation formula on the CFRP plate reinforced beam under the secondary loading proposed in the paper is correct.

CONCLUSION

By carrying out the bending destruction tests on two pieces of test beams in the paper, it was found that CFRP plate can apparently improve the stress characteristics of the reinforced beam under the secondary loading, restrict the development of average crack spacing and crack width. Based on the crack calculation formula of concrete beam, the calculation formula on the average crack spacing and the maximum crack width of CFRP plate reinforced concrete beam under the secondary loading were established, the calculation result is well in agreement with the test results. The calculation formula is simple and could be used for the design on the CFRP plate reinforced concrete beam.

ACKNOWLEDGEMENTS

This work is financially supported by “the Fundamental Research Funds for the Central Universities” (Grant no. 2572021BJ01) and “Funding for doctoral education in Heilongjiang Province” (Grant no. LBH-Z20036).

REFERENCES

[1] Cheng DH, Ye X, Zhang LB. (2013), “Research of mechanical properties on loaded concrete beam reinforced with prestressed CFRP plate” *China Civil Engineering Journal*, (S1): 319-328.

[2] China Association for Engineering Construction Standardization. (2003), “Technical specification for strengthening concrete structures with carbon fiber reinforce polymer laminate (CECS 146:2003)” *China Planning Press.*

[3] Triantafillou T, Matthys S, Audenaert K, et al. (2001), “Externally bonded FRP reinforcement for RC structures” *International Federation for Structural Concrete (fib)*.
[4] 440 ACI C. (2004), “Guide for the design and construction of externally bonded FRP systems for strengthening concrete structures” *American Concrete Institute*.
[5] Liu XP, Guo C. (2014), “Finite element analysis of reinforce RC beams considering loading history with Pre-Stressed CFRP plates” *Advanced Materials Research*, v 1025-1026, p 862-867.
[6] Cheng J, Wang RH, Jia B. (2011), “Finite-element analysis for CFRP reinforced old RC beam under secondary loading” *Advanced Materials Research*, v 243-249, p 5531-5535.
[7] Jiang SH, Hou JG, He YM. (2015), “Reliability research of serviceability limit states for RC beams strengthened with prestressed CFRP plates considering prestress loss” *China Civil Engineering Journal* ,(11):36-43.
[8] Wang MR. (2013), “Calculation of flexural bearing capacity of reinforced concrete beams strengthened with CFRP plates considering under secondary loading” *Journal of China & Foreign Highway*,(06):102-106.
[9] Zhuang JB, Ye LP, Bao YZ, Wu YB. (2006), “Crack width of reinforced concrete beams strengthened with CFRP plates” *Journal of Southeast University (Natural Science Edition)*, (01):86-91.
[10] Ministry of Construction of China (2010), “GB 50010-2010. Design Code for Concrete Structure” *China Architecture & Building Press*.
[11] TAN J, ZHENG WZ, WANG Y. (2010), “Calculation method of creak width of concrete beams strengthened with CFRP sheet” *Journal of Harbin Institute of Technology*, (02): 180-185.
[12] Li ZJ. (2006), “Testing Research and Numerical Analysis on Flexural Behaviors of CFRP Strengthened Reinforced Concrete Beams Under Secondary Load” *Master Dissertation of Zhengzhou University*.
[13] Huang N. (2015), “The Research of Flexural behaviors of RC beams Strengthened with CFRP under Secondary Loading” *Master Dissertation of Ningbo University*.
[14] BU LT, SONG L, SHI CX. (2007), “Experimental and theoretical study on flexural behavior of RC beams strengthened with carbon fiber plates (CFP)” *Journal of Building Structures*,(01):72-79.
[15] LU XZ, TENG JG, YE LP, JIANG JQ. (2006), “Finite Element Analysis of Intermediate Crack-Induced Debonding in FRP Strengthened RC Beams” *Engineering Mechanics*, (06):85-93.

CIVIL ENGINEERING JOURNAL

Article no. 62

THE CIVIL ENGINEERING JOURNAL 4-2021

IMPROVED ANALYSIS OF A PROPPED CANTILEVER UNDER LATERAL VIBRATION

Victor O. Okonkwo [1], Chukwurah H. Aginam[1] and Charles M. O. Nwaiwu[1]

Nnamdi Azikiwe University, Faculty of Engineering, Department of Civil Engineering, P.M.B. 1105 Awka, Nigeria; vo.okonkwo@unizik.edu.ng

ABSTRACT

Continuous systems can be analysed as lumped masses connected by massless elements. This reduces the structure's degree of freedom and therefore simplifies the analysis. However, this over simplification introduces an error in the analysis and the results are therefore approximate. In this work, sections of the vibrating beam were isolated and the equations of the forces causing vibration obtained using the Hamilton's principle. These forces were applied to the nodes of an equivalent lumped mass beam and the stiffness modification needed for it to behave as a continuous beam obtained. The beam's stiffness was modified using a set of stiffness modification factors $\phi_1$to ϕ_4. It was observed that by applying these factors in the dynamic analysis of the beam using the Lagrange's equation, we obtain the exact values of the fundamental frequency irrespective of the way the mass of the beam was lumped. From this work we observed that in order to obtain an accurate dynamic response from a lumped mass beam there is need to modify the stiffness composition of the system and no linear modification of the stiffness distribution of lumped mass beams can cause them to be dynamically equivalent to the continuous beams. This is so because the values of the modification factors obtained for each beam segment were not equal. The stiffness modification factors were obtained for elements at different sections of the beam

KEYWORDS

Lagrange equations, Stiffness matrix, Inertia matrix, Lumped mass, Natural frequency

INTRODUCTION

Most imposed loads on structures are dynamic in nature. They either vary in time or in space. The structure therefore vibrates frequently under the effect of these loads. Structural and mechanical systems in general consist of structural components which have distributed mass and elasticity [1]. All bodies possessing mass and elasticity are capable of vibration [2, 3].The dynamic analysis of structures can be done using the Newton's equation of motion. This is possible for very simple structures with few degrees of freedom. But as the degrees of freedom increase the resulting equations become very cumbersome and an energy method is preferred [4].

The earliest energy method for such analysis is the Lagrange's equations. These equations were formulated for lumped masses connected by massless elements [5]. The masses are assumed to be concentrated at specified points known as nodes. When used to model a system with a continuous distribution of mass, this method will give an approximate result. The accuracy of the results will however increase with an increase in the number of lumped masses and uniformity in their spacing. An increase in the number of lumped mass increases the size of the resulting matrix and hence the size of the required computational analysis. A better energy method is the Hamilton's principle. This is an extension of the principle of minimum potential energy. This method enables us to formulate partial differential equations for the analysis of the structure as uniform systems (i.e.

structures with uniformly distributed masses) [6, 7]. The results are exact. Its major drawback is that it is very difficult to formulate the differential equations of complex structural systems using this method.

The prevalence of computers has increased the use of numerical methods in structural analysis [8]. Finite difference method, Ritz method, Rayleigh-ritz method and finally the finite element method is today widely used in such analysis. The finite element method is the most popular and like the Ritz approach incorporates the use of shape function. These shape functions are used to formulate inertia matrix known as the consistency matrix [9]. If the shape function is truly representative of the deformed shape of the structure, the consistency matrix should be equal to the equivalent mass matrix. The equivalent mass matrix for a segment of a continuous system is one that returns precisely the dynamic properties of the original segment in discretized form [10]. The power of the finite element method is further enhanced by its ability to subdivide the structure into finite elements, the smaller the size of the finite elements the better the results from their analysis. This has made it a widely applied tool in researches structural analysis [11, 12, 13]. However increasing the number of elements however increases the size of the matrices to analyze and therefore increases the computational cost.

Despite the rapid advances in these numerical approaches, the lumping of continuous masses has persisted due to its visual appeal and its simplification of the analysis. Mass lumping distorts the mass distribution and leads to a less representative inertia matrix [14]. This introduces an error in the analysis which ultimately affects the values of the computed natural frequencies of the structure. It has limited number of coordinates and may not fully account for the structural characteristics of a system accurately [15]. Despite these limitations It is still widely used in introductory topics in structural dynamics and in advanced research involving complex systems [16 - 19].

Efforts have been made in time past to generate better equivalent mass matrices for analysis of continuous systems [20, 21, 22]. Also Ericson and Parker [23] suggested that varying the stiffness of the structural system would lead to better analysis results. This was implemented for longitudinally vibrating bars using a set of two stiffness modification factors [24]. In this work, the variation of the structure's stiffness distribution as a means of nullifying the effect of lumping of continuous mass in laterally vibrating beams was explored.

Mathematical Theory

The partial differential equation governing the free lateral vibration of a beam is given by [26]

$$EIu^{IV} + \mu\ddot{u} = 0 \tag{1}$$

Where EI is the flexural rigidity of the beam and μ is its mass per unit length. For a harmonic vibration and by applying the boundary conditions for the beam we obtain four equations that can be solved numerically to give us the roots $\beta_j L$ from which the natural frequency of vibration ω_j is computed.

$$\beta^4 = \frac{\mu\omega^2}{EI} \tag{2}$$

The mode shape is obtained as [25]

$$\emptyset_j(x) = \cosh\beta_j x + b_{2j}\sinh\beta_j x - \cos\beta_j x + b_{4j}\sin\beta_j x \tag{3}$$

Where

$$b_{2j} = \frac{\cos\beta_j L - \cosh\beta_j L}{\sinh\beta_j L - \sin\beta_j L} \tag{4}$$

$$b_{4j} = \frac{\cosh \beta_j L - \cos \beta_j L}{\sinh \beta_j L - \sin \beta_j L} \quad (5)$$

Equation (3) is the equation of the j[th] mode of vibration of the fixed-pinned beam. The first mode of vibration (j = 1) can be obtained by substituting $\beta_j L = \beta_1 L = 3.92660232$ into (3). The second mode of vibration (j = 2) can be obtained by substituting $\beta_j L = \beta_2 L = 7.06858275$ into the equation. The general solution by mode superposition is [24][25]

$$u_1(x_1, t) = \sum_{j=1}^{\infty} \phi_j(x_1)\left(A_j \cos w_j t + B_j \sin w_j t\right) \quad (6)$$

Where the constants A_j and B_j can be determined from the initial conditions.

.

METHODS

The vibrations of structural systems are governed by two essential components; the structure's mass distribution and the structure's stiffness [24, 27]. These properties are represented by the structure's inertia matrix and stiffness matrix. If we alter the mass distribution we will expect a corresponding change in the stiffness distribution. The lumping of continuous mass at specified nodes alters the mass distribution (inertia matrix). There is need to find the corresponding modification in the stiffness distribution needed to restore the vibration characteristics of the system. This as in [24] was done by equating two equations. One is the force equilibrium equation while the other is the equation of motion of a vibrating system.

The force equilibrium equations and the equations of motion are force equations. Force equilibrium equations have been largely applied in statics [28]. Just as in [24]. It can also be applied in dynamics if the equations for the vector of fixed end moments/forces {F} are formulated. The structure with continuous mass distribution was analyzed using the Hamilton's principle and the equations for the fixed end forces {F} and nodal displacements {D} formulated for any arbitrary segment of a laterally vibrating beam at time t = 0. These were used to get the vector of nodal forces {P} causing the vibration.

The equations of motion were used to simulate the lumped mass beam. For a vibrating element of the real beam (beam with continuous mass) and that of a corresponding element of a lumped mass beam to be equivalent then their nodal deformation {D} and forces acting on their nodes {P} must be equal [24].

Figure 1 shows a propped cantilever beam under inertia forces. A segment of the beam shown is being restrained by the fixed end forces F_1 to F_4.

From the D'Alembert principle the forces on the vibrating beam can be calculated from its inertia force [29]. For an elementary part of the beam at a distance z from the origin this force is $\mu \ddot{u} dz$. (See Figure 1)

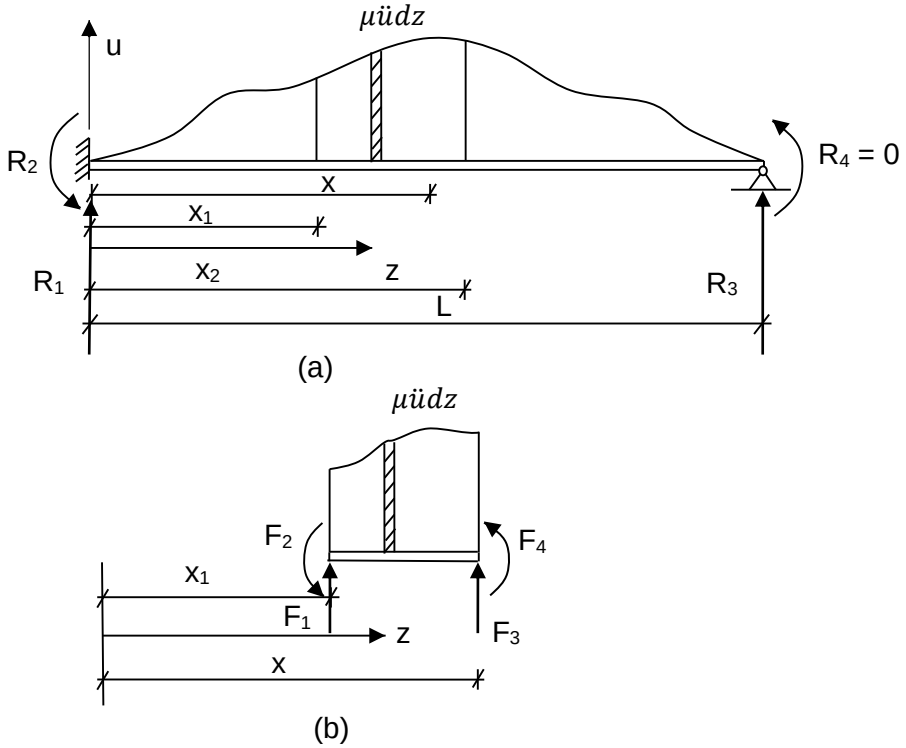

Fig. 1 - (a) A fixed-pinned beam under lateral vibration due to the inertial forces $\mu\ddot{u}$

(b) A segment of the beam under longitudinal vibration due to inertial forces $\mu\ddot{u}$

`

Using the principle of virtual work and the flexibility method we determine the fixed end forces F_1 to F_4 of the isolated element of the excited beam of Figure 1b to be

$$F_1 = -6\sum_{j=1}^{\infty}\frac{EIA_j}{L^3(\xi_2-\xi_1)^3}W_1 \tag{7}$$

$$F_2 = -2\sum_{j=1}^{\infty}\frac{EIA_j}{L^2(\xi_2-\xi_1)^2}W_2 \tag{8}$$

$$F_3 = \sum_{j=1}^{\infty}\frac{EIA_j}{L^3(\xi_2-\xi_1)^3}\Big[6W_1 + \beta_j^3L^3(\xi_2-\xi_1)^3\Big(\sinh\beta_jL\xi_2 - \sinh\beta_jL\xi_1 - \sin\beta_jL\xi_2 + \sin\beta_jL\xi_1 + b_{2j}\big(\cosh\beta_jL\xi_2 - \cosh\beta_jL\xi_1\big) - b_{4j}\big(\cos\beta_jL\xi_2 - \cos\beta_jL\xi_1\big)\Big)\Big] \tag{9}$$

$$F_4 = \sum_{j=1}^{\infty}\frac{EIA_j}{L^2(\xi_2-\xi_1)^2}\big[-6W_1 + 2W_2 - \beta_j^3L^3(\xi_2-\xi_1)^3\big(-\sinh\beta_jL\xi_1 - b_{2j}\cosh\beta_jL\xi_1 + \sin\beta_jL\xi_1 + b_{4j}\cos\beta_jL\xi_1\big) + \big(\cosh\beta_jL\xi_2 + b_{2j}\sinh\beta_jL\xi_2 + \cos\beta_jL\xi_2 - b_{4j}\sin\beta_jL\xi_2\big) - \big(\cosh\beta_jL\xi_1 + b_{2j}\sinh\beta_jL\xi_1 + \cos\beta_jL\xi_1 - b_{4j}\sin\beta_jL\xi_1\big)\big] \tag{10}$$

Where

$$W_1 = \beta_j^3L^3\Big(\frac{(\xi_2+\xi_1)(\xi_2^2-\xi_1^2)}{2} - \frac{2(\xi_2^3-\xi_1^3)}{3}\Big)\big(-\sinh\beta_jL\xi_1 - b_{2j}\cosh\beta_jL\xi_1 + \sin\beta_jL\xi_1 + b_{4j}\cos\beta_jL\xi_1\big) + b_{2j}\big(\beta L(\xi_1-\xi_2)\cosh\beta_jL\xi_2 + 2\sinh\beta_jL\xi_2 - \beta_jL(\xi_2-\xi_1)\cosh\beta_jL\xi_1 - 2\sinh\beta_jL\xi_1\big) -$$

$$b_{4j}\left(-\beta_j L(\xi_1-\xi_2)\cos\beta_j L\xi_2 - 2\sin\beta_j L\xi_2 + \beta_j L(\xi_2-\xi_1)\cos\beta_j L\xi_1 + 2\sin\beta_j L\xi_1\right) + \beta_j L(\xi_1 - \xi_2)\sinh\beta_j L\xi_2 - \beta_j L(\xi_2-\xi_1)\sinh\beta_j L\xi_1 + \beta_j L(\xi_1-\xi_2)\sin\beta_j L\xi_2 - \beta_j L(\xi_2-\xi_1)\sin\beta_j L\xi_1 + 2\cosh\beta_j L\xi_2 - 2\cosh\beta_j L\xi_1 - 2\cos\beta_j L\xi_2 + 2\cos\beta_j L\xi_1 \quad (11a)$$

$$W_2 = \beta_j^3 L^3\left(\frac{(2\xi_2+\xi_1)(\xi_2^2-\xi_1^2)}{2} - \frac{\xi_1(\xi_2-\xi_1)^2}{2} - (\xi_2^3-\xi_1^3)\right)\left(-\sinh\beta_j L\xi_1 - b_{2j}\cosh\beta_j L\xi_1 + \sin\beta_j L\xi_1 + b_{4j}\cos\beta_j L\xi_1\right) - \left(\frac{\beta_j^2 L^2(\xi_2-\xi_1)^2}{2}\right)\left(\cosh\beta_j L\xi_1 + b_{2j}\sinh\beta_j L\xi_1 + \cos\beta_j L\xi_1 - b_{4j}\sin\beta_j L\xi_1\right) + \beta_j L(\xi_1-\xi_2)\sinh\beta_j L\xi_2 - 2\beta_j L(\xi_2-\xi_1)\sinh\beta_j L\xi_1 + \beta_j L(\xi_1-\xi_2)\sin\beta_j L\xi_2 - 2\beta_j L(\xi_2-\xi_1)\sin\beta_j L\xi_1 - 3\cos\beta_j L\xi_2 + 3\cos\beta_j L\xi_1 + 3\cosh\beta_j L\xi_2 - 3\cosh\beta_j L\xi_1 + b_{2j}\left(\beta_j L(\xi_1-\xi_2)\cosh\beta_j L\xi_2 - 2\beta_j L(\xi_2-\xi_1)\cosh\beta_j L\xi_1 + 3\sinh\beta_j L\xi_2 - 3\sinh\beta_j L\xi_1\right) - b_{4j}\left(-\beta_j L(\xi_1-\xi_2)\cos\beta_j L\xi_2 + 2\beta_j L(\xi_2-\xi_1)\cos\beta_j L\xi_1 - 3\sin\beta_j L\xi_2 + 3\sin\beta_j L\xi_1\right) \quad (11b)$$

$$\xi_1 = {}^{x_1}/_{L}\ ,\ \xi_2 = {}^{x_2}/_{L} \quad (12)$$

For us to be able to evaluate these equations (for the fixed end forces F_1, F_2, F_3 and F_4) there is need to derive an expression for A_j for a fixed-pinned beam.

Consider a uniform propped cantilever beam under the action of its self weight as shown in Figure 2. μ is the mass per unit length of the beam and *g* is the acceleration due to gravity.

From the equation of elastic curve and by considering the initial boundary conditions and the equation for the static deflection of the uniform beam under its self weight, let the initial deflection of the beam (at time t = 0) be

$$u(x,0) = bL\left(\frac{5x^3}{L^3} - \frac{2x^4}{L^4} - \frac{3x^2}{L^2}\right) \quad (13)$$

where *b* is a dimensionless constant equal to $\frac{\mu g L^3}{48EI}$.

Then from [19] by substituting equations (3) and (13)

$$A_j = \frac{\mu}{M_j}\int_0^L u(x,0)\emptyset_j\,dx = \frac{b\mu L^2}{M_j}\left[\frac{-(\cosh\beta_j L+\cos\beta L)}{\beta_j^2 L^2} + \frac{18(\cosh\beta_j L-\cos\beta_j L)}{\beta_j^4 L^4} - \frac{48(\sinh\beta_j L-\sin\beta_j L)}{\beta_j^5 L^5} + b_{2j}\left(\frac{-2(\sinh\beta_j L+\sin\beta_j L)}{\beta_j^2 L^2} + \frac{18(\sinh\beta_j L-\sin\beta_j L)}{\beta_j^4 L^4} - \frac{48(\cosh\beta_j L+\cos\beta_j L-2)}{\beta_j^5 L^5}\right)\right] \quad (14)$$

Equation (14) is an expression for the constant A_j for a propped cantilever beam under an initial lateral displacement caused by its self weight. It can be substituted into Equations (7) to (10) to obtain the values of the fixed end forces F_1, F_2, F_3 and F_4. With these equations the force equilibrium equations for segments of a vibrating beam can be written and the inherent nodal forces in the system that is causing motion calculated. An arbitrary segment of a vibrating element is identified by means of the normalized distances ξ_1 and ξ_2 of its nodes from an origin. Having obtained the fixed end forces, the vector of nodal forces {P} is obtained from the force equilibrium.

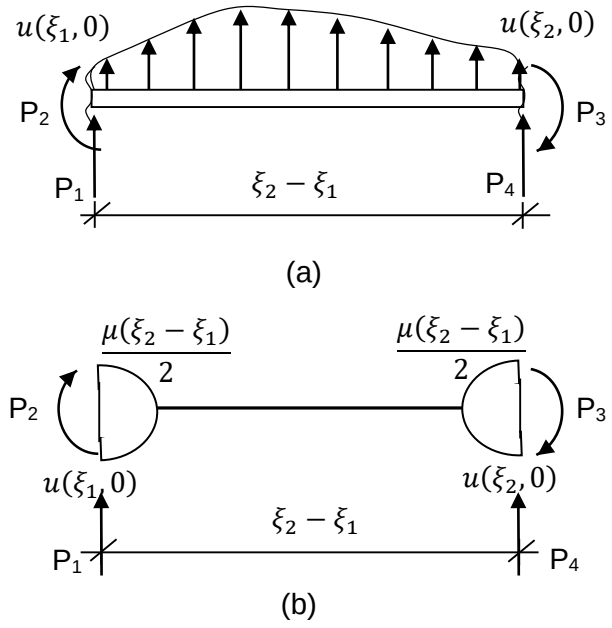

Fig. 3 – (a)An isolated segment of the laterally vibrating continuous beam showing the nodal forces P_1, P_2, P_3 and P_4
(b) An equivalent lumped mass segment showing the nodal forces

If a segment of a vibrating beam is isolated it will be in equilibrium with the application of the force vector {P} (see Figure 3). The force vector {P} represents the effect of the removed adjourning elements on the isolated segment. When the continuous bar is represented by a lumped mass bar just like the real segment the equivalent segment is supported by the same nodal forces P_1, P_2 P_3 and P_4 and has the same nodal displacements as the continuous/real bar.

The equation of motion for the lumped mass vibrating beam is taken as [24]

$$[m]\{\ddot{u}\} + [k_d]\{u\} = \{P\} \tag{15}$$

Where [m] is the inertial matrix, {u} is a vector of nodal displacement and k_d is the stiffness of the lumped mass segment under consideration. The proposed stiffness matrix for the lumped mass segment k_d is written as

$$[k_d] = \begin{bmatrix} \frac{12EI}{l^3}\phi_1 & \frac{6EI}{l^2}\phi_2 & -\frac{12EI}{l^3}\phi_3 & \frac{6EI}{l^2}\phi_4 \\ \frac{6EI}{l^2}\phi_2 & \frac{4EI}{l}\phi_1 & -\frac{6EI}{l^2}\phi_4 & \frac{2EI}{l}\phi_3 \\ -\frac{12EI}{l^3}\phi_3 & -\frac{6EI}{l^2}\phi_4 & \frac{12EI}{l^3}\phi_1 & -\frac{6EI}{l^2}\phi_2 \\ \frac{6EI}{l^2}\phi_4 & \frac{2EI}{l}\phi_3 & -\frac{6EI}{l^2}\phi_2 & \frac{4EI}{l}\phi_1 \end{bmatrix} \tag{16}$$

Where ϕ_1, ϕ_2, ϕ_3 and ϕ_4 are the stiffness modification factors for lateral vibration. They are to help redistribute the stiffness of the lumped mass segment in such a way as to annul the effect of the discretization of the beam mass due to the lumping of its distributed mass on selected nodes.

By rearranging (15) we obtain

$$\begin{Bmatrix}\phi_1\\ \phi_2\\ \phi_3\\ \phi_4\end{Bmatrix}=\begin{bmatrix}\frac{12EI}{l^3}u_{11} & \frac{6EI}{l^2}u_{21} & -\frac{12EI}{l^3}u_{31} & \frac{6EI}{l^2}u_{41}\\ \frac{4EI}{l}u_{21} & \frac{6EI}{l^2}u_{11} & \frac{2EI}{l}u_{41} & -\frac{6EI}{l^2}u_3\\ \frac{12EI}{l^3}u_{31} & -\frac{6EI}{l^2}u_{41} & -\frac{12EI}{l^3}u_{11} & -\frac{6EI}{l^2}u_{21}\\ \frac{4EI}{l}u_{41} & -\frac{6EI}{l^2}u_{31} & \frac{2EI}{l}u_{21} & \frac{6EI}{l^2}u_{11}\end{bmatrix}^{-1}\begin{Bmatrix}P_1+\frac{\mu(\xi_2-\xi_1)}{2}\omega^2u_{11}\\ P_2\\ P_3+\frac{\mu(\xi_2-\xi_1)}{2}\omega^2u_{31}\\ P_4\end{Bmatrix} \quad (17)$$

Equation (17) is a mathematical expression for calculating the four stiffness modification factors ϕ_1, ϕ_2, ϕ_3 and ϕ_4 for a segment of a beam under lateral vibration. μ is the mass per unit length of the beam. ω is the fundamental frequency of the vibrating mass, u_{11}, u_{21}, u_{31}, u_{41} are the values of nodal displacements u_1, u_2, u_3 and u_4 for the first mode of vibration.

Equation (6) was used to evaluate the total displacements u_1 to u_4 at the nodal points of a segment of the vibrating beam. Though the equation represents the summation of an infinite series, an evaluation of the first few terms provides values of very good precision.

The values of a_{2j}, and a_{4j} for j = 1, 2, 3, 4, 5, 6, 7 can be evaluated from (4) and (5). These are substituted into (7) – (10) to obtain the fixed end forces, which are applied to the force equilibrium equations to get the nodal forces P_1, P_2, P_3 and P_4. And finally (17) is evaluated to obtain the stiffness modification factors ϕ_1, ϕ_2, ϕ_3 and ϕ_4.

For this beam there are two possible cases, and the method of obtaining the stiffness modification factors depends on the case being considered.

a) When ξ_1 is greater or equal to zero and ξ_2 is less than 1

In this case the segment of the fixed-pinned beam under consideration is not positioned to the far right of the beam (the end that is pinned). Hence the process of calculating the stiffness modification factors will be as outlined above.

b) When ξ_2 is equal to 1

In this case the segment under consideration is located at the far right of the fixed-pinned beam. This implies that the segment is fixed at the left end and pinned at the right end hence its stiffness matrix is different from that of (16). The proposed stiffness matrix for this beam segment is therefore

$$[k_d]=\begin{bmatrix}\frac{3EI}{l^3}\phi_1 & \frac{3EI}{l^2}\phi_2 & -\frac{3EI}{l^3}\phi_3 & 0\\ \frac{3EI}{l^2}\phi_2 & \frac{3EI}{l}\phi_1 & -\frac{3EI}{l^2}\phi_4 & 0\\ -\frac{3EI}{l^3}\phi_3 & -\frac{3EI}{l^2}\phi_4 & \frac{3EI}{l^3}\phi_1 & 0\\ 0 & 0 & 0 & 0\end{bmatrix} \quad (18)$$

By substituting (18) into (15) and putting $P_4 = 0$ because of the hinged end we obtain a set of three equations with four unknowns ($\phi_1 to\ \phi_4$). To solve it there is need to know the value of one of the unknowns. By assuming $\phi_4 = 1$ we obtain the values of the other three as

$$\begin{Bmatrix}\phi_1\\ \phi_2\\ \phi_3\end{Bmatrix}=\begin{bmatrix}\frac{3EI}{l^3}u_{11} & \frac{3EI}{l^2}u_{21} & -\frac{3EI}{l^3}u_{31}\\ \frac{3EI}{l}u_{21} & \frac{3EI}{l^2}u_{11} & 0\\ \frac{3EI}{l^3}u_{31} & 0 & -\frac{3EI}{l^3}u_{11}\end{bmatrix}^{-1}\begin{Bmatrix}P_1+\frac{\mu(\xi_2-\xi_1)}{2}\omega^2u_{11}\\ P_2-\frac{3EI}{l^2}u_{31}\\ P_3+\frac{\mu(\xi_2-\xi_1)}{2}\omega^2u_{31}+\frac{3EI}{l^2}u_{21}\end{Bmatrix} \quad (19)$$

Note that $\phi_4 = 1$.

Equations (17) and (19) provide a way of calculating the stiffness modification factors ϕ_1 to ϕ_4 for a element of a fixed-pinned beam under lateral vibration are calculated. Using these equations the values of stiffness modification factors at different values of ξ_1 and ξ_2 for the lateral vibration of

a fixed-pinned beam can be obtained. A numerical demonstration of these steps are presented Table 1 below.

Tab 1 - Calculation of the Stiffness modification factor for an element positioned at $\xi_1 = 0, \xi_2 = 0.5$ on a propped cantilever beam under lateral vibration

$\xi_1 = 0, \ \xi_2 = 0.5$	
From Equation (6)	
$u_{11} = 0$	$u_{31} = -0.2500280951625$
$u_{21} = 0$	$u_{41} = -0.2501752736690$
From Equations (7) to (10)	
$F_1 = 8.98435096276653$	$F_3 = 11.92853399194589$
$F_2 = 0.92592074058035$	$F_4 = -0.98636146391392$
From force equilibrium equations (see Figure 3)	
$P_1 = 26.98284153031153$	$P_3 = -6.06995657559912$
$P_2 = 5.92589392980464$	$P_4 = 3.01291063063430$
From equation (17) taking EI = 1	
$\phi_1 = 1.11502214241540$	$\phi_3 = 1.45734448442994$
$\phi_2 = 0.90229998347702$	$\phi_4 = 1.24678725977081$

A sample Matlab program for the calculation of the stiffness modification factors can also be written.

RESULTS

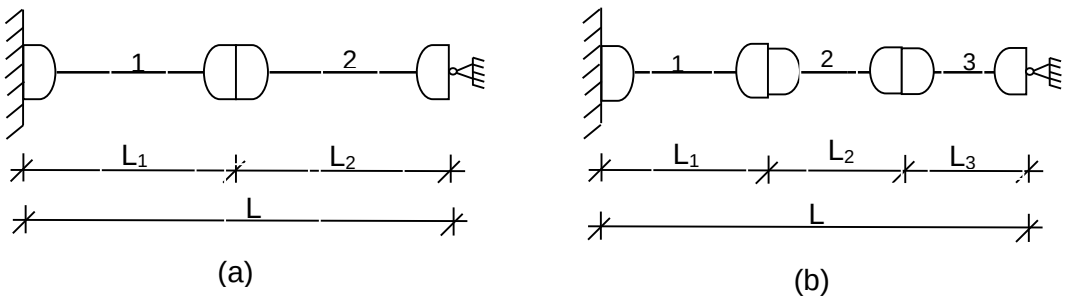

Fig. 4 - Some lumped mass propped cantilever beams

For the propped cantilever beam of Figure 4a, the lumped mass is at a distance L_1 from the fixed end. By solving it for different values of L_1 using the steps outlined in Table 1 and comparing results with that from the finite element model we obtain the results presented in Table 2. For the finite element model the inertia matrix used was the popular consistency matrix derived from the shape functions.

Tab 2 - Natural frequency of a lumped mass propped cantilever of Figure 4a

S/N	L_1/L	L_2/L	Natural frequency ω in $\sqrt{EI/\mu L^4}$		
			Lagrange without ϕ	Lagrange with ϕ	Finite Element Model
1	1/10	9/10	87.1627	15.4182	373.5870
2	2/10	8/10	35.1220	15.4182	93.3968
3	3/10	7/10	22.1424	15.4182	41.5097
4	4/10	6/10	17.0103	15.4182	23.3492
5	5/10	5/10	14.8131	15.4182	14.9435
6	6/10	4/10	14.2915	15.4182	10.3774
7	7/10	3/10	15.3490	15.4182	7.6242
8	8/10	2/10	19.1366	15.4182	5.8373
9	9/10	1/10	35.582	15.4182	4.6122

From the results in Table 2 we observe that the values of the natural frequency obtained from the lumped mass beam varied with the relative values of L_1 and L_2. It varied more with increase in the difference between L_1 and L_2 and gave the best prediction of the fundamental frequency when L_1 was equal to L_2. The results in Table 2 also shows that using the Lagrange's equations it is possible to obtain a near accurate value of natural frequency by a careful section of the relative values of L_1 and L_2. For instance at L_1/L= 0.7 the value of natural frequency obtained was 15.35Hz which has an error of only 0.45%. This is not so with the finite element at the best value is only available when $L_1 = L_2$. However with the application of the stiffness modification factors the obtained values of fundamental natural frequency was exact irrespective of the relative values of L_1 and L_2.

The natural frequency values obtained from a finite element model continued to decrease steadily with an increase in the ratio of L_1 to L_2. It gave the maximum value at L_1/L = 1/10, L_2/L = 9/10. The trend is better appreciated in the plot of natural frequency against L_1/L presented in Fig 5.

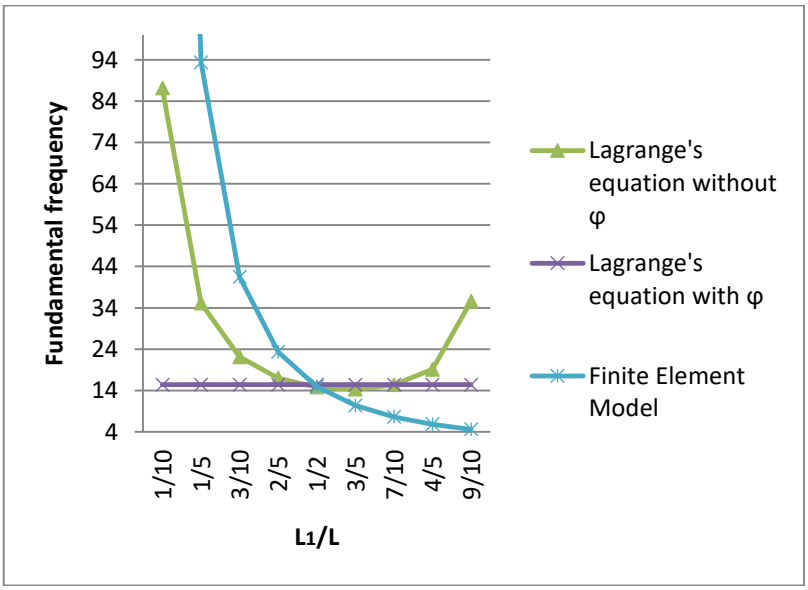

Fig. 5 - Fundamental frequencies as functions of L_1/L for the propped cantilever beam presented in Fig. 4a

From Figure 5 it is observed that the plots for analysis with and without stiffness modification factors and finite element model tend to converge at L_1/L = 0.5. At this point $L_1 = L_2$. It shows that

analysis with Lagrange's equation without ϕ gives its best results when the lumps are evenly spaced. This is also true of the finite element model as its best result of 14.94Hz with an error of 3.1% was obtained when L_1 was equal to L_2. The error margins increased continuously as the difference between L_1 and L_2 increased. The plot of natural frequencies obtained with the application of the stiffness modification was a horizontal line showing that it was not affected by the relative values of L_1 and L_2.

To further study the effect of mass lumping and the stiffness modification factors on the accuracy of results the beam of Figure 4b was analyzed using the Lagrange's equation and the finite element model. The result is presented in Table 3.

Tab. 3 - Natural frequency of a lumped mass propped cantilever of Fig. 4b

S/N	L_1	L_2	L_3	Natural frequency ω in $\sqrt{EI/\mu L^4}$		
				Lagrange without ϕ	Lagrange with ϕ	Finite Element Model (FEM)
1	1/12	1/12	10/12	45.6106	15.4182	245.1372
2	1/12	2/12	9/12	28.0664	15.4182	87.5877
3	1/12	3/12	8/12	20.7803	15.4182	44.4924
4	1/12	4/12	7/12	17.2032	15.4182	26.8425
5	1/12	5/12	6/12	15.4543	15.4182	17.9366
6	1/12	6/12	5/12	14.8974	15.4182	12.8258
7	1/12	7/12	4/12	15.4312	15.4182	9.6244
8	1/12	8/12	3/12	17.4598	15.4182	7.4876
9	1/12	9/12	2/12	22.6398	15.4182	5.9907
10	1/12	10/12	1/12	39.6405	15.4182	4.9016
11	2/12	1/12	9/12	28.1887	15.4182	138.8296
12	2/12	2/12	8/12	21.2239	15.4182	61.2843
13	2/12	3/12	7/12	17.7105	15.4182	34.3255
14	2/12	4/12	6/12	15.9719	15.4182	21.8969
15	2/12	5/12	5/12	15.4212	15.4182	15.1687
16	2/12	6/12	4/12	15.9704	15.4182	11.1231
17	2/12	7/12	3/12	18.0181	15.4182	8.5034
18	2/12	8/12	2/12	23.1101	15.4182	6.7106
19	2/12	9/12	1/12	36.8379	15.4182	5.4303
20	3/12	1/12	8/12	20.7848	15.4182	89.5397
21	3/12	2/12	7/12	17.6069	15.4182	45.1938
22	3/12	3/12	6/12	16.0110	15.4182	27.2375
23	3/12	4/12	5/12	15.5023	15.4182	18.1792
24	3/12	5/12	4/12	16.0011	15.4182	12.9836
25	3/12	6/12	3/12	17.7862	15.4182	9.7320
26	3/12	7/12	2/12	21.5862	15.4182	7.5638

27	3/12	8/12	1/12	26.4053	15.4182	6.0465
28	4/12	1/12	7/12	17.0131	15.4182	62.8185
29	4/12	2/12	6/12	15.5421	15.4182	34.7074
30	4/12	3/12	5/12	15.0313	15.4182	22.1212
31	4/12	4/12	4/12	15.3490	15.4182	15.3211
32	4/12	5/12	3/12	16.5433	15.4182	11.2307
33	4/12	6/12	2/12	18.5256	15.4182	8.5814
34	4/12	7/12	1/12	20.0733	15.4182	6.7686
35	5/12	1/12	6/12	15.0016	15.4182	46.6862
36	5/12	2/12	5/12	14.4051	15.4182	27.5194
37	5/12	3/12	4/12	14.4924	15.4182	18.3201
38	5/12	4/12	3/12	15.1630	15.4182	13.0819
39	5/12	5/12	2/12	16.1582	15.4182	9.8055
40	5/12	6/12	1/12	16.7747	15.4182	7.6200
41	6/12	1/12	5/12	14.0630	15.4182	36.1680
42	6/12	2/12	4/12	13.9468	15.4182	22.3849
43	6/12	3/12	3/12	14.2934	15.4182	15.4255
44	6/12	4/12	2/12	14.8462	15.4182	11.2985
45	6/12	5/12	1/12	15.1337	15.4182	8.6329
46	7/12	1/12	4/12	16.5351	15.4182	28.9079
47	7/12	2/12	3/12	16.6705	15.4182	18.5901
48	7/12	3/12	2/12	17.1969	15.4182	13.1734
49	7/12	4/12	1/12	17.5268	15.4182	9.8571
50	8/12	1/12	3/12	14.7732	15.4182	23.6730
51	8/12	2/12	2/12	15.0215	15.4182	15.7046
52	8/12	3/12	1/12	15.1414	15.4182	11.3879
53	9/12	1/12	2/12	16.9415	15.4182	19.7664
54	9/12	2/12	1/12	17.1041	15.4182	13.4574
55	10/12	1/12	1/12	22.0751	15.4182	16.7688

To produce the results of Table 3, the lumped mass of Figure 4b were moved at L/12 and the fundamental natural frequency calculated at all possible positions of the lumped masses. The results in the Table show that the calculated natural frequency varied with the relative values of L_1, L_2 and L_3. The same was observed in frequency values obtained from a finite element analyses. To appreciate the trend in variation of the obtained natural frequency with the spacing of the lumped mass we present an interaction plot showing the variation of frequency with the values of L_1/L and L_2/L in Figure 6.

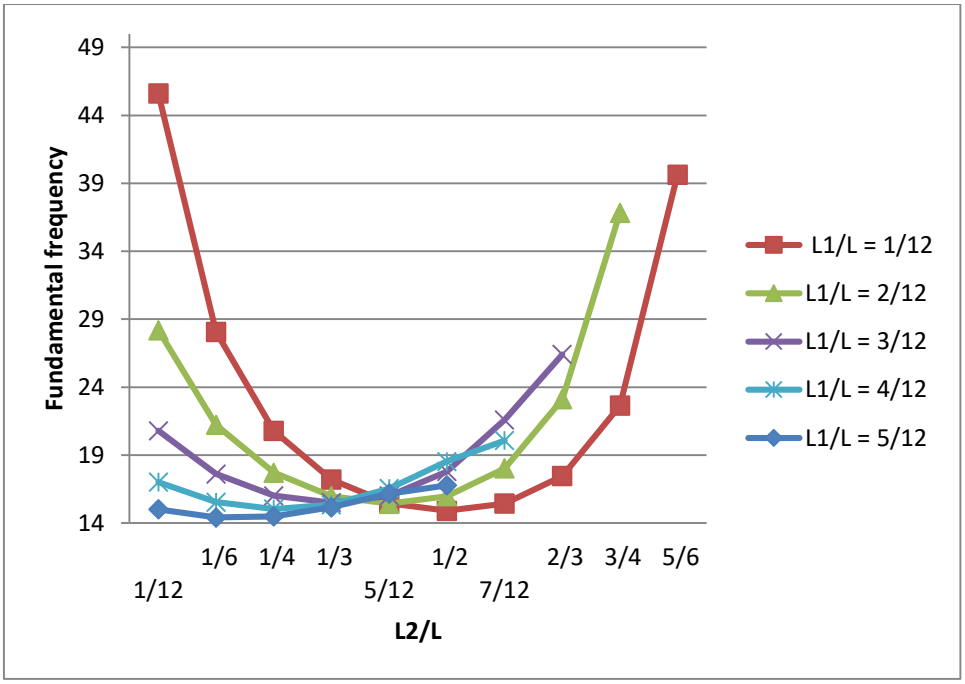

Fig. 6 - Interaction plots of fundamental frequency against L_2/L at different values of L_1/L using the Lagrange's equations

Figure 6 shows the interaction plots for the L_1/L and L_2/L when using Lagrange's equation on the lumped masses. In Figure 6 only the values of L_1 and L_2 were considered because if we know the values of L_1 and L_2 the values of L_3 becomes defined and can be obtained from subtracting L_1 and L_2 from the total length of the beam. We first observe that each of the curves tend to have a U shape. This shows that for almost all values of L_1/L there are for each two possible values of L_2/L that will give a fundamental frequency value of the beam to a good precision. The curves are not parallel and this shows that there is some level of interaction between the values of L_1 and L_2 on the natural frequency values obtained. The curves all appear to converge between the values of L_2/L = 1/3 and L_2/L = 5/12. At this value the value of L_1/L tend to have minimal effects on the calculated natural frequency.

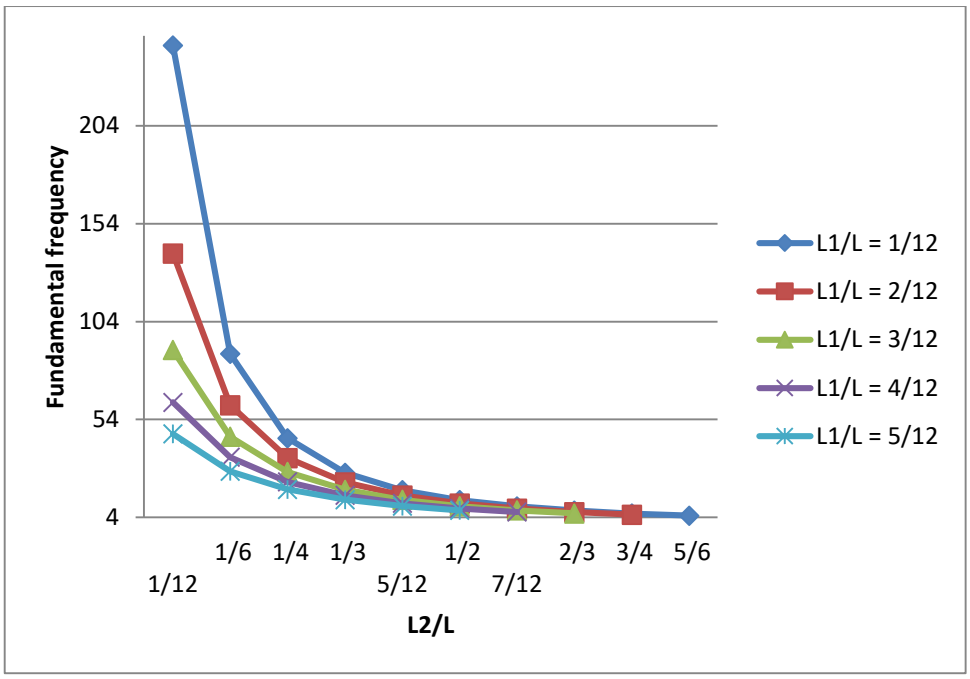

Fig. 7 - Interaction plots of calculated fundamental frequency against L_2/L at different values of L_1/L using the finite element model

Unlike that obtained in Figure 6 the plots in Figure 7 are like exponential plots. The values of calculated frequency decreases with increases in the values of L_2/L at constant L_1/L. Likewise the values of calculated frequency also decreases with increase in the values of L_1/L at constant L_2/L. For every value of L_1/L there is one possible value of L_2/L that will give a good approximation of the exact fundamental frequency. By zooming into the graph (see Figure 8) we observe that the lines of equal values of L_1/L are near parallel in the neighborhood of ω = 15Hz.

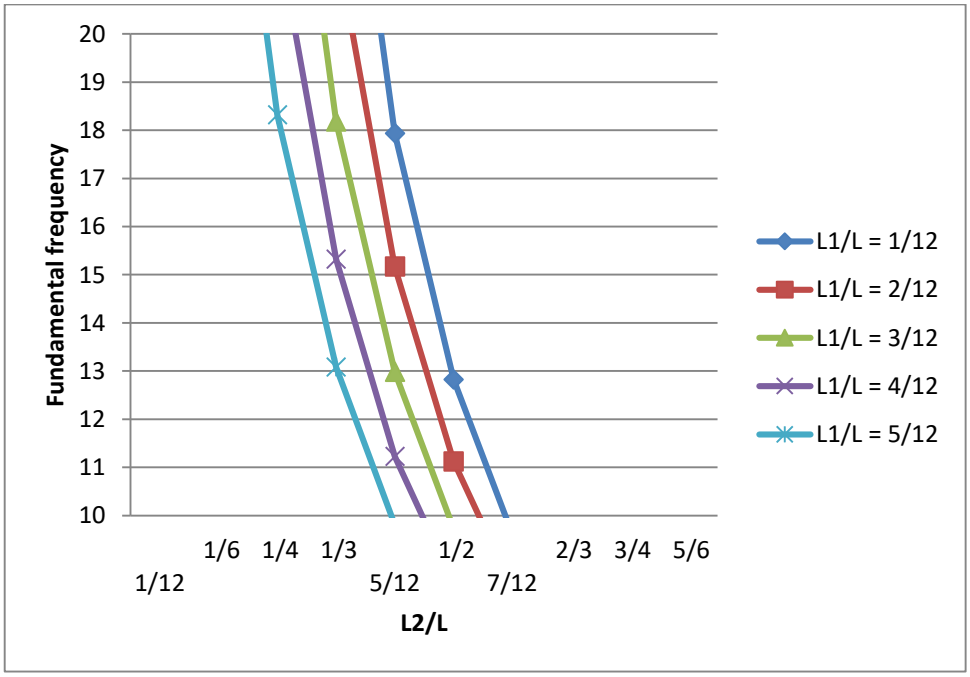

Fig. 8 - Enlarged Interaction plots of calculated fundamental frequency against L_2/L at different values of L_1/L using the finite element model

From Figure 8 it would be observed that there seems to be not interaction between L_1/L and L_2/L between values of L_2/L= 1/3 and ½. At these values any change in the values of L_1/L does not have significant effects on the calculated values of the fundamental frequency. This is evident in the near parallel nature of the lines of points of equal L_1/L in Figure 8.

From the Tables 2 and 3 it would be observed that the natural frequencies obtained from the use of Lagrange's equations on the propped cantilever that had its mass lumped had some measure of errors. When the stiffness of the system was however modified using the stiffness modification factors, the use of Lagrange's equations was able to predict accurately the fundamental frequencies irrespective of the position of lumped mass.

CONCLUSION

This work improved the values of fundamental frequencies obtained in the analysis of continuous systems as having discrete masses connected by mass-less elements using a propped cantilever as a case study. Even though the stiffness modification factors is a product of some rigorous mathematical manipulation, its implementation is largely simplified by the use of Matlab software. Hence the calculation of the stiffness modification can be automated. From this work we can infer that

1) To obtain an accurate dynamic response from a lumped mass beam there may be need to modify the stiffness composition/distribution of the system.
2) There is no linear modification of the stiffness distribution of a lumped mass beam under lateral vibration that can cause it to be dynamically equivalent to the continuous beam. This is so because the values of ϕ_1 , ϕ_2, $\phi_3$and ϕ_4 obtained for each segment as shown in Table 1 are not equal.
3) A careful selection of the relative positions of the lumped masses can lead to results with very good accuracy.
4) Having more lumps will lead to a better results just as breaking a structure into more elements in finite element analysis will give a better result.

This work lays the foundations for precise analysis of structures by lumping its distributed mass at select nodes. The mass lumping is an idealization that simplifies the analysis of the structure while the stiffness modification factors helps in keeping the results of the analysis accurate.

In the formulation of the equations of end forces only the deformation due to bending moments were considered. The effects of shearing and axial stresses on deformation were ignored in order to simplify the analysis. Further work including their effects is recommended.

ACKNOWLEDGEMENTS

We want to specially thank Late Prof I. O. Onyeyili, the former deputy vice-chancellor of Nnamdi Azikiwe University for his technical support to us in carrying out this research

REFERENCES

[1] A. A. Shabana, *Vibration of Continuous Systems. In:Theory of Vibration*, Mechanical Engineering Series, Springer, New York, NY pp 175-251, 1991

[2] W. T. Thomson and M. D. Dahleh, *Theory of Vibrations with Applications*. 5th Edition, Prentice Hall New Jersey, 1998

[3] S. Rajasekaran, *Structural Dynamics of Eathquake Engineering: Theory and Application using Mathematica and Matlab*, Woodhead Publishing Limited Cambridge, 2009

[4] J. Humar, *Dynamics of structures*, 3rd Edition, CRC Press, London, 2012

[5] M. Simsek, “Vibration analysis of a functionally graded beam under a moving mass by using different beam theories”, *Composite Structures* vol. 92, no. 4, pp 904-917, Elsevier, 2010, https://doi.org/10.1016/j.compstruct.2009.09.030

[6] Chung J., Yoo H. H., “Dynamic Analysis of a rotating cantilever beam by using the finite element method”, *Journal of Sound and Vibration*,vol. 249, Issue 1, pp 147-164, Elsevier, 2002, https://doi.org/10.1006/jsvi.2001.3856

[7] L. Li, Y. Hu, X.Li, “Longitudinal vibration of size dependent rods via non-local strain gradient theory”, *International Journal of Mechanical Science,* vols. 115-116, pp 135-144, Elsevier, 2016, https://doi.org/10.1016/j.ijmecsci.2016.06.011

[8] Y. Saad and H. A. V. Vorst, “Iterative Solution of Linear Systems in the 20th Century”, *Journal of Computational and Applied Mathematics* Vol 123, Issue 1-2 pp 1-33, 2000, https://doi.org/10.1016/S0377-0427(00)00412-X

[9] N. J. Fergusson, W. D. Pilkey, “Frequency-dependent element matrices”, *Journal of Applied Matrices*, vol.59. issue 1, pp 1-10, 1992, https://doi.org/10.1115/1.2899418

[10] Downs B., “Vibration Analysis of Continuous systems by Dynamic discretization”,*Journal of Mechanical Design*, vol. 102, Issue 2. 1980. https://doi.org/10.1115/1.3254757

[11] A. Houmat, Nonlinear free vibration of a shear deformable laminated composite annular elliptical plate, ActaMechanica. Springer 208:281. https://doi.org/10.1007/s00707-009-0148-5

[12] P. Beaurepaire and G. I. Schueller, “Modelling of the Variability of fatigue Crack growth using cohesive zone element”, *Engineering Fracture Mechanics* vol. 78 Issue 12 pp 2399-2413 Elsevier. 2011. https://doi.org/10.1016/j.engfracmech.2011.05.011

[13] F. Tornabene, F. Nicholas, F. Uberlini, V. Erasmo, “Strong Formulation Finite Element Method based on Differential Quadrature: A Survey”, *Applied Mechanics Review* vol. 67 pp 1-50 ASME 2015. https://doi.org/10.1115/1.4028859

[14] G. Cocchetti, M. Pagani, U. Perego, “Selective mass scaling for distorted solid –shell elements in explicit dynamics:Optimal scaling factor and stable time step estimate”, *International Journal for Numerical Methods in Engineering*, vol. 101, no. 9, pp 1-30 2013. https://doi.org/10.1002/nme.4829

[15] X. Hua, T. C. Lin, T. Peng, W. E. Wali, “Dynamic Analysis of spiral level geared rotor systems applying finite elements and enhanced lumped parameters”, *International Journal of Automotive Technology*, vol.13. no. 1, pp 97-107, 2012. DOI: 10.1007/s12239-012-0009-4

[16] G. Kouroussis, G. Gazetas, I. Anastasopoulos, C. Conti, O. Verlinden, “Lumped mass model of vertical dynamic coupling of a railway track on elastic homogenous or layered halfspace”, *Proceedings of the 8th International Conference on Structural Dynamics EURODYN* Belgium, pp 676-683, 2011

[17] M. Blundell, D. Harty, *The multibody systems approach to vehicle dynamics*, Butterworth-Heinemann Uk, pp 185-334, 2015

[18] G. Kouroussis, O. Verlinden, “Prediction of railway ground vibrations: Accuracy of a coupling lumped mass model for representing the track/soil interaction”, *Soil Dynamics and Earthquake Engineering*, vol. 69, pp. 220-226, Elsevier, 2015. https://doi.org/10.1016/j.soildyn.2014.11.007

[19] K. K. Reichl, D. J. Inman, Lumped mass model of a 1D metastructure for vibration suppression with no additional mass, Journal of Sound and Vibration, vol. 403, pp. 75-89, Elsevier, 2017. https://doi.org/10.1016/j.jsv.2017.05.026

[20] H. Ahmadian, M. I. Friswell, J. E. Mottershead, “Minimization of the discretization error in mass and stiffness formulations by an inverse method”. *International Journal for Numerical Methods in Engineering*, vol. 41, no. 2, pp 371-387, 1998. https://doi.org/10.1002/(SICI)1097-0207(19980130)41:2<371::AID-NME288>3.0.CO;2-

[21] C. Hager, B. I. Wohlmuth, “Analysis of a space-time discretization for dynamic elasticity problems based on mass-free surface elements”, *SIAM Journal on Numerical Analysis*, vol. 47, no. 3, pp 1863-1885, 2009. https://doi.org/10.1137/080715627

[22] D. Wang, W. Liu, H. Zhang, “Superconvergent Isogeometric free vibration analysis of Euler-Bernoulli Beams and Kirchhoff plates with higher order mass matrices”, *Computer Methods in Applied Mechanics and Engineering*, vol. 286, pp. 230-267, 2015. https://doi.org/10.1016/j.cma.2014.12.026

[23] T. M. Ericson, R. G. Parker, “Planetary gear modal vibration experiments and correlation against lumped-parameter and finite element models”, *Journal of Sound and Vibration*, vol. 332, no.9, pp 2350-2375 Elservier, 2013. https://doi.org/10.1016/j.jsv.2012.11.004

[24] I. O. Onyeyili, C. H. Aginam, V. O. Okonkwo, “Analysis of a propped cantilever under longitudinal vibration by a modification of the system’s stiffness distribution”, *IOSR Journal of Mechanical and Civil Engineering*, vol. 13, Iss. 5, pp 65-78, 2016

[25] T. R. Tauchert, 1974. *Energy Principles in Structural Mechanics*. International Student Edition, McGraw-Hill Kogakusha Ltd Tokyo, 1974

[26] J. Buskiewicz, “A Dynamic Analysis of a coupled beam/slider system”, *Applied Mathematical Modelling* vol. 32, Issue 10, pp 1941 – 1955, 2008. https://doi.org/10.1016/j.apm.2007.06.028

[27] V. O. Okonkwo, Dynamic Analysis of frames by the modification of the system’s stiffness distribution, Unpublished PhD Thesis, Civil Eng. NnamdiAzikwe University, Awka

[28] V. O. Okonkwo, Analysis of Multi-storey steel frames, Unpublished MEng Thesis, Civil Eng. Nnamdi Azikwe University, Awka

[29] R. L. Bisplinghoff, H. Ashley, R. L. Halman, *Aeroelasticity*, Cambridge Mass Addison-Wesley Publishing Company Inc. pp 90, 1955

CIVIL ENGINEERING JOURNAL

Article no. 63

THE CIVIL ENGINEERING JOURNAL 4-2021

THE HYDRAULICS OF NATURE-LIKE FISHWAYS

Xi Mao[1], Sheng Huang[1], Yuchen Xu[1], Zhong Cheng[1], Jiehao Zhang[2], Xiaofan Liu[3], Yong Wang[4], Kai Tang[1], Yunbo Yang[1], Lu Jiang[1] and Zetang Guan[1]

1. *Sichuan Agricultural University, College of Water Conservancy and Hydropower Engineering, Yaan, Road Xinkang 46, China; maowhiteknight@163.com*
2. *Yunnan Institute of Water & Hydropower Engineering Investigation, Design and Research，Kunming, Road Qinnian 376, China*
3. *Yalong River Hydropower Development Company, Ltd., Chengdu, Road Shuanglin 288, China*
4. *Sichuan Agricultural University, College of Forestry, Chengdu, Road Huimin 211, China*

ABSTRACT

Nature-like fishway arrangements are commonly used because these structures imitate the characteristics of natural rivers and effectively allow fish to migrate past river sections blocked by hydraulic structures. In this paper, physical models were analyzed, and the velocity distributions of two different fishway structures (Types I and II) were compared. Results showed that the maximum mainstream velocity of the Type I structure was 5.3% lower than that of the Type II structure. However, the average mainstream velocity of the Type I structure was 21.1% greater than that of the Type II structure. The total per-cycle length of the mainstream path in the Type II structure was 2.1 times greater than that of the Type I structure, which indicated that the length of the mainstream path was somewhat proportional to the average velocity of the mainstream. When the flow rate was kept constant, the average velocity of the mainstream decreased by increasing the total length of the mainstream caused by the internal structure of the fishway, and the average velocity of the mainstream increased when the total length of the mainstream was shortened.

KEYWORDS

Ecological restoration, Energy dissipation, Flow velocity, Hydraulics, Nature-like fishway

INTRODUCTION

The construction of hydraulic structures, such as gates and dams, alters the natural state of rivers, blocking the migration channels of aquatic organisms, especially fish. Fishways are effective engineering measures that restore fish migration channels [1]. Commonly used fishways can generally be considered either technical fishways or nature-like fishways [2] [3].

Nature-like fishways use the roughness of river bottom and bank, as well as river stones, to dissipate energy [4]. Although nature-like fishways are prone to get dry when the upstream water level is low, construction is inexpensive and the necessary materials can be obtained nearby [5]. These fishways are suitable for the migration of many fish species, and fish may pass through such fishways continuously with high efficiency [6]. Water flows in nature-like fishways are highly diverse. Fishway water flow conditions are suitable for most fish species, and rock arrangement patterns can be rearranged to best suit specific species [7]. The main factors influencing fishway flow conditions are the total difference in water level between the beginning and the end of the

fishway, the average water level difference within a single pond, the arrangement of the internal structure of the fishway, and the average slope of the fishway. In this paper, the internal structures of nature-like fishways were analyzed to characterize the different flow conditions produced by different structures.

MODEL TEST

In this study, the main fish-passing objects were *schizothorax oconnoris* and *schizothorax macropogons*, both of which belonged to migratory fish. The optimal swimming speed was 0.8 m/s, and the flow rate should be controlled in 0.5–0.8 m^3/s[1]. For the pool fishway, the water depth of the pool room should be determined by the height and habit of the fish object, generally 1.0–1.5 m. For the natural-like fishways, the water depth in the fishways should be determined according to the ecological habits of the target fish species. The minimum water depth of the fishways can be appropriately increased when there are more bottom fish in the key fish-passing objects. The slope of natural-like fishways should be as gentle as possible, generally controlled within 2%[8].

Considering the fish species and habits, the average water depth H of this study was controlled at 0.109d, the flow rate was $0.03d^2$, and the longitudinal bottom slope ratio was 2%. The average height of baffle h was 0.108d, so the ratio of submergence of baffles h/H was 0.99. For the targeted species of fish, the minimum design dimension of slot width of fishway was 0.28m, and the depth of flow downstream of the tip of the groyne or the central slot was 0.2m. The flow rate was measured by the triangular sharp-crested weir. The velocity was measured by a micro propeller flow meter, and the vertical average velocity of a measuring point was calculated by the “three-point method”[9].

The following two structures were used to simulate the nature-like fishway based on obstacle arrangement, as shown in Figure 1. The fishway structure with regular geometry could effectively divide the mainstream area and rest area in each level of the fish pool, which is conducive to more efficient migration of fish.

(a)Type I *(b)Type II*

Fig. 1 – Schematic image showing the two nature-like fishway structures.

The vertex on the right bank of the model was considered the origin of the coordinate plane; the *x*-axis was parallel to the direction of river flow, and the *y*-axis was perpendicular to river flow. Velocity was measured in a 0.077*d* by 0.077*d* grid, where *d* was the width of the model. The specific size constants used are given in the section diagrams, as shown in Figure 2 and Figure 3.

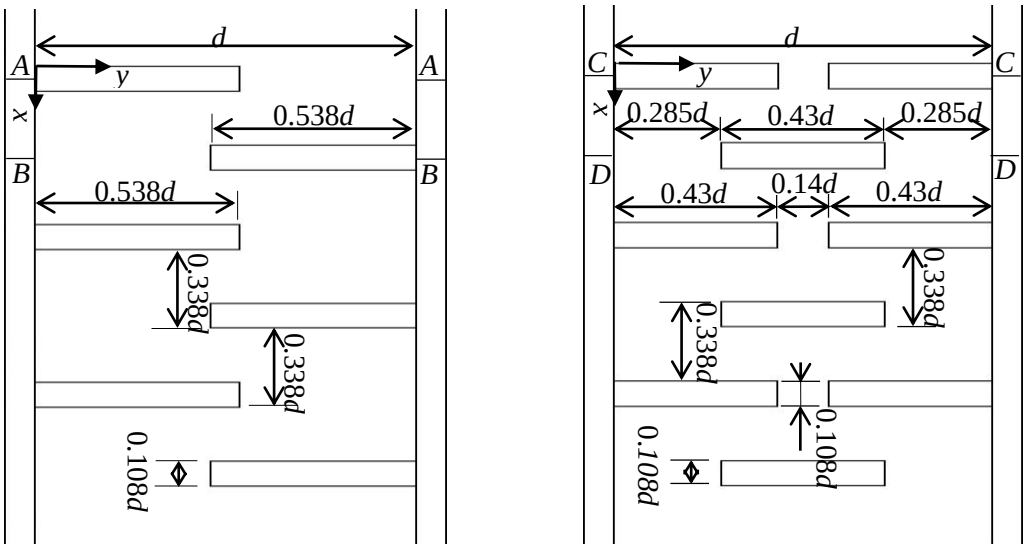

(a)- Type I (b)- Type II

Fig. 2 – Schematic diagram showing the model structure.

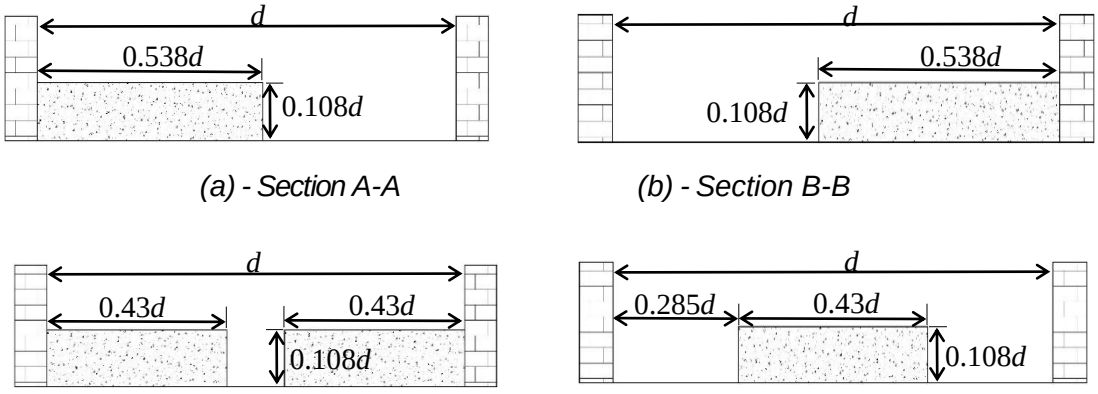

(a) - Section A-A (b) - Section B-B

(c) - Section C-C (d) - Section D-D

Fig.3 – The Section diagram of model structure.

MODEL TEST RESULTS AND ANALYSIS

Flow velocity in each model cross-section

When the structure of each pool in a fishway is the same, the flow velocity in the fishway changes regularly. Therefore, only one complete cycle was analyzed in this study. The variation of depth-averaged velocities in various cross-sections in the two models are shown in Figure 4.

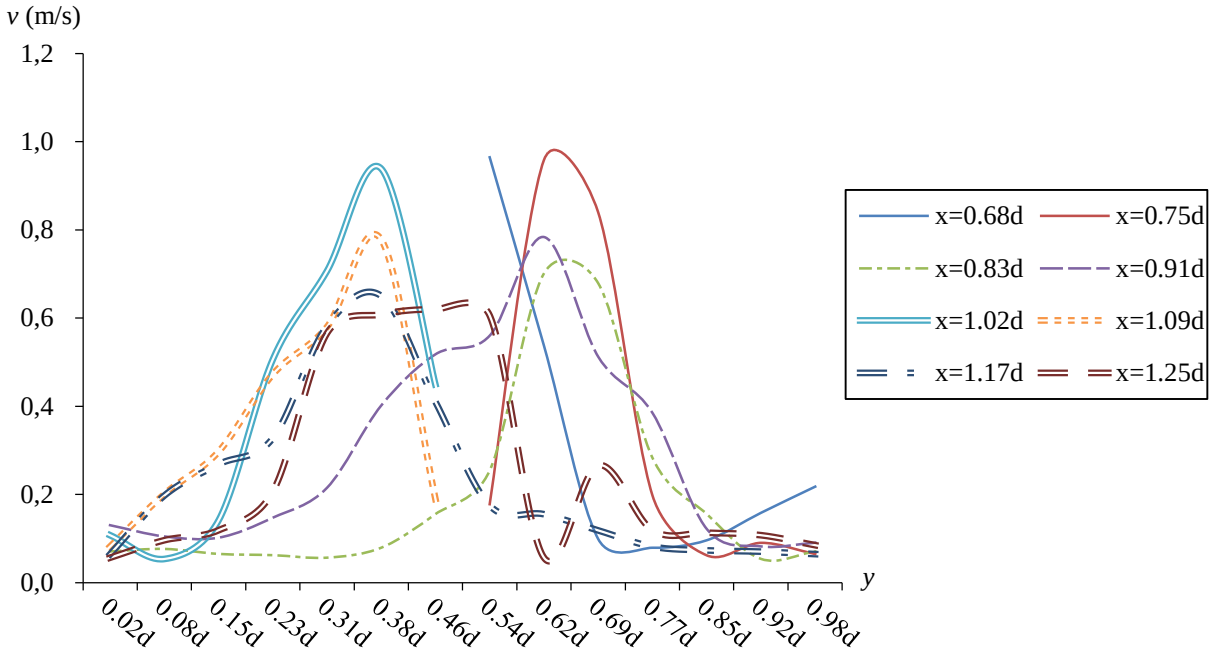

Fig. 4 (a) - Depth-averaged velocities variation chart of a period section (type I)

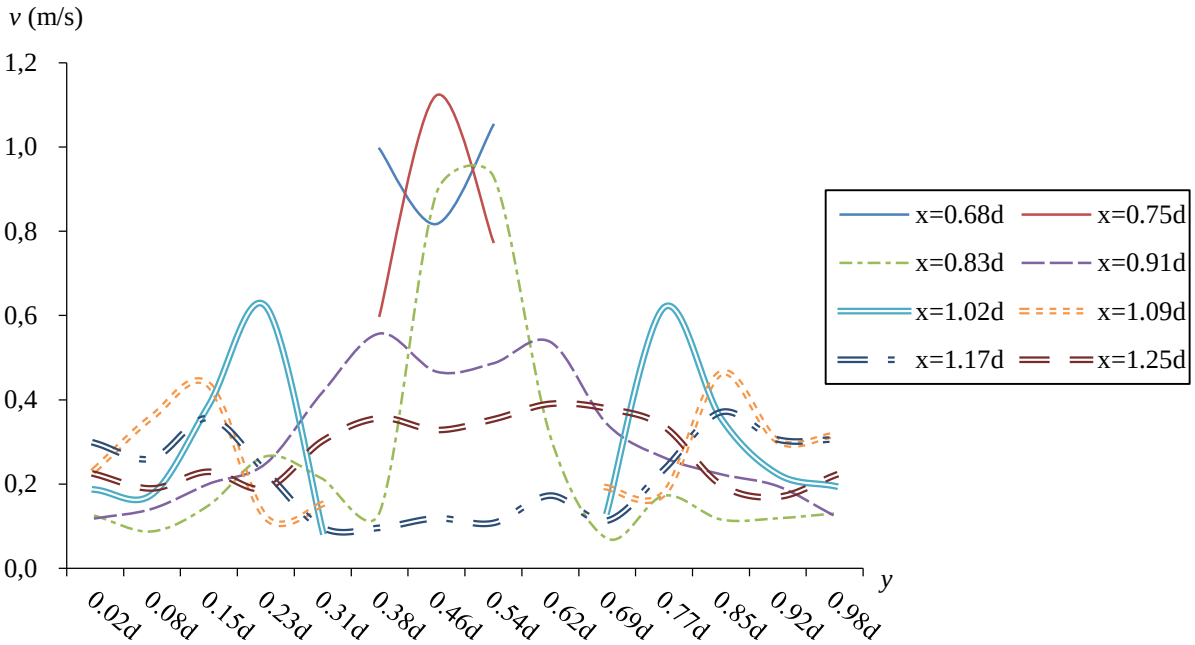

Fig. 4 (b) - Depth-averaged velocities variation chart of a period section (type II)

(1) In the Type I structure, the sectional velocity presented the trend of symmetry between the first and second halves of the section.

(2) In the Type I structure, the average water velocity during each cycle was roughly the same, decreasing little over the course of the cycle along the river.

(3) The cross-sectional water velocity diagram of the Type II structure was symmetrically distributed around the center of the river channel, with the maximum velocity located near the transition between sections. In the first half of each cycle, flow velocities were highest near the

riverbank, decreasing towards the middle of the cycle. During the second half of each cycle, the flow velocities near the banks of the river were greater than that in the center of the river.

(4) Average flow velocities between sections in the Type II structure were roughly equivalent, with little decrease along the river channel; the average flow velocity in the first half of the cycle was greater than that in the second half.

Mainstream flow velocity and overall velocity

Variations in the velocity of the main flow are shown in Figure 5, and the distributions of velocity measurement in the two different nature-like fishway structures are shown in Figure 6.

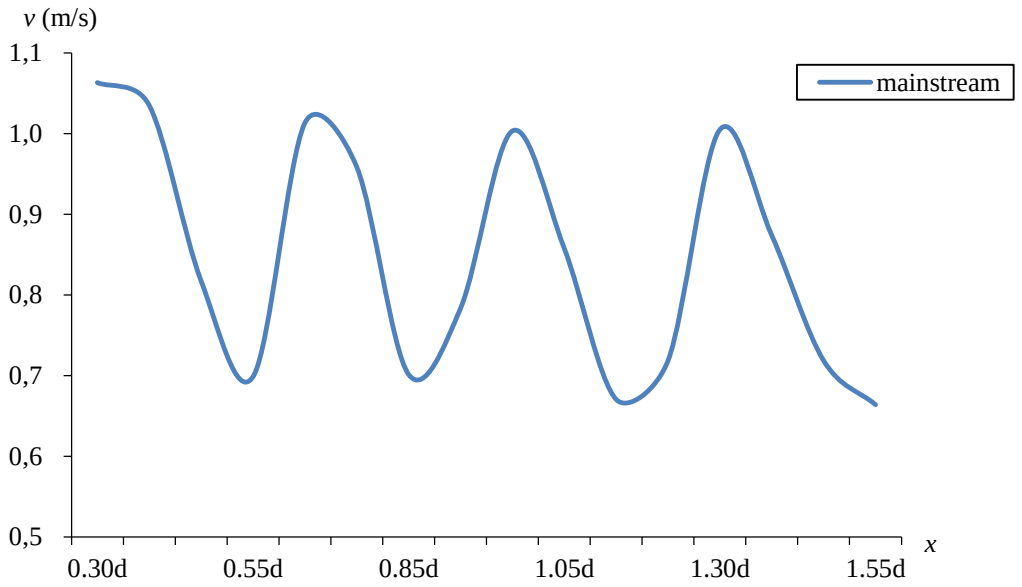

Fig. 5 – (a) - Changes in mainstream flow velocity over the course of the cycle (type I)

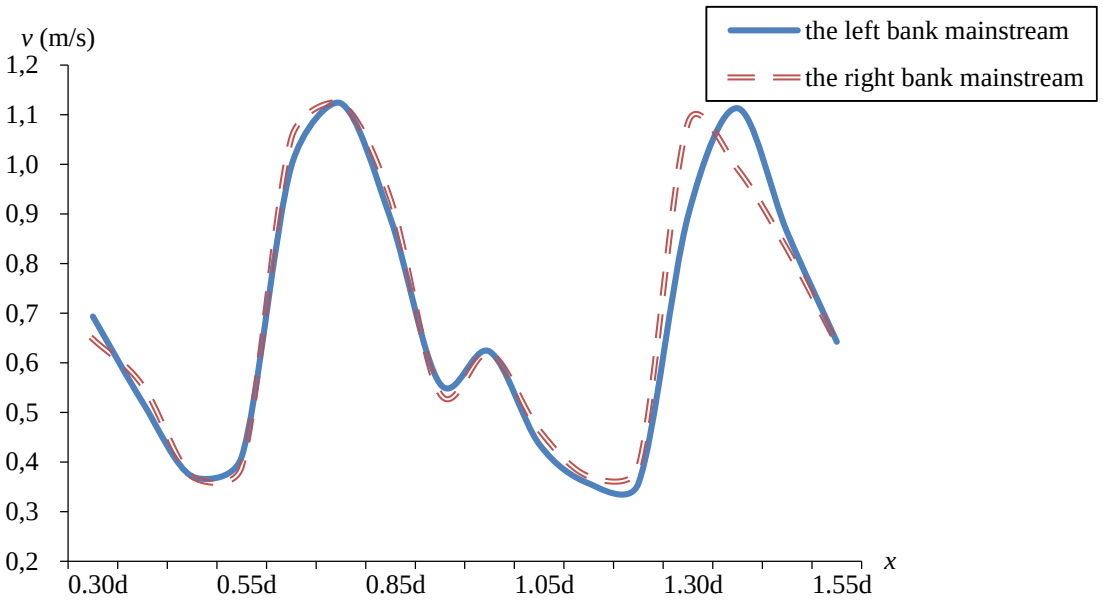

Fig. 5 – (b) - Changes in mainstream flow velocity over the course of the cycle (type II)

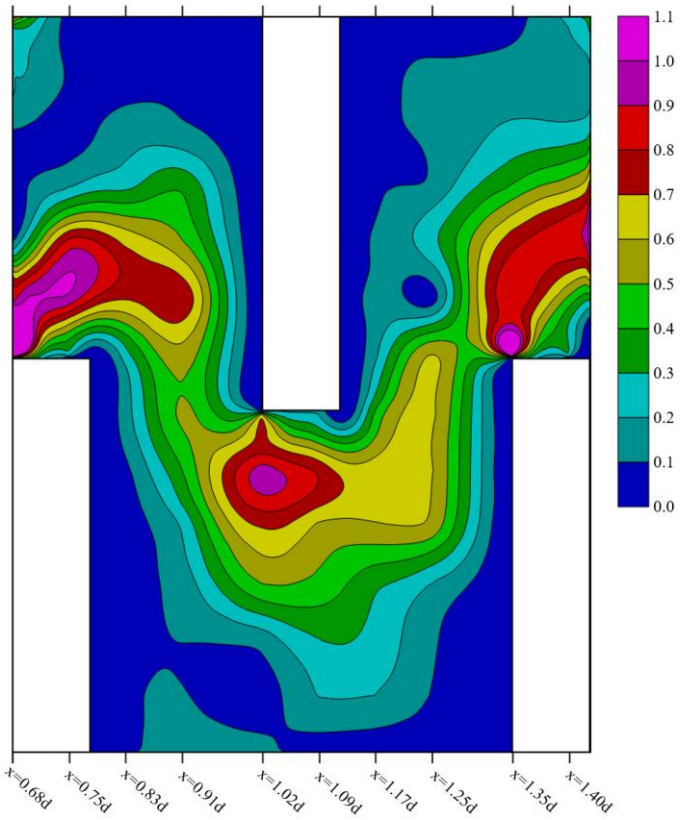

Fig.6 – Velocity plane map of (a) - type I (m/s)

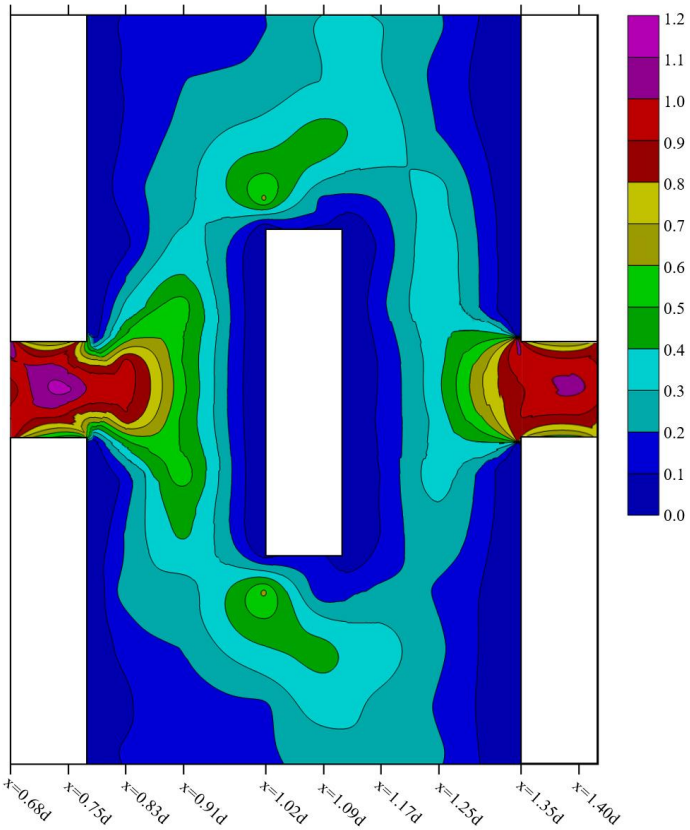

Fig.6 – Velocity plane map of (b) - type II (m/s)

Previous studies have shown that the flow velocities of most nature-like fishways in China are within the recommended range (0.6–1.2 m/s) [10]. In the Type I structure, 9.65% of the total area had a flow velocity of 0.6–1.2 m/s, and the velocity distribution was relatively uniform. In the Type II structure, only 4.05% of the total area had a velocity of 0.6–1.2 m/s, and most of the changes in velocity in these areas were concentrated near obstacles where the cross-sectional pattern changed. Compared with Type I structures, more fish migration areas had high flow velocities in Type II structures. The remaining areas in Type II structures, with low flow rates, could be used as resting areas for migrating fish.

Water flow continuity was calculated using the following equation:

$$Q = A \times v \tag{1}$$

where Q was the model flow rate, which was a fixed value; A was the section area; and v was the mean velocity in the section, and its value is the average velocity of the vertical average of different measuring points in the same cross-section.

The main flow of the water in the fish channel was analyzed first. When the main flow passed around an obstacle, the cross-sectional volume of the water flow was suddenly reduced due to the narrowing effect of the obstacle on the water flow channel. Because the flow rate did not change, the velocity of the water flow at the obstacle increased. Once the water flowed past the obstacle, the narrowing effect ceased, increasing the cross-sectional volume of the flow and decreasing flow velocity. Thus, flow velocity changed in a periodic manner corresponding to obstacle locations.

Because the bottoms and sides of the fishway were not completely smooth, layer resistance must be considered. Water loses energy as it flows downstream. Water flow head loss over the course of the cycle was thus calculated using the following equations:

$$□_f = \frac{v^2 l}{C^2 R} \tag{2}$$

$$C = \frac{1}{n} R^{\frac{1}{6}} \tag{3}$$

$$□_f = \frac{n^2 v^2 l}{R^{\frac{4}{3}}} \tag{4}$$

where h_f was the frictional head loss; C was the Xie Cai coefficient; n was the roughness coefficient; l was the length of the flow path; and R was the hydraulic radius.

When the water flow suddenly encounters a solid boundary, the distribution of flow velocities throughout the flow section changes rapidly. This concentrated resistance in a small area is known as local resistance [11]. The effects of local resistance on head loss in the fishway water flow were calculated using the following equation:

$$h_j = \zeta \frac{v^2}{2g} \tag{5}$$

where h_j was the local head loss; ζ was the loss coefficient along the flow path; and g was the acceleration due to gravity (a constant).

The main flows of Type I and Type II nature-like fishway structures exhibited periodic fluctuations in velocity along the direction of water flow as shown in Figure 5. This meant that both fishways reached the pseudo-uniform condition of flow. And the balance between the sum of local head loss h_j and frictional head loss h_f and the bottom drop at each fishway cycle was effective, namely the law of conservation of energy.

Due to its planar symmetry, the Type II structure had two mainstreams, on either side of the middle baffle, with similar velocity profiles.

The maximum mainstream flow velocity in the Type I structure was 1.063 m/s, and the average mainstream flow velocity was 0.815 m/s. The maximum mainstream flow velocity in the Type II structure was 1.123 m/s, and the average mainstream flow velocity was 0.673 m/s. Although the maximum flow velocity of the Type I structure was 5.3% lower than that of the Type II structure, the average flow velocity of the Type I structure was 21.1% greater than that of the Type II structure.

This was due to the difference in the lengths of the mainstream path between the two structures. The main flow paths of both structures are shown in Figure 7. The Type I structure had one main flow path per cycle (1.02*d*), while the Type II structure had two main flow paths per cycle: the main flow path close to the left bank was 1.18*d* long, while the main flow path close to the right bank was 1.21*d* long (Figure 7b). Excluding the overlapping portion, the total length of the main flow path in the Type II structure was 2.17*d*. In total, the main flow path of the Type II structure was 2.1 times longer than that of the main flow path of the Type I structure. Thus, the maximum flow velocity in the Type I structure was lower than that in the Type II structure, but the average mainstream flow velocity was higher.

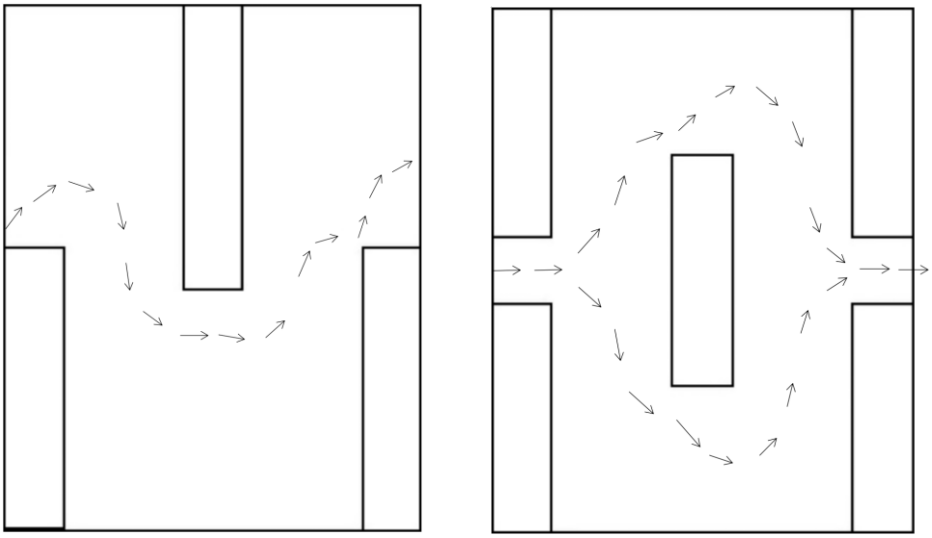

(a) type I *(b) type II*

Fig.7 – Schematic showing mainstream flows in both structures.

The volumetric energy dissipation rate

The volumetric energy dissipation rate is generally used to judge the adaptability of pool fishway to fish passing objects, and its calculation formula is as follows:

$$E = \frac{\rho g Q \Delta h}{V} \tag{6}$$

where E was the volumetric energy dissipation rate; ρ was the density of water; g was the gravitational acceleration; Δh was the water level drop of adjacent pools; and V was the volume of water in a pool.

According to the research results of Larinier et al., the volumetric energy dissipation rate should not be greater than 150–200 W/m^3[12]. After calculation, the volumetric energy dissipation rate of type I fishway was 26.8 W/m^3, and that of type II fishway was 25.1 W/m^3, both meeting the requirements.

CONCLUSION

(1) The main flows of Type I and Type II nature-like fishway structures exhibited periodic fluctuations in velocity along the direction of water flow, and both had reached the pseudo-uniform condition of flow.

(2) The maximum flow velocity in the Type I structure was 1.063 m/s, which was 5.3% lower than that of the Type II structure (1.123 m/s). This was because, in the Type II structure, the obstacles more severely narrowed the water flow channel, leading to a greater sudden proportional decrease in the cross-sectional volume of the water flow. Because the flow rate did not change during these

volume fluctuations, the main flow velocity at obstacles in the Type II structure increased more than the main flow velocity at obstacles in the Type I structure.

(3) The average flow velocity in the mainstream of the type I structure increased by 21.1% compared with that of the Type II structure. The main reason was the local energy loss due to flow expansion downstream of the flow constriction in the central slot in the longer flow path of the type II fishway. The secondary causes included the frictional head losses proportional to the length of the flow path.

(4) In the Type I structure, 9.65% of the total area had a flow velocity greater than 0.6 m/s, while 4.05% of the total area of the Type II structure had a velocity greater than 0.6 m/s.

(5) The volumetric energy dissipation rate of Type I and Type II nature-like fishway were 26.8 and 25.1 W/m^3 respectively, both meeting the requirements.

ACKNOWLEDGEMENTS

This work was supported by Sichuan Agricultural University (grant number: 2121997944, 065H0600, 1921993122, 2021993131).

REFERENCES

[1] Mao X, Li J, An R, Zhao W, Li K., Li R, Deng Y, Liang X., Yang M, Zhang J., Tang K., 2019. Study of key technologies for fishways in the plateaus of western China. Global Ecology and Conservation, vol. 20, e00755.

[2] Mao X., 2018. Review of fishway research in China. Ecological Engineering, vol. 115: 91-95.

[3] Nyqvist D, Elghagen J, Heiss M, Calles O., 2018. An angled rack with a bypass and a nature-like fishway pass Atlantic salmon smolts downstream at a hydropower dam. Marine and Freshwater Research, vol. 69(12): 1894-1894.

[4] Gustafsson S., 2012. Macroinvertebrate colonization of a nature-like fishway : The effects of habitat design. Ecological Engineering, vol. 61(19): 345-353.

[5] Li G, Sun S, Zhang C, Liu H, Zheng T., 2019. Evaluation of flow patterns in vertical slot fishways with different slot positions based on a comparison passage experiment for juvenile grass carp. Ecological Engineering, vol. 133: 148-159.

[6] Tamario C, Degerman E, Donadi S, Spjut D, Sandin L., 2018. Nature- like fishways as compensatory lotic habitats. River Research and Applications, vol. 34(3): 253-261.

[7] Muraoka K, Nakanishi S, Kayaba Y., 2017. Boulder arrangement on a rocky ramp fishway based on the swimming behavior of fish. Limnologica - Ecology and Management of Inland Waters, vol. 62: 188-193.

[8] Li S, Ding X, Liu D., 2014. Review of natural-like fishway. Yangtze River, vol. 96: 70-73. (in Chinese)

[9] State Key Laboratory of Hydraulics and Mountainous River Development and Protection, Sichuan University, 2016. Hydraulics(5th edition)(Volume one) 533 pp. (in Chinese)

[10] Chen K, Tao J, Chang Z, Cao X, Ge H., 2014. Difficulties and prospects of fishways in China: An overview of the construction status and operation practice since 2000. Ecological Engineering, vol. 70: 82-91.

[11] Mao X, Zhang J, Tang K, Zhao W., 2019. Designs for T shape fishways. The Civil Engineering Journal 2019, vol. 28 no. 2: 270-280.

[12] Larinier M, Travade F, Porcher J., 2002. Fishways: biological basis, design criteria and monitoring.

CIVIL ENGINEERING JOURNAL

Article no. 64

THE CIVIL ENGINEERING JOURNAL 4-2021

EXPERIMENTAL VERIFICATION OF PUNCHING SHEAR RESISTANCE OF FLAT SLAB FRAGMENTS

Simona Šarvaicová and Viktor Borzovič

Slovak University of Technology in Bratislava, Faculty of Civil Engineering, Department of Concrete Structures and Bridges, Bratislava, Radlinského 11, Slovakia; simona.sarvaicova@stuba.sk; viktor.borzovic@stuba.sk

ABSTRACT

The paper deals with the loading test results of an experimental reinforced concrete flat slab fragments, which were supported by an elongated rectangular column. The slab specimens were 200 mm thick and were designed without any shear reinforcement. During the experimental test, in addition to the shear resistance of the flat slab, deformation state during the whole loading was also examined. Deformations were measured in two ways, using LVDT sensors placed under the slab specimen and by photogrammetric measurement based on measuring the deformations of the code marks glued on the top surface of the specimen. Based on the photogrammetry, it was also possible to determine the concrete strains on the specimen upper surface. The concrete strains on the bottom surface were measured around the column using the strain gauges. By experimentally obtained punching shear resistance, the accuracy of the standard design models for prediction punching resistance was compared. The results of the experiments were also compared with the results of a numerical non-linear analysis performed in the Atena program.

KEYWORDS

Flat slabs, Punching, Shear resistance, Elongated column support, deformation measuring

INTRODUCTION

Punching shear resistance of locally supported slabs is still a current and discussed topic in the field of assessment of load-bearing structures of buildings. Punching shear of slabs supported on a rectangular column, where we assume an uneven distribution of shear load, has been investigated in many scientific research teams in the Slovak Republic and abroad.

The punching shear resistance of slabs supported by a rectangular column is lower than the shear resistance of slabs supported by a square column with approximately the same length of control perimeter. This phenomenon is due to the fact that the formulas for the evaluation of the punching shear resistance of the slabs include empirical factors that take into account only the geometry of the column, but do not take into account the deformed shape of the slab [1]. In addition to the influence of the column geometry, the influence of various other aspects was investigated, such as the influence of loading conditions or new types of shear reinforcement [2, 3].

This research follows an analysis from 2019 [4], when, based on a nonlinear analysis in the Atena program, it was preliminarily concluded that in the case of uniform loading around the entire specimen, the length of the control perimeter is not reduced. In order to confront this statement, the specimen was further analyzed with a 0.15 m x 0.95 m column, which was subjected to a load test as well as a 3D nonlinear analysis in the Atena program.

DESIGN MODELS

Eurocode 2

The shear resistance in flat slabs without shear reinforcement is ensured by several aspects. It mainly depends on the aggregate interlock in shear crack, compressed concrete area under neutral axis and longitudinal reinforcement. These facts are considered in the empiric formula which determines the punching shear resistance of a slab according to EC2.

$$V_{Rd,c}=\frac{C_{Rk,c}}{\gamma_C} k\left(100\ \rho_l\ f_{ck}\right)^{1/3} u_1 d \tag{1}$$

where:

$C_{Rk,c}$ - empirical factor [MPa];
γ_C - partial safety factor, γ_C = 1.5 [-];
k - the size factor, $k = 1 + (200[mm]/d)^{0.5} \leq 2.0$ [-];
ρ_l - reinforcement ratio, $\rho = (\rho_x \rho_y)^{0.5}$ [-];
f_{ck} - characteristic concrete compressive cylinder strength [MPa];
u_1 - shear-resisting basic control perimeter at distance of 2d from the face of a column [mm];
d - effective depth [mm].

Model Code 2010

Model Code 2010 is based on the Critical shear crack theory (Ruiz, Muttoni 2014). The shear resistance which depends on the crack widths is proportional to the slab rotation ψ. However, the load rotation is significantly non-linear. This fact was investigated with the result of a quadrilinear moment-curvature diagram which has been simplified for the design application. There are four levels of approximation of rotation calculation around the supported area. For this analysis the Level III of Approximation was used. The values of r_s and m_{Ed} were calculated from a linear elastic model.

$$V_{Rd,c} = k_\psi \frac{\sqrt{f_{ck}}}{\gamma_c} b_0 d_v \tag{2}$$

$$k_\psi = \frac{1}{1.5+0.9\, k_{dg}\, \psi\, d} \leq 0.6 \tag{3}$$

where:

k_ψ - parameter considering rotations of the slab [-];
b_0 - shear-resisting control perimeter at distance of 0.5d from the face of a column [mm];
d_v - shear-resisting effective depth [mm];
k_{dg} - parameter considering the maximum aggregate size, $k_{\mathrm{dg}} = \frac{32}{16+d_{\mathrm{g}}} \geq 0.75$ [-];
d_g - maximum aggregate size [mm];
ψ - slab rotation [-].

$$\psi = 1.2 \frac{r_s}{d} \frac{f_{ym}}{E_s} \left(\frac{m_{Ed}}{m_{Rd}}\right)^{1.5} \tag{4}$$

where:

r_s - the distance from the column's axis to the line of the contraflexure of the radial bending moments [m];
f_{ym} - yield strength of the main reinforcement [MPa];
m_{Ed} - average design bending moment per unit of length [kNm/m];
m_{Rd} - average design bending capacity of a slab per unit of length [kNm/m].

prEurocode 2

This model is also based on the Critical shear crack theory, but the expression of equation is closer to EC2 (2004). More details about this design model are available to see in CEN TC250/SC2.

$$V_{\mathrm{Rd,c}} = \frac{0.6}{\gamma_{\mathrm{C}}} k_{\mathrm{pb}} \left(100 * \rho f_{\mathrm{ck}} \frac{d_{\mathrm{dg}}}{\sqrt{d_{\mathrm{v}} \frac{r_{\mathrm{s}}}{8}}} \right)^{1/3} b_0 d_{\mathrm{v}} \quad (5)$$

$$k_{\mathrm{pb}} = \sqrt{5.\mu_{\mathrm{p}} \frac{d_{\mathrm{v}}}{b_0}} < 2.5 \quad (6)$$

where:

d_{dg} - a size parameter which describes the failure zone roughness considering the concrete class and aggregate properties; d_{dg} = 16 mm + $d_{g,max} \leq$ 40 mm if $f_{ck} \leq$ 60 MPa [mm];

μ_p - a coefficient accounting for the shear force gradient and bending moments in the region of the control perimeter, for internal column: $\mu_p = 8/k_e$ [-];

k_e - a factor considering an influence of reduced control perimeter, $k_e = b_0/b_{0,red}$ [-];

$b_{0,red}$ - reduced control perimeter due to significantly elongated cross-section of a column [mm].

The non-linear analysis

The non-linear analysis was performed in Atena - program based on finite element method [5]. Several research teams dealt with non-linear analysis in Atena, including [6], who focused on the strengthening of flat slabs. According to the linear analysis, there is a partial decrease in shear forces at a distance of 1.5*d* from the support corners [4]. Figure 1 shows the decrease in shear forces of a specimen supported by a column with cross-sectional dimensions of 950 x 150 mm using different loading conditions. However, in the non-linear analysis, the reduction of the control perimeter length was not demonstrated despite the fact that the ratio of the longer column cross-sectional dimension to the effective depth was c_{max} / d > 3. This phenomenon is caused by several aspects including redistribution of stresses around the support. Model calibration was implemented on the basis of previous experiments [7].

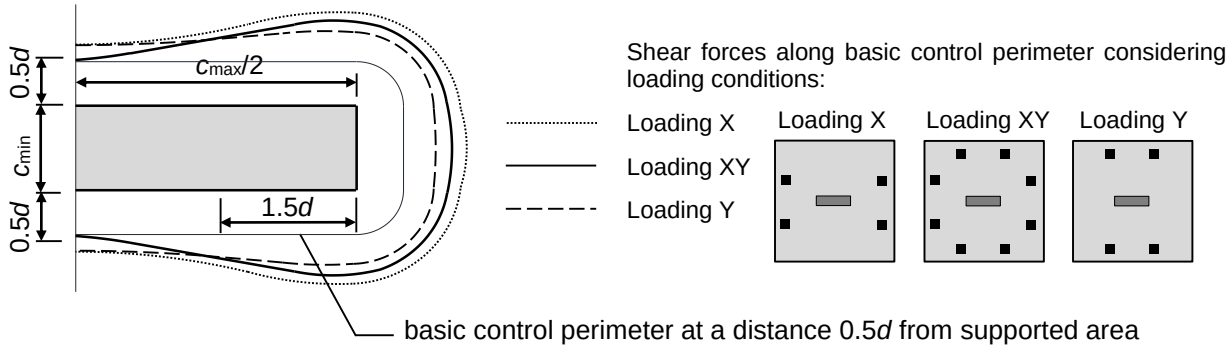

Fig. 1 - The distribution of shear forces along the basic control perimeter

Because 3D non-linear evaluations are time consuming, symmetry conditions were used and only a quarter of the whole specimen was modeled (Figure 2).

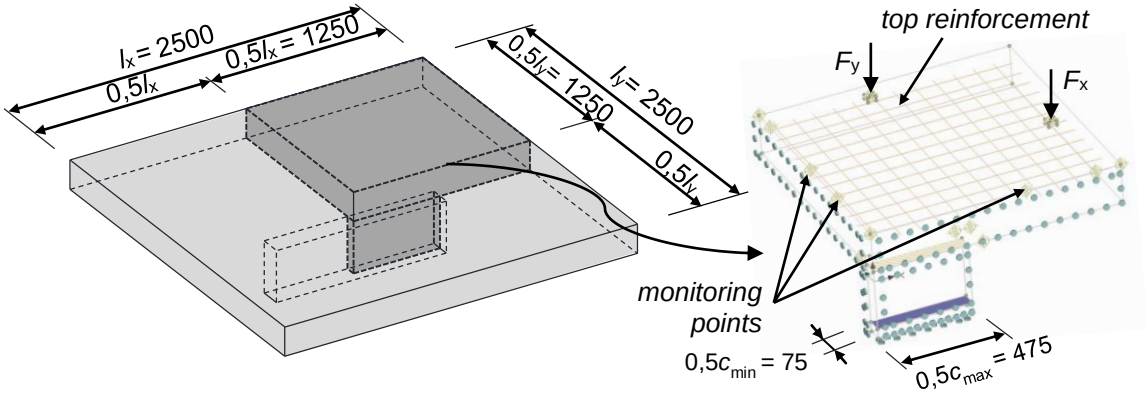

Fig. 2 Fragment model of specimen modeled in Atena

EXPERIMENTAL PROGRAM

Experimental specimens

The size of test specimens was 2.5 m x 2.5 m with thickness of 0.2 m. These dimensions are based on laboratory conditions and the overall arrangement of the experimental set-up. Concrete samples were taken during the concreting to determine the material properties. The measured concrete cylinder strength at time of testing is listed in Table1. The maximum aggregate size $d_{g,\,max}$ = 16 mm was used. The slab fragment was reinforced with steel reinforcement of B500B with yield strength f_{ym} = 550 MPa: 16 mm diameter bars equally spaced at 100 mm in both orthogonal directions and 10 mm bars equally spaced at 200 mm on the compression face. The specimens were not reinforced with transverse reinforcement. Other specimens' characteristics are listed in Table1.

The concrete of supporting column reached 89 MPa of cylinder strength. It is reinforced with 12 bars with diameter Ø = 12 mm spaced evenly along the column perimeter.

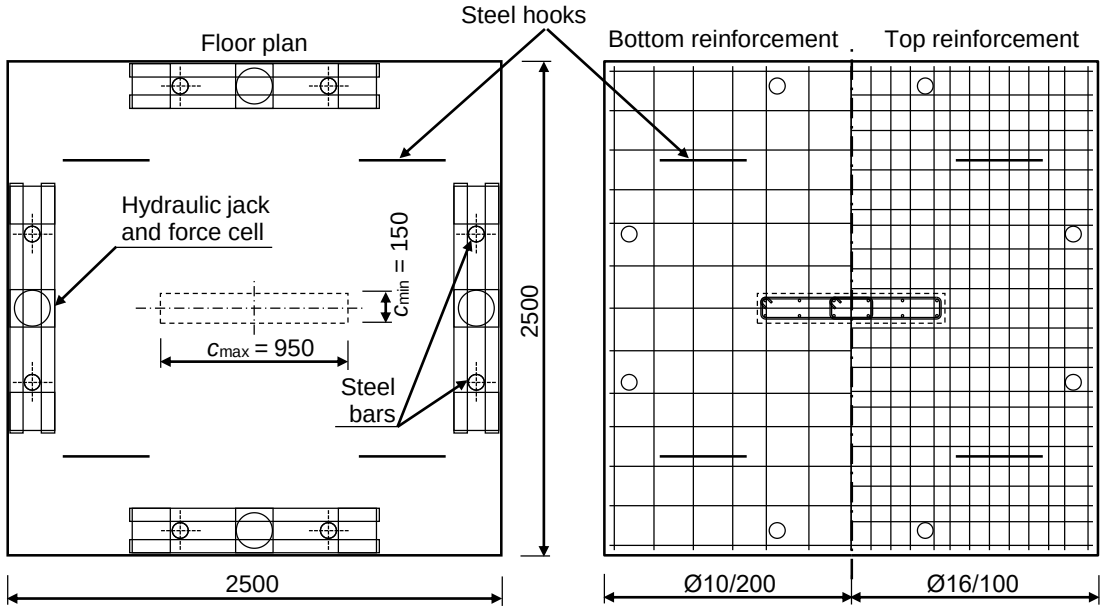

Fig. 3 - Geometry and reinforcement of experimental specimen

Tab. 1 - Specimen's characteristics

Test	f_c [MPa]	c_{nom} [m]		d [m]	ρ [%]	Reinforcement	
		Top	Bottom			Top	Bottom
D00	29.9	0.025	0.02	0.159	1.26	Ø16/100	Ø10/200
D01	22.3	0.02	0.02	0.164	1.26	Ø16/100	Ø10/200

Experimental set-up

The experimental set-up consists of four hydraulic jacks placed around the specimen perimeter, which are spread by a system of beams. These beams are made of two UPE profiles which are fixed to steel bars (Ø = 42 mm) placed among them and anchored to the laboratory floor. Concentrated forces are transferred from the hydraulic jacks to the bottom distribution pair of beams, which are supported with calottes to ensure joint connection of the frame and specimen.

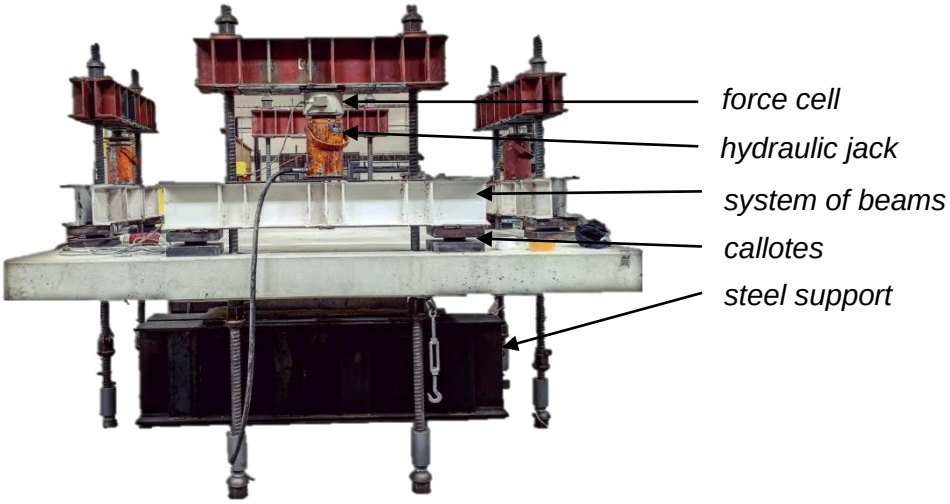

Fig. 4 - Experimental set-up

Loading conditions

The first loading step of approximately 20 kN was performed to activate the experimental set-up. Gradually even loading of the specimen was performed in individual loading steps of 50 kN and 100 kN, i.e. 12.5 kN (or 25 kN) per one hydraulic jack. Just before the expected failure, the loading step was reduced to 25 kN. Short pauses were taken between the individual steps to stabilize the specimen deformations, to record photos for the photogrammetry measurement and to draw newly occurred cracks.

Measuring devices

The concentrated load in the form of eight forces distributed around the specimen perimeter was measured by four load cells connected to one hydraulic system. The loading force from one hydraulic jack was applied to the specimen at two points with a mutual distance of approximately 1 m (distance of steel calottes).

Several measuring devices were also installed on the specimen, recording its deformation behavior during the entire process of loading until its failure. Strain gauges were glued to the bottom

surface around the support according to the scheme in Figure 5a. Using the strain gauges, it was possible to determine the concrete strains both in the radial and tangential direction. Specimen deformations were measured in two directions using LVDT sensors located in the slab axis lines (Figure 4b). The full stroke range of used LVDT sensors varies from 50 mm located close to column to 300 mm located between to steel rods. The deflection measured in millimeters could be determined up to an accuracy of five decimal places.

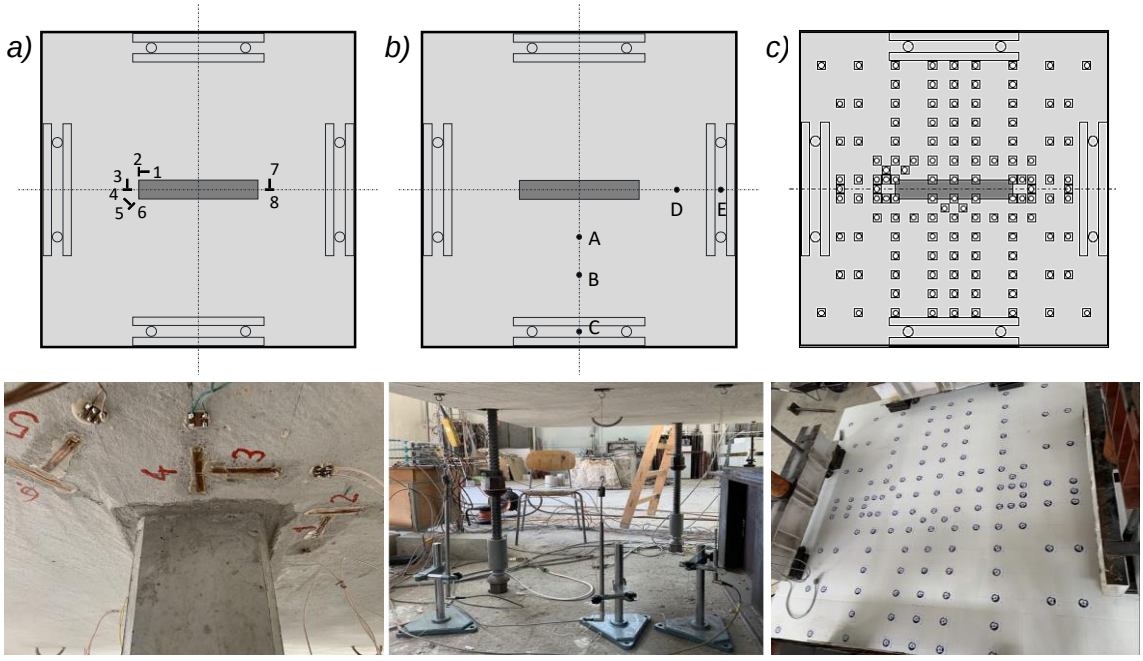

Fig. 5 - The sensor layout scheme: a) strain gauges b) LVDT sensors c) code marks on the top surface of the specimen used for convergent photogrammetry measurement

In cooperation with the Department of Geodesy in Faculty of civil engineering of Slovak university of technology in Bratislava, a method of measurement using convergent photogrammetry was implemented in this experimental test. Multi-image convergent photogrammetry was performed to achieve 3D coordinates of observed points [8]. The Nikon D800E DSLR camera (full frame 36 Mpixel sensor) equipped with a Nikkor 35mm AF-S ED 1:1.8G lens was used to take photos around the specimen in each loading step (Figure 6). To eliminate the blur motion caused by poor illumination conditions, an external flash was used. An exposure time of 1/250 s was achieved at the following camera settings: aperture priority – F/8, ISO 200, autofocus.

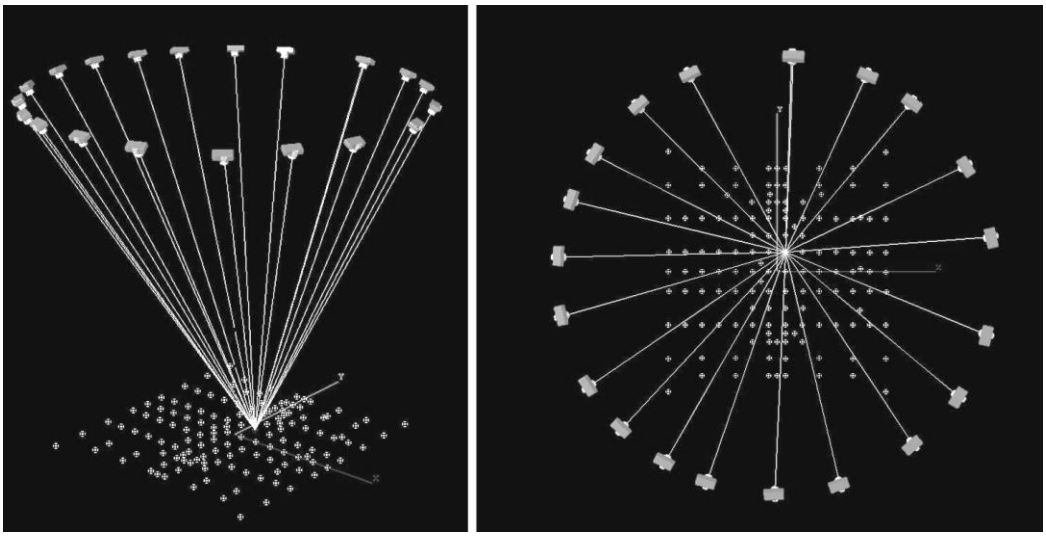

Fig. 6 - Image configuration – axo view (left) and top view (right)

131 observed points were signalized by RAD (Ringed Automatically Detected) coded targets, which enable automatic detection and measurement with subpixel precision. Images were processed by Photomodeler Software [9] on the principles of bundle block adjustment. The project scale was determined using two scale bars attached to the specimen surface – the length of the scale bars was derived from the calibration plate of the Comet L3D scanner with an accuracy of 0.01 mm. The results of photogrammetric processing are shown below.

Tab. 1 - Multi-image convergent photogrammetry precision details

Precision [mm]	Number of photos per loading step	Angle intersection [deg]	Rays per points	Max. residual [pix]	RMS residual [pix]
m_x = 0.003-0.008	20	51-57	7-21	0.21	0.04
m_y = 0.003-0.010					
m_z = 0.007-0.014					

TEST RESULTS

The failure was fragile in both experimental tests, indicating that the collapse of the specimen was due to the achievement of shear resistance. The experimentally obtained values of shear resistance were compared to selected design models, which verified their reliability (Table 2). The V_{test} given in Table 2 is the sum of the maximum forces measured in the load cells and the body force of the specimen with a value of 31 kN.

Tab. 2: Results obtained from experimental test and Atena compared to design models

	Basic control perimeter [m]		Punching shear resistance [kN]				D00		D01	
			D00		D01					
	u_1	u_{red}*	$V_{R,c}$	$V_{R,c,red}$	$V_{R,c}$	$V_{R,c,red}$	V_{test} / $V_{R,c}$	V_{test} / $V_{R,c,red}$	V_{test} / $V_{R,c}$	V_{test} / $V_{R,c,red}$
Test	4.07		852		688		-		-	
Atena	4.09		875		721		0.97		0.95	
EC2 [10]	4.20	3.25	856	663	794	623	0.99	1.29	0.87	1.10
prEC2 [11]	2.70	1.75	778	628	723	588	1.09	1.36	0.95	1.17
MC2010 [12]	2.70	1.75	760	590	707	552	1.12	1.44	0.97	1.25
* note – reduced length of basic control perimeter evaluated as $u_{red} = 2c_{min} + 6d$ [m]										

Based on the shear strength obtained from the experiment and non-linear analysis, the length of the control perimeter was derived using the shear resistance evaluation formula according to EC2 [10].

The concentration of shear forces around the corners of the support can be confirmed by the formation of the first appeared shear cracks in this area. First, radial cracks formed and with increasing load were joined by newly formed tangential cracks. However, by comparing the experimentally obtained shear resistance with the values according to the design models, the necessity to reduce the length of the control perimeter was demonstrated for both specimens compared to selected design models, as their reliability reaches 0.87 to 1.12 considering the full length of control perimeter.

Deformations

Figure 7 shows specimen deformations in the lines of the main axes. According to design model EC2, a slab supported by a square column would have the same shear resistance as a slab supported by a column with a rectangular cross-section with the same length of control perimeter. The EC2 design model therefore only takes into account the length of the control perimeter, not the geometry of the support. However, by comparing the deformation courses of the slab, the influence of the column geometry on its shear resistance can be confirmed. Significantly larger deflection of the specimen was measured in the direction perpendicular to the longer side of the column c_{max}.

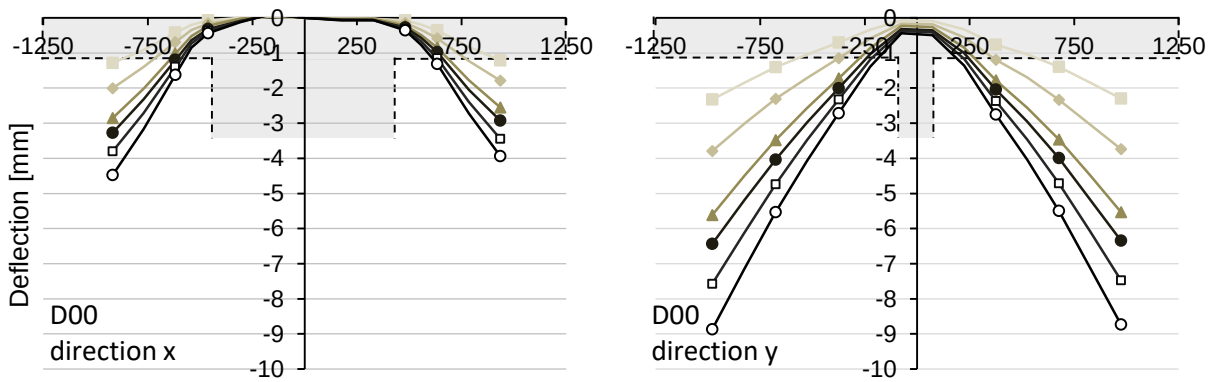

Fig. 7 - Deflected profiles of the specimens

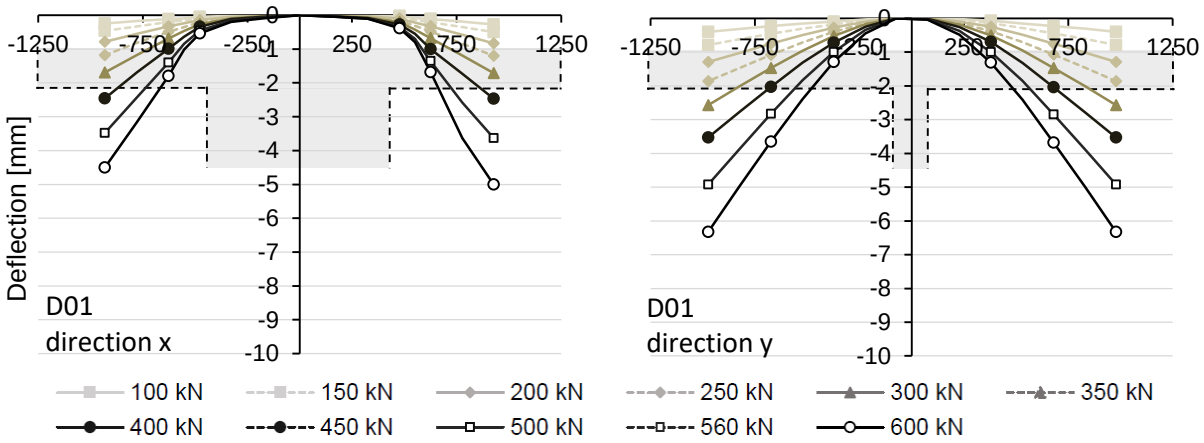

Fig. 8 - Deflected profiles of the specimens

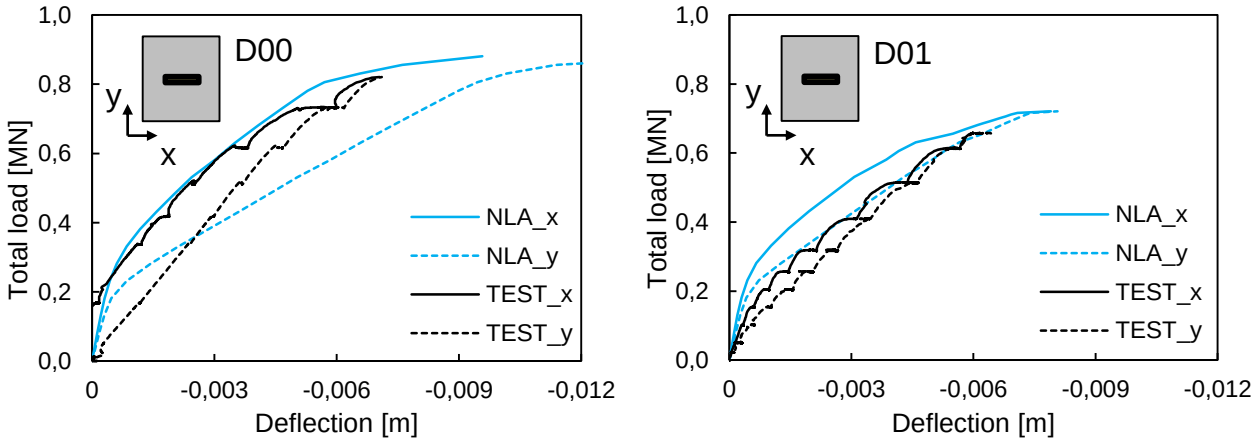

Fig. 9 - Maximum deflection evaluated in NLA compared to maximum deflection measured in experimental test (LVDT at C and E points according to Figure 5b)

In the case of specimen D00, the deflection in the direction perpendicular to the longer side of the column reached significantly higher values. This phenomenon is caused by the fact that the drawn deflection is already captured on the specimen with developed cracks, which arose as a result of previous loading, which had to be suspended and the specimen was unloaded again.

Strains

The concrete strains on the top surface of the specimen were evaluated on the basis of the results of photogrammetric measurements. The maximum strains reached a value of up to 4.1 ‰. Figure 8 shows the course of the concrete strains in the individual loading steps. On the top surface of the slab, no significant differences were observed in the concrete strains in the section through the center of the longer side of the column compared to the area of its corners.

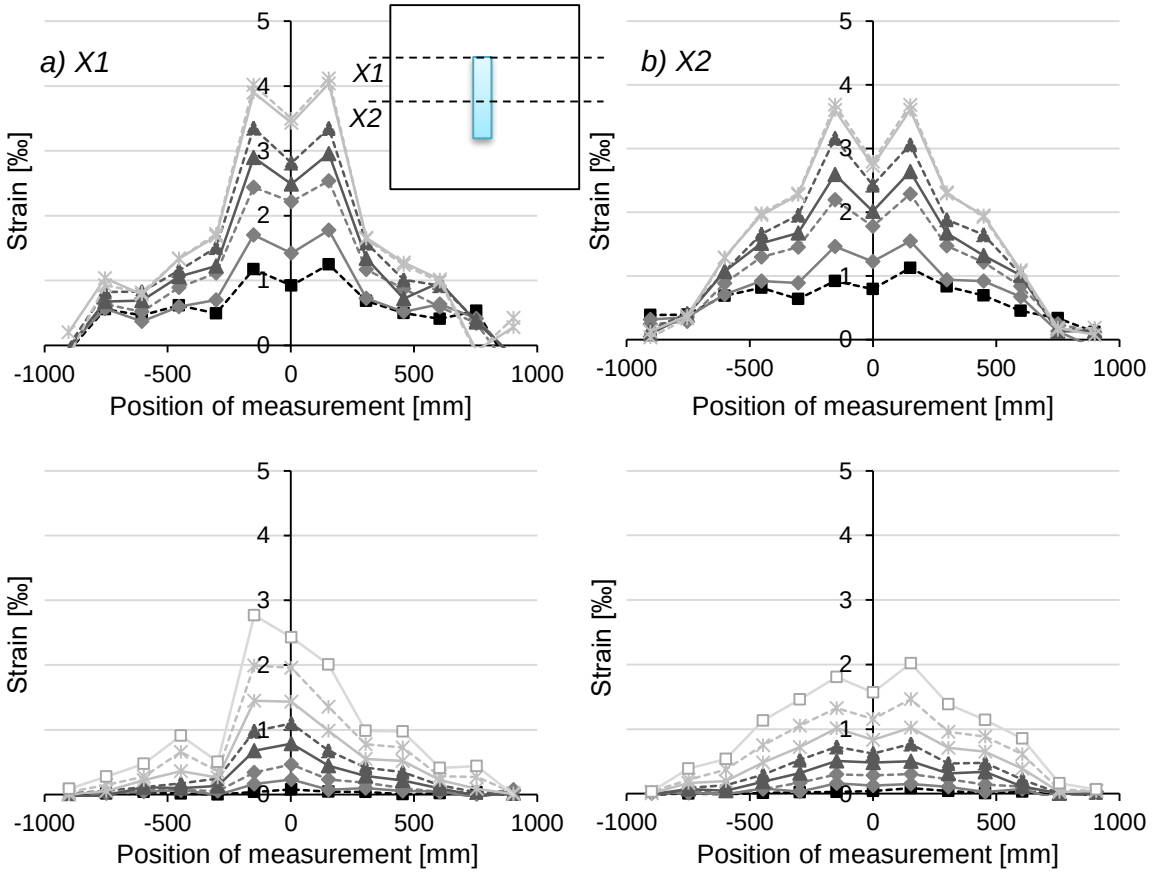

Fig. 10 - Concrete strains (‰) on the top surface of the specimen in the direction of the x-axis in individual loading steps

The concrete strains were measured on the bottom surface of the specimen in the area around the support using strain gauges glued in both the radial and tangential directions according to the diagram in Figure 5a. The largest concrete strains were measured in the tangential around the corners of the support (strain gauges no. 3 and 7), on the contrary, the contrary, the concrete strains in the radial direction reached the lowest values at these points (Figure 10).

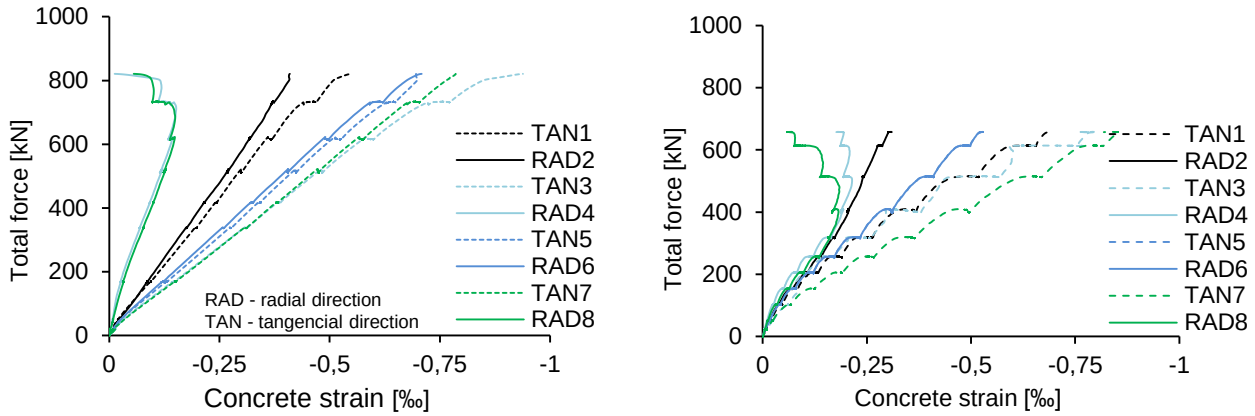

Fig. 11 - Concrete strains on the bottom surface of the specimen measured in strain gauges

CONCLUSION

The subject of this paper is to acquaint with the results of experimental tests of slab fragments supported by a rectangular column, the results of which were confronted with numerical nonlinear analysis and predictions according to selected design models. Based on these comparisons, the following conclusions were derived:

1. Both experimental tests and non-linear analysis shown the necessity to reduce the length of the control perimeter. Compared to the design models EC2, MC2010 and prEC2 (2018), reliability reaches from 0.87 to 1.12 considering the full length of the control perimeter for this support geometry and uniform loading.

2. The formation of the first cracks in the radial direction was recorded around the corners of the support, thus demonstrating the stress concentration in these areas.

3. The largest concrete strains on the bottom surface of the specimen were measured in the tangential direction at points near the corners of the support.

4. Measured deformations in the x and y directions were compensated just before the failure, which seems to be a results of forces redistribution. A similar result was demonstrated by Atena in the case of specimen D01.

5. Photogrammetric measurement records the whole deformation behavior of the specimen in contrast to LVDT sensors located at specific points. The results obtained from non-linear analysis have shown better agreement to actual slab behavior observed in experimental test than the photogrammetric measurement in the case of specimen D01.

ACKNOWLEDGEMENTS

This work was supported by the Slovak Research and Development Agency under the contract No. APVV-15-0658 and Scientific Grant Agency of the Ministry of Education, science, research and sport of the Slovak Republic and the Slovak Academy of Sciences No 1/0645/20.

REFERENCES

[1] Sagaseta J., Tassinari L., Fernández Ruiz M., Muttoni A., 2014. Punching of flat slabs supported on rectangular columns. Engineering Structures 77: 17-33.

[2] Mečár J., Bujňáková P., Sobek V., 2019. Optimized design of flat slabs with different novel type of punching reinforcement, In: Proc. International Conference on Sustainable Materials, Systems and Structures, Challenges in Design and Management of Structures, 18-23.
[3] Sucharda O., Smirakova M., Vaskova J., Mateckova P., Kubosek J., Cajka R., 2018. Punching Shear Failure of Concrete Ground Supported Slab. In: International Journal of Concrete Structures and Materials, 12(1).
[4] Šarvaicová S., Borzovič V., Augustín T., 2019. The influence of a column shape cross-section on the punching capacity. In: MBMST 2019 conference proceeding. 455-462.
[5] Červenka V., Jendele L., Červenka J., 2018. ATENA program documentation, Part 1, Theory. (Prague: s.n).
[6] Nováček J., Zich M., 2016. Study of Flat Slabs Strengthening against Punching Shear. In: Solid State Phenomena 249. 221-226.
[7] Augustín T., Fillo Ľ., Halvonik J., 2019. Punching resistance of slab-column connections with openings, Structural Concrete 21, 278-290.
[8] Marčiš M., Fraštia M., Bajtala M., Augustín T., 2017. Measurement of flat slab deformations by the multi-image photogrammetry method. In: Slovak Journal of Civil Engineering. Vol. 25, no. 4, 19-25.
[9] https://www.photomodeler.com/
[10] European Commitee for Standardization. Eurocode 2: Design of concrete structures, Part 1-1: General rules and rules for buildings, 2004.
[11] prEN 1992-1-1 Eurocode 2: Design of concrete structures – Part 1-1: General rules, rules for buildings, bridges and civil engineering structures. Review 11. Upgrated draft D5. 2020.
[12] Fédération Internationale du Béton (fib). Bulletin n. 65/66 Model Code 2010. Final draft (Vol. 1, 2. fib). Lausanne, 2012.

CIVIL ENGINEERING JOURNAL

Article no. 65

THE CIVIL ENGINEERING JOURNAL 4-2021

FIELD MEASUREMENT AND NUMERICAL STUDY OF EXTERNAL WIND PRESSURE OF RIBBED COOLING TOWER

Yi-chen Yuan [1] , *Zi-hou Yuan* [2, 4*], *Ming-xiang Chen* [3*]

1. *Huazhong University of Science and Technology, School of Civil and Hydraulic Engineering, Wuhan, Hubei, 430070, China; hustyyc@126.com*
2. *Wuhan Textile University, Hubei Key Laboratory of Digital Textile Equipment, Wuhan, Hubei, 430073, China; whuyzh@163.com*
3. *Wuhan University, School of Civil Engineering, Wuhan, Hubei, 430072, China；2002025@wtu.edu.cn*
4. *Southeast University, Key Laboratory of Concrete and Pre-stressed Concrete Structure of Ministry of Education, Nanjing , Jiangsu ,211189, China；whuyzh@163.com*

ABSTRACT

The hyperbolic thin-shell cooling tower is a typical wind-sensitive structure, and the full-size measurement is the most direct and important way to study the distribution of wind pressure on the surface of the cooling tower. But due to the limitations of engineering conditions and meteorological conditions, the field measured data are relatively lacking, and the field test data of ribbed cooling towers are less. In order to analyze the wind pressure distribution on the surface of the cooling tower, we chose a ribbed cooling tower in Toksun County, Xinjiang, China, where there is strong wind all year round, and field measurements were carried out to understand the wind load characteristics of the tower under the perennial dominant wind direction and the maximum wind direction. It is found that the absolute value of the negative pressure on the leeward side is larger than that in the code and the fluctuating wind pressure coefficient fluctuates greatly when the field measured wind speed is greater than 10m/s (15 meters above the ground). And for circular section cooling tower, the Reynolds number (Re) has great influence on wind pressure. With the increase of Re, the absolute value of the average negative pressure of the tail wind pressure coefficient increases, which should be paid attention to in design. Meanwhile, the regression curves of the average wind pressure coefficients measured on site under several typical working conditions are given by using the least square method, and its form is consistent with the standard (but the coefficients are different). Finally, Fluent software is used to calculate the external wind pressure of the cooling tower, and the variation law of numerical calculation is consistent with that of the field measured results, the Chinese code and German code.

KEYWORDS

Ribbed cooling tower, Wind pressure coefficient, Field measurement, Code, Reynolds number

INTRODUCTION

Wind load is one of the main loads of hyperbolic cooling towers. In 1965, the cooling tower group of Ferrybridge power station in England collapsed when the average wind speed was only

19m/s. And the cooling tower at Scotland's Ardeer power plant collapsed under strong winds in 1973[1].

These accidents have attracted the attention of the International Wind Engineering Society and experts at home and abroad. Experts have measured the wind pressure distribution characteristics on the cooling tower surface [2], wind tunnel test flow characteristics compensation [3,4], effect of group tower and adjacent landform on wind pressure distribution on the surface of tower [5], buckling stability and ultimate bearing capacity of tower cylinder under wind load [6,7], and fluctuating wind pressure causes random dynamic response of ventilator shell [8].

The hyperbolic circular section cooling tower is a typical streamlined wind-sensitive three-dimensional thin-walled space structure, and the wind pressure distribution on the surface is significantly affected by Re. Re of actual cooling tower is about 1×10^7~1×10^8. However, Re of the structural model and the prototype differs by 2 ~ 3 orders of magnitude. At present, it is impossible to simulate the flow pattern of the cooling tower structure under such high Re by increasing the test wind speed or the scale ratio of the model. Although some scholars have tried to change the surface roughness of cooling tower to simulate the high Re effect of large scale ratio model about surface circulation [9], full scale measurement is still the most direct and important way to study the wind pressure distribution of cooling tower [10,11].

An earlier literature report on the field measurement of surface wind pressure of cooling tower was the four-tower combined test of the West Burton power plant in the UK in 1960 [12]. In 1971, Niemann carried out field measurement of the Weisweiler cooling tower in Germany [13]. In 1974, Sollenberger and Scanlan conducted field measurements of Martin's Creek cooling tower in Pennsylvania, USA [14]. Peking University and xi 'an institute of thermal engineering carried out field measurements on two prototype cooling towers(90m height) in Matou, Hebei province(in 1981) and Maoming, Guangdong province(in 1982) and their data has been adopted by Chinese codes [15]. Due to the limitation of tower height and measuring instruments at that time, dynamic characteristics and surface wind load pulsation characteristics could not be fully considered [16]. In 2015, Chen carried out field measurement of large-scale cooling tower in Xu-zhou, China. The measured results of the prototype large cooling tower are updated [17, 18, 19, 20, 21].

Unfortunately, the measured wind speed of cooling tower was not big before. Under the condition of ultra-high Re, the distribution data of wind pressure (average and extreme) on the surface of cooling tower are lack. And the wind load code has not made clear provisions. Besides, the field test data of ribbed cooling tower is very few.

In order to analyze the distribution law of average and extreme wind pressure on the surface of cooling tower, field measurements were carried out on a ribbed cooling tower.

The cooling tower is a kind of double-curved thin shell structure of cast-in-place reinforced concrete. The tower height is 155m, the throat height is 116.25m, and the throat diameter is 68m. 60 ribs are arranged in equal space on the outer wall of the cooling tower. The tower tube is supported by 40 pairs of rectangular cross section "X" shaped pillars of reinforced concrete (see Figure 1).

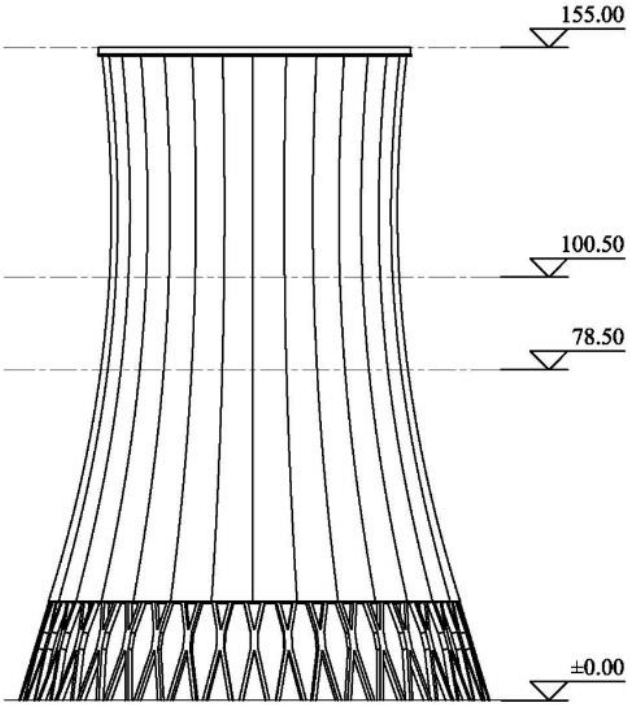

Fig. 1 – Chematic diagram of the cooling tower

The cooling tower is located in Toksun County, Turpan Region, Xinjiang. The site of the cooling tower is flat, with no mountain or obstacle. There is strong wind all year round in Toksun County. The local recorded maximum wind speed was over 40.0m/s, and the maximum wind speed we measured was 25.06m/s. It is extremely rare for such high wind speeds to be measured at the cooling tower site. Re of the cooling tower throat is up to 1.06*E8.

According to the original data, the distribution curve of wind pressure under the perennial dominant wind direction was gotten. And we compared it with Code for Design of Cooling for Industrial Recirculating Water [22] (GB/T50102-2014) to find out the differences of average wind pressure distribution between two curves. The influence of Re on the average wind pressure, fluctuating wind pressure and wind pressure at the end of the cooling tower was analyzed. And the distribution of extreme values on the cooling tower surface under the condition of ultra-high Re is analyzed. In addition, the validity of the numerical simulation method was verified by the measured data.

Figure 2 illustrates the main research content.

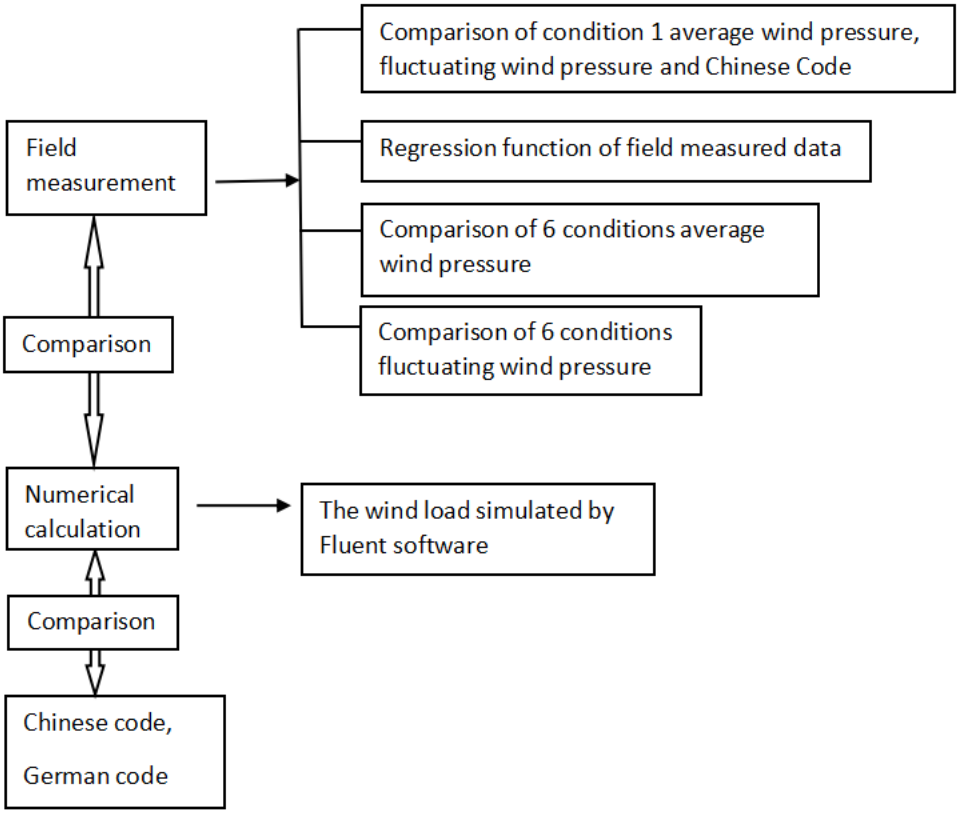

Fig.2 – General layouts of research works

ANALYSIS OF FIELD MEASUREMENT RESULTS

Field measurements of wind pressure, wind speed and direction were carried out for two years at intervals of 10-sec, and a total of 6,220,800 sets of data were recorded. The wind pressure monitoring position was selected as 78.5 meters high section. And the 30 measuring points on the cooling tower were arranged in the center of the two ribs and uniformly arranged along the annular direction (see Figure 3).

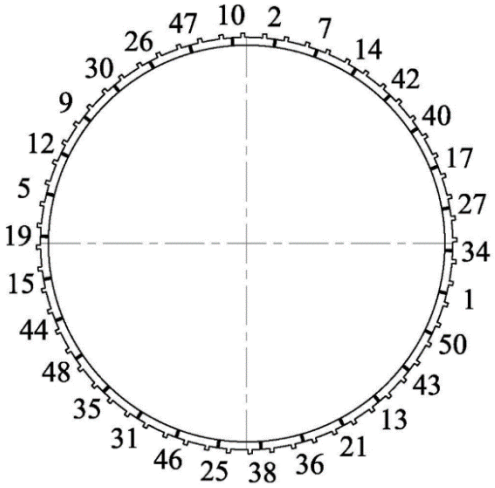

Fig.3 – Layout of measuring points with a height of 78.5 meters

Calculation of wind pressure coefficient

The ratio of the actual pressure or suction caused by wind on the surface of buildings to the wind pressure of incoming flow is called the wind pressure coefficient [23].

Average wind pressure $$\overline{p}_i = \frac{\sum_{j=1}^{N} p_{ij}}{N},$$ ..... .(1)

Fluctuating wind pressure $$\sigma_{pi} = \sqrt{\frac{\sum_{j=1}^{N} (p_{ij} - \overline{p}_i)^2}{N - 1}}$$ ..... (2)

Where, p_{ij} is the pressure value measured at the measuring point i at the moment j, and N is the total number of measured pressure values.

Average wind pressure coefficient $$C_{pi} = \frac{\overline{p}_i - p_\infty}{0.5\rho v^2}$$ ..... .(3)

Where, p_∞ is the reference static pressure, and ρ ,V represent air density and incoming wind speed, respectively.

Fluctuating wind pressure coefficient $$C_{opi} = \frac{\sigma_{pi}}{0.5\rho v^2}$$ ..... .(4)

Due to the limitations of test conditions and the influence of tower landform and surrounding buildings, it is very difficult to get the accurate incoming wind speed in the wind pressure measurement. Therefore, the average wind pressure and fluctuating wind pressure at each measuring point are obtained by dimensionless normalization of the maximum wind pressure at the tower (i.e., stagnation pressure) in this paper.

Load Code for the Design of Building Structures (GB50009-2012) [23] stipulates that the average wind time interval is 10min, and the wind pressure data is averaged according to the measured sample data with 10min as the basic time interval. Because of the high wind speed of the northwest wind in history, the northwest wind is chosen as the calculation condition (wind direction of each working condition is relatively stable). Firstly, working condition 1 and working condition 2 are calculated (each working period is 10min). Because the wind speed and pressure data fluctuate greatly within 10min, working conditions 3 to 6 are calculated (all time periods are less than 10min, in order to ensure the wind speed and wind direction are relatively stable). Re (cooling tower throat) is calculated using the average wind speed (cooling tower throat) (see Table 1).

Tab. 1 - Calculated condition

Serial number	Time	Maximum wind speed (m/s)	average wind speed (m/s) (15 meters above the ground)	average wind speed (m/s)(cooling tower throat)	Re(cooling tower throat)
1	2016-04-23 18:43:03--18:53:03	14.53	8.4	11.42	$46.78*10^6$
2	2016-04-24 14:30:03--14:40:03	25.06	12.7	17.27	$70.74*10^6$
3	2016-04-24 14:30:42--14:32:22	23.2	16.6	22.57	$92.46*10^6$
4	2016-4-23 18:36:13--18:37:23	12.59	9.7	13.19	$54.03*10^6$
5	2016-04-29 20:12:03--20:13:03	13.18	11.27	15.32	$62.76*10^6$
6	2016-04-23 20:29:24--20:30:22	8.04	6.61	8.99	$36.83*10^6$

Wind pressure distribution of condition 1

The distribution of average wind pressure coefficient, and fluctuating wind pressure coefficient (measured value of working condition 1) are compared with the distribution of average wind pressure coefficient (ribbed, non-ribbed) in the code (GB/T50102-2014) [22] (see Figure 4).

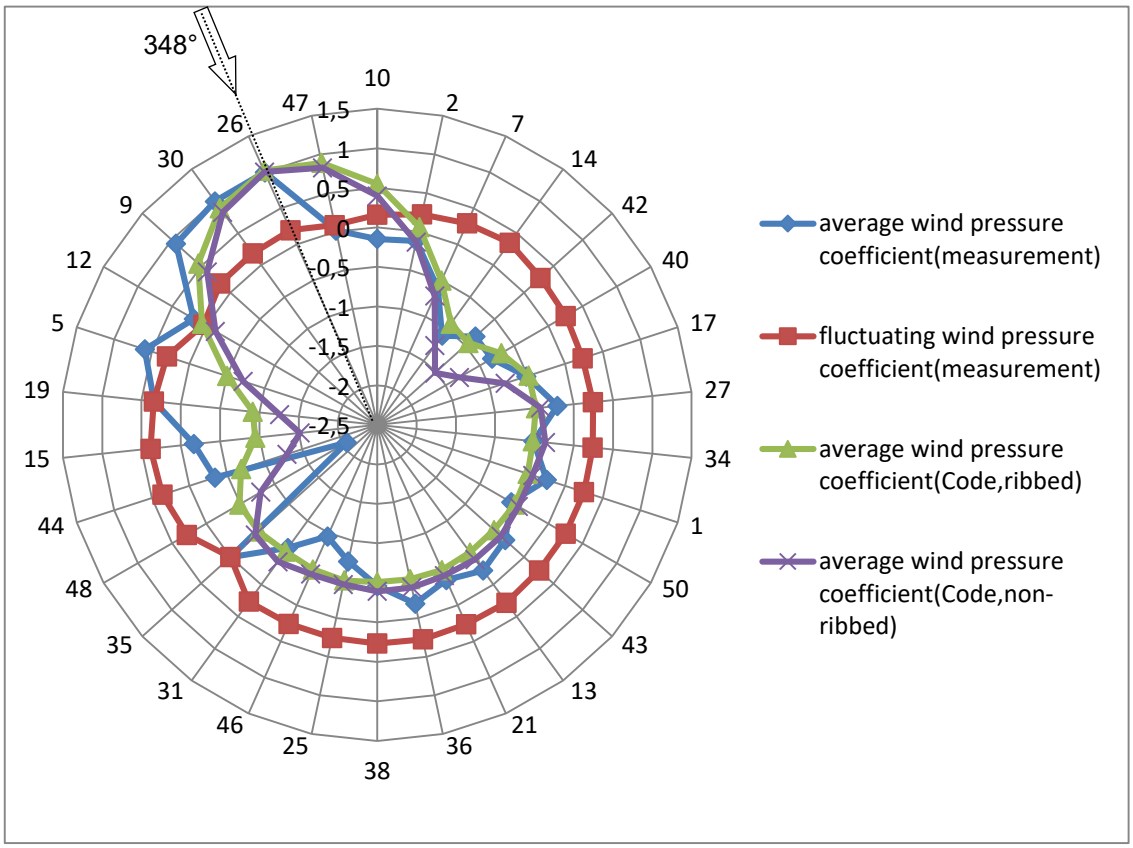

Fig.4 – Comparison of wind pressure coefficient

Figure 4 shows that the measured average wind pressure on the cooling tower surface in working condition 1 is basically consistent with GB/T50102-2014.

Next, the average wind pressure coefficient of 6 kinds of field measured data in Table 1 is regressed into the form of the code (GB/T50102-2014).

$$C_p(\theta) = \sum_{k=0}^{9} \alpha_k \cos k\,\theta = \alpha_0 + \alpha_1 \cos\theta + \alpha_2 \cos 2\,\theta + \cdots + \alpha_9 \cos 9\,\theta \quad (5)$$

In which,

θ=0°, 12°, 24°, 36°, 48°, 60°, 72°, 84°, 96°, 108°, 120°, 132°, 144°, 156°, 168°, 180° (corresponding to 16 measuring points).

θ=0° is the wind direction corresponding to the maximum average wind pressure in 10min.

The coefficient of wind pressure distribution curve of ribbed cooling tower obtained by regression of measured data is

[α]'= [-0.5993, 0.4784, 0.6235, 0.3063, -0.0696, -0.0488, 0.091, 0.0773, 0.0601, 0.0454]. While [α]'= [-0.31816, 0.42197, 0.48519, 0.38374, 0.13956, -0.05178, -0.07171, 0.00106, 0.03127, -0.00025] in the code (GB/T50102-2014).

Comparison of 6 working conditions

The distribution of the average wind pressure coefficient measured in the field from working conditions 1 to 6 is compared with that in GB/T50102-2014, regression curve. (see Figure 5).

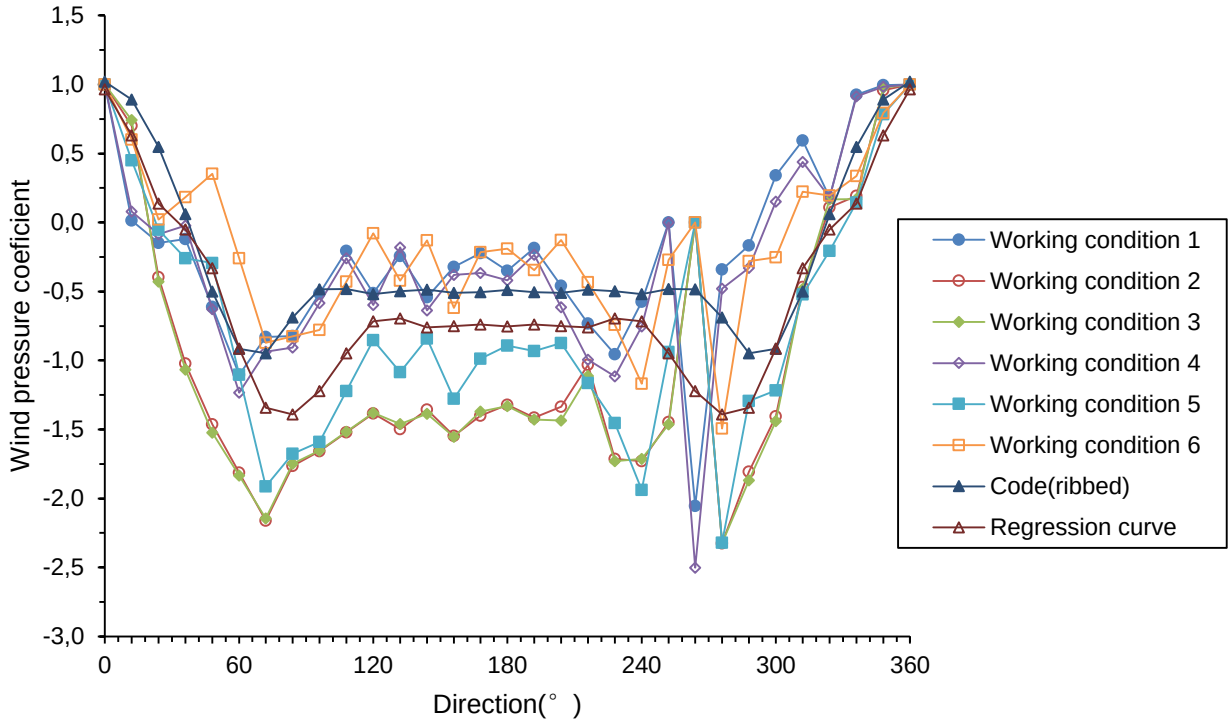

Fig. 5 – Distribution comparison of average wind pressure coefficient

From Figure 5, average wind pressure coefficients in working conditions 1, 4 and 6(the average wind speed is less than 10m/s) are close to the code value (GB/T50102-2014), while average wind pressure coefficients in working conditions 2,3,5(the average wind speed is greater than 10m/s) are far from the code value (GB/T50102-2014). The higher the wind speed is, the higher the surface wind pressure of the cooling tower is. And average wind pressure coefficients in working conditions 2, 3, 5 are greater than the code value (GB/T50102-2014).

In addition, the distribution law of wind pressure coefficient at the end of cooling tower varies with Re (see Table 2).

Tab. 2: Comparison table of the average wind pressure coefficient of cooling tower tail in the field measurement and in the code (GB/T50102-2014) with Re variation

Working conditions	Average wind speed (m/s)	Re	Average wind pressure coefficient of cooling tower tail in the field measurement	Average wind pressure coefficient of cooling tower tail in the code
Working Condition 1	8.4	$46.78*10^6$	-0.37	-0.50
Working Condition 2	12.7	$70.74*10^6$	-1.42	-0.50
Working conditions3	16.6	$92.46*10^6$	-1.51	-0.50
Working conditions4	9.7	$54.03*10^6$	-0.39	-0.50
Working conditions5	11.27	$62.76*10^6$	-0.97	-0.50
Working conditions6	6.61	$36.83*10^6$	-0.27	-0.50

It can be seen from Table 2 that when the wind speed is 9.7m/s (working condition 4), the average wind pressure coefficient of cooling tower tail in the field measurement is the closest to that in GB/T50102-2014. The larger the wind speed is (the greater Re is), the larger the absolute value of the average negative pressure of the tail wind pressure coefficient is. This rule should be paid attention to in the design.

The characteristics of the flow field outside the tower are analyzed from the mechanism. In the transcritical region, with the increase of Re, the transition point moves upstream until near the forward standstill point, the separation point moves forward, and the absolute value of minimum pressure coefficient and back pressure coefficient increases.

Comparison diagram of the measured fluctuating wind pressure coefficient distribution under working conditions 1~ 6 is shown in Figure 6. From Figure 6, working conditions 2 and 3 have the maximum average wind speed, and have large fluctuations in fluctuating wind pressure. The lower the wind speed is, the lower the fluctuating wind pressure is.

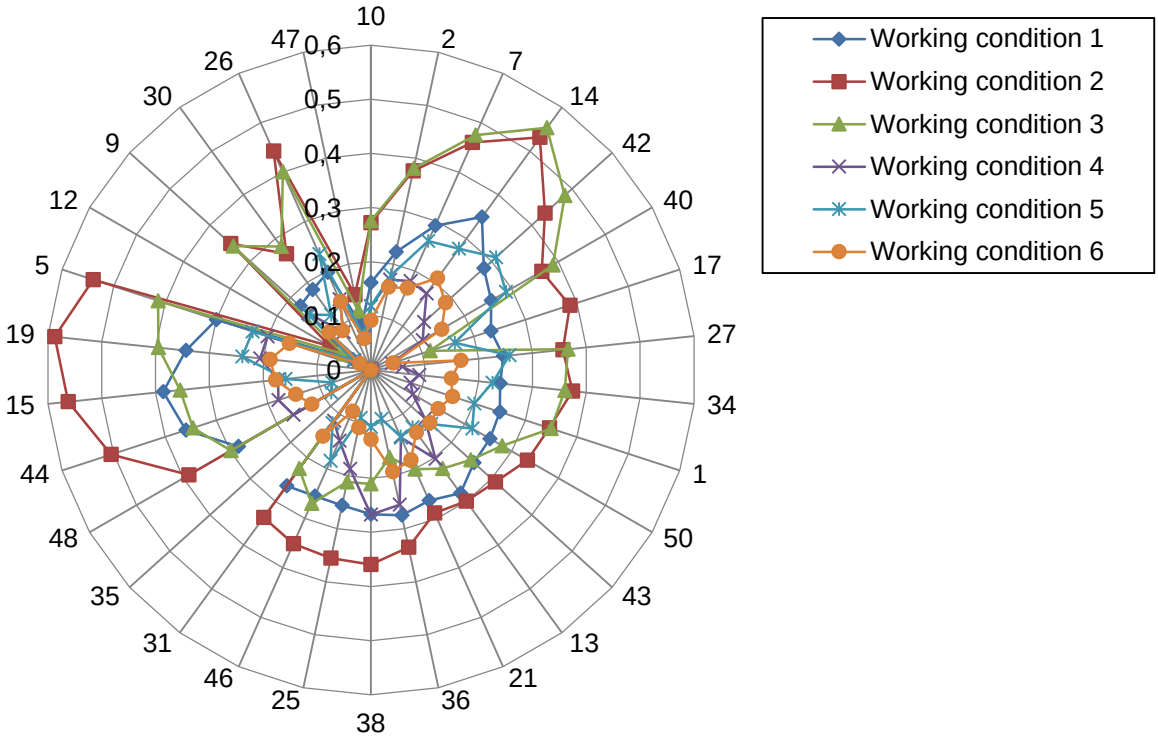

Fig.6 – Comparison diagram of fluctuating wind pressure coefficient

NUMERICAL CALCULATION

Because there are few field measured data, it is necessary to compare it with numerical simula tion calculation to gather experience for wind pressure simulation calculation of cooling tower.

The numerical modeling

The numerical analysis does not consider the deformation of the cooling tower under the action of wind load. The physical model adopted by the calculation is shown in Figure 1. In the rectangular region adopted in this paper, the boundary of the windward face is 5H away from the model center (H is the height of the cooling tower), and its left and right boundary and upper boundary are also 5H away from the model center. In order to better simulate the development of the model's wake, the boundary of its downstream outlet is 10H away from the model center. The total number of cooling tower grid units is 2.2 million.

The boundary condition of numerical analysis is:

1) The velocity inlet boundary condition on the windward surface of the region is given, and the wind profile of the atmospheric boundary layer is simulated by exponential law.

The section function of turbulence kinetic energy k and turbulence dissipation ratio is:

$$k(z) = 1.5u^2(z)I_u^2(z) \quad (6)$$

$$\varepsilon(z) = C_u^{3/4}k(z)^{3/2}/l \quad (7)$$

Where Cu =0.09, l is the integral scale of turbulence, and the value here is 0.07 times the building characteristic scale.

UDF function is used to custom entry wind function.

2) Outflow boundary condition is used in export.

3) Symmetric boundary conditions are applied to the top and both sides of the computational domain. The symmetric boundary conditions are equivalent to the wall surface of free slip, and the normal velocity on the boundary is 0.

4) Non-slip wall conditions are adopted on the surface and ground of the building.

The realizable k-epsilon turbulence model is used. The inlet turbulence intensity is $I_u(z)=0.1(z/z_G)^{-\alpha-0.05}$.

B-type geomorphic conditions are adopted, and u_{10}=18m/s is taken as the reference wind speed.

SIMPLE algorithm is adopted in pressure velocity coupling. And the first order discrete scheme is adopted in the momentum equation, the turbulent kinetic energy equation and the dissipation rate equation of the turbulent kinetic energy.

The criterion for calculating iterative convergence is that the residual of all variables drops below 10^{-5} and the variation of parameters in the flow field tends to be steady. The non-equilibrium wall function method is used to deal with the turbulence near the wall.

Comparison among numerical simulation, field measurement results and Code

The wind load can be simulated by Fluent software. And the average wind pressure coefficients measured in the field are compared with that in the Chinese code (GB/T50102-2014) [22], in the German code (VGB-R 610Ue, 2005) [24] (6 VGB curves are given according to the surface roughness from the German Code) and in numerical simulation (see Figure 7).

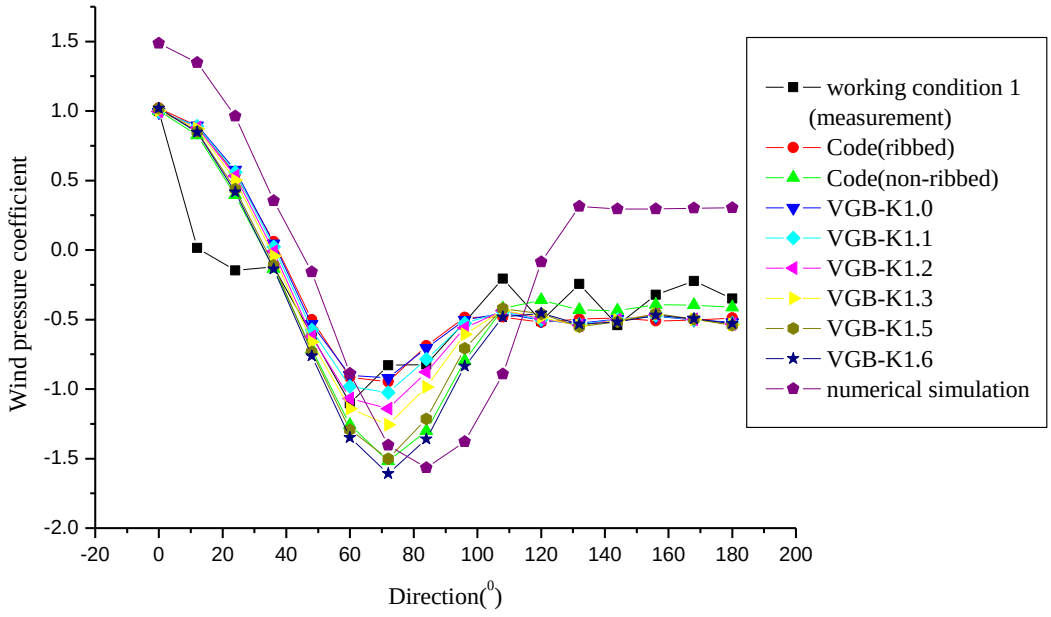

Fig. 7 – The comparison diagram of the average wind pressure coefficient between the numerical calculation and the field measurement, the Chinese code and the German code

From Figure 7, the variation law of the numerical simulation results is consistent with that in the field measurement and the code.

CONCLUSIONS

In this paper, the wind pressure of the ribbed cooling tower has been measured on site, and the wind load of the cooling tower has been calculated by Fluent. The conclusions of this study are as follows:

(1) The maximum wind speed reached 25.06m/s during the field measurement, and the corresponding wind pressure data is very valuable.

(2) When the wind speed is 9.7m/s (working condition 4), the average wind pressure coefficient of cooling tower tail in the field measurement is the closest to that in the code (GB/T50102-2014).

When the average wind speed is greater than 10m/s, the absolute value of the negative pressure at the end of the cooling tower is greater than the absolute value of the code (GB/T50102-2014). The greater the wind speed is, the greater the absolute value of the negative pressure is at the end of the cooling tower. This rule should be paid attention to in the design.

(3) The higher the average wind speed is, the greater the pressure pulsation is.

(4) The variation law of numerical simulation result is consistent with that of the field measurement and the code. This indicates that the numerical simulation can be used to qualitatively analyze the wind pressure of the cooling tower.

DATA AVAILABILITY:

The data in this paper are reliable and can be used.

ACKNOWLEDGEMENTS

This research was supported by National Science Foundation of China (11502177), Key Laboratory of Concrete and Pre-stressed Concrete Structure of Ministry of Education (Southeast University) Project (CPCSME2019-08), the Opening Foundation of Hubei Key Laboratory of digital textile equipment (DTL2019019), Wuhan Textile University Project (201608006,201703002,2016JXTD06,2017XNFZ02).

The authors declare no conflict of interest.

REFRENCES

[1] Zhao, Lin, Yaojun Ge, and Ahsan Kareem, 2017. Fluctuating Wind Pressure Distribution Around Full-Scale Cooling Towers. Journal of Wind Engineering and Industrial Aerodynamics 165 : 34–45. doi:10.1016/j.jweia.02.016.

[2] Sun, T.F., Z.F. Gu, L.M. Zhou, P.H. Li, and G.L. Cai, 1992.Full-Scale Measurement and Wind-Tunnel Testing of Wind Loading on Two Neighboring Cooling Towers. Journal of Wind Engineering and Industrial Aerodynamics 43, no. 1–3: 2213–2224. doi:10.1016/0167-6105(92)90660-3.

[3] KAREEM, A., and C.M. CHENG, 1999.Pressure and Force Fluctuations on Isolated Roughened Circular Cylinders of Finite Height in Boundary Layer Flows. Journal of Fluids and Structures 13, no. 7–8: 907–933. doi:10.1006/jfls.1999.0247.

[4] Cheng, X.X., L. Zhao, Y.J. Ge, J. Dong, and C. Demartino, 2017.A Comprehensive High Reynolds Number Effects Simulation Method for Wind Pressures on Cooling Tower Models. Wind and Structures 24, no. 2: 119–144. doi:10.12989/was.2017.24.2.119.

[5] Orlando, Maurizio, 2001.Wind-Induced Interference Effects on Two Adjacent Cooling Towers. Engineering Structures 23, no. 8: 979–992. doi:10.1016/s0141-0296(00)00110-3.

[6] Noh, Hyuk Chun, 2006.Nonlinear Behavior and Ultimate Load Bearing Capacity of Reinforced Concrete Natural Draught Cooling Tower Shell. Engineering Structures 28, no. 3: 399–410. doi:10.1016/j.engstruct.2005.08.016.

[7] Ke, Shitang, and Yaojun Ge, 2015.Extreme Wind Pressures and Non-Gaussian Characteristics for Super-Large Hyperbolic Cooling Towers Considering Aeroelastic Effect. Journal of Engineering Mechanics 141, no. 7: 04015010. doi:10.1061/(asce)em.1943-7889.0000922.

[8] Zahlten, Wolfhard, and Claudio Borri, 1998. Time-domain simulation of the non-linear response of cooling tower shells subjected to stochastic wind loading. Engineering structures 10.20 : 881-889.

[9] Zou, Yun-feng, Xu-hui He, Hai-quan Jing, Shuai Zhou, Hua-wei Niu, and Zheng-qing Chen,2018. Characteristics of Wind-Induced Displacement of Super-Large Cooling Tower Based-on Continuous Medium Model Wind Tunnel Test. Journal of Wind Engineering and Industrial Aerodynamics 180: 201–212. doi:10.1016/j.jweia.2018.08.001.

[10] Ke, Shitang, Hao Wang, and Yaojun Ge, 2019. Comparison of Stationary and Non-Stationary Wind-Induced Responses of a Super-Large Cooling Tower Based on Field Measurements. Thin-Walled Structures 137: 331–346. doi:10.1016/j.tws.2019.01.017.

[11] Wang, H., S.T. Ke, and Y.J. Ge, 2019. Research on Non-Stationary Wind-Induced Effects and the Working Mechanism of Full Scale Super-Large Cooling Tower Based on Field Measurement. Journal of Wind Engineering and Industrial Aerodynamics 184: 61–76. doi:10.1016/j.jweia.2018.11.015.

[12] Armitt J, 1980.Wind loading on cooling towers. Journal of Structural Division.

[13] Niemann, H.-J., and H. Pröpper, 1975.Some Properties of Fluctuating Wind Pressures on a Full-Scale Cooling Tower. Journal of Wind Engineering and Industrial Aerodynamics 1: 349–359. doi:10.1016/0167-6105(75)90029-x.

[14] Sollenberger N J, Scanlan R H, 1974.Pressure-difference measurements across the shell of a full-scale natural draft cooling tower. Proceedings of the symposium on fullscale measurements of wind effects (Canada: University of Western Ontario).

[15] Sun Tianfeng, 1983. Full-size measurement and wind tunnel research on wind pressure distribution of non-ribbed hyperbolic cooling towers. Acta Aerodynamica Sinica 4.

[16] Wang, Hao, Shitang Ke, Yaojun Ge, and Yukio Tamura, 2018. Extreme and Spectrum Characteristics of Wind Loads on Super-Large Cooling Tower Under Different Four-Tower Combinations. Advances in Structural Engineering 22, no. 5: 1238–1250. doi:10.1177/1369433218810888.

[17] Cheng, XX, L Zhao, YJ Ge, R Dong, and C Demartino, 2016. Wind Effects on Rough-Walled and Smooth-Walled Large Cooling Towers. Advances in Structural Engineering 20, no. 6: 843–864. doi:10.1177/1369433216664354.

[18] Cheng, XX, J Dong, Y Peng, L Zhao, and YJ Ge, 2017.Effects of Free-Stream Turbulence on Wind Loads on a Full-Scale Large Cooling Tower. Advances in Structural Engineering 21, no. 10 : 1437–1453. doi:10.1177/1369433217747404.

[19] Cheng, X.X., S.T. Ke, P.F. Li, Y.J. Ge, and L. Zhao,2019.External Extreme Wind Pressure Distribution for the Structural Design of Cooling Towers. Engineering Structures 181: 336–353. doi:10.1016/j.engstruct.2018.12.038.

[20] Cheng, XX, G Wu, L Zhao, PF Li, and YJ Ge, 2019.Wind-Induced Internal Pressures on Large Cooling Towers. Advances in Structural Engineering 22, no. 15: 3249–3261. doi:10.1177/1369433219861727.

[21] Cheng, X.X., L. Zhao, Y.J. Ge, S.T. Ke, and X.P. Liu, 2015. Wind Pressures on a Large Cooling Tower. Advances in Structural Engineering 18, no. 2: 201–219. doi:10.1260/1369-4332.18.2.201.

[22] Ministry of Construction of PRC.GB/T50102-2014, 2014.Code for Design of Cooling for Industrial Recirculating Water. (Beijing: China Electric Power Press).

[23] Ministry of Construction of PRC.GB50009-2012, 2012. Load Code for the Design of Building Structures. (Beijing: China Architecture ＆Building Press).

[24] VGB-R 610Ue, 2005.Structural design of cooling towers.

CIVIL ENGINEERING JOURNAL

Article no. 66

THE CIVIL ENGINEERING JOURNAL 4-2021

REDUCING THE LATERAL DISPLACEMENT OF LEAD RUBBER BEARING ISOLATORS UNDER THE NEAR FIELD EARTHQUAKES BY CROSSWISE DISSIPATERS CONNECTED TO RIGID SUPPORT STRUCTURE

Kourosh Talebi Jouneghani [1], Mahmood Hosseini [2], Mohammad Sadegh Rohanimanesh[3] and Morteza Raissi[4]

1. *Department of Civil Engineering, Central Tehran Branch, Islamic Azad University, Tehran, Iran; kou.talebijouneghani.eng@iauctb.ac.ir*
2. *Department of Civil Engineering, Faculty of Engineering, Eastern Mediterranean University (EMU), Famagusta 99628, North Cyprus via Mersin 10, Turkey; mahmood.hosseni@emu.edu.tr*
3. *Department of Civil Engineering, Central Tehran Branch, Islamic Azad University, Tehran, Iran; m.s.rohanimanesh@iauctb.ac.ir*
4. *Department of Civil Engineering, University of Science and Technology (IUST), Tehran, Iran; mraissi@iust.ac.ir*

ABSTRACT

The purpose of base isolation is to absorb earthquake energy, prolong the life of the structure, and enable the structure to be similar to a rigid body. However, since resonance can occur due to the closeness of the period of structures to the long period and large velocity pulses of the near field earthquakes, the stability of these buildings greatly reduces, and with the large displacement above isolation level, sometimes, tendency of overturning is created in isolators leading to their destruction. The main objective of this study is to significantly reduce the lateral displacement of base isolation subjected to near field earthquakes. In this research, seismic response calculation has been carried out for five steel moment frame structure with the 3, 5, 8, 11, and 14 stories in two states of with and without stiff core structure and energy dissipaters. The analyses has been done under fourteen scaled records of seven near-source and seven far-source earthquakes. It has been shown that the lateral displacement of base isolation system can be reduced by 87% for low-rise buildings, and 77% for high-rise buildings.

KEYWORDS

Reduction of lateral displacement, Base isolation, Near field earthquake, Long period large velocity pulse, Stiff support structure, Energy dissipater

INTRODUCTION

Based on the official records, many buildings collapse due to major earthquakes, and more importantly, due to the lack of having appropriate earthquake-resistant designs. Mortality rates due to earthquakes can be significantly restrained if buildings are equipped with suitable earthquake-resistant designs which mainly rely on the ductile behavior of the design. When efforts are made to protect the integrity of the building by boosting the stiffness, unluckily, the acceleration of floors can rise successively leading to the destruction of the building.

Seismic isolation has arisen as an alternate earthquake-resistant design method. This method has increasingly become popular since it offers to protect both structural and non-structural mechanisms and the contents of a building. Hence, seismic isolation attempts to reduce floor accelerations to focus on limits while keeping base displacements below a reasonable range. This is achieved by

simultaneously balancing three factors. First, seismic isolation elongates the natural period of the building by using laterally flexible isolation elements. In other words, this reduces spectral accelerations and thus the effective seismic forces. Second, the isolation system allows the superstructure to move flexibly that offers rigid-body motion decreasing inter-story drift ratios. Third, the system provides damping via the isolation elements. This causes dissolving the energy input from the earthquake and is particularly indispensable in restraining the base displacements.

The effects of earthquakes have been investigated both near and far from the faults. Primarily, near-field earthquakes were defined by Bolt [1] in 1975. According to Bolt, if the earthquake occurs in the vicinity of a site, it is considered a near-field earthquake. Hence, the distance of the center of the earthquake from the site is vital for the classification; for instance, Bolt [1] stated that if the site is within a radius of 15 km of the fault, the earthquake is classified as near-field. These types of ground motions are essentially famous for their critical energy pulses. In spite of the small magnitude of near-field earthquakes, they carry tremendous destructive potential. As these earthquakes take place in the vicinity of an active fault, they have long-period pulse maps [2]. A thorough investigation of the main parameters of near-field earthquakes for concrete structures has been carried out by Talebi Jouneghani et al. [3].

Comprehensive studies have been carried out to address the main concerns on seismic isolation within the last decades [3-22]. These studies show an accurately designed seismic isolation system effectively diminishes floor accelerations and inter-story drift ratios to acceptable levels without triggering unsatisfactorily large base displacements in case of far-field earthquakes. However, regarding near-field pulse-like earthquakes, the isolation system performs poorly, and researchers are still in dispute whether this system is appropriate for the mentioned situation.

Lu et al. [4] experimentally investigated sliding isolation systems. They reported when the isolation period is close enough to the pulse period, resonance-like behavior is more likely caused. To tackle this problem, the utilization of high damping at the isolation system was pursued to reduce excessive base displacements. However, other problems were caused by using high damping at the isolation systems. By utilizing a two degree of freedom model, Kelly [5] revealed that using additional damping could substantially reduce excessive base displacement; however, this causes the enhancement in inter-story drifts and floor acceleration. Jangid and Kelly [6] showed a similar result, but floor accelerations suddenly increase in isolation damping leading to transmit higher accelerations into superstructure when subjected to near–field earthquakes. Hall [7] showed that by utilizing an "optimum" amount of excessive damping, it is possible to reduce base displacements without expanding floor acceleration or understory drifts afterward. Alhan and Gavin [8] proved that an optimum mix of isolation stiffness and damping to certain levels could be achieved to decrease base displacements without significantly enhancing floor accelerations in an 8-story building.

Alhan and Guvin [9] examined the reliability of the floor isolation system to protect vibration-sensitive equipment in a probabilistic study. The results indicated it could not save the structures in the close area of the fault. In another research, Jangid [10] has investigated the seismic response of shear-type multi-story buildings equipped with lead-rubber bearings under near-field effects. They observed that the lead rubber bearings with higher yield displacement, which is soft bearings, have a better performance than the bearings with low yield displacement in the case of near-field ground motions. Alhan C and Göktas Y. [11] investigated the near-field earthquake records. A significant difference was observed when comparing far-field and near-field earthquake records in terms of long velocity pulses and large vertical acceleration. As a result of the proximity and the long-term periodicity of pulses to the period of structures in this area, destructive shocks are caused in the buildings with base isolation. Recently, the effects of near field ground motions on the base-isolated buildings were assessed by Providakis [12]. In his study, the base-isolated structures were equipped with lead rubber and friction pendulum bearings along with supplemental damping. He showed although the use of supplemental damping in limiting the absolute floor accelerations for both lead rubber bearing and friction pendulum system isolators in cases of near-field earthquake motions are effective, the absolute floor accelerations of the investigated types of lead rubber bearing and friction

pendulum system isolated buildings under specific far-field motions increases. Other studies [11, 13-14] demonstrated that floor acceleration could enhance if seismically isolated structures were exposed to near field earthquakes with a pulse period close to their solution period. They also suggested additional base displacements in case of near field earthquake probably result in the pounding of the seismically isolated building provided that the isolation system displacement surpasses the seismic gap left around it. Moreover, it was observed that substantial increases in floor acceleration are caused by such a pounding [15]. Likewise, Taflanidis and Jia [16] conducted the most dangerous base-isolated structures supplied unit lead rubber bearing through a proposed simulation-based framework. They demonstrated that the seismic risk test in their work. The study revealed that when the deformation of bearings exceeds the isolation gap, the seismic risk amplifies. It was recently revealed by Mazza and Vulcano [17] and Mazza et al. [18] that the isolators might even take tensile loads when vertical components of near-field earthquakes with high peak values are in question with a possible failure of isolation system caused by high seismic displacement demands. Alhan and Sahin [19] investigated the role of isolator characteristics in reducing the floor accelerations of seismically isolated buildings with flexible superstructures under near-field earthquakes. They found that higher isolation damping would decrease floor accelerations up to the creation point, but further increases in isolation damping may cause higher floor accelerations.

In another study, Mazza and Vulcano [20] proved that supplemental damping is crucial to control the base displacements of seismically isolated buildings. However, it may not guarantee better performance in terms of structural and non-structural damage subjected to near-field earthquakes. In addition, for relatively short pulse periods, some undesirable results are created. Nigdeli et al. [21] offered a harmony study optimization metrology for seismically isolated buildings subjected to both near-field and far-field earthquakes to optimize isolation system parameters such as isolation period and damping ratio. Alhan and Davas [22] stated that "Benchmark buildings with base isolation systems of different isolation periods and characteristic force ratios are subjected to synthetically developed near-field earthquake records at different fault-distances with different velocity pulse periods, and their seismic performances are reported." In their study, for seismically isolated buildings, protecting vibration-sensitive equipment in operating conditions in case of large magnitude pulse-like near field earthquakes with very long pulse periods is a very challenging task. Furthermore, the ratio of the isolation period to the pulse period has a huge impact on the peak base displacement demands and the peak floor acceleration demands when subjected to long and short pulse periods, respectively. It is reported that the mentioned effect becomes even more tangible for shorter fault-distances and smaller characteristic force ratios.

Responses of base isolation systems subjected to near-field ground motions are one of the well-researched areas. However, researches have indicated that base isolation systems utilized in near-field earthquakes have experienced substantial lateral displacement. Moreover, a large number of structures equipped with base isolation have overturned. Consequently, in this study, a new method is adopted to limit the lateral displacement of base isolation in all types of structures under near-field earthquakes, add more stability to the structure, and reduce the destructive effects of this phenomenon. Furthermore, a support structure with viscous dampers is employed to reduce the effects of the resonance due to near-field earthquakes.

MODULATION

Design of structures

As it is shown in Figure 1, five steel moment frame structures of 3, 5, 8, 11, 14 stories with square plans are the designed models, and all of them are equipped with a Chevron brace with a yard for the establishment of supporting structures. All of the structures are designed by the LRFD method in ETABS 2016; later, they are transferred to PERFORM 3D for nonlinear time history analyses.

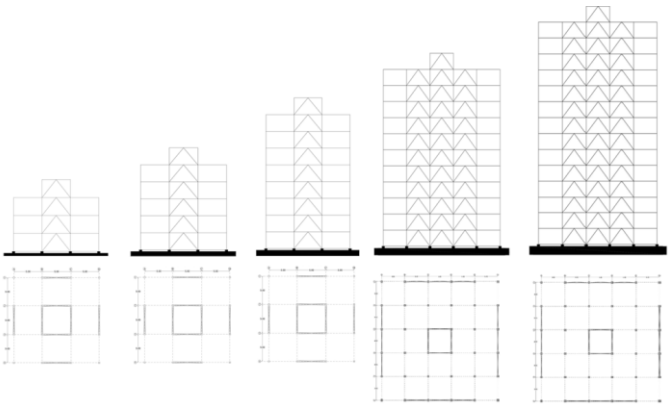

Fig. 1 – Structures without a rigid support

Rigid support structure

The rigid support structure is a square column situated in the middle of the base structure. The stiffness of this column in all types of structures is the same as the stiffness of the braces in one direction of the same structure. This column is designed in the center of the base, and it is rigidly connected to the foundation. In addition, the structures are connected to the column in the roof by horizontally crosswise viscous dampers, as is shown in Figure 2. It is notable that all of the rigid support structures are designed in PERFORM 3D.

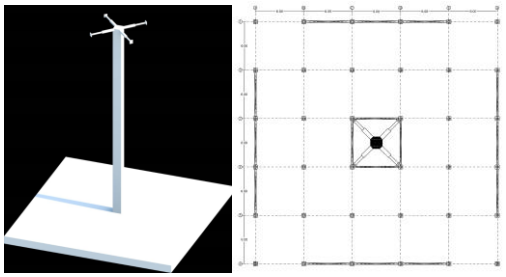

Fig. 2 – Rigid support structure with dampers

Base isolation system

The base of lead rubber bearing (LRB) isolators is designed based on International Building Code (IBC) [23]. The initial design of the Base isolation is by force-displacement method, in which effective stiffness (K_{eff}) is required. As a result, the target period T_D can be determined using Equation (1).

$$T_D = 2\pi\sqrt{\frac{W_t}{gK_{eff}}} \tag{1}$$

In Equation (1), W_t is the total weight of the superstructure. Moreover, Equation (2) is used to estimate the displacement of the design.

$$D_D = \frac{g}{4\pi^2}\frac{S_{D1}T_D}{B_D} \tag{2}$$

In Equation (2), B_D is the damping factor, and S_{D1} is the spectral pseudo acceleration obtained from the design spectrum. The parameters selected to define the utilized isolators, lead rubber bearing, in PERFORM 3D are demonstrated in Figure 3 and Table 1.

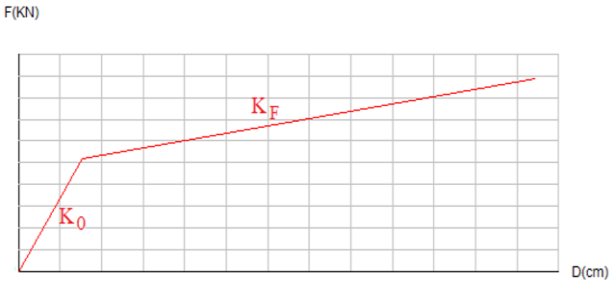

Fig. 3 – Force-displacement relationship for lead rubber bearing

Tab. 1 - Force-displacement relationship for lead rubber bearing

Structures	K_0 (KN)	K_F (KN)	F_u (KN)	D_{max} (m)
3 story	400	40	14	0.200
5 story	485	48.5	16.5	0.225
8 story	530	53	19	0.255
11 story	605	60.5	22.5	0.311
14 story	675	67.5	26	0.311

The fluid viscous damper system

According to the Iranian manual for structural damping systems in the design and retrofitting of buildings [24], the force in the viscous damper is calculated using Equation 3.

$$F = C_o \left|\dot{D}\right|^{\alpha} \operatorname{sgn}\left[\dot{D}\right] \tag{3}$$

In Equation 3, C_0 is the damping factor, $\dot{D}$ is the relative velocity between the two ends of the damper, α is the numerical power of damper velocity, and sgn is the sign function. Moreover, the parameters selected to define the utilized fluid viscous damper in PERFORM 3D are similar to LRBs, which are indicated in Figure 4 and Tables 2-6.

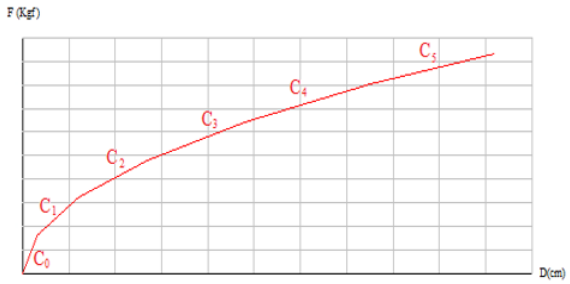

Fig. 4 – Force-displacement relationship for fluid the viscous damper the in 3-story structure

Tab. 2 - Characteristics of the fluid viscous damper in the 3-story structure

Segment	Deformation rate	Coefficient(C)
1	0.6	2222
2	2.4	1333
3	5.4	952.4
4	9.6	740.7
5	15	606.1
Axial Force =C (Deformation rate)$^{0.5}$ force at last Segment=20000Kgf		

Tab. 3 - Characteristics of the fluid viscous damper in the 5-story structure

Segment	Deformation rate	Coefficient(C)
1	0.6	4444
2	2.4	2667
3	5.4	1905
4	9.6	1481
5	15	1212
Axial Force =C (Deformation rate)$^{0.5}$ force at last Segment=40000Kgf		

Tab. 4 - Characteristics of the fluid viscous damper in the 8-story structure

Segment	Deformation rate	Coefficient(C)
1	0.6	6667
2	2.4	4000
3	5.4	2857
4	9.6	2222
5	15	1818
Axial Force =C (Deformation rate)$^{0.5}$ force at last Segment=60000Kgf		

Tab. 5: Characteristics of the fluid viscous damper in the 11-story structure

Segment	Deformation rate	Coefficient(C)
1	0.6	8889
2	2.4	5333
3	5.4	3810
4	9.6	2963
5	15	2424
Axial Force =C (Deformation rate)$^{0.5}$ force at last Segment=80000Kgf		

Tab. 6: Characteristics of the fluid viscous damper in the 14-story structure

Segment	Deformation rate	Coefficient(C)
1	0.6	11110
2	2.4	6667
3	5.4	4762
4	9.6	3704
5	15	3030
Axial Force =C (Deformation rate)$^{0.5}$ force at last Segment=100000Kgf		

Equation of motion

In 1999, Naeim F and Kelly JM [25] evaluated the relative displacement (u) of each degree of freedom with respect to the ground. The equation is as follows:

$$M\ddot{u} + C\dot{u} + Ku = -Mr\ddot{u}_g \quad (4)$$

Where, r is a vector that couples each degree of freedom to the ground motion. When this structural model is superimposed on a base isolation system with the base mass m_b, stiffness k_b, and damping c_b, Equation 4 becomes:

$$M\ddot{v} + C\dot{v} + Kv = -Mr(\ddot{u}_g + \ddot{\upsilon}_b) \quad (5)$$

Where v is the displacement relative to the base slab, and $\ddot{\upsilon}_b$ is the relative displacement of the base slab to the ground. Now, the overall equation of motion for the combined building and the base slab is:

$$r^T M(\ddot{v} + r\ddot{\upsilon}_b + r\ddot{u}_g) + m_b(\ddot{\upsilon}_b + \ddot{u}_g) + c_b\dot{\upsilon}_b + c_d\dot{\upsilon}_d + k_b\upsilon_b = 0 \quad (6)$$

In Equation 6, υ_d is the displacement relative to the fluid viscous dampers, which can be rewritten in the following form:

$$r^T M\ddot{v} + (m + m_b)\ddot{\upsilon}_b + c_b\dot{\upsilon}_b + c_d\dot{\upsilon}_d + k_b\upsilon_b = -(m + m_b)\ddot{u}_g \quad (7)$$

Equation 7 identifies $r^T M$ as the total mass m of the building. Therefore, $m + m_b$ is the total mass carried by the isolation system. Equation 7 can be written in matrix form as follows:

$$M^*\ddot{v}^* + C^*\dot{v}^* + K^*v^* = -M^*r^*\ddot{u}_g \quad (8)$$ Where:

$$M^* = \begin{bmatrix} m + m_b & r^T M \\ Mr & M \end{bmatrix} \quad C^* = \begin{bmatrix} c_b + c_d & 0 \\ 0 & C \end{bmatrix} \quad K^* = \begin{bmatrix} k_b & 0 \\ 0 & K \end{bmatrix} \quad r^* = \begin{bmatrix} 1 \\ 0 \end{bmatrix} \quad v^* = \begin{bmatrix} \upsilon_b \\ v \end{bmatrix}$$

Ground motion information

For time-history analyses by PERFORM 3D, the ground motions should be scaled such that the average value of the 5 percent damped response spectra for the suite of motions is not less than the design response spectrum of the site for periods ranging from 0.2T to 1.5T. T is the fundamental period of structure in the fundamental mode for the direction of the response being analyzed (standard no. 2800) [26].

Tab. 7 - Characteristics of NF earthquake motions

No.	Earthquake	M	Station	Distance(km)	PGA(g)	PGV(cm/s)	PGD(cm)
1	Northridge	6.69	LA Dam	11.79	0.576	77.09	20.1
2	Chi Chi	7.62	TCU068	3.01	0.5	277.56	715.8
3	San Fernando	6.61	Pacoima Dam	11.86	0.827	34.43	18.67
4	Palm springs	6.06	North Palm springs	10.57	0.669	73.55	11.87
5	Kocaeli	7.4	Sakarya	3.2	0.41	82.05	205.9
6	Gazil	6.8	Karakyr	12.82	0.599	64.94	24.18
7	Whittier narrows	5.99	Santa-fe springs	11.73	0.398	23.75	1.76

Tab. 8 - Characteristics of FF earthquake motions

No.	Earthquake	M	Station	Distance(km)	PGA(g)	PGV(cm/s)	PGD(cm)
1	Imperial Valley	6.53	Brawley Airport	43	0.158	36.09	22.63
2	Loma Prieta	6.9	Richmond City Hall	87.87	0.124	17.34	3.58
3	Tabas(Iran)	6.8	Tabas	55.24	0.851	121.22	95.06
4	Kobe	6.9	KJMA	18.27	0.854	95.75	24.56
5	Chi Chi	7.62	TCU065	26.67	0.831	129.55	93.85
6	Kocaeli	7.51	Sakarya	33.24	0.376	79.49	70.56
7	Northridge	6.7	Huntington BchWaikiki	69.5	0.086	5.01	1.63

Discussion and results

When the time history analyses, the acceleration response, the velocity, and displacement of the classes for all of earthquakes has been discovered, it is observed that the changes in the output responses of all earthquakes are very close to each other. Therefore, only the Northridge earthquake responses are presented.

As shown in Figures 5 - 15 and Table 9, the response of the structures is extracted under near-field scaled Northridge (North. NF) and far-field scaled Northridge (North. FF) records. Hence, the reduced amounts in most displacements of the upper level of base isolation are observed according to the following Figures and tables:

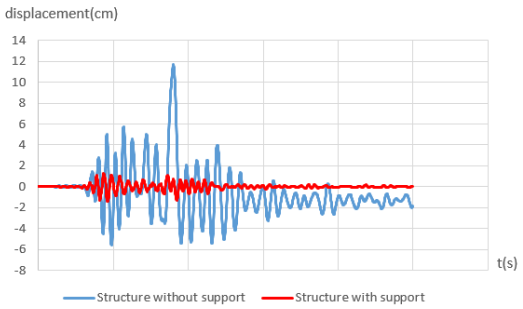

Fig. 5 – Displacement of North. FF earthquake for the 3-story structure

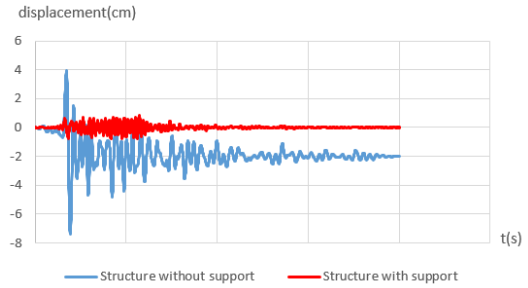

Fig. 6 – Displacement of North. NF earthquake for the 3-story structure

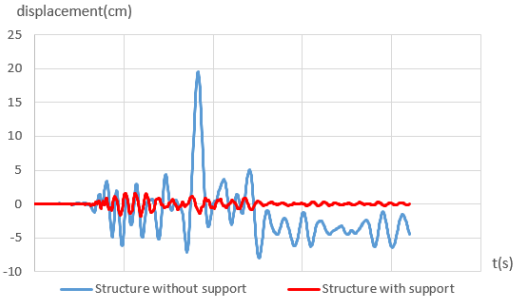

Fig. 7 – Displacement of North. FF earthquake for the 5-story structure

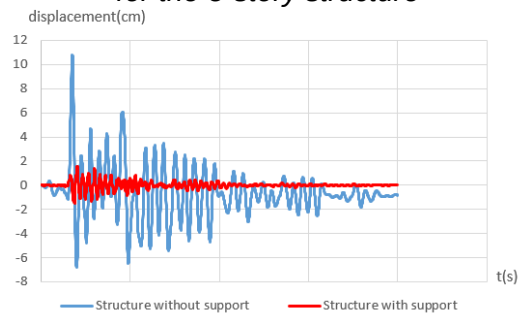

Fig. 8 – Displacement of North. NF earthquake for the 5-story structure

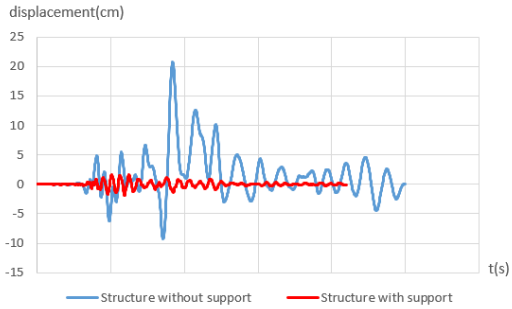

Fig. 9 – Displacement of North. FF earthquake for the 8-story structure

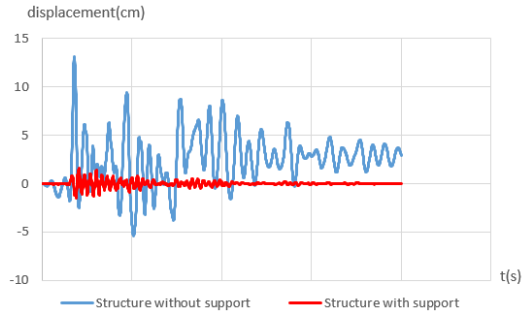

Fig. 10 – Displacement of North. NF earthquake for the 8-story structure

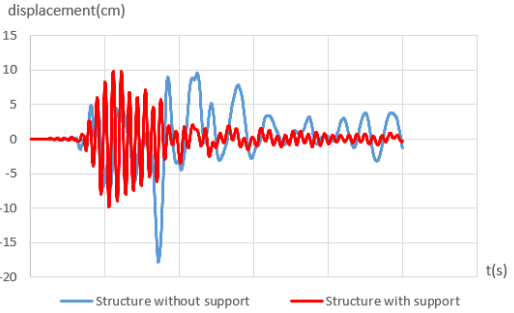

Fig. 11 – Displacement of North. FF earthquake for the 11-story structure

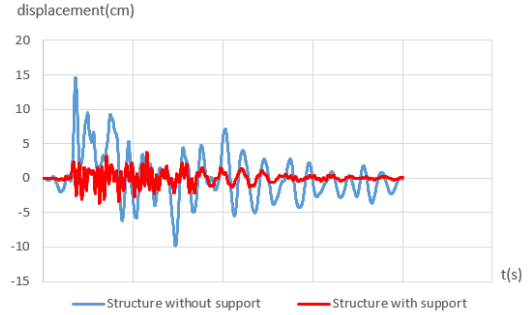

Fig. 12 – Displacement of North. NF earthquake for the 11-story structure

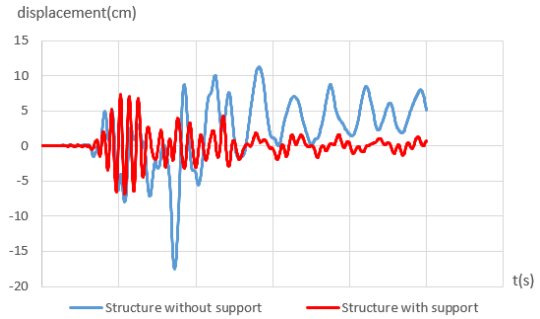

Fig. 13 – Displacement of North. FF earthquake for the 14-story structure

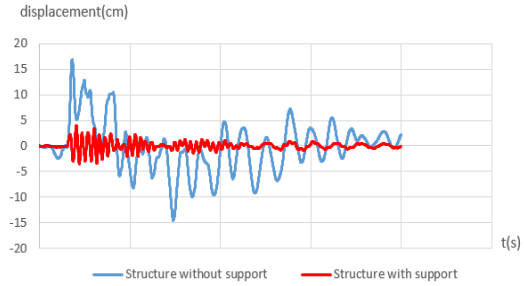

Fig. 14 – Displacement of North. NF earthquake for the 14-story structure

Tab. 9 - The reduced amounts of lateral displacement of the upper level of the base isolation in structures with rigid support under the North. FF and North. NF earthquakes

Field / Structure	Far	Near
3 story	88 %	87 %
5 story	90.3 %	85.6 %
8 story	90.6 %	84.8 %
11 story	44.7 %	74.5 %
14 story	58.3 %	77 %

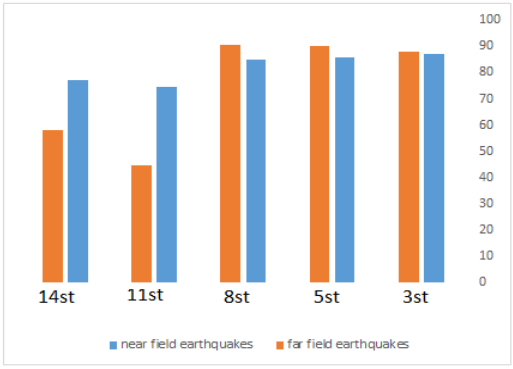

Fig. 15 – The reduced amounts of lateral displacement of the upper level of base isolation in structures with rigid support under the North. FF and North. NF earthquakes

As shown in Figures 16 - 26 and Table 10, the response of these structures is extracted similar to the previous section, (North. NF) and (North. FF). Furthermore, reduced amounts in most base shears of the upper level of base isolation are observed in the following figures and tables:

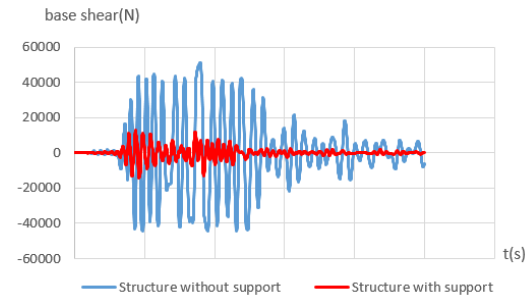

Fig. 16 – Base shear of North. FF earthquake for the 3-story structure

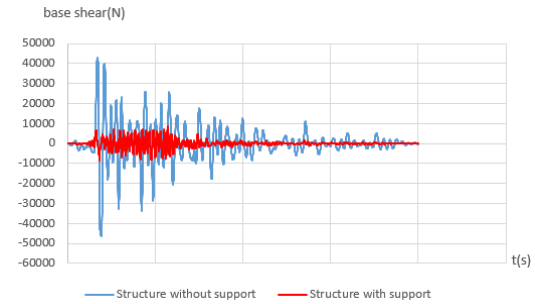

Fig. 17 – Base shear of North. NF earthquake for the 3-story structure

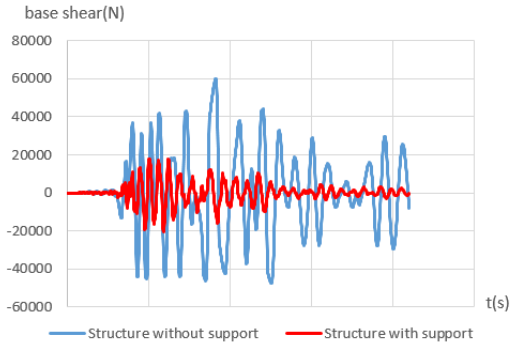

Fig. 18 – Base shear of North. FF earthquake for the 5-story structure

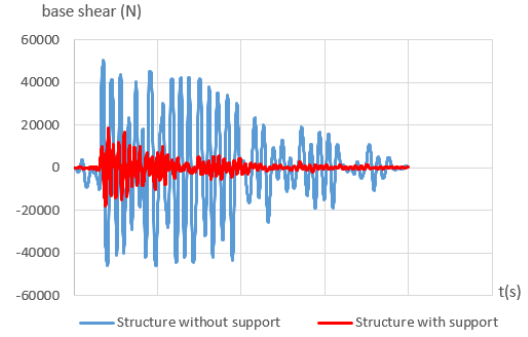

Fig. 19 – Base shear of North. NF earthquake for the 5-story structure

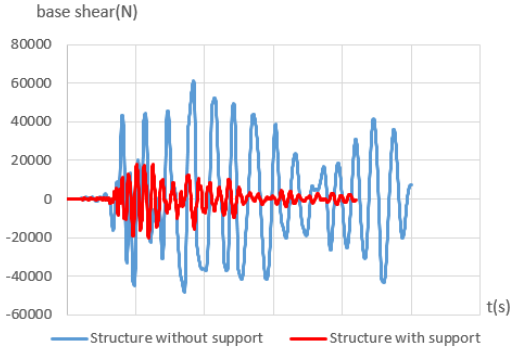

Fig. 20 – Base shear of North. FF earthquake for the 8-story structure

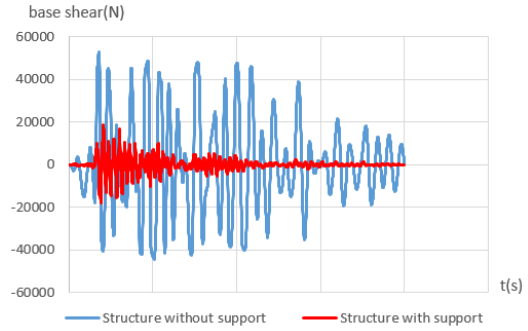

Fig. 21 – Base shear of North. NF earthquake for the 8-story structure

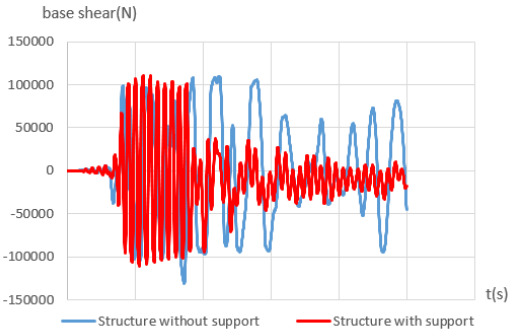

Fig. 22 – Base shear of North. FF earthquake for the 11-story structure

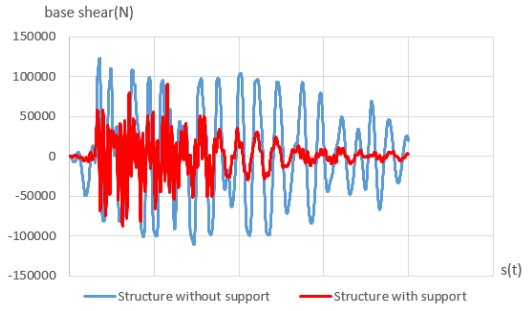

Fig. 23 – Base shear of North. NF earthquake for the 11-story structure

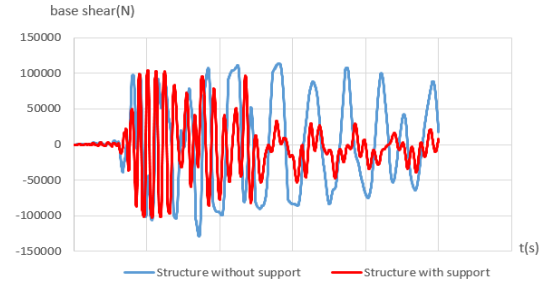

Fig. 24 – Base shear of North. FF earthquake for the 14-story structure

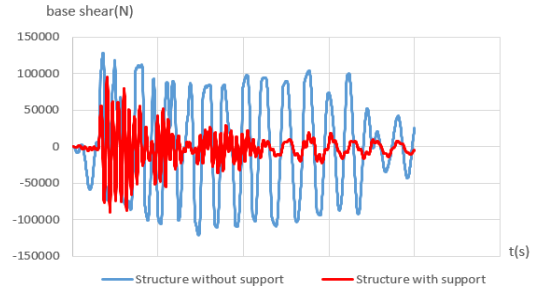

Fig. 25 – Base shear of North. NF earthquake for the 14-story structure

Tab. 10 - The reduced amounts of base shear of the upper level of base isolation in structures with rigid support under the North. FF and North. NF earthquakes

Field / Structure	Far	Near
3 story	71%	78%
5 story	66%	64%
8 story	55%	45%
11 story	15%	26%
14 story	19%	25%

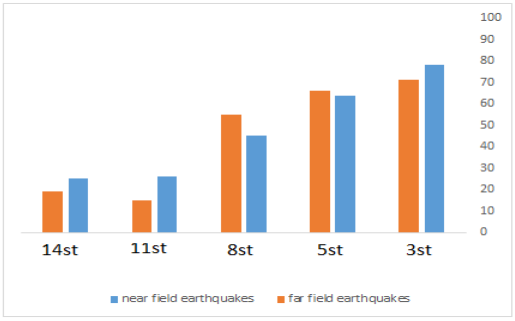

Fig. 26 – The reduced amounts of base shear of the upper level of base isolation in structures with rigid support under the North. FF and North. NF earthquakes

The results demonstrate that the structures with viscous dampers have four main advantages. The first considerable effect of support structures with viscous dampers in the near-field earthquakes is reducing the displacement of the upper level of base isolation and decreasing the base shear in all of the structures, especially in shorter buildings. Similarly, the same effect of the mentioned structure is observed in the far-field earthquakes.

As shown in Figures 27 - 37 and Table 11, the velocity of stories in the structures is extracted as (North. NF) and (North. FF) records, and reduced amounts in the velocity of the stories were observed through the following figures and tables:

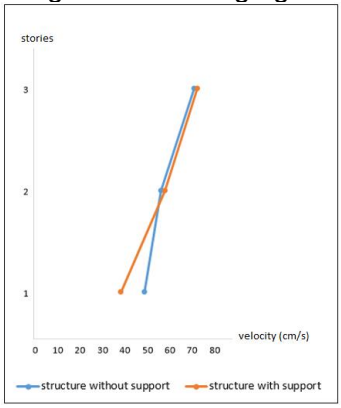

Fig. 27 – Stories velocity of North. FF earthquake for the 3-story structure

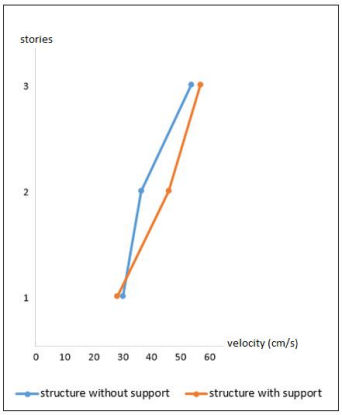

Fig. 28 – Stories velocity of North. NF earthquake for the 3-story structure

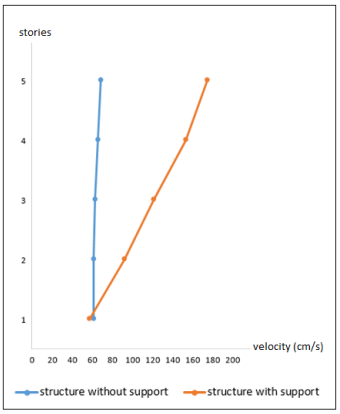

Fig. 29 – Stories velocity of North. FF earthquake for the 5-story structure

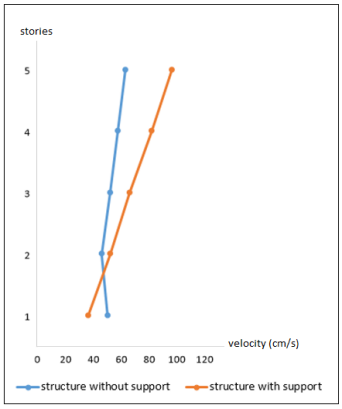

Fig. 30 – Stories velocity of North. NF earthquake for the 5-story structure

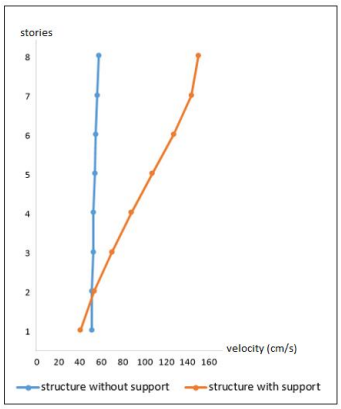

Fig. 31 – Stories velocity of North. FF earthquake for the 8-story structure

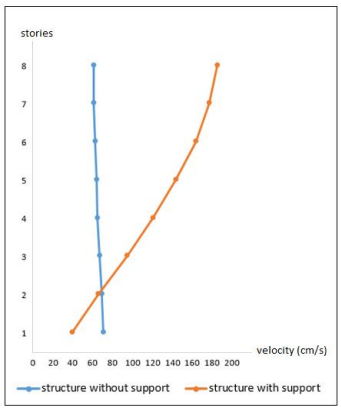

Fig. 32 – Stories velocity of North. NF earthquake for the 8-story structure

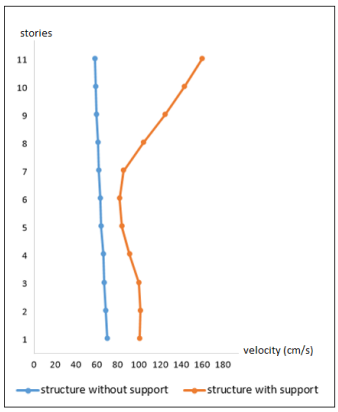

Fig. 33 – Stories velocity of North. FF earthquake for the 11-story structure

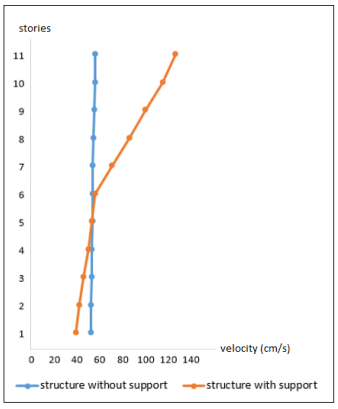

Fig. 34 – Stories velocity of North. NF earthquake for the 11-story structure

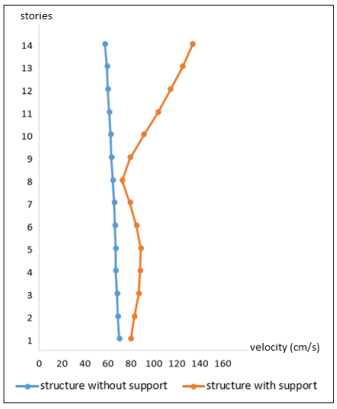

Fig. 35 – Stories velocity of North. FF earthquake for the 14-story structure

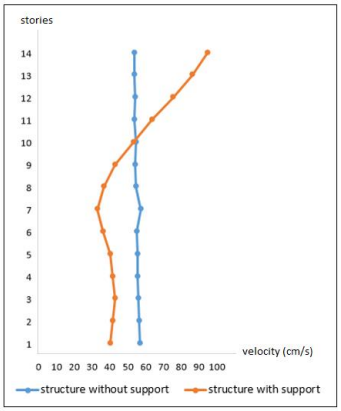

Fig. 36 – Stories velocity of North. NF earthquake for the 14-story structure

Tab. 11 - The reduced amounts of velocities in structures with rigid support under the North. FF and North. NF earthquakes

Field / Structure	Far	Near
3 story	-5 %	8 %
5 story	86 %	23 %
8 story	90 %	81 %
11 story	68 %	32 %
14 story	45 %	73 %

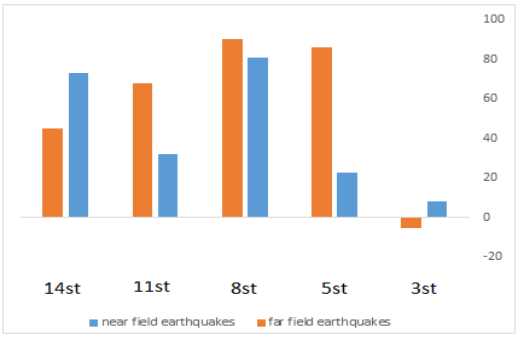

Fig. 37 – The reduction amounts of velocities in structures with rigid support under the North. FF and North. NF earthquakes

The second significant feature of support structures with viscous damper in near-field earthquakes is reducing the story velocity in all structures, especially in tall buildings. Evidently, the same effects are observed when the structure is subjected to far-field earthquakes.
As shown in Figures 38-48 and Table 12, the response of these structures is extracted as (North. NF) and (North. FF) records, and reduced amounts in the acceleration of the stories could be observed in the following figures and tables:

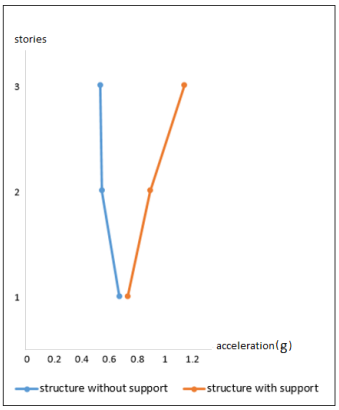

Fig. 38 – Stories acceleration of North. FF earthquake for the 3-story structure

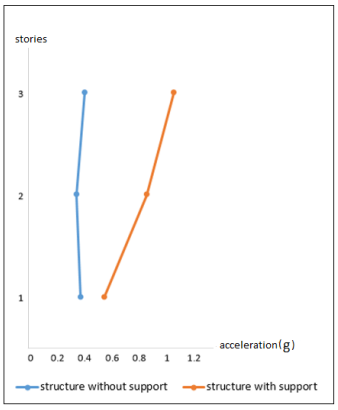

Fig. 39 – Stories acceleration of North. NF earthquake for the 3-story structure

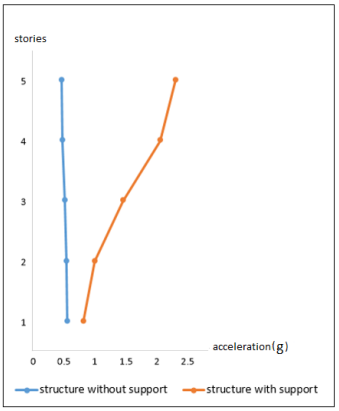

Fig. 40 – Stories acceleration of North. FF earthquake for the 5-story structure

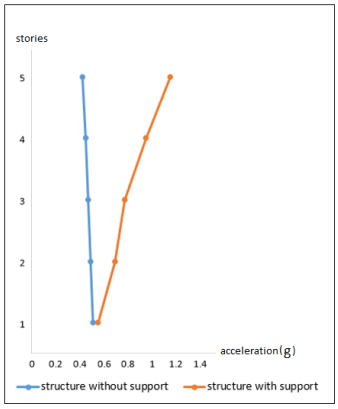

Fig. 41 – Stories acceleration of North. NF earthquake for the 5-story structure

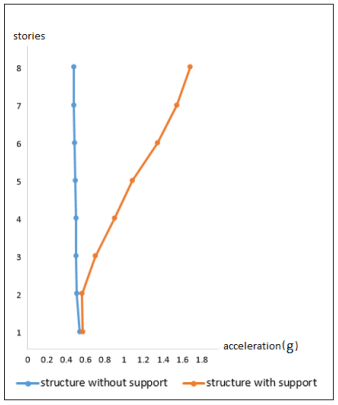

Fig. 42 – Stories acceleration of North. FF earthquake for the 8-story structure

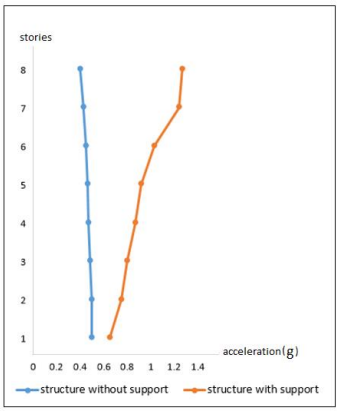

Fig. 43 – Stories acceleration of North. NF earthquake for the 8-story structure

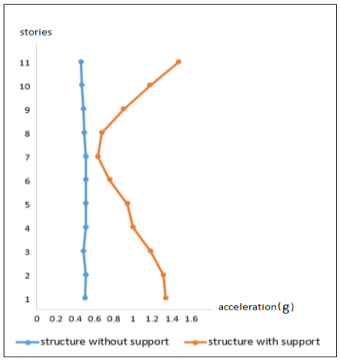

Fig. 44 – Stories acceleration of North. FF earthquake for the 11-story structure

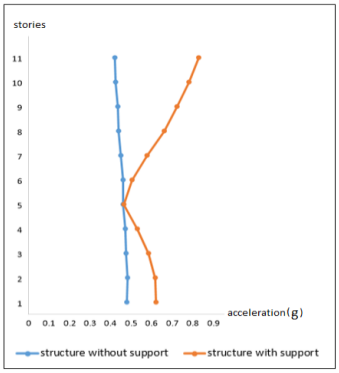

Fig. 45 – Stories acceleration of North. NF earthquake for the 11-story structure

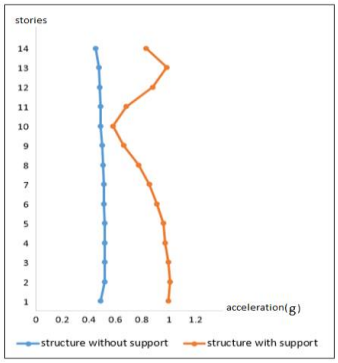

Fig. 46 – Stories acceleration of North. FF earthquake for the 14-story structure

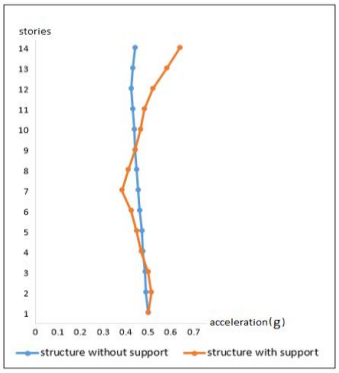

Fig. 47 – Stories acceleration of North. NF earthquake for the 14-story structure

Tab. 12 - The reduced amounts of accelerations in structures with rigid support under the North. FF and North. NF earthquakes

Field / Structure	Far	Near
3 story	*58* %	119 %
5 story	197 %	75 %
8 story	10 %	103 %
11 story	109 %	37 %
14 story	-6 %	6 %

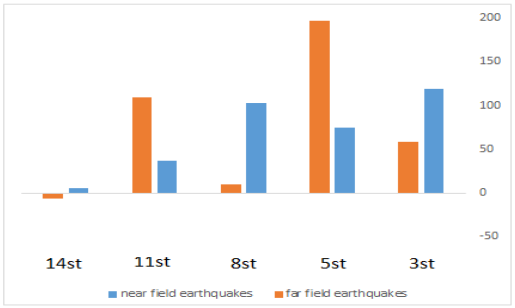

Fig. 48 – The reduced amounts of accelerations in structures with rigid support under the North. FF and North. NF earthquakes

The third vital strength of support structures with viscous damper in near-field earthquakes is reducing the stories' acceleration in all of structures, especially in short structures. The mentioned effects are also evident in all types of structure subjected to far-field earthquakes.

The fourth important advantage of the support structures with viscous dampers is changing the first modal shape of the structure from shear to torsional. This important effect plays a significant role in reducing the effect of modal mass on the first action of the structure. Despite early long pulses in near-field earthquakes records, the risk of structural collapse in base isolation is greatly reduced.

CONCLUSIONS

The base isolation is usually designed to reduce the destructive effects of an earthquake, prolong the effective life of a building, and help the structures to be similar to a rigid body. Although using a base isolation system could improve the mentioned features, in case of a near-field earthquake, it may cause a significant reduction in the structures' stability leading to the building overturn and destruction. The previous studies have demonstrated that the structure with a base isolation design usually experiences critical lateral displacement leading to the structure's overturn. Consequently, one of the main concerns in the utilization of base isolations is the inconsistent performance of the design when subjected to near-field earthquakes. Therefore, if the lateral displacement is handled properly and its amplitude is decreased enough to be safe for the structure and its residents, the application of such a system is fully justified.

As a remedy to the mentioned problem, in this study, a safe method for reducing the lateral displacement of base isolation under near-field earthquakes was proposed. For all the models in the study, a support structure is designed which is connected crosswise with a viscous damper to the roof, and it is rigidly connected to the foundation of the building. Analyses of the results revealed that the implementation of the proposed method has five main advantages which are as follows:

- The lateral displacement of the base isolation in all types of structures subjected to near-field earthquakes is significantly reduced.
- The base shear was proved to substantially decrease when subjected to near-field ground motions.
- The acceleration of the stories is observed to experience a major decrease as a result of the support structure in all types of buildings when subjected to near-field earthquakes.
- The velocity of the stories in the case of a near-field earthquake is remarkably dropped in all types of buildings.
- The first modal shape of the structures has shifted from shear to torsional.

These advantages demonstrate that most of the destructive effects of the resonance, which could be caused by near-field earthquakes, leading to the overturn of the buildings are eliminated. Hence, the method justifies the application of the lead rubber bearing isolation systems. Moreover, this method could help to save the structural and non-structural properties of the building, and more importantly, this method could reduce the mortality rates caused by near-field earthquakes.

REFRENCES

[1] Bolt, B.A., 1971. The San Fernando Valley, California, Earthquake of February 9 1971: Data on seismic hazards. *Bulletin of the seismological society of America*, *61*(2), pp.501-510.

[2] Hudson, D.E. and Housner, G.W., 1958. An analysis of strong-motion accelerometer data from the San Francisco earthquake of March 22, 1957. *Bulletin of the seismological society of America*, *48*(3), pp.253-268, https://doi.org/10.1785/BSSA0480030253.

[3] Jouneghani, K.T., Hosseini, M., Rohanimanesh, M.S. and Dehkordi, M.R., 2017. Evaluating main parameters effects of near-field earthquakes on the behavior of concrete structures with moment frame system. *Advances in Science and Technology. Research Journal*, *11*(3), https://doi.org/10.12913/22998624/74135.

[4] Lu, L.Y., Lin, C.C. and Lin, G.L., 2013. Experimental evaluation of supplemental viscous damping for a sliding isolation system under pulse-like base excitations. *Journal of Sound and Vibration*, *332*(8), pp.1982-1999, https://doi.org/10.1016/j.jsv.2012.12.008.

[5] Kelly, J.M., 1999. The role of damping in seismic isolation. *Earthquake engineering & structural dynamics*, *28*(1), pp.3-20, https://doi.org/10.1002/(SICI)1096-9845(199901)28:1%3C3::AID-EQE801%3E3.0.CO;2-D.

[6] Jangid, R.S. and Kelly, J.M., 2001. Base isolation for near-fault motions. *Earthquake engineering & structural dynamics*, *30*(5), pp.691-707, https://doi.org/10.1002/eqe.31.

[7] Hall, J.F., 1999. The role of damping in seismic isolation. *Earthquake engineering & structural dynamics*, *28*(12), pp.1717-1720.

[8] Alhan, C. and Gavin, H., 2004. A parametric study of linear and non-linear passively damped seismic isolation systems for buildings. *Engineering structures*, *26*(4), pp.485-497, https://doi.org/10.1016/j.engstruct.2003.11.004.

[9] Alhan, C. and Gavin, H.P., 2005. Reliability of base isolation for the protection of critical equipment from earthquake hazards. *Engineering structures*, *27*(9), pp.1435-1449, https://doi.org/10.1016/j.engstruct.2005.04.007

[10] Jangid, R.S., 2007. Optimum lead–rubber isolation bearings for near-fault motions. *Engineering structures*, *29*(10), pp.2503-2513, https://doi.org/10.1016/j.engstruct.2006.12.010.

[11] Alhan, C. and Göktaş, Y., 2009. Effects of near-field earthquakes on seismically isolated buildings. In *InProceedings, WCCE-ECCE-TCCE joint conference: earthquake and tsunami* (pp. 22-24).

[12] Providakis, C.P., 2009. Effect of supplemental damping on LRB and FPS seismic isolators under near-fault ground motions. *Soil Dynamics and Earthquake Engineering*, *29*(1), pp.80-90, https://doi.org/10.1016/j.soildyn.2008.01.012.
[13] Mazza, F. and Vulcano, A., 2009. Nonlinear response of RC framed buildings with isolation and supplemental damping at the base subjected to near-fault earthquakes. *Journal of Earthquake Engineering*, *13*(5), pp.690-715, https://doi.org/10.1080/13632460802632302.
[14] Lu, L.Y., Shih, M.H., Tzeng, S.W. and Chien, C.C., 2003, February. Experiment of a sliding isolated structure subjected to near-fault ground motion. In *Proceedings of the 7th pacific conference on earthquake engineering* (pp. 13-15).
[15] Matsagar, V.A. and Jangid, R.S., 2010. Impact response of torsionally coupled base-isolated structures. *Journal of vibration and control*, *16*(11), pp.1623-1649, https://doi.org/10.1177%2F1077546309103271.
[16] Taflanidis, A.A. and Jia, G., 2011. A simulation-based framework for risk assessment and probabilistic sensitivity analysis of base-isolated structures. *Earthquake Engineering & Structural Dynamics*, *40*(14), pp.1629-1651, https://doi.org/10.1002/eqe.1113.
[17] Mazza, F. and Vulcano, A., 2012. Effects of near-fault ground motions on the nonlinear dynamic response of base-isolated rc framed buildings. *Earthquake Engineering & Structural Dynamics*, *41*(2), pp.211-232, https://doi.org/10.1002/eqe.1126.
[18] Mazza, F., Vulcano, A. and Mazza, M., 2012. Nonlinear dynamic response of RC buildings with different base isolation systems subjected to horizontal and vertical components of near-fault ground motions. *The Open Construction and Building Technology Journal*, *6*(1), http://dx.doi.org/10.2174/1874836801206010373.
[19] Alhan, C. and Şahin, F., 2011. Protecting vibration-sensitive contents: an investigation of floor accelerations in seismically isolated buildings. *Bulletin of Earthquake Engineering*, *9*(4), pp.1203-1226, https://doi.org/10.1007/s10518-010-9236-0.
[20] Mazza, F. and Vulcano, A., 2009. Nonlinear response of RC framed buildings with isolation and supplemental damping at the base subjected to near-fault earthquakes. *Journal of Earthquake Engineering*, *13*(5), pp.690-715, https://doi.org/10.1080/13632460802632302.
[21] Nigdeli, S.M., Bekdaş, G. and Alhan, C., 2014. Optimization of seismic isolation systems via harmony search. *Engineering optimization*, *46*(11), pp.1553-1569, https://doi.org/10.1080/0305215X.2013.854352.
[22] Alhan, C. and Öncü-Davas, S., 2016. Performance limits of seismically isolated buildings under near-field earthquakes. *Engineering Structures*, *116*, pp.83-94, https://doi.org/10.1016/j.engstruct.2016.02.043.
[23] International Code Council, “International Building Code”, Section 1623, Seismically Isolated Structures, 2000.
[24] Iranian manual for structural damping system in designed and retrofitting of buildings (N.766), 2018.
[25] Naeim, F. and Kelly, J.M., 1999. Design of seismic isolated structures: from theory to practice, mechanical characteristics and modeling of isolators. New York: Wiley; p. 93–121.
[26] Interpretation of "Iranian code of practice for seismic resistant design of building (standard No. 2800, 4th edition)", 2017.

CIVIL ENGINEERING JOURNAL

Article no. 67

THE CIVIL ENGINEERING JOURNAL 4-2021

EXPERIMENTAL STUDY ON MECHANICAL PROPERTIES OF POLYURETHANE POWDER COMPOSITES

Kexin Zhang[1, 2], Dachao Li[2], Xinyuan Shen[2], Xingwei Xue[2], *Dandan Gu[3]*

1. *MOE Key Lab of Disaster Forecast and Control in Engineering, Jinan University, No.601 Huangpu Dadao West, Guangzhou, Guangdong Province, PR of China; jt_zkx@sjzu.edu.cn; zkx0204@yahoo.com*
2. *Shenyang Jianzhu University, School of Traffic Engineering, Department of Bridge, Shenyang, No. 25 Hunnan Middle Road, PR of China;*
3. *Shenyang Institute of Technology, School of Energy and Hydraulic Engineering, East Section of Binhe Road, Shenfu New District, Liaoning Province, PR of China*

ABSTRACT

In recent years, there have been cases of strengthening bridge structures with polyurethane cement mortar. To further explore the properties of polyurethane materials, the effects of emery, lime, quartz sand and cement on the mechanical properties of polyurethane powder composites are studied by three-point flexural test. In the flexural test, the polyurethane cement composite formed a control group by changing the content of polyester polyol. The flexural strength and ductility are improved to a certain extent due to the addition of polyester polyol. The average flexural strength of other polyurethane powder composites such as polyurethane emery test block is 45.1 MPa and the corresponding strain is 6203 με, the average flexural strength of polyurethane lime test block is 33.4 MPa and the corresponding strain is 6470 με, the average flexural strength of polyurethane quartz sand test block is 49.23 MPa and the corresponding strain is 7521 με. The results show that the flexural strength of polyurethane emery material and polyurethane quartz sand material is higher than that of polyurethane cement, which can be used to replace cement to a certain extent to reduce the cost of polyurethane composite material.

KEYWORDS

Polyurethane cement (PUC) material, Mechanics performance tests, Polyurethane powder composites, Constitutive relation

INTRODUCTION

Bridges are important parts of roads and railways, which play indispensable roles in logistics and transportation [1-3]. However, with the development of society, traffic has become increasingly busy. Under certain conditions, such as vehicle load, acid rain, and the rapid increase of temperature, a series of defects of stress cracks, concrete deterioration, and steel corrosion have occurred in the bridge structure [4-6]. After decades of operation, the Bridges built in the early stage are generally aged, and most of them are in the working state of "defcet". Although after years of reinforcement and transformation, the number of dangerous Bridges is still very large. The practice shows that the bearing capacity of the old bridge structure can be restored and improved by using appropriate reinforcement methods. Countries all over the world try to improve the service life of the old bridge by means of reinforcement, so that its bearing capacity can be effectively guaranteed.

Therefore, how to strengthen the bridge economically, quickly, and effectively becomes one of the key points in the development of bridge industry [7-10].

Polyurethane cement composite (PUC) has the characteristics of light weight, high strength and high toughness, and the material itself has good bonding strength and acid and alkali corrosion resistance, which can not only solve the durability problems of reinforced beams caused by composite mortar cracking and falling off, but also the material itself can be reinforced for the main beam. The traffic management department has used the reinforcement method of polyurethane cement composite material in some actual old bridge reinforcement in recent years. Some domestic scientific research institutions not only study the mechanical properties of polyurethane cement, but also use it comprehensively with the reinforcement method of prestressed steel wire rope, as the embedded material to participate in the stress of the structure, so that the active and passive reinforcement methods cooperate, and become the additional passive reinforcement material for the prestressed reinforcement [11-13]. Scholars have carried out a series of studies on its excellent properties in building materials：

Sun Quansheng et al. [14] tested the tensile and flexural resistance of polyurethane cement through laboratory tests. Zhang Shengran et al. [15] used steel wire rope and polyurethane cement composite steel wire rope to strengthen the bending of 3 m ordinary reinforced concrete T beam and made a total of 5 test beams without reinforcement, with 5 separate steel wire rope reinforcement and 3, 5 and 7 steel wire ropes reinforcement of polyurethane cement. They analyzed and verified the reinforcement effect of polyurethane cement steel wire rope on rigidity, strength and bearing capacity. Liu Guiwei, Wang Jianlin et al. [16] through the preparation of materials received pu concrete composite material (MPC), Ningbo-Taizhou-Wenzhou highway of Zhejiang Ningbo Bai Xi bridge has carried on the polyurethane composite reinforcement concrete. Zhang Hongxiang et al. [17] and Gao Feng [18] completed the experimental study of taking MPC composite materials to strengthen 13m hollow slab girders. During the whole test, the MPC material and the concrete section did not slip. They established the calculation formula of strain and bending capacity of hollow slab beams after MPC reinforcement, and also verified the feasibility of ANSYS software in the study of simulating MPC reinforcement of RC beams. Gu Dandan et al. [19,20] found that the material can improve the bearing capacity of hollow slab bridges. Haleem K. Hussain et al. [21-23] tried to get polyurethane cement (PUC) composites with polyurethane and fly ash. They carried out flexural and flexural tests on the composites and obtained the stress-strain curves of the materials at different densities. Based on the material research, the bending reinforcement tests of seven T-section beams under different failure degrees are carried out. The results show that the ultimate bearing capacity of the beams strengthened by polyurethane cement composite (PUC) is improved.

However, the cost of the cement in the polyurethane cement is high. If other cheaper materials are used as filling materials, it is a feasible way to greatly reduce the cost of the polyurethane cement material. In this paper, the same weight of quartz sand, lime, emery and other materials will be added to the polyurethane material, through flexural test to explore its mechanical properties.

POLYURETHANE RAW MATERIALS AND PREPARATION

Polyurethane Cement Composite (PUC)

The main chemical composition is shown in Table 1. Polyols usually account for 49% and isocyanates account for 51%. Polyurethane has excellent performance in mechanical property of good wear resistance, molding properties and chemical corrosion resistance.

Tab.1 - Polyurethane ratio

Composition		Percentage（%）
Polyols raw material	Polyether	49
	Silicone Oil	1
	Water	0-1
Isocyanate raw material		50-51

Preparation of Polyurethane Powder

Polyurethane raw materials and silicon carbide, limestone, quartz sand and cement powder according to the quality than the mixture of polymerization reaction, the quality ratio of polyester polyols: isocyanate: powder = 1:1:2, by comparing polyurethane concrete stress and strain characteristics, set up the control group, formulate the polyester polyols: isocyanate: powder = 1.15:1 and polyester polyols: Isocyanate: powder = 1.3:1:2 high density polyurethane powder composite material, and for the convenience of explanation. Three groups of polyurethane cement test blocks are named as group A, group B, and group C shown in Table 2. The preparation process is shown in Figure 1 and Figure 2. The size of the test mold is based on the Chinese cement mortar strength inspection method GB/T 17671-2020. The polyurethane powder composite material and defoaming agent are mixed mechanically for 3-5 mins, then molded into a 40 mm × 40 mm × 160 mm cuboid specimen and 70 mm × 70 mm × 70 mm cube specimen. The test blocks after molding are shown from Figure 3 to Figure 6.

Tab. 2 - Specific composition table of polyurethane material sample block

Types of Polyurethane Powder	Composition	Percentage (%)
Group A Polyurethane Cement	Polyether Polyols	25
	Isocyanate	25
	Cement	50
Group B Polyurethane Cement	Polyether Polyols	28
	Isocyanate	24
	Cement	48
Group C Polyurethane Cement	Polyether Polyols	30
	Isocyanate	23
	Cement	47
Polyurethane Emery	Polyether Polyols	25
	Isocyanate	25
	Silicon Carbide	50
Polyurethane Lime	Polyether Polyols	25
	Isocyanate	25
	Calcium Carbonate	50
Polyurethane Quartz Sand	Polyether Polyols	25
	Isocyanate	25
	Quartz Sand	50

Fig. 1 - Pouring diagram of polyurethane material

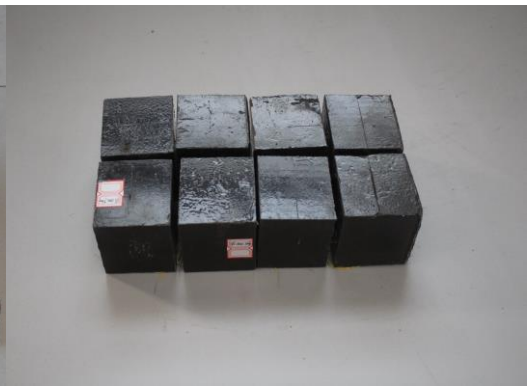

Fig. 2 – Compression strength specimen

Fig. 3 - Polyurethane cement specimen

Fig. 4 - Polyurethane emery specimen

Fig. 5 - Polyurethane quartz specimen

Fig. 6 - Polyurethane lime specimen

LOADING AND MEASURING SCHEME

Because polyurethane composite material is a new type of material, there is no current specification for its use. Therefore, JTG E30-2005 Test Rules for Cement and Cement Concrete in Highway Engineering is adopted for experimental study. Referring to the test method for the flexural strength of cement concrete cube in the code, the three-point flexural strength test is carried out on the universal tester. According to the rules, the test process should first be the center of the test piece and the press geometric alignment, and then determine the test loading speed. When the test is ready, start loading. When the polyurethane material test block is close to failure and begins to deform rapidly, the test machine is no longer adjusted; When the failure of the polyurethane material test block is determined, the failure ultimate load F is recorded. After the completion of the test, the

test data are statistically processed. The flexural strength of polyurethane cement specimens should be calculated as follows:

$$\sigma_c = \frac{1.5Fl}{bh^2} \quad (3\text{- }1)$$

In the formula：

σ_c The flexural strength of polyurethane cement, Mpa;

F The ultimate load, N;

L Distance between support points, mm;

b The width of the prism, mm;

h The height of the prism, mm;

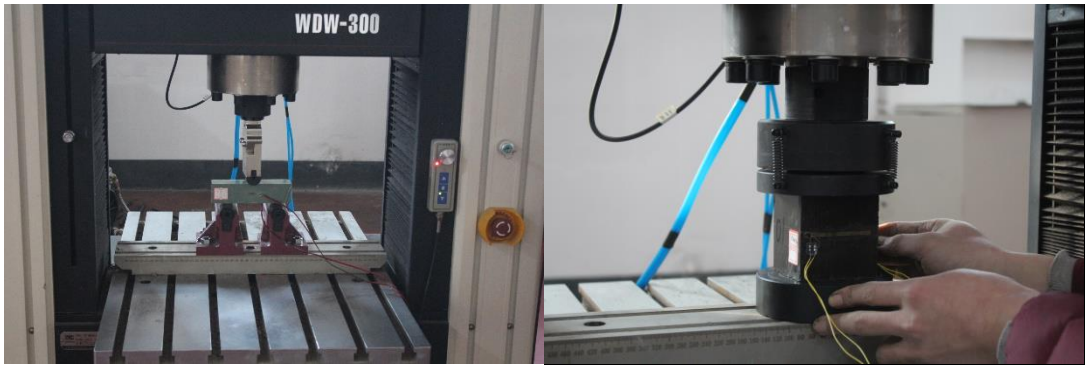

（a） （b）

Fig. 7 - Loading device diagram

EFFECT OF DIFFERENT POWDERS ON MECHANICAL PROPERTIES OF POLYURETHANE COMPOSITES

Bending test results

In bending test, a multifunctional testing machine is used to load and dynamic strain acquisition instrument is used to collect. By averaging the values of the two strain gauges, the actual strain value can be derived. There are three flexural test blocks of group A polyurethane cement participating in the flexural test this time. The flexural stress-strain curve of group A polyurethane cement test blocks is shown in Figure 8 and the average is shown in Figure 9. Strain and stress present a positive proportional function in the curve. The peak strength is 37.2 MPa. The peak strain is 10848 με. The peak stress of each block is shown in Table 3.

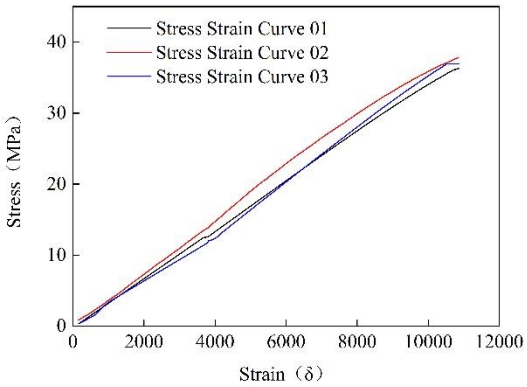

Fig. 8 – Stress and strain curve of group A (The material ratio is 1:1:2)

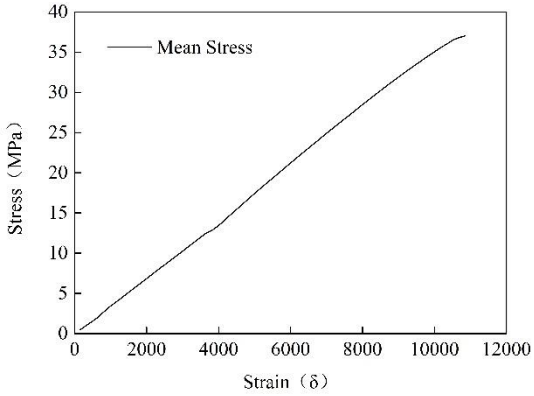

Fig. 9 – Stress and strain curve of group A (The material ratio is 1:1:2)

Tab. 3 - The flexural strength of group A polyurethane cement

Serial Number	1	2	3	Average
Strength (MPa)	36.3	37.8	37.0	37.2

There are three flexural test blocks of group B polyurethane cement (polyol: isocyanate: cement =1.15:1:2) participating in the flexural test this time. The flexural curve of group B polyurethane cement test blocks are shown in Figure 10 and Figure 11. The curve reveals a linear relationship with the load increasing. The average peak flexural strength is 38.9 MPa. Meanwhile, the strain peak value is 23520 με. The peak stress of each bending specimen is shown in Table 4. The results show that the stress of polyurethane cement increased by 1.8MPa and strain increased by 116.7% compared with group A polyurethane cement (polyol: isocyanate: cement =1:1:2) due to the addition of polyester polyols. The flexural strength of cement =1.15:1:2 is slightly improved, and the ductility is greatly enhanced.

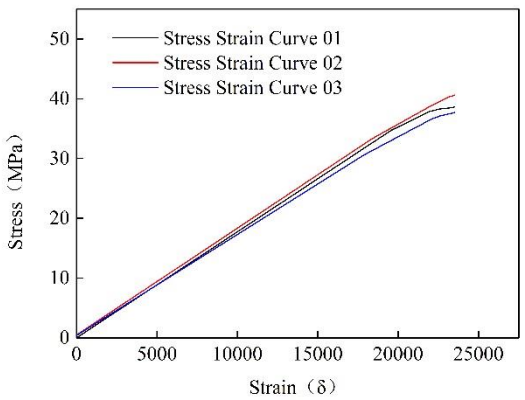

Fig. 10 - Stress-strain curve of group A polyurethane cement (Polyol: isocyanate: cement =1.15:1:2)

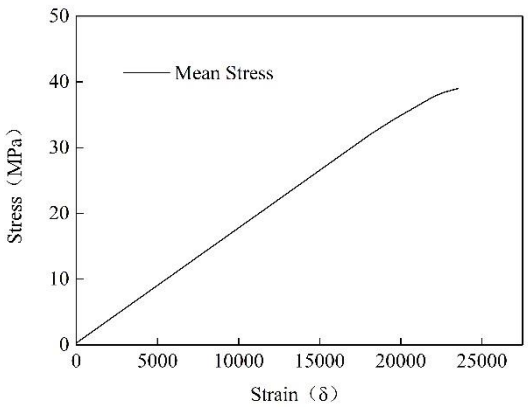

Fig. 11 - Stress-strain curve of group A polyurethane cement (average) (Polyol: isocyanate: cement =1.15:1:2)

Tab. 4 - The flexural strength of group B polyurethane cement

Serial Number	1	2	3	Average
Strength (MPa)	38.6	40.6	37.7	38.9

The flexural curve of group C is shown in Figure 12. There are three flexural test blocks of group C polyurethane cement (polyol: isocyanate: cement =1.3:1:2) participating in the flexural test this time. The average curve of flexural capacity is shown in Figure 13.TThe peak stress of each flexural specimen is shown in Table 5. The results showed that the stress of polyurethane cement increased by 5.4 MPa and the strain increased by 203.5% compared with group A polyurethane cement (polyol: isocyanate: cement =1:1:2) due to the addition of polyester polyols. Compared with group B polyurethane cement (polyol: isocyanate: cement =1:1:2), the stress of polyurethane cement increased by 5.4 MPa and the strain increased by 203.5%. (polyol: isocyanate: cement =1.15:1:2) increased by 3.6 MPa and strain increased by 40.1%, indicating that the flexural strength and ductility of polyurethane cement (polyol: isocyanate: cement =1.3:1:2) are improved to a certain extent with the increase of the content of polyurethane polyol.

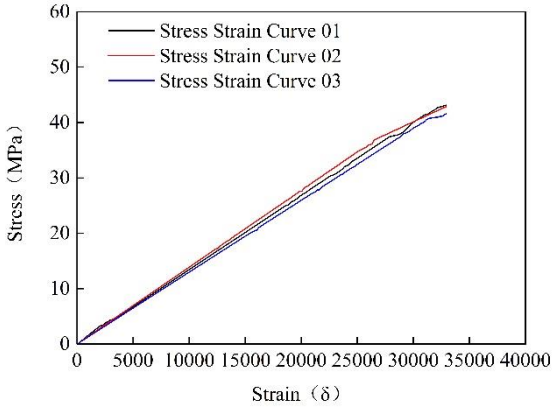

Fig.12 - Stress-strain curve of polyurethane cement (Polyol: isocyanate: cement =1.3:1:2)

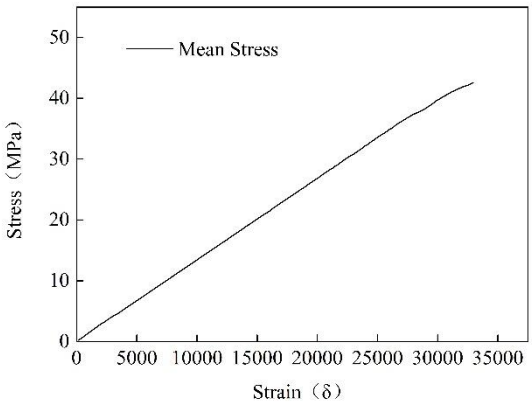

Fig.13 - Stress-strain curve of polyurethane cement (average) (Polyol: isocyanate: cement =1.3:1:2)

Tab.5 - The flexural strength of group B polyurethane cement

Serial Number	1	2	3	Average
Strength (MPa)	43.1	42.9	41.6	42.5

Three pieces of polyurethane emery flexural test blocks were used in the test. Its stress-strain curve are shown in Figure 14 and Figure 15. The average flexural strength at the peak is 45.1 MPa, and the strain is 6203 με. The peak stress of each flexural test block is shown in Table 6.

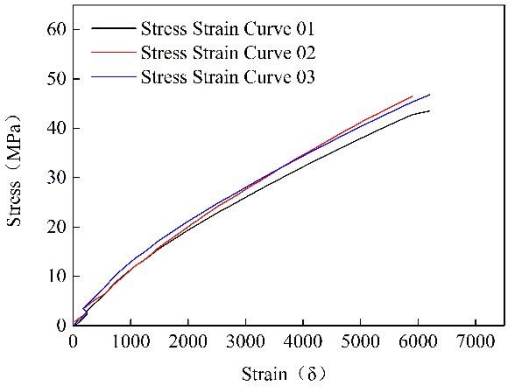

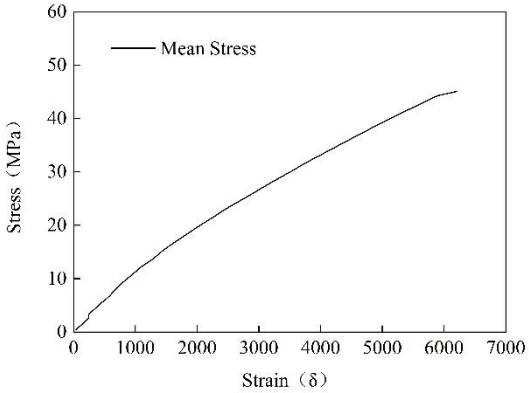

Fig.14 - Polyurethane emery curve *Fig.15 - Polyurethane emery curve (average)*

Tab. 6 - The flexural strength of polyurethane emery test block

Serial Number	1	2	3	Average
Strength (MPa)	43.5	46.5	45.3	45.1

There are three polyurethane lime flexural test blocks participating in the flexural test, which are collected by dynamic strain acquisition instrument. The flexural curve of polyurethane lime test block is shown in Figure 16 and Figure 17. The peak average flexural strength is 31.4 MPa. At the same time, the strain is 5723 με. When the loading reached a certain peak, the stress increased more slowly than the strain. When the load reaches the peak value. The peak flexural strength of each polyurethane lime test block is shown in Table 7.

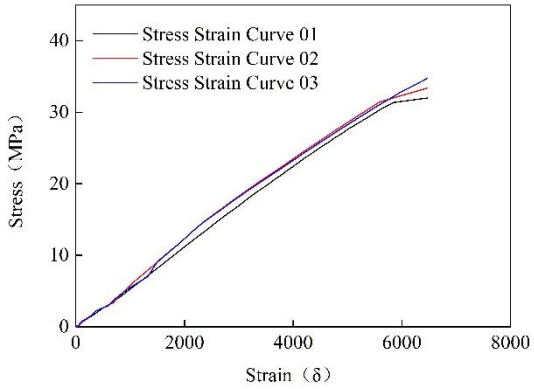

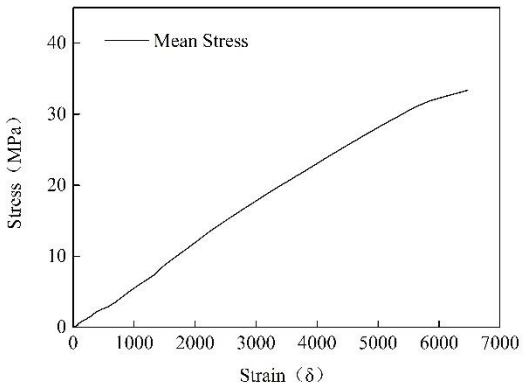

Fig. 16 – Stress and strain curve of polyurethane lime

Fig. 17 – Stress and strain curve of polyurethane lime (average)

Tab. 7 - The flexural strength of polyurethane lime test blocks

Serial Number	1	2	3	Average
Strength (MPa)	32.0	33.4	34.7	33.4

There are three flexural test blocks of polyurethane quartz sand participating in the flexural test this time. The curve of polyurethane quartz sand test blocks is shown in Figure 18 and Figure 19. The peak stress of each polyurethane flexural test block is shown in Table 9. The slope of the stress-strain curve decreases slightly when the loading reaches the middle and late stage, and the stress increases more slowly than the strain. When the loading reaches the peak, the average flexural strength is 49.2 MPa, and the strain is 7521με. It can be seen that in the rubber sand sample composed of polyurethane, emery, lime and quartz sand, the test block of polyurethane quartz sand has the best flexural strength and higher strain than other composites, indicating that its ductility is also better than other composites.

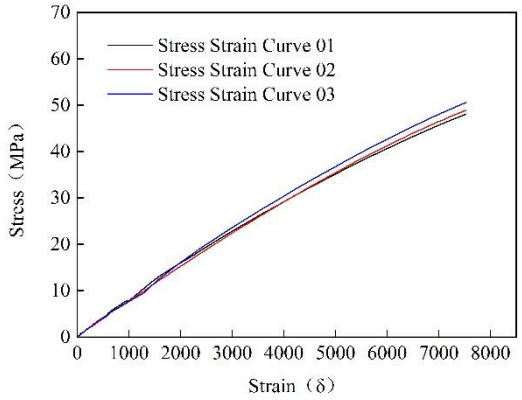

Fig. 18 – Stress and strain curve of polyurethane quartz sand

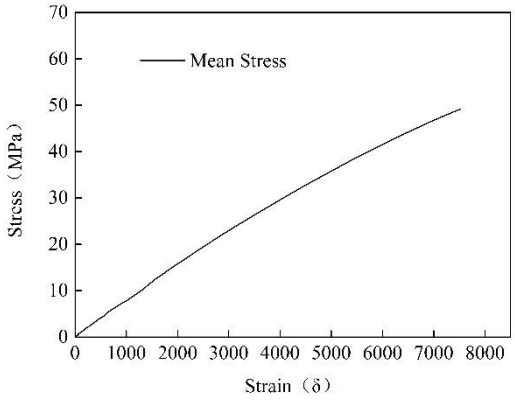

Fig. 19 – Stress and strain curve of polyurethane quartz sand (average)

Tab.9 - The flexural strength of polyurethane quartz sand test block

Serial Number	1	2	3	Average
Strength (MPa)	48.1	48.9	50.6	49.2.

Table 10 is a summary of the average flexural strength of each polyurethane powder composite. As shown in Table 10, the flexural strength of the polyurethane cement in the polyurethane mortar test blocks with the same composition ratio is 37.1 MPa, and the average flexural strength of the polyurethane emundant test block is 45.1 MPa, which is 21.6% higher than that of the polyurethane cement test block in group A. The average flexural strength of polyurethane lime test block is 33.4 MPa, which is 9.9% lower than that of group A polyurethane cement test block. The average flexural strength of polyurethane quartz sand test block is 49.2 MPa, which is 32.6% higher than that of group A polyurethane cement test block. These three kinds of the strength of the polyurethane lime block only less than the flexural strength of polyurethane cement group A, while polyurethane emery block polyurethane and quartz sand block strain less than polyurethane cement, but its flexural strength is superior to polyurethane, the flexural strength of cement in theory can replace cement with silicon carbide, quartz powder to reduce the cost of PU composite material.

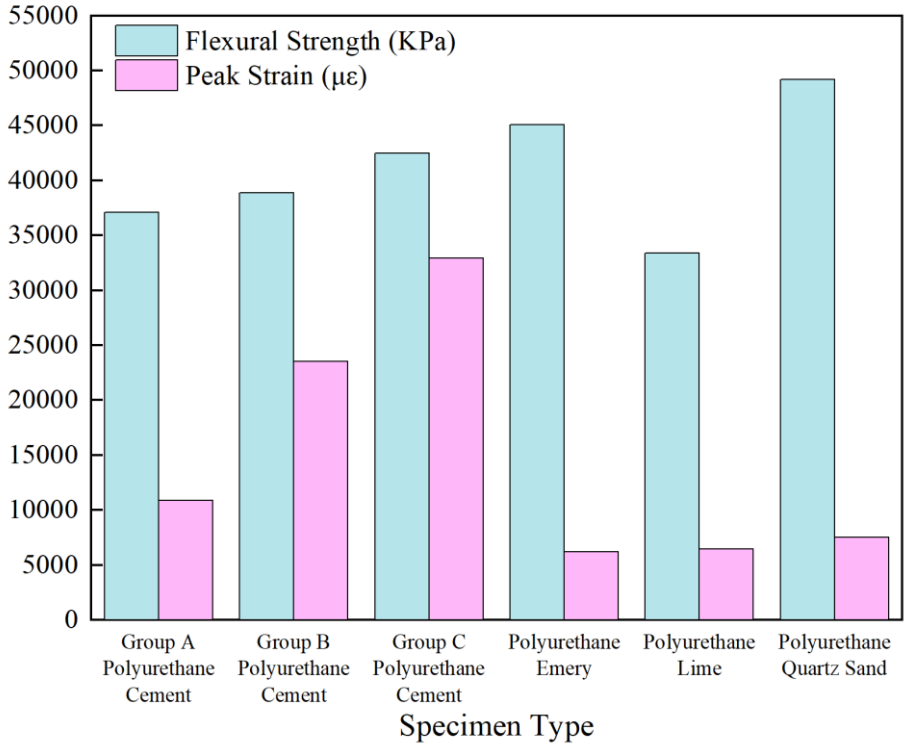

Fig. 20 – Summary of the flexural strength of each specimen

4.2 Compression test results

In compression test, the strain value is the average of the measured values of the two resistance strain gauges. The compressive stress-strain curve of each test block is shown in Figure 21 and Figure 22. At the initial stage of loading, the compressive strength of the six groups of cube specimens is very similar. In the later stage of loading, the stress-strain curve is nonlinear. In the three groups of polyurethane cement. The compressive strength of group C is the highest with a value of 71.52 MPa. In the three groups of other materials. In the other three groups of polyurethane powder types, polyurethane quartz sand has the greatest compressive strength. Its maximum compressive strength is 76.70 MPa.

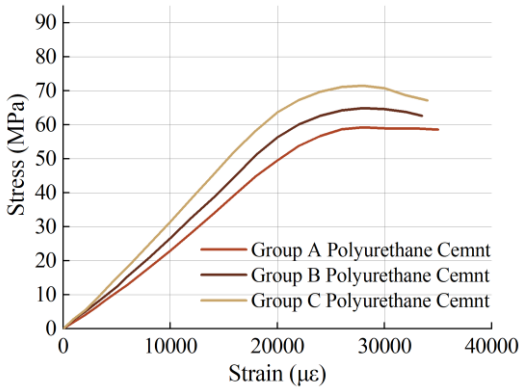

Fig. 21 – Compression strength of polyurethane cement

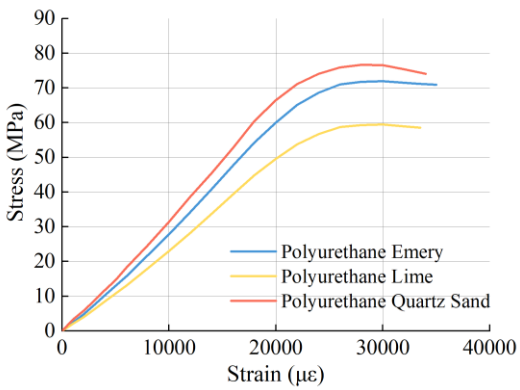

Fig. 22 – Compression strength of other polyurethane powder

CONCLUSION

In this paper, by studying the influence of different powders on the mechanical properties of polyurethane powder composites, the powder is mainly divided into emery, lime, quartz sand and cement. The stress-strain curve and the following conclusions can be listed as follows:

1. The average peak flexural strength of group A polyurethane cement (polyol: isocyanate: cement =1:1:2) is 37.1 MPa, and the strain is 10854με.The average peak flexural strength of polyurethane cement of group B (polyol: isocyanate: cement =1.15:1:2) is 38.9 MPa, and the strain is 23520με. Compared with group A, the stress of polyurethane cement of group B is 1.8 MPa higher and the strain is 116.7%. The average peak flexural strength of group C polyurethane cement (polyol: isocyanate: cement =1.3:1:2) is 42.5 MPa, and the strain is 32942 με. Compared with group A polyurethane cement, the stress increases by 5.4 MPa and the strain increases by 203.5%. The results show that the flexural strength and ductility of polyurethane cement are improved obviously because the composition proportion of polyester polyols is increased in polyurethane cement. In the compressive test, the maximum compressive strength is 76.70 MPa. The material composition with maximum compressive strength is polyurethane quartz sand.
2. The average peak flexural strength of polyurethane emery test block is 45.1 MPa, and the strain is 6203 με. The average peak flexural strength of polyurethane lime test block is 33.4 MPa, and the strain is 6470 με. The average peak flexural strength of polyurethane quartz sand test block is 49.2 MPa, and the strain is 7521 με. In the flexural test blocks composed of polyurethane and emery, lime and quartz sand, the flexural strength of polyurethane lime test block is less than that of polyurethane cement, and the flexural strength of polyurethane emery test block and polyurethane quartz sand test block is greater than that of polyurethane cement. As a summary, emery and quartz sand powder can be used to replace cement in order to reduce the cost of polyurethane composites.

ACKNOWLEDGEMENTS

Thanks to the Open Fund Project of Laboratoryof Ministry of Education for Disaster and Control of Major Engineering, Jinan University (20200904012)

REFERENCES

[1] XUE, Rui, WU, Yu, ZHOU, & Junmin. Research And Application Of Bridge Reinforcement.
[2] D Bennett. ,2008. The history and aesthetic development of bridges. Thomas Telford.
[3] Podolny, W. , & Fleming, J. F. . , 1972. History development of cable-stayed bridges. Journal of the Structural Division, 98.
[4] Fang, R. , & Yang, X. . , 2015. Cause and Countermeasure of Structure Disease of Bridge. International Conference on Transportation Information & Safety.
[5] Diao, & Yan. (2014). Stone arch bridge disease detection and evaluation. Applied Mechanics & Materials, 501-504, 1332-1335.
[6] Fu, Z. , Sun, G. , Tong, S. , & Jie, X. . , 2017. Research on fatigue diseases evaluation of steel bridge deck based on fuzzy comprehensive method. Industrial Construction.
[7] Kang, J. T. , Wang, N. , Liu, C. Z. , Chen, C. W. , & Li, L. . , 2011. Study on disease analysis and reinforcement technology of truss arch bridge. Advanced Materials Research, 243-249, 1972-1977.
[8] Li, H. , & F Liu. , 2015. Bridge Inspection and Reinforcement Technology Application.
[9] Zhu, H. , Yang, Y. , & Fan, W. , 2015. External prestressing bridge reinforcement technology review. Matec Web of Conferences.
[10] Chen, K. , Wang, C. , Wang, T. , Zhu, Z. , & Jiang, H. , 2020. Preparation and performances of form-stable polyethylene glycol/methylcellulose composite phase change materials. Journal of Polymer Research, 27(8).
[11] Sonoda, K. , Okino, M. , Hayashi, H. , & Kita, H. . , 2010. Reliability of epoxy bonded steel plate method for repairing damaged rc slabs of bridge. Proceedings of the Japan Society of Civil Engineers(398), 245-254.

[12] Zhao, S. W. , & Qiao, X. P. . , 2011. Experimental study on reinforced hollow beam with carbon fiber reinforced polymer and external prestressed strand. Applied Mechanics & Materials, 94-96, 495-499.
[13] Gang, Zhishen, Wei, Yang, Jiang, & Jianbiao, et al. , 2014. Flexural strengthening of rc beams using distributed prestressed high strength steel wire rope: theoretical analysis. Structure & Infrastructure Engineering: Maintenance, Management, Life-Cycl.
[14] Gang, Zhishen, Wei, Yang, Jiang, & Jianbiao, et al. , 2014. Flexural strengthening of rc beams using distributed prestressed high strength steel wire rope: theoretical analysis. Structure & Infrastructure Engineering: Maintenance, Management, Life-Cycl.
[15] Zhang, K. , & Sun, Q. . , 2018. Experimental study of reinforced concrete t-beams strengthened with a composite of prestressed steel wire ropes embedded in polyurethane cement (pswr-puc). International Journal of Civil Engineering,Transaction A:Civil Engineering, 16(9), 1109-1123.
[16] Zhang, J. F. , Zhuang, B. Z. , & Zhang, K. X. . , 2016. Experimental study to investigate mechanical properties of polyurethane-cement composite. Low Temperature Architecture Technology.
[17] Zhang, H. X. , Chen, C. , & Tian-Lai, Y. U. ., 2015. The application of simply supported t beam strengthened by mpc material. Low Temperature Architecture Technology.
[18] Hussain, H. K. , Lian, Z. Z. , & Gui, W. L. . , 2013. An experimental study on strengthening reinforced concrete t-beams using new material poly-urethane-cement (puc). Construction & Building Materials, 40(Mar.), 104-117.
[19] Dan-Dan, G. U. , Sun, Q. S. , & University, N. F. . , 2015. Study of static tests for using mpc composite material to strengthen void plate girder bridge. World Bridges.
[20] Lee, Y. H. , Oh, S. H. , Lee, J. K. , & Chung, Y. S. . , 2011. A structural performance test of reinforced concrete bridge slab with inverted-t girder. Journal of the Korean Society of Civil Engineers B. 31 2 a, 31(2A).
[21] Hussain, H. K. , Lian, Z. Z. , & Gui, W. L. . , 2013. An experimental study on strengthening reinforced concrete t-beams using new material poly-urethane-cement (puc). Construction & Building Materials, 40(Mar.), 104-117.
[22] Hussain, H. K. , Liu, G. W. , & Yong, Y. W. ., 2014. Experimental study to investigate mechanical properties of new material polyurethane–cement composite (puc). Construction & Building Materials, 50(jan.), 200-208.
[23] Liu, G. , Otsuka, H. , Mizuta, Y. , & Shimitsu, A. . , 2006. A foundational study on static mechanical characteristics of the super lightweight and high strength material using fly-ash. Journal of the Society of Materials Science Japan, 55(8), 738-745.

CIVIL ENGINEERING JOURNAL

Article no. 68

THE CIVIL ENGINEERING JOURNAL 4-2021

A DEMOUNTABLE GIRDER - COLUMN JOINT

Aleš Polák

Czech Technical University in Prague, Faculty of Civil Engineering, Department of Building Structures, Prague, Thákurova 7, Czech Republic; ales.polak@fsv.cvut.cz

ABSTRACT

Traditional precast reinforced concrete structures are characterised by joints of individual components executed with the use of cement grouts or mortars, or by welding reinforcement. The joints produced in this way cannot be demounted in the case of need without damaging the precast components. Demountable precast structures with a long life cycle enable repeated assembly and demounting thus contributing to the saving of the basic input resources and the environment. The main feature of demountable precast structures are patent-protected joints which allow the assembly of the precast components without the necessity of using “wet” processes. The article addresses the characteristics of a demountable girder - column joint. It presents the results of static load tests carried out within extensive experimental research. To conclude, the article specifies the benefits and the applications of demountable structures.

KEYWORDS

Prefabrication, Demountable Structure, Sustainability, Experimental Research, Girder, Column

INTRODUCTION

Today’s dynamically developing society poses increasing demands on the flexibility of buildings. However, traditional prefabricated systems, which are characterized by limited adaptability and relatively high demands in the case of a change in their use, are not in correspondence with this dynamic. Nearly all building reconfigurations due to a change in its use, or the building relocation caused by production, transportation or demographic requirements are associated with a complete or partial demolition of the currently existing systems, as the reuse of the components connected by traditional wet processes is very limited. Thus, numerous prefabricated buildings are demolished after reaching their moral obsolescence, which is usually much earlier than the end of their physical life span. As a result, additional costs related to a premature demolition and recycling of buildings are incurred. In addition to these costs, considerable amounts of energy are consumed during the whole process of a premature demolition of the structure, and a lot of environmentally harmful gases are released into the air.

A potential solution mitigating the adverse effects of standard precast reinforced concrete structures is the use of new structural systems with a long life cycle. The possibility of reusing demountable structures can make a significant contribution to environmental protection and, ultimately, can also significantly reduce the costs that would otherwise be needed mainly for the fabrication of new elements of the traditional precast reinforced concrete system.

A characteristic feature of the demountable system are mutual joints of individual precast components, which can be easily demounted, if necessary, without impairing the possibilities of the precast components’ further use. In addition to their structural function, these joints should enable reassembly without the use of wet processes and, at the same time, they should be fully demountable.

The introduction should present the scientific background of the study and state clearly its objectives.

ENVIRONMENTAL IMPACT OF REINFORCED CONCRETE STRUCTURES

The crucial criterion governing the selection of a building structure these days, apart from the erection time, is usually its acquisition price, regardless of any other costs related to the use of the structure and its demolition. Within the environmental protection policy, building structures should be assessed in a complex way covering their entire life cycle. This means starting from the production of materials and the erection of the structure, through its operation and maintenance, to the subsequent demolition, including the recycling of materials or structural elements, considering even the number of construction elements subsequently deposited in landfills. Only after the assessment of all these aspects and their impacts on the environment, can a suitable building structure be objectively chosen [1].

The significance of the impact of concrete structures on the environment is evident mainly with regard to their production volumes, even though the amounts of harmful emissions associated with the production of one kg of concrete is relatively small compared to other structural materials. The per capita concrete production in developed countries ranges between 1.5 and 3 tonnes per year. This results in the huge consumption of non-renewable primary resources (for the production of cement, mining gravel and aggregate deposits), which leads to their total depletion. At the same time, considerable amounts of energy are consumed in obtaining these raw materials [2].

Compared to traditional precast reinforced concrete structures, demountable precast structures consume approximately the same amount of the primary building materials for their production. For some demountable structural components, the proportion of steel used may even be higher than for traditional structures. This is mainly due to the difference in the connection of both types of structures, where, in the case of demountable structures, the mutual joints of individual components are usually secured by connecting steel elements. Nevertheless, from the perspective of the overall comparison of the structure's life cycle costs, the potential higher proportion of steel in demountable structures is economically negligible.

By using demountable systems with a long life cycle, significant savings in the basic input resources can be achieved thus offsetting the current threat of mineral depletion. In terms of the amount of energy used, the most energy intensive phases of the life cycle of precast structures are the extraction of the necessary raw materials and the production of the precast components. By the reuse of demountable structures with a long life cycle, or a long design life, respectively, the amounts of energy required to provide the input materials and produce new components, but also the emissions of harmful gases, can be, to a significant extent, reduced.

The comparison in Figure 1 points out that in the case of reuse, demountable systems are significantly more ecological and less energy intensive compared to traditional precast systems.

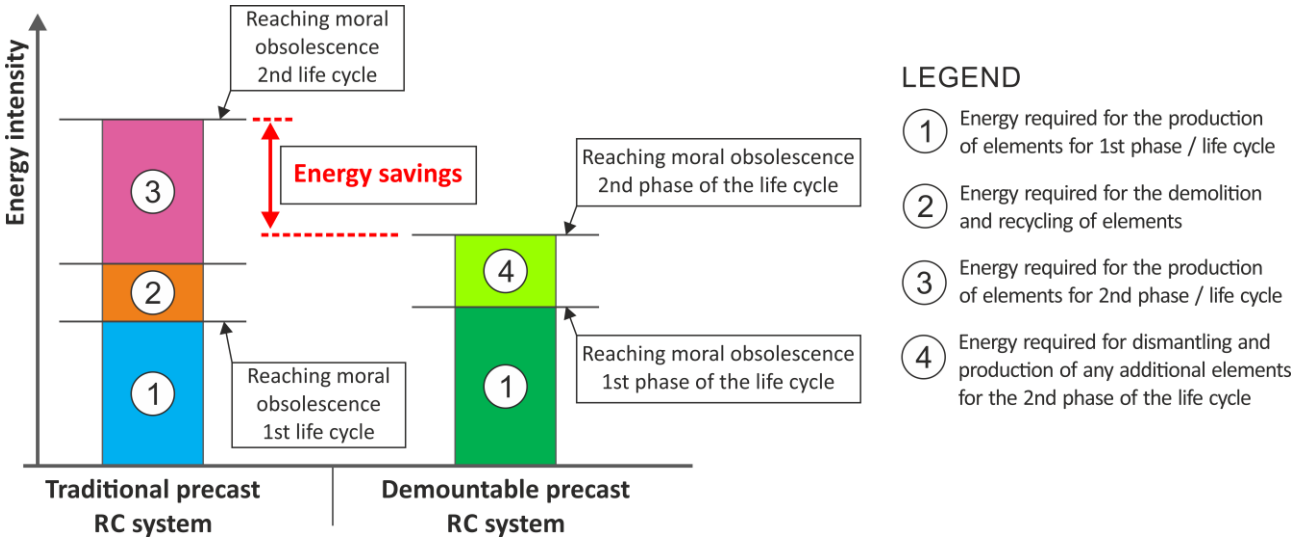

Fig. 1 – Comparison of energy intensity for traditional and a demountable precast reinforced concrete system

At the same time, demountable structures consume only a fraction of the energy during their disassembly that would otherwise be needed for demolition. Moreover, individual components of the demountable structure can be reused. This construction method is very environmentally friendly compared to standard precast reinforced concrete structures, and, at the same time, it saves natural resources.

The constant pressure to reduce the energy and material intensity of newly designed buildings, together with the sustainability imperative in the construction industry, requires a new approach to the design of buildings covering the building's entire life cycle from its erection, through demolition to recycling and disposal at the end of the physical life of individual structural components and building parts. Material-saving solutions, together with low energy intensity implementation methods and design solutions creating the preconditions for the maximum return and recycling rate of the used materials and products, are one of the ways to achieve sustainable development [4].

The possibility of "recycling" reinforced concrete structures at the level of precast components results in significant energy and material savings mitigating the negative impact of the building industry on the environment. Compared specifically with the hitherto common recycling of building materials, the proposed solution of the "reuse of precast reinforced concrete components" represents a qualitatively higher degree of recycling. Not only is it not necessary to recycle precast reinforced concrete members, but it is also not necessary to spend new energy on the production of the basic materials mounted in new components. This advantage of the designed multi-purpose demountable system is becoming extremely important, especially with regard to the highly energy intensive production of the basic materials for the fabrication of reinforced concrete structures and their significant contribution to the ever-deteriorating environmental condition [5].

DEMOUNTABLE GIRDER - COLUMN JOINT

Joint Characteristics

A characteristic features of the demountable precast system are patent-protected dry demountable joints of load-bearing components. The main advantage of these joints is their potential reassembly and the disassembly of the supporting structure. An equally important benefit over the classic assembly of precast structures is the elimination of wet processes, i.e. connection of precast components in a "dry" way.

The design of joints is based on the production and assembly tolerances achievable at the current production technology level of precast reinforced concrete components (in the range of up

to ± 5 mm in component dimensions) and the achievable assembly tolerances (in the range up to ± 3 mm in component mounting). The resulting deviations of assembled structures generally depend on the precision of manufactured components, the precision of their alignment and mounting. In the case of demountable structures, the mounting precision, in particular, may apply to a significant extent [6].

The basic joint of the skeletal system is a demountable joint of a girder and a column ("girder - column" joint). This joint consists of anchor and mounting steel plates embedded in a precast column and a girder, and connecting steel elements additionally mounted during the assembly. The demountable "girder - column" joint is designed to enable easy assembly of the column structure using precast columns one or two to three storeys in height [7].

From the structural perspective, these are short brackets embedded in columns with girders mounted on them. The demountable joint (CZ patent No. 305 454 B6) is composed of a special welded steel element, which enables a significantly fast mounting of the bracket using the principle of a self-locking interlocking joint (Figure 2). The disadvantage is higher labour intensity during the production of fittings, but, on the other hand, the need to use high-strength screws is eliminated, and the assembly time required for fastening the bracket is shortened. Another significant advantage of this type of joint is that the steel element can be mounted manually without the use of other tools (wrenches, nut runners).

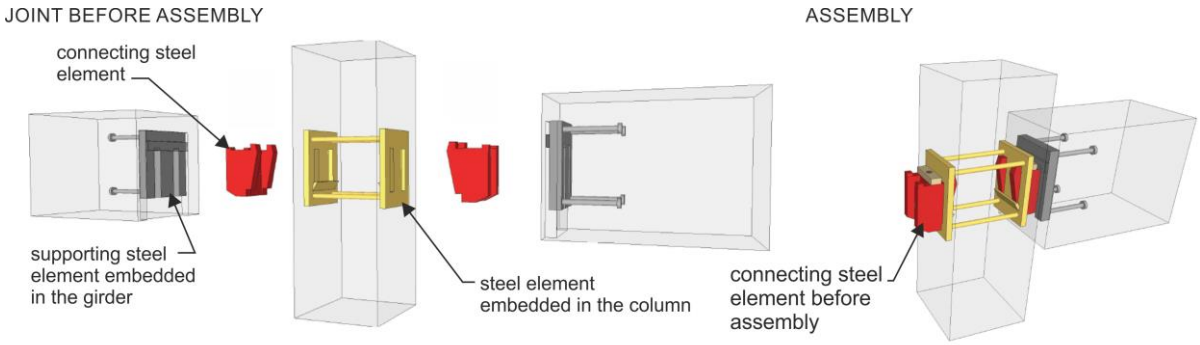

Fig. 2 – Scheme of the "girder - column" joint

Figure 3 displays the anchor and mounting steel plates for both versions of joints before their mounting into the concreting formwork. The fittings embedded in the column, including the connecting element (bracket), can be seen on the left, and the fittings embedded in the girder on the right.

Fig. 3 – Steel fittings embedded in the column including the connecting element (on the left) and the girder (on the right) [3]

Experimental research into a demountable girder - column joint

The experimental research into the essential parts of the load-bearing demountable precast system was carried out in cooperation with the Technical and Test Institute for Construction Prague, SOE. The subject of the experimental static load test of a section of the load-bearing precast skeletal system was the verification of the function and the load-bearing capacity of demountable girder - column joints under flexural and shear loading. The test was divided into two parts – loading of the girder with bending and a shear force, and loading of the girder with a shear force only.

The test configuration (Figure 4) of the section of the demountable precast reinforced concrete system was composed of two columns with dimensions of 300 × 300 × 2000 mm and a girder embedded between them with cross-sectional dimensions of 300 × 400 mm and 4800 mm in length. The girder was connected to the columns at an axial height of 1200 mm. The columns were supported in steel footing and secured against shifting and rotation by means of wooden wedges. The steel footing was immovably fixed to the floor with screws. Steel load-distribution elements were mounted on the girder. The precast components were made of C45/55 concrete. The test configuration was fitted with 14 linear deformation sensors (LVDT), which recorded the horizontal and vertical deformations depending on the applied load.

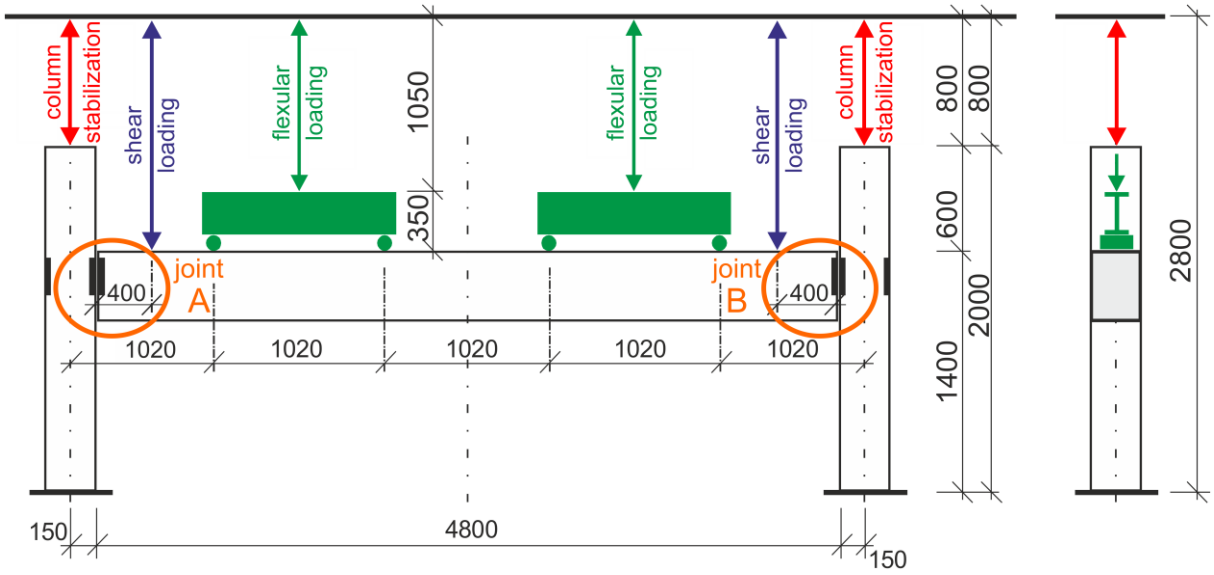

Fig. 4 – Scheme of the test configuration

Flexural loading

The test configuration was loaded by hydraulic presses mounted on a compression testing machine. The configuration was loaded step by step, first, the columns were loaded axially (constant load value of 2 × 100 kN). The load on the girder was applied in individual steps of 2 × 30 kN with unloading to the basic value of 2 × 30 kN. The gradual unloading was performed to determine permanent deformations. Under a load of 2 × 210 kN, the first tensile cracks appeared in the area around the girder mid-span, and further crack development was recorded during the subsequent loading. Under a load of 2 × 300 kN, the cracks on the lower face of the girder, in the middle of its length, reached 200–350 mm in length and 0.5–1.0 mm in width. The distance of individual cracks from each other ranged from 80 to 150 mm. Under the ultimate load of the configuration, the concrete was crushed and the compressed reinforcement at the upper face of the girder mid-span warped. The total maximum achieved load value was 2 × 440 kN (load value without the weight of the girder and the load-distribution device).

Fig. 5 – Test configuration (on the left) and the distribution of LVDT sensors at joint B (on the right)

Shear loading

The test configuration (Figure 6) was loaded in successive steps in the same way as in the case of flexural loading. Under a load of 2 × 360 kN, shear cracks due to flexural loading developed. Under increasing loads, these cracks continued to develop. Under a load of 2 × 420 kN, cracks appeared on the upper face of the girder. The width of these cracks increased up to a limit load of 2 × 520 kN. Under this load, the concrete at the upper face of the girder failed, and the concrete reinforcement was torn out. The loading was subsequently terminated.

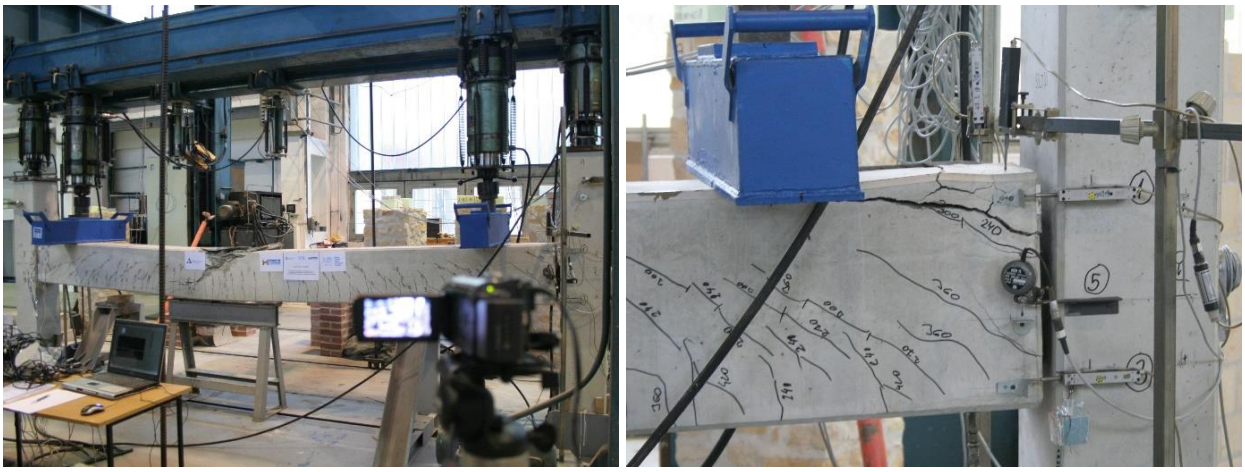

Fig. 6 – Test configuration (on the left), crack formation on the upper edge of the girder (on the right)

After the termination of loading, the girder was unloaded, and so were the columns. The type of girder failure (Figure 7) at both joints (A, B) was similar. The columns showed no failure in the joint area with the girder, and not even hairline cracks were recorded.

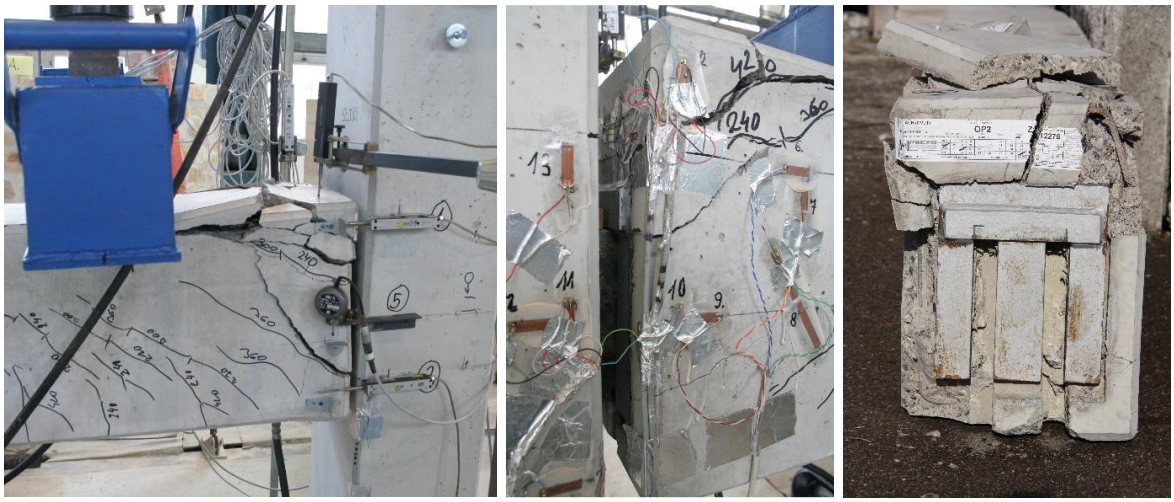

Fig. 7 – Joint failure at reaching the ultimate loading

Evaluation

Under flexural loading, the measured deformations showed a linear pattern until a load of 2 × 300 kN was reached, which exerted a bending moment on the girder of 423.3 kNm. The limit load was reached at a value of 2 × 440 kN – exerting the maximum bending moment on the girder (including the own weight of the girder and the load-distribution device) of 615.68 kNm, which is the bending moment corresponding to a continuous uniform load on the girder of 210.83 kN/m. After reaching the maximum bending moment, the steel elements of the girder - column demountable joints did not show any signs of damage. Tensile cracks 0.15–0.25 mm wide with a mutual distance of approx. 80–100 mm were recorded in the joint area on the girder.

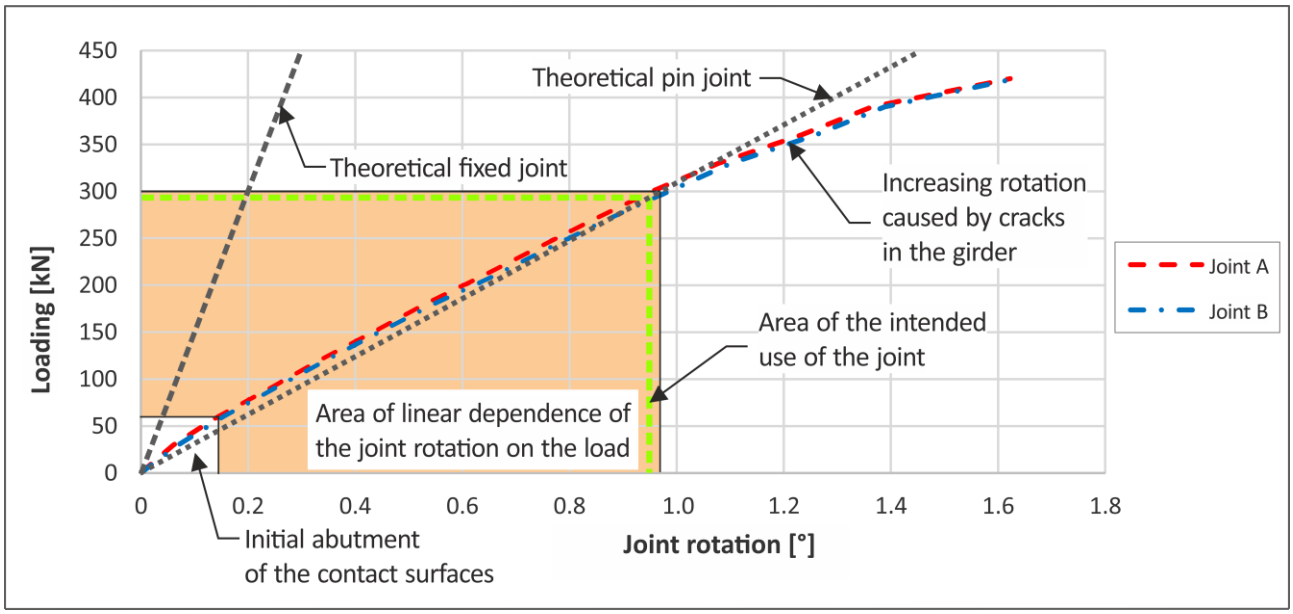

Fig. 8 – Dependence of girder - column joint rotation on loading and marking of key areas

The graph above (Figure 8) shows the dependence of the rotation of girder - column joints (deviation of the joint face from the vertical axis of the column) on the load. In the initial phase (up to a load of 2 × 60 kN), the contact interfaces – steel surfaces of the connecting short bracket and steel surfaces of the fittings embedded inside the girder – abut on one another. Starting from this loading, the area of linear dependence of the joint rotation on the applied load (orange) follows - bounded by

a load of 2 × 300 kN. Thus, this linear area also includes the area of the intended use of the joint (the area boundary is marked by a green dashed line), which corresponds to the load (assumed permanent load of the floor structure, including the own weight of floor panels and the floor layer composition, of 5.5 kN/m2 and imposed load of 2.5 kN/m2) exerted by a floor structure with a maximum span of 8.4 m.

It can be derived from the joint rotation - loading dependence pattern that from the structural perspective, the demountable girder - column joint behaves like a perfect hinge. At no load phase did a negative bending moment occur in this joint.

Under shear loading, the girder - column joint was loaded up to the shear force value per joint of 458.3 kN (including the own weight of the girder and the load-distribution device), which corresponds to 86.7% of the ultimate load. Starting from this load, a significant development of cracks in the area above the embedded steel anchor elements was recorded in the girder. At the limit load, a total shearing force of 528.3 kN acted on one joint (including the own weight of the girder and the load-distribution device). Under this load, the concrete in the upper part of the girder failed, and the steel anchor elements were torn out of the girder, but, at the same time, no cracks were recorded in the area of the embedded fittings in the column.

The graph below (Figure 9) displays the comparison of the experimentally identified load-bearing capacity of the demountable girder - column joint Vmax, exp and the theoretical design value of the load-bearing capacity of an identically reinforced concrete girder in shear VRd, theor (identified under ČSN EN 1992-1-1) with theoretical design values of the shear force corresponding to the load per joint for the considered grid of columns of 6.0 × 6.0 m, 6.0 × 7.2 m and 6.0 × 8.4 m (the same permanent and imposed loads were considered as in the previous comparison of flexural load-bearing capacity).

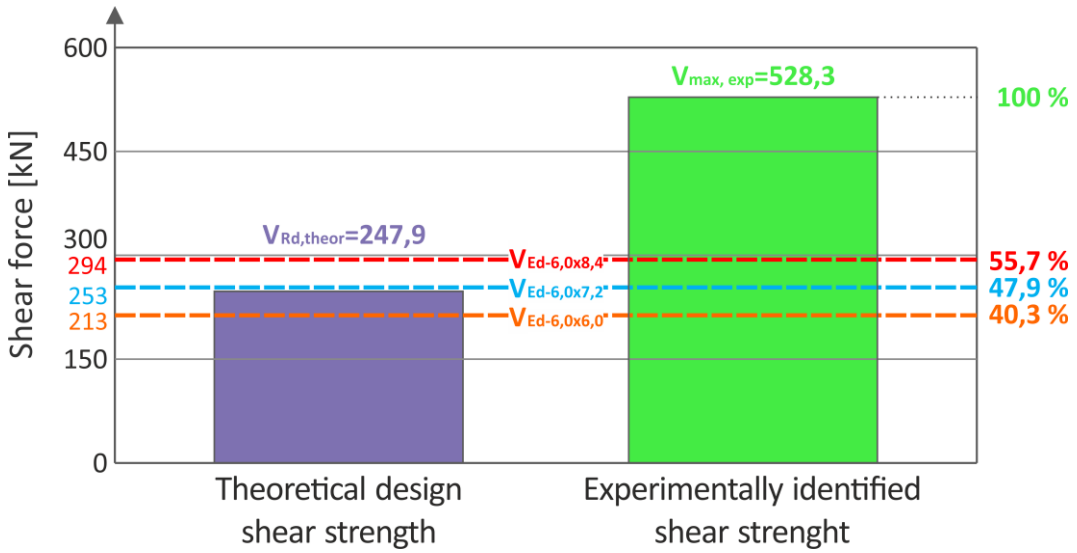

Fig. 9 – Comparison of the theoretical design and experimentally identified shear strength values with the design values of shear forces for the respective grids of columns

The theoretical design load-bearing capacity of the girder in shear was set at 247.9 kN thus corresponding to 46.9% of the experimentally identified load-bearing capacity. Comparing the experimentally identified shear strength of the demountable girder - column joint with the theoretical design values of shear forces corresponding to the loading of the above grid of columns, it is evident that the design values of bending moments are in the range of 40.3% (bay of 6.0 × 6.0 m) to 55.7 % (bay of 6.0 × 8.4 m).

No problems with the mounting or disconnection of individual precast components were recorded during the assembly of the test configuration and its subsequent disassembly. The assembly tolerances also proved to be satisfactory.

CONCLUSION

Demountable girder - column joint

The demountable girder - column joint proved the functionality of the proposed design solution during both the assembly of the test configuration and its subsequent disassembly. At the same time, no problems during the mounting or disconnection of individual precast components were recorded. Thus, the assembly tolerances of the joint appeared to be satisfactory. The experimental verification of the joint has shown that:

- from the structural perspective, the girder - column joint can be classified as a perfect hinge;
- the joint's steel fittings embedded in the column remained free of any visible failure after reaching the ultimate loading;
- the steel fittings embedded in the girder remained free of any visible damage after reaching the ultimate loading – only indentation at the point of abutting surfaces was recorded;
- the joint failure under loading with a shear force occurred in the upper part of the girder due to exceeding the concrete tensile strength and simultaneous tear out of the concrete shear reinforcement;
- the experimentally identified shear strength of the joint was by 79.7 % higher than the assumed maximum design load.

Therefore, the design of the joint's structural solution manifested sufficient load-bearing capacity for its assumed use.

Benefits and application of demountable structures

Demountable precast reinforced concrete structures meet the requirements of sustainable structures. Their main benefits in relation to the environment include the potential reuse of the precast components during one life cycle at a different time, place or a spatial layout thus reducing significantly the negative effects associated with the demolition and recycling of the existing structures and the manufacturing of new structures.

The basic difference of demountable precast reinforced concrete structures compared to the traditional precast system is the connection of individual components by means of discrete, usually steel, joints. The advantage of these demountable discrete joints of precast components is the possibility of their execution without welding and the use of "wet" processes and the related independence of climatic conditions. Another indisputable advantage is the acceleration of the whole assembly phase of the structure.

The necessary precondition for the application of demountable precast reinforced concrete structures, and the associated achievement of a favourable economic return but also an environmentally friendly policy, is their repeated use. Thus, the use of demountable systems will be desirable mainly in buildings with a premature moral obsolescence and a shorter functional life, such as buildings for preschool and primary education, accommodation and hotel facilities, buildings for production activities with an expected change in the production programme, but also for temporary buildings – start-up apartments, housing or civic amenities in places with a high temporary concentration of labour (long-term construction sites of primary importance – nuclear power plants, dams, etc.), or apartment buildings in areas affected by natural disasters, where the other advantages of demountable structures such as the speed of construction and independence of the assembly works on climatic conditions, will also undoubtedly apply.

ACKNOWLEDGEMENTS

The paper was written with support from the TA02010837 grant project "A Multipurpose Demountable Prefabricated Reinforced Concrete Building System with Controlled Joint Properties and Possibility of Repeated Use". The senior researcher of the project is prof. Ing. Jiří Witzany. DrSc.

Ing. Radek Zigler, Ph.D., doc. Ing. Tomáš Čejka, Ph.D., Ing. Jiří Karas, CSc., Ing. Pavel Kokeš and Ing. Aneta Libecajtová have made significant contributions to this project.

REFERENCES

[1] Richard R. B., 2006. Industrialised, flexible and demountable bulding systems: quality, economy and sustainbility. The CRIOCM 2006 International Symposium, pp. 11.
[2] Procházka J. 2007. Environmentální aspekty navrhování betonových konstrukcí (ČVUT v Praze)
[3] Witzany J. et al., 2016. Závěrečná zpráva TAČR TA02010837 Víceúčelový demontovatelný železobetonový stavební systém s řízenými vlastnostmi styků a možností opakovaných využití
[4] Polák A., 2015. Experimental Analysis of Demountable Precast Structure. In: Experimental Stress Analysis (České vysoké učení technické v Praze, Fakulta stavební), 321-324. ISBN 978-80-01-05734-6.
[5] Witzany J., Zigler R., Čejka T., Polák A. 2015. A demountable precast reinforced concrete building system of multi-story buildings. In: Proceedings of International Structural Engineering and Construction. Fargo: ISEC Press, 219-224. ISBN 978-0-9960437-1-7. ISSN 2644-108X. DOI: 10.14455/ISEC.res.2015.138
[6] Witzany J., Zigler R., Čejka T., Polák A. 2020. Stavební systémy nové generace, 2. díl: Demontovatelný stěnový systém. Časopis stavebnictví. 12(05): 44-50. ISSN 1802-2030
[7] Witzany J., Zigler R. 2020. Stavební systémy nové generace, 1. díl. Časopis stavebnictví. 12(04): 28-35. ISSN 1802-2030.

CIVIL ENGINEERING JOURNAL

Article no. 69

THE CIVIL ENGINEERING JOURNAL 4-2021

FLEXURAL SIMULATION ANALYSIS OF RC T-GIRDERS STRENGTHED WITH POLYURETHANE CEMENT-PRESTRESSED STEEL WIRE ROPES

Kexin Zhang[1], Xinyuan Shen[1],Dachao Li[1], Wenyu Hou[1], Fei Teng[1], Xing wei Xue[1]and Quansheng Sun[2]

1. *Shenyang Jianzhu University, School of Traffic Engineering, Department of Bridge Engineering, Shenyang, No.25 hunnan Zhong Road, China; jt_zkx@sjzu.edu.cn*
2. *Northeast Forestry University, School of Civil Engineering, Department of Bridge Engineering, Harbin, No.26 Hexing Road, China; hrbsqs@126.com*

ABSTRACT

To verify the effectiveness of polyurethane cement-prestressed steel wire ropes for flexural reinforcement of reinforced concrete T-girders, this paper conducts flexural test research on 7 pieces of T-girder specimens. Through the ABAQUS finite element program to build a model for numerical simulation, the results show polyurethane cement prestressed steel wire rope reinforcement can significantly increase the yield load and ultimate load of reinforced girders. Taking a girder in the test (20mm reinforcement thickness of polyurethane cement) as an example, yield load and ultimate load increased by 61.5% and 102.3% compared to unreinforced girder. The finite element model calculation results of T-girder bending reinforcement are in good agreement with the bending reinforcement test, and the error is only about 2%. For different strength concrete, the yield load increases slightly with the increase of concrete strength. For T-girders with different reinforcement ratios, the bearing capacity of strengthened girders changes significantly with the increase of longitudinal reinforcement ratio. The yield load of girders with reinforcement ratio of 1.82% and 1.35% is 29.84% and 65.85% higher than that of girders with reinforcement ratio of 0.91%. The yield deflection is 13.18% and 3.99% higher than that of girders with reinforcement ratio of 0.91%. It can be concluded that the bending reinforcement method of polyurethane cement prestressed steel wire ropes can effectively strengthen the main girder and ensure the structural safety.

KEY WORDS

Finite element analysis (FEA), Finite element modelling, T-girder strengthening, Polyurethane cement-prestressed steel wire ropes

BACKGROUND

Due to the rapid increase of vehicle load and the influence of natural conditions, a series of defects are inevitable in the bridge structure. These diseases will directly affect the stiffness and bearing capacity of the old bridge structure [1-3]. Practice has shown that the load-bearing capacity of old bridge structures can be restored and improved by using appropriate strengthening methods [4-5]. The accurate simulation analysis of cracking damage and bearing capacity of concrete girder bridge can provide a certain theoretical basis for the safety

evaluation, maintenance and reinforcement of existing bridges [7-9]. With the development of electronic computers, the emergence and application of finite elements can provide solid and nonlinear analysis for reinforced concrete structures, which greatly promotes the efficiency of simulation analysis. Nowadays, finite element software simulation has become one of the indispensable work in bridge test [10], [11].

In recent years, many scholars have conducted experimental analyses on the mechanical properties and reinforcement effects of reinforced concrete structures by means of finite element procedures. Cao Ming[12] used the finite element software ABAQUS to perform nonlinear analysis of reinforced concrete structures, summarized the basic principles and characteristics of the concrete principal structure model, and applied the calculation method to a finite element analysis of a simply supported girder to verify the reliability of the method. Yuan Ming [13] et al used a nonlinear finite element method to simulate and analyze the plastic damage of concrete box girders, and compared the simulation results with the experimental data to verify. The feasibility of introducing damage factors into the nonlinear analysis method of prestressed concrete box girder is verified, and the structural flexural and shear properties and damage characteristics can be accurately obtained; Zhang Haixia[14] et al used ABAQUS finite element software to apply different cell types for concrete, CFRP bars or laths and binder, especially Spring2 nonlinear spring cells to simulate the bonding effect of concrete with embedded CFRP bars or laths on the surface. Through finite element analysis, they obtained more accurate limit values of pull-out specimens, and correctly simulated the stress process of strengthened girders. Xu Chuanxue[15] et al clarified the main influencing factors by analyzing the long-term deformation of in vitro prestressed reinforced girders, and analyzed the law and degree of influence of each influencing factor on the long-term stiffness of reinforced concrete girders. Then the simulation results of various factors are given by finite element software to verify the reliability of analysis and simulation. Their research provides a reliable theoretical basis for the reinforcement of external prestress.

In this paper, 7 reinforced concrete T-section girders are strengthened by polyurethane cement prestressed steel wire rope flexural strengthening method for experimental study. Based on the plastic damage model, the nonlinear finite element analysis of reinforced concrete structure is carried out by using the test aided finite element software ABAQUS. Then, the parameters such as the number of steel wires embedded in polyurethane cement, the thickness of reinforced polyurethane cement, concrete strength grade and section reinforcement ratio are compared and analyzed.

T-GIRDER FLEXURAL STRENGTHENING RESULTS

Overview of Flexural Reinforcement Test

A total of 7 T-section simply supported girder specimens were tested in this section. The concrete for all specimens was made according to the same mix ratio. The specimens are of the same size, with an overall length of 3000 mm, a net span of 2700 mm, a shear-bend section length of 900 mm and a pure-bend section length of 900 mm. The longitudinal tensile steel bars are two 18 mm diameter tertiary rebar, the longitudinal reinforcement rate is 0.91%, the measured yield strength is 418 MPa, and the erection reinforcement is 10mm diameter secondary rebar, the measured yield strength is 250 MPa. In order to prevent insufficient shear strength, the configuration along the length of the specimen is 8 mm diameter first-class light round reinforcement, pure bending section spacing of 150 mm, shear bending section spacing of 80mm. The specific parameters of the cross-section are shown in Figure 1.

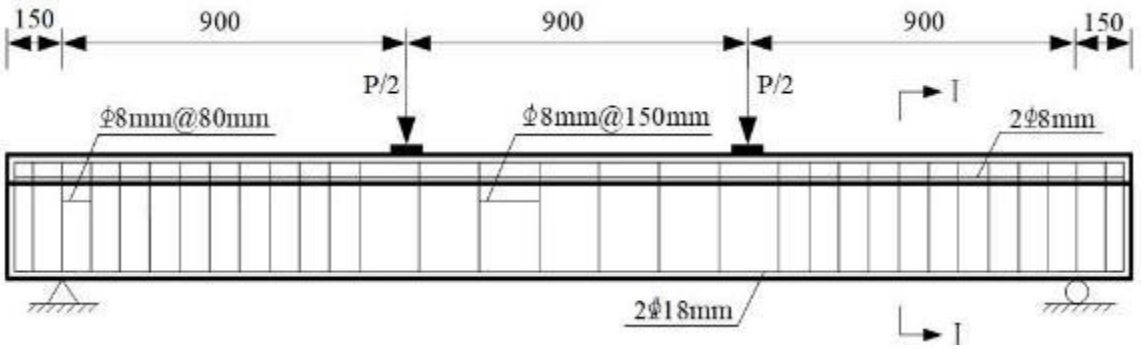

Fig. 1 - Longitudinal section size and reinforcement (unit: mm)

In order to study the influence of embedded materials of prestressed steel wire ropes on the performance of strengthened girders, a control girder without reinforcement is set up. The reinforced girders are divided into two parts, one part is the prestressing steel wire rope reinforced girder, 4 pieces in total. The other part is polyurethane cement prestressed steel wire ropes reinforced girders, 7 pieces in total, with specific parameters and girder numbers as shown in Table 1.

Tab. 1 - Reinforcement parameters of girders

Groups	Girder number	Number of wire ropes	Pre-stress (MPa)	Embedded materials	Material thickness (mm)	Anchorage?
Control girder	CB	-	-	-	-	No
prestressed steel wire ropes	A2	5	700	Mortar	20	Yes
prestressed steel wire ropes-polyurethane cement	A4	0	700	PUC	20	No
	A5	5	700	PUC	20	Yes
	A8	5	700	PUC	30	Yes
	A9	2	700	PUC	20	Yes
	A9-1	2	700	PUC	25	Yes

Test measurements

Strain gauges were set up on concrete, steel reinforcement, steel wire rope, polyurethane cement and composite mortar to measure the material strain in each part. Four strain gauges affixed to the two tensile main reinforcement bars, arranged in the loading point section and the span section, respectively. Each wire rope in the pure bending section of the loading area to arrange 1 specification of strain gauges, staggered arrangement of the strain gauges of each wire rope. Polyurethane cement material is arranged with 4 strain gauges, 2 strain gauges are arranged at the bottom of the girders. The strain gauges of the composite mortar were arranged in the same form as the polyurethane cement, and the specific strain measurement arrangement positions are shown in Figure 2 and Figure 3.

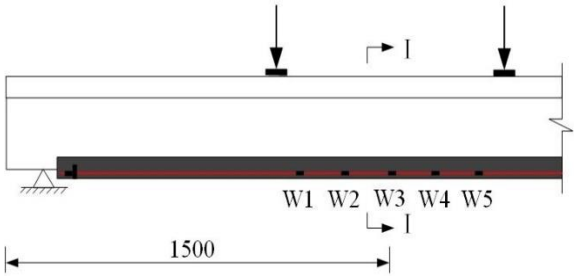

Fig.2 - Longitudinal arrangement of strain gauges in steel wire ropes

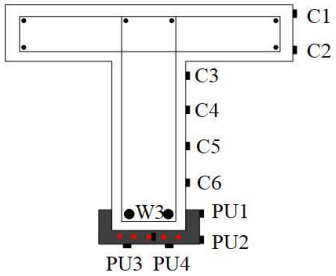

Fig.3 - Strain gauges of steel wire ropes arrangement (cross section)

Test results and analysis

Load-deflection curves of girders are shown in Figure 4. The reinforced girders first exhibit a linear elastic phenomenon like that of the unreinforced girders, but with a higher initial stiffness. When the load reaches 150 kN, the slope of the curve starts to decrease and the wire rope starts to reach the nominal yield strength. Despite the decrease in slope, the stiffness still maintains a high level. Compared with the A2 girder reinforced with cement mortar prestressed steel wire rope, the A5 girder has higher load carrying capacity and overall stiffness. Girder A4 is a polyurethane cement reinforced girder, and there is no prestressing steel wire rope in the polyurethane cement. Girder A4 has greater initial stiffness than the control girder, but slightly less stiffness than girder A5.

The load-deflection curves of girders A5, A8, A9 and A9-1 are shown in Figure 5. Both A9 and A9-1 girders have 2 prestressing steel wires. Both A5 and A8 girders have 5 prestressing steel wires. These two control groups differ only in the thickness of the polyurethane cement material. Compared with A5 and A9 girders with 20mm thickness polyurethane cement, A8 and A9-1 girders have higher structural stiffness. The thickened polyurethane cement material also has a more significant effect on limiting cracks during loading, reducing the formation and expansion of cracks and increasing the overall stiffness of the girder. In addition, the deflections of girder A9-1 and A8 were reduced compared with those of girder A9 and A5, respectively. Due to the different number of wire ropes, but the reduction was not significant.

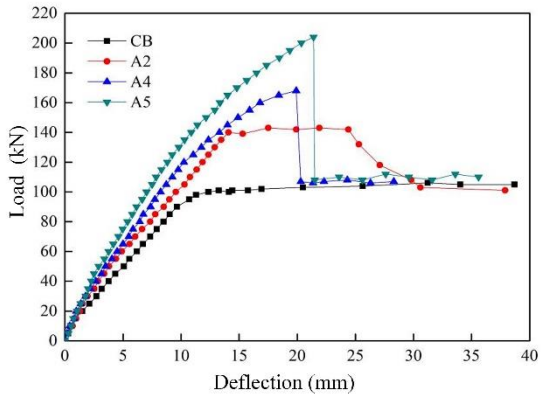

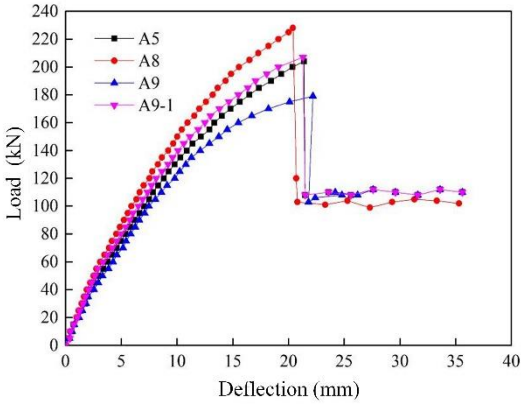

Fig.4 -Different load-deflection curves *Fig.5 – Different load-deflection curves*

When girder A5 reaches a yield load of 120 kN, the net strain increases in the wire rope after subtracting the initial tension strain is 2155 με. Under this load, the net increase of the

wire rope of girder A2 has risen to 2804 με, which can indicate that the polyurethane cement material embedded in the prestressed wire rope can delay the yielding of the girder reinforcement and effectively increase the load carrying capacity of the main girder when the wire rope strains of both types of girders reach the same level.

The A9 and A9-1 girder reinforcement, wire rope and polyurethane cement material strains are shown in Figure 9. Both reinforcement girders are arranged with 2 prestressing steel ropes, and the A9 and A9-1 girders are embedded in 20 mm and 25 mm polyurethane cement materials respectively. From the graphs, it can be seen that the load-strain curves of the reinforcement, wire ropes and polyurethane cement materials in the two girders have similar trends. Since the thickness of the steel wire rope embedded in the polyurethane cement material in girder A9-1 is 5 mm greater than that of A9, the strain on the steel reinforcement, steel wire rope and polyurethane cement in girder A9-1 is smaller than that of girder A9 under the same load. As the wire rope enters the nominal yield state, the tensile strain difference between the two girders of polyurethane cement material under the same load becomes progressively larger, due to the steel bars entering the yield state, when the prestressing wire rope in the girder is also approaching the nominal yield strength.

Tab. 2 - Cracking load, yield load and ultimate load

Groups	Girder number	Cracking strength (kN)	Increase proportion (%)	Yield strength (kN)	Increase proportion (%)	Ultimate strength (kN)	Increase proportion (%)
Control girder	CB	20.0	-	74.3	-	101.0	-
Prestressed wire ropes	A2	40.0	100.0	96.7	30.1	141.3	39.9
Polyurethane cement-prestressed wire ropes	A4	25.0	25.0	98.8	33.0	168.7	67.0
	A5	45.0	125.0	120.0	61.5	204.3	102.3
	A8	55.0	175.0	137.0	84.4	228.5	126.2
	A9	30.0	50.0	110.3	48.5	179.0	77.2
	A9-1	35.0	75.0	130.2	75.2	207.8	105.7

FINITE ELEMENT SIMULATION ANALYSIS OF FLEXURAL REINFORCEMENT

Model parameter selection

(1) Concrete stress-strain curve

The ABAQUS plastic damage model can simulate the stiffness recovery, damage, crack development and closure behavior of concrete structural members under reciprocal loading[16]. The plastic damage model is chosen for modeling the flexural test of polyurethane cement-prestressed steel wire ropes. The plastic damage model is modeled using the yield strengthening criterion and the flow law, which are used to calibrate the parameters in the model.

In order to make the model simulation results closer to the actual situation, the concrete uniaxial stress-strain relationship and loading stress paths need to be provided. The concrete intrinsic structure relationship given by the code[17] was used as the stress-strain relationship. The material elasticity modulus E and the elastic stress are σ_{t0} (σc_0) used to determine the stress-strain relationship in the elastic phase of the material, and the material stress-strain

relationship provided by the code is used to determine the relationship in the inelastic phase. Then the expressions are respectively:

Under tension:

$$y=\frac{x}{\alpha_t(x-1)^{1.7}+x} \quad x>1 \tag{3-1}$$

In the formula: $x=\varepsilon/\varepsilon_t$, $y=\sigma/f_t$, α_t are the parameters of the falling section of the uniaxial tensile stress-strain curve.

Under pressure:

$$\begin{cases} y=\alpha_a x+(3-2\alpha_a)x^2+(\alpha_a-2)x^3 & x\leqslant 1 \\ y=\dfrac{x}{\alpha_t(x-1)^2+x} & x>1 \end{cases} \tag{3-2}$$

In the formula: $x=\varepsilon/\varepsilon_t$, $y=\sigma/f_t$, α_a and α_t are the parameters of the rising and falling phases of the uniaxial compressive intrinsic relationship curve, respectively.

(2) Damage factors

Concrete research scholars have used the following methods to calculate the damage factor of the material [18-20], and the results obtained are also relatively good, so the damage factor is calculated in this paper according to the equation in the literature [18]. The damage factors in the literature [18] for uniaxial compression and tension are calculated as:

$$d_c=\begin{cases} 1-\sqrt{k_c\left[\alpha_a+(3-2\alpha_a)x+(\alpha_a-2)x^2\right]} & x\leqslant 1 \\ 1-\dfrac{\sqrt{1-k_t(1.2-0.2x^5)}}{\alpha_d(x-1)^2+x} & x>1 \end{cases} \tag{3-3}$$

$$d_t=\begin{cases} 1-\sqrt{1-k_t(1.2-0.2x^5)} & x\leqslant 1 \\ 1-\dfrac{1}{\alpha_t(x-1)^{1.7}+x} & x>1 \end{cases} \tag{3-4}$$

In the formula: $k_c=f_c/(\varepsilon_c E_0)$, $k_t=f_t/(\varepsilon_t E_0)$

(3) The rest of the parameters

The selection of parameters in the model affects the convergence of the calculated results. In this paper, the coefficient of viscosity of concrete material is taken as 0.001 and the expansion angle φ is taken as 35°. The plastic damage parameters of C40 concrete are shown in Table 3.

Tab.3: The plastic damage parameters of C40 concrete

ε	φ	σ_{b0}/σ_{c0}	μ	K_c
0.100	35.000	1.160	0.001	0.667

Intrinsic relationship between reinforcement, wire ropes, and polyurethane cement materials:

In the finite element analysis of flexural reinforcement, in order to make the model both simple and better simulate the reinforcing effect of the reinforcement, only the stress-strain relationship of the reinforcement in the monotonic loading mode is considered in the model building process. At this time, the reinforcement principal model curve includes elastic section, yield section, and hardening phase. The elastic-plastic hardening model is used in Figure 8, where the bond slip between the reinforcement and concrete is not considered in the model. The stress-strain curves of the wire rope material and the polyurethane cement material were

measured using the actual curves of this test with reference to the literature[21-23], and the test results are shown in Figure 9 and Figure 10.

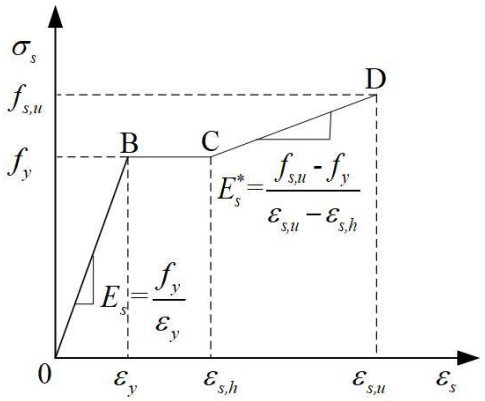

Fig. 8 - Steel Bar Stress - Strain Curves (Elastic-plastic reinforcement model)

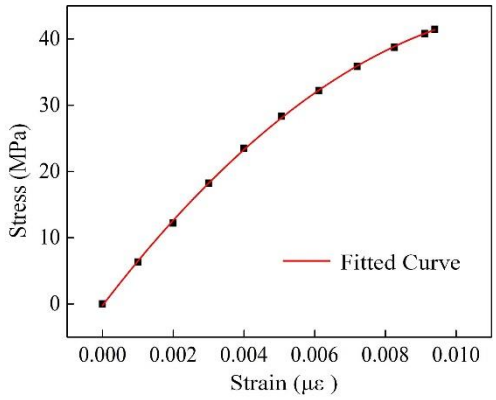

Fig.9 - Fitting curve of strain-stress (PUC)

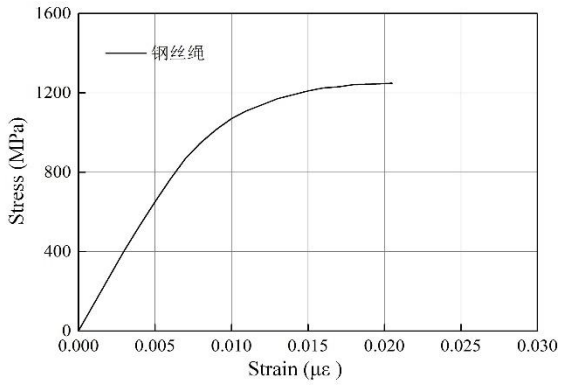

Fig.10 - Wire Ropes Stress-strain Curves

Finite element simulation of reinforced concrete girder flexural resistance

The finite element model in this section is used to compare the test girder CB girder and to verify the effect of numerical simulation. The finite element units are selected as follows:

Solid units are selected for concrete, bearing plates; Wire units are selected for main reinforcement and hoop bars.

Poisson's ratio: concrete: 0.2, bearing plates: 0.25.

In the model, the concrete and bearing plates are connected with Tie, and the main reinforcement and rectangular hoop reinforcement in the concrete are embedded in Embedded region. Constraints are added to the centerline of the mat, with vertical constraints applied at one end and horizontal and vertical constraints at the other end, to simulate the simply supported girder boundary conditions. The cell mesh size is 20 mm × 20 mm × 20 mm, and the mesh of the unreinforced girder is divided as shown in Figure 11. The model does not consider the bond slip between the reinforcement and concrete.

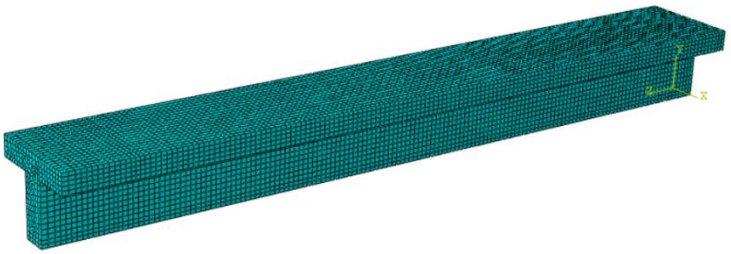

Fig.11 - Finite element model of the T girder

In the following, we will use “FEM-CB” to represent the finite element model and “EXP-CB” to replace the actual model, and the calculation results are as follows:

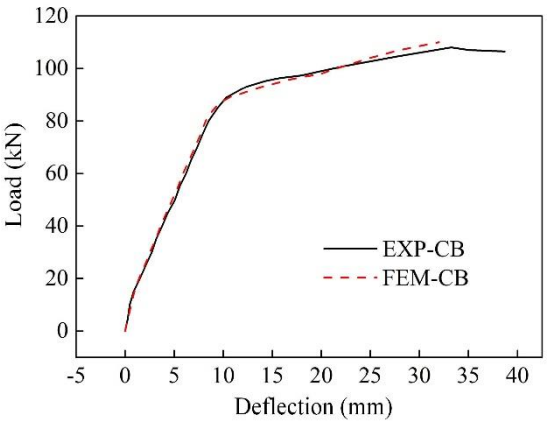

Fig.12 - Load-deflection curve

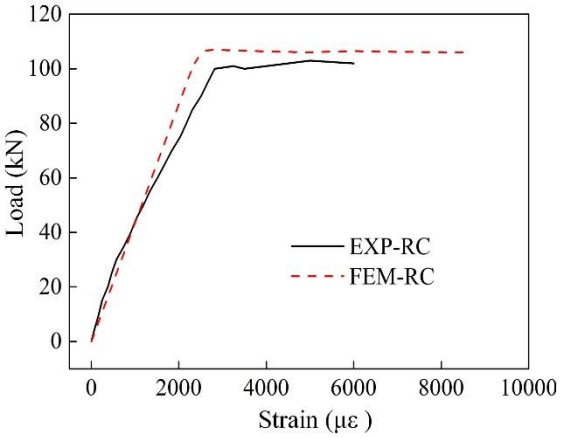

Fig.13 - Load-steel strain curve

Tab. 4 - Calculated value of Abaqus and test value comparison

Specimens number	Yield strength/kN	Yield deflection/mm	Ultimate strength/kN
EXP-CB (CB)	78	8.2	106
FEM-CB	80	8.0	108
Error	0.026	-0.024	0.019

As seen from the test curve in Figure 12 and the data in Table 4: the calculated result of Abaqus program is similar to the test result. When the longitudinal reinforcement in the span section yields, the deflection of the girder increases rapidly and the width of the crack expands continuously. The area of the concrete compressed zone gradually decreases with the extension of the crack, but the compressive stress undergone keeps increasing, and the calculation is terminated when the girder deflection exceeds the test deflection. From the data in Table 4 of the test curve: it can be seen that the error of the yielding load is only 2.6% for

the FEM simulated values compared with the test values; Deflection error at the yield point of only 2.4%; The error for the ultimate load is only 1.9%.

Figure 13 shows the comparative load-strain curves of EXP-RC girder and FEM-RC. From the figure, it can be seen that the calculated curve of ABAQUS program and the test curve basically match. Compared with the experimental curves, there are some differences between the ABAQUS simulation curves and the experimental test curves. The main difference is that there is a certain difference between the intrinsic structure relationship of the bars entered in the model and the actual curve relationship of the bars, and the curve relationship obtained from the test is the test result of one bar. The values of the reinforcement entered is the average of the test results of the two bars. The actual test result curve is short, which is caused by the failure or breakage of the strain gauge during the actual loading process.

Comparative finite element analysis of flexural reinforced girders

The finite element model of the prestressed wire rope polyurethane cement reinforced girder was established based on the test data of the reinforced T-girder in the previous section and numerical analysis was performed. The reinforced wire rope diameter is 4 mm, and the unit is selected as Wire, which is simplified according to the actual curve of stress-strain relationship. Finite element model of reinforced girder can be seen in Figure 14, and steel bars model are in Figure 15. Polyurethane cement material, Solid unit was selected and the stress-strain curve relationship was adopted from the measured axial tensile curve Figure 15. The initial tensile strength of the wire rope is achieved by the cooling method and is embedded in the polyurethane cement material by means of embedded. Tie is chosen for the contact between the polyurethane cement material and the concrete.

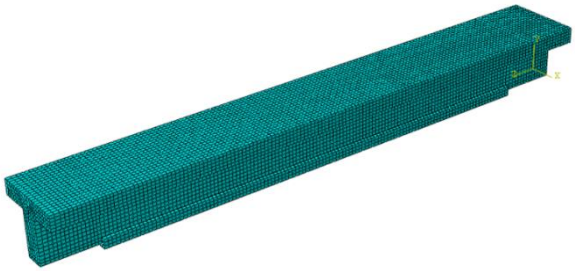

Fig.14 - Finite element model of reinforced girder

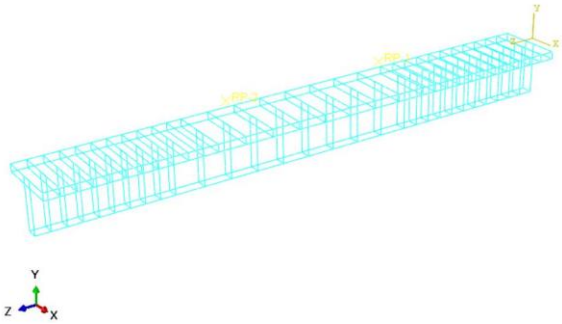

Fig.15 - Finite element model of reinforcement cage

Finite element calculation results of flexural strengthening test girder

Three girders A5, A8 and A9 with different thicknesses of polyurethane cement and different numbers of wire ropes were selected as representatives for finite element calculations of flexural strengthening test girders. The ABAQUS finite element simulation results and test results of reinforced girders A5, A8 and A9 are shown in Table 5 below. The errors of both results are within 5%.

Tab. 5 - Comparison table between simulated and experimental value (Strengthened girders)

Specimen number	Yield strenth (kN)	Yield deflection (mm)	Ultimate strenth (kN)	Fracture deflection of reinforcement layer (mm)
EXP-A5	120.0	8.82	204.3	21.4
FEM-A5	123.0	9.03	208.0	20.4
Error	2.5%	2.3%	1.8%	4.7%
EXP-A8	137.0	9.08	228.5	20.4
FEM-A8	142.0	9.26	235	21.0
Error	3.6%	2.0%	2.8%	3.9%
EXP-A9	110.3	7.48	179.0	22.2
FEM-A9	107.2	7.81	175.3	21.6
Error	-2.8%	4.4%	2.1%	-2.7%

The finite element calculation clouds of specimen A5 are shown in Figure 16 ~ Figure 19.

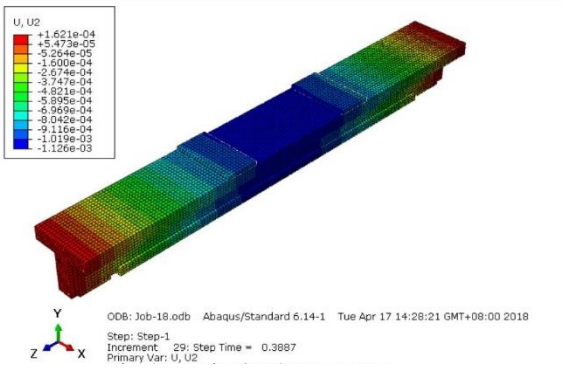

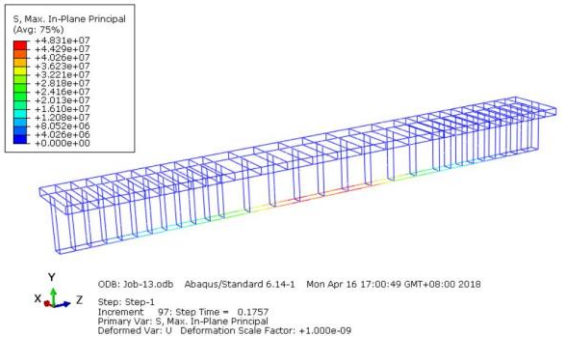

Fig.16 -Displacement cloud diagram of A5 Fig.17 - Reinforcement stress cloud diagram of A5

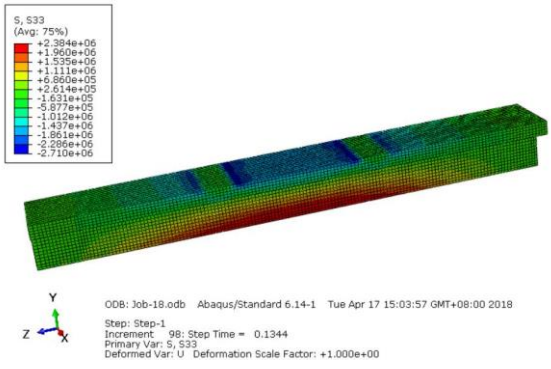

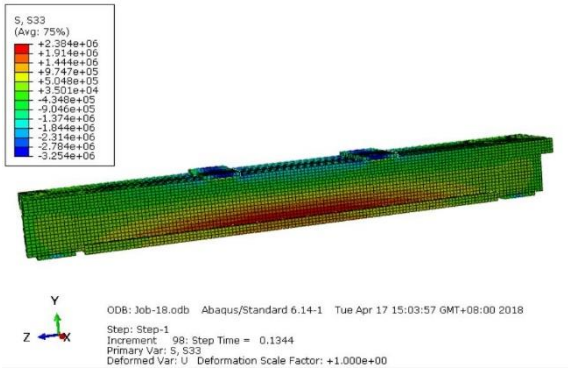

Fig.18 - Concrete stress cloud diagram of A5 *Fig.19 - PUC stress cloud diagram of A5*

As shown in Figure 20, the finite element calculation curve of specimen A5 is compared with the test curve. The finite element calculation curves formed by the member deflection, PUC strain, steel strain and concrete compression strain similar to the experimental test result.

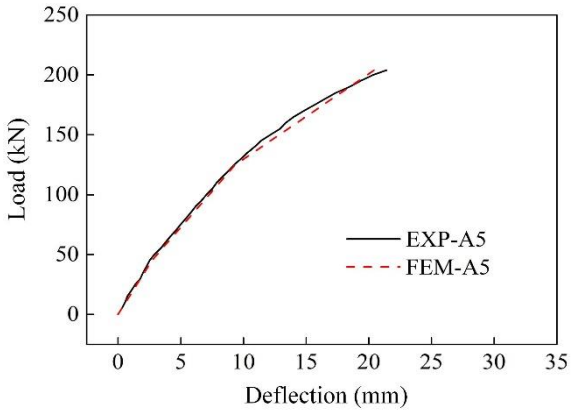

(a) Load and deflection curve

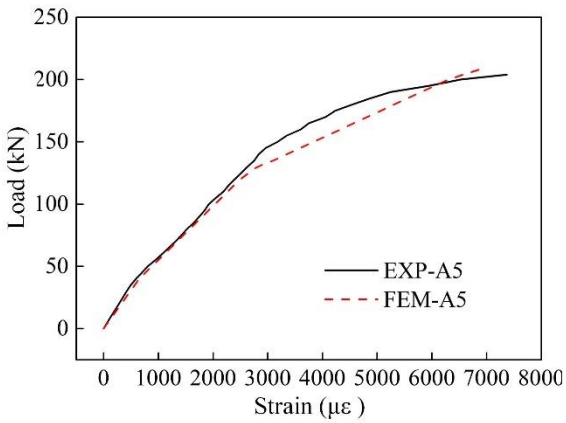

(b) Load and PUC strain curve

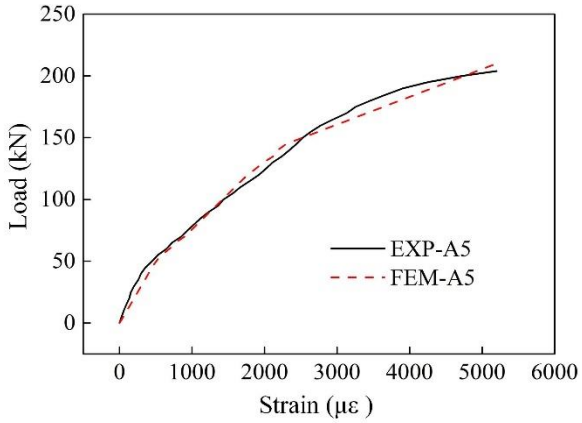

(c) Load and strain curve (steel bar)

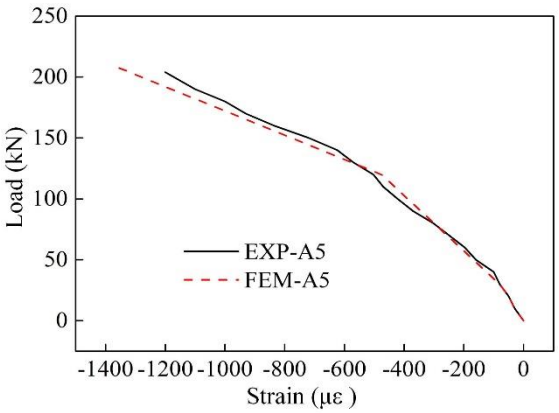

(d) Load and concrete strain curve

Fig.20 - Simulation results of Abaqus and test results (specimen A5)

Based on the simulation analysis of the form of reinforcement with 5 wire ropes embedded in 20mm thick polyurethane cement, finite element simulation analysis was conducted for reinforced girder A8 with different thickness of polyurethane cement and reinforced girder A9 with different number of pre-stressed wire ropes. Finite element simulation curves and test curves were plotted. The finite element calculation curves of specimens A8 and A9 are compared with the test curves in Figure 21 and Figure 22. The load-deflection curve, load-bottom PUC strain curve, load-tension zone reinforcement strain curve, and load-compression zone concrete strain curve in the span calculated by the finite element are similar to the test results. It shows that the calculation model can better reflect the force process of the member. Throughout the loading process, especially after yielding of the reinforcement, the load carrying capacity of the member is increased to a large extent due to the presence of the polyurethane cement material. The calculation results are convincing and can be used to supplement the reinforcement test and the in-depth study of the reinforcement test girder.

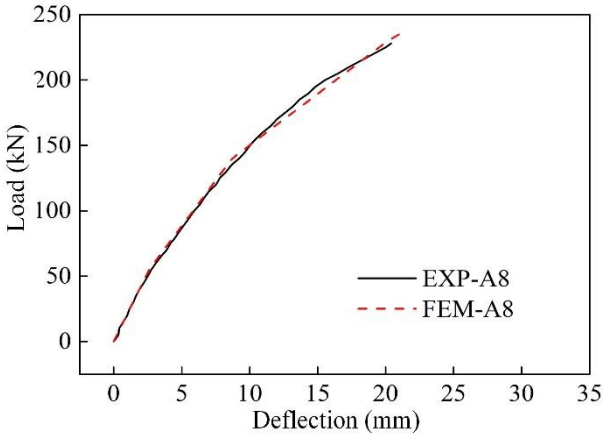

(a) Load and deflection curve

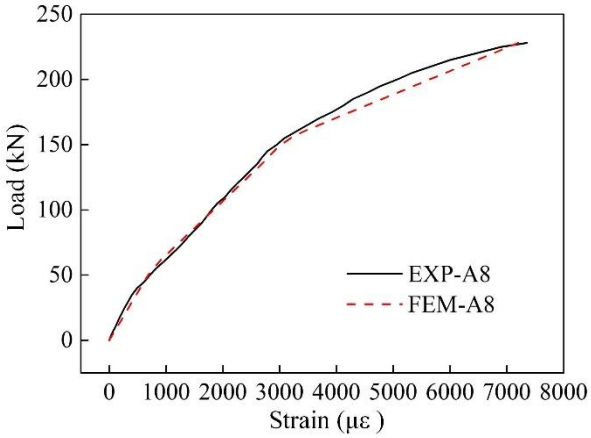

(b) Load and strain curve (PUC)

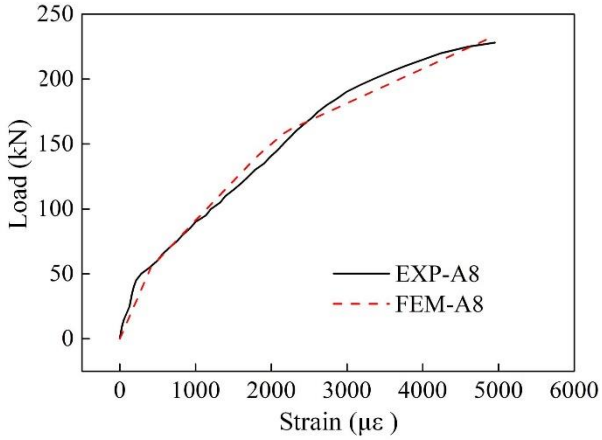

(c) Load and strain curve (steel bar)

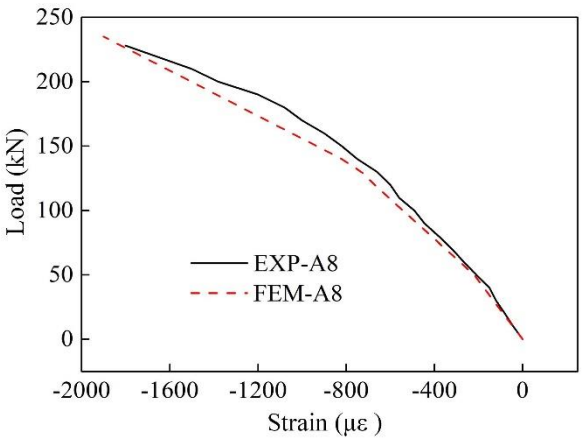

(d) Load and compressive strain curve (concrete)

Fig.21 - Simulation results of Abaqus and test results (specimen A8)

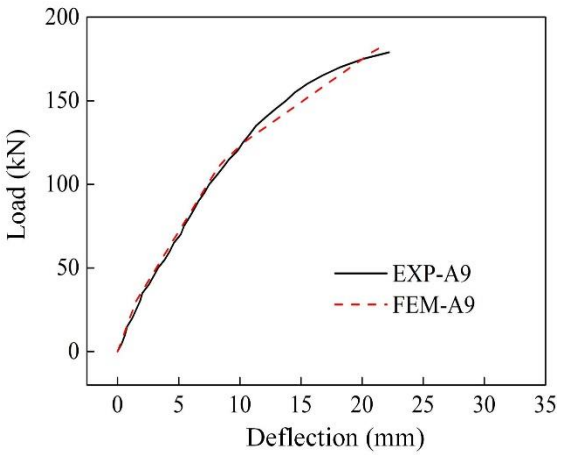

(a) Load and deflection curve

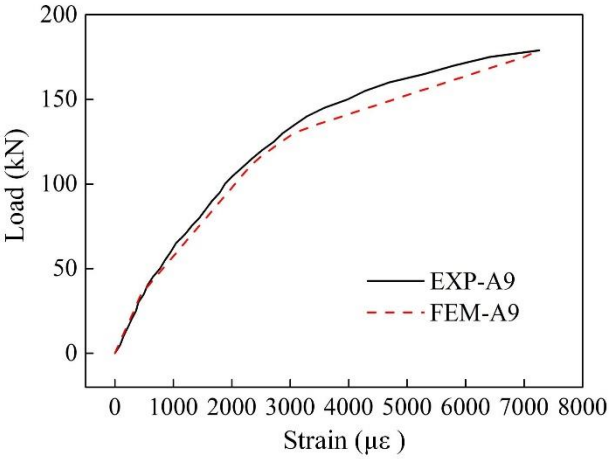

(b) Load and strain curve (PUC)

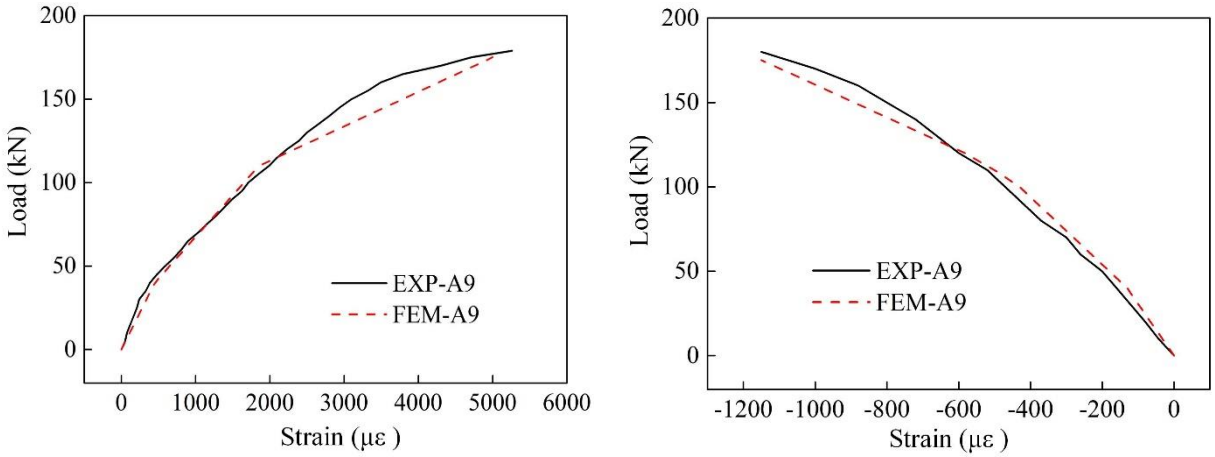

(c) Load and strain curve (steel bar) (d) Load and compressive strain curve (concrete)
Fig.22 - Simulation results of Abaqus and test results (specimen A9)

Effect of concrete strength on reinforcement performance

The concrete strengths were 30 MPa, 40 MPa and 50 MPa respectively. The strengthening girders were identical to those of the test girders, with a reinforcement rate of 0.91%. The reinforcement layer was a 20 mm thick polyurethane cement material embedded with five prestressing steel ropes, and the loading method was symmetrical loading at two points. The calculation results of FEA are shown in Table 6.

Tab.6 - Calculation table of influence of concrete strength on flexural reinforcement

Specimen number	Yield strength (kN)	Yield deflection (mm)	Ultimate strength (kN)	Fracture deflection of reinforcement layer (mm)
FEM-C30	120.00	8.82	200.40	19.98
FEM-C40	123.00	9.03	208.00	20.40
FEM-C50	125.00	9.11	212.20	20.63

As can be seen from Table 6, the yield strength of reinforced girders increases slightly with the improvement of concrete strength. Taking C30 concrete members as a reference, the yield strength increases by 2.5% and 4.1% respectively, when the deflection values are also very close. The increase of yield strength was 3.79% and 5.89% for C30 concrete members as reference, the fracture deflection of the reinforcement layer of the members increased with the improvement of concrete strength of the reinforced members. The ultimate deflection of the members increased by 2.10% and 3.25% respectively.

The simulation results of concrete reinforced girders with different strengths are shown in Figure 23. The deflection trends of reinforced girders of different strengths are approximately the same. Similarly, the strain trends for steel and polyurethane cement are essentially the same, with the material curves almost coinciding for reinforced girders of different strengths, but with a slight increase in the maximum strain of the material at damage as the strength

increases. When damage to the reinforcement layer occurs, the reinforced girder with the highest concrete strength has the highest load-bearing capacity.

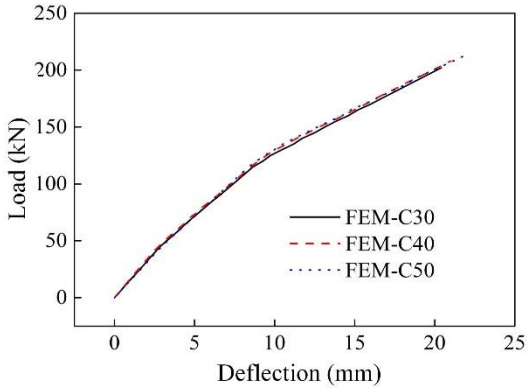

(a) Load and deflection curve

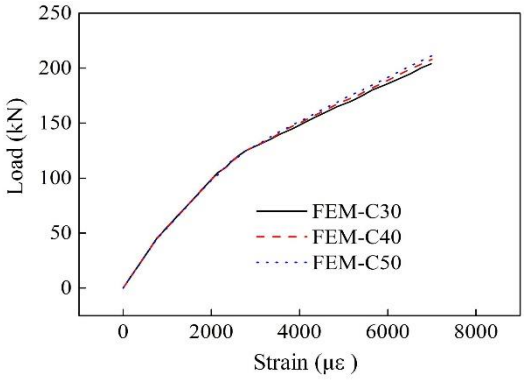

(b) Load and PUC strain curve

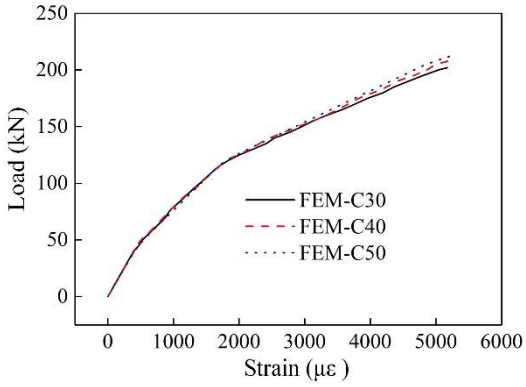

(c) Load and reinforcement strain curve

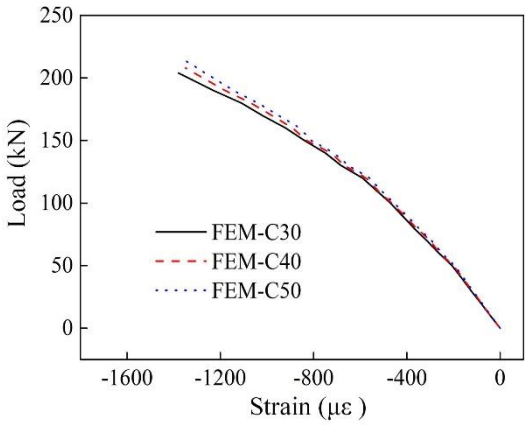

(d) Load and concrete compressive strain curve

Fig.23 - Simulation results of Abaqus (Specimens of different concrete strength)

Effect of original girder reinforcement rate on reinforcement performance

In order to study the effect of reinforcement rate of main reinforcement on the performance of reinforced girders, the reinforcement rates in the model were taken as 0.91%, 1.82% and 2.73%, respectively. The concrete strength is adopted according to the values of flexural reinforcement tests in Chapter 3, and the reinforcement layer is 5 prestressing steel ropes embedded in 20 mm thickness of polyurethane cement material, loaded symmetrically at two points in the span. The finite element calculation results are shown in Table 7.

Tab. 7 - Calculation table of influence of reinforcement ratio on flexural reinforcement

Specimen number	Yield strength (kN)	Yield deflection (mm)	Ultimate strength (kN)	Fracture deflection of reinforcement layer (mm)
FEM-0.91	123	208	9.03	20.4
FEM-1.35	159.7	249.3	10.22	20.2
FEM-1.82	204	299.2	9.39	20.53

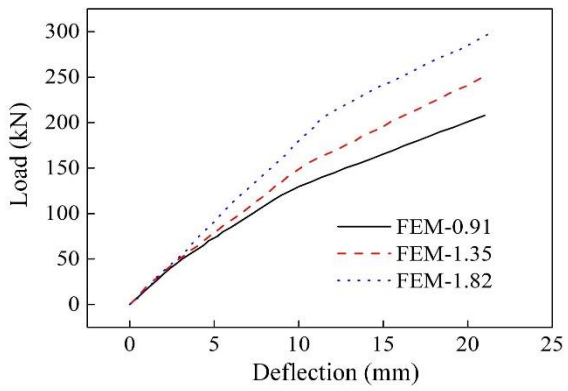

(a) Load and deflection curve

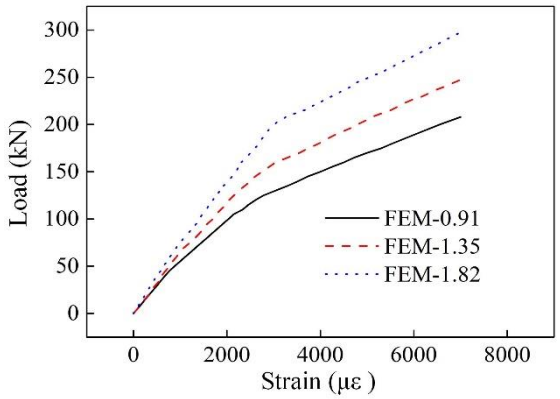

(b) Load and PUC strain curve

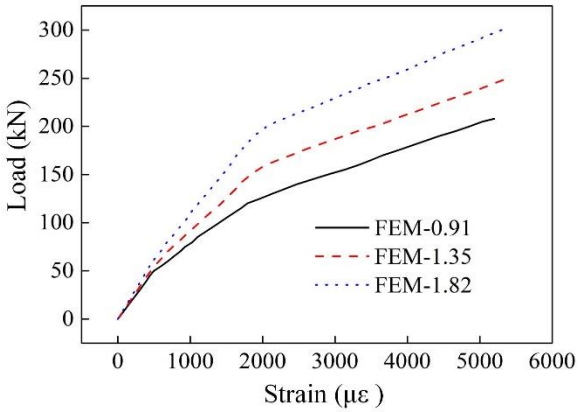

(c) Load and reinforcement strain curve

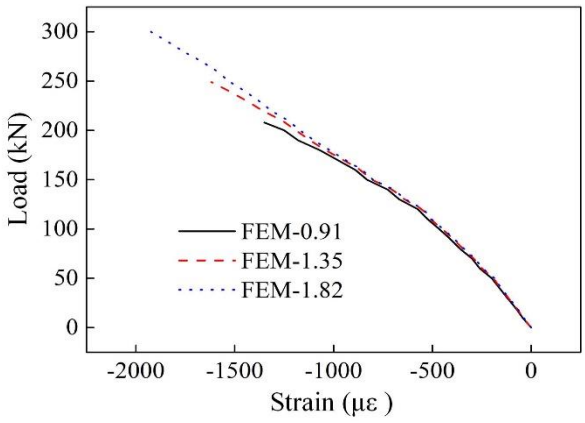

(d) Load and concrete compressive strain curve

Fig.24 - Simulation results of Abaqus (Specimens of different reinforcement ratio)

From Table 7, it can be seen that the load carrying capacity of reinforced girders varies significantly with the increase in the reinforcement rate of longitudinal bars, and the yield loads of girders with reinforcement rate of 1.82% and 1.35% increase by 29.84% and 65.85%, respectively, compared to girders with reinforcement rate of 0.91%, and the yield deflections of girders with reinforcement rate of 1.82% and 1.35% increase by 13.18% and 3.99%, respectively. The ultimate bearing capacity of the girders at reinforcement layer fracture damage increased by 19.86% and 43.85% with the increase of reinforcement rate, and the

ultimate deflection did not change much with the increase of reinforcement rate, which were -0.98% and 0.64%, respectively.

The finite element calculation results of the reinforced girder with different reinforcement rates are shown in Figure 24. As the reinforcement rate increases the concrete strain of the member increases, and the member with the most longitudinal reinforcement exhibits the greatest load-bearing capacity when the final damage occurs. The strain of polyurethane cement and steel reinforcement becomes larger with increasing reinforcement ratio and the load carrying capacity of the member increases.

4 CONCLUSION

In this paper, 7 T-girder specimens were studied in flexural tests. The effect of each design parameter on the reinforcement effect was elaborated through the experimental analysis of the flexural performance of polyurethane cement prestressed steel wire rope reinforced girders. Through the ABAQUS finite element program to· establish a model for numerical simulation, and the actual test for flexural parameters analysis compared to the following conclusions:

(1) Compared with prestressing steel wire rope reinforcement, polyurethane cement-prestressing steel wire rope reinforcement can effectively improve the yield strength and ultimate strength of the reinforced girder. Taking girder A5 (20 mm thick polyurethane cement) as an example, the yield load and ultimate load increased by 61.5% and 102.3% compared with CB control girder. While the yield load and ultimate load of girder A2 (20 mm thick cement mortar) increased by 30.1% and 39.9%, far less effective than the polyurethane cement prestressed steel wire rope reinforcement.

(2) A reasonable finite element model for flexural reinforcement of T-girder is established. The simulation results are similar to the test results. The finite element simulation results are in good agreement with the flexural reinforcement test, the ABAQUS program is calculated correctly, and the established finite element reinforcement model is reasonable.

(3) For different strengths of concrete, the yield load increases slightly as the concrete strength of the reinforced girder increases, but the value of yield deflection is close. Taking the C30 concrete members as reference, the yield strength increases by 3.79% and 5.89%, and the ultimate deflection and ultimate bearing capacity increase by the same trend of 2.10% and 3.25%, respectively.

(4) For T-girders with different reinforcement ratios, the bearing capacity of reinforced girders changes significantly with the increase of longitudinal reinforcement ratio. The yield loads of girders with reinforcement ratio of 1.82% and 1.35% increase by 29.84% and 65.85%, respectively, and the yield deflections increase by 13.18% and 3.99%, respectively, compared with those of girders with reinforcement ratio of 0.91%. The ultimate deflection does not change much with the increase of reinforcement rate, which is -0.98% and 0.64% respectively.

REFERENCES

[1] Zhou, Y. 2007. Practice and discuss of bridge disease measuring and punishing methods. Urban Roads Bridges & Flood Control.

[2] Liu, G. J. 2008. The analysis of T-girder bridge diseases and reinforcement technology. Shanxi Architecture.

[3] Ye, W., Ji, L., Highway, S. O., & University, C. 2014. Disease analysis and reinforcement method for a simply supported t-shaped girder bridge. Modern Transportation Technology.

[4] Wang, Y. M. 2012. Analysis of maintenance and reinforcement about bridge pier and abutment. Transportation Standardization.
[5] Fan, H. B. 2010. Inspection and maintenance & reinforcement of state-province artery bridge system. Enterprise Science and Technology & Development.
[6] Chen, W. C., & Jian-Qin, M. A. 2006. Discussion on main diseases of the prestressed continuous rigid-frame bridge and its maintenance and reinforcement mornitoring. Communications Standardization.
[7] Laane, A., & Lebet, J. P. 2005. Available rotation capacity of composite bridge plate girders under negative moment and shear. Journal of Constructional Steel Research, 61(3), 305-327.
[8] RA Parmelee, RB Corotis. 2004. Analytical and experimental evaluation of existing florida dot bridges. finite element method.
[9] Huang, S. N., Lu, X. Z., Zheng, J. C., & Zhu, W. 2012. Overload-induced progressive collapse simulation for a reinforced concrete arch bridge. Engineering Mechanics, 29(SUPPL. 2).
[10] Ghoneim, G. , & Ghali, A. . 2011. Nonlinear analysis of concrete structures. Canadian Journal of Civil Engineering, 9(3), 489-501.
[11] Dharaneepathy, M. V., & Anandavalli, N.. 2008. Nonlinear analysis of shock-loaded reinforced concrete structures. International Journal of Structural Stability & Dynamics, 4(02), 223-236.
[12] Cao, M. 2012. Research on damage plastic calculation method of abaqus concrete damaged plasticity model. Transportation Standardization.
[13] Yuan, M., Yuan, S., & Yan, D. H. 2008. Analysis on plastic damage of prestressed concrete box girder. Journal of Highway and Transportation Research and Development.
[14] Zhang, H. X., & Lu-Yuan, H. E. 2014. Numerical simulation analysis on bond-slip behavior of concrete strengthened with near-surface mounted cfrp bars based on abaqus. Engineering Mechanics.
[15] Chuan-Xue, X. U., & Liu, F. 2016. Analysis of the influence factors of long-term rigidity of girder by external prestressing. Jiangsu Construction.
[16] Zhang, Z., & iu, Y. 2011. Concrete damaged plasticity model in abaqus. Building Structure.
[17] China Academy of Building Research. 2016. GB50010-2010 Code for design of concrete structures. Beijing: China Architecture & Building Press.
[18] Cao, M. 2012. Research on damage plastic calculation method of abaqus concrete damaged plasticity model. Transportation Standardization.
[19] V Birtel , P Mark. 2006. Parameterised finite element modelling of RC girder shear failure.
[20] Yuan, M., Yuan, S., & Yan, D. H. Analysis on plastic damage of prestressed concrete box girder. Journal of Highway and Transportation Research and Development.
[21] Zhang, K., & Sun, Q. 2018. Experimental study of reinforced concrete t-girders strengthened with a composite of prestressed steel wire ropes embedded in polyurethane cement (PSWR-PUC). International Journal of Civil Engineering,Transaction A:Civil Engineering, 16(9), 1109-1123.
[22] Zhang, K., Qi, T., Zhu, Z., Xue, X., & Shen, X. 2021. Strengthening of a Reinforced Concrete Bridge with a Composite of Prestressed Steel Wire Ropes Embedded in Polyurethane Cement. Journal of Performance of Constructed Facilities, 35(5), 04021063.
[23] Zhang, K., & Sun, Q. 2019. Bending Fatigue Properities Research of Polyurethane Cement (PUC). Civil Engineering Journal, (2).

CIVIL ENGINEERING JOURNAL

Article no. 70

THE CIVIL ENGINEERING JOURNAL 4-2021

THE ROLE OF TECHNICAL AND NATURAL SCIENCES IN STONE MONUMENTS CARE

Katerina Kovarova[1] and Eva Matouskova[2]

1. *Czech Technical University, Faculty of Civil Engineering, Department of Geotechnics, Prague, Thákurova 7, Czech Republic; katerina.kovarova@fsv.cvut.cz*
2. *Czech Technical University, Faculty of Civil Engineering, Department of Geomatics, Prague, Thákurova 7, Czech Republic; eva.matouskova@fsv.cvut.cz*

ABSTRACT

Stone monuments maintenance requires the systematic approach which should be based on the cooperation among specialists through more branches, especially from humanities, natural and technical sciences. The main aim of this article is to present the benefit of the cooperation among geologists and civil engineers and share preliminary results of the Czech Ministry of Culture project DG20P02OVV021 “Stone surface topography and its application in stone element restoration field”. Historic stone surfaces often contain stonemasons tool traces as an undoubtable part of historical monument value. The study and protection of the testimony of past is therefore very important. As a part of our project, we are conducting field and laboratory research of historic stone surfaces bearing the original tool traces. The studied area is the Prague urban conservation zone for its stone monuments richness from Romanesque to present days. First, the geological research of the stone masonry surface is conducted in the cooperation with archaeologists. The tool traces are documented, and the state of stone is described. Because of the negative influence of weathering processes on the stone durability, respectively tool traces, we decided to monitor the chosen historical stone surface using the hyperspectral analysis. Based on the analysis of the results we will be able to better understand the behaviour of stone surface and traces on it during the time.

KEYWORDS

Stone monuments, Tool traces, Weathering, Hyperspectral analysis, Prague

INTRODUCTION

A value of historical stone monument consists of many variables, including the traces of craftsmanship processing which should be taken into the attention during the conservation and restoration interventions. Stonemasons work traces are an integral part of the monument expression. Moreover, these traces help reveal working practices of old masters and the craft development over time. The above reasons explain the importance of studying and preserving traces of tools on the surfaces of historical buildings. The presented article is an extract of studies that systematically map the cutting work of stones in the territory of Prague from Romanesque time to the present day. Our work is based on a documentation and assessment of stone craftsman processing traces of historical buildings in the Prague urban conservation zone.

Stone monuments maintenance requires the systematic approach which should be based on the cooperation among specialist through more branches, especially from humanities, natural and technical sciences. Therefore, the main aim of this article is to present the benefit of the cooperation among geologists and civil engineers. If we talk about stone masonry maintenance and survey, first the building stone characterisation, including petrographic analysis and evaluation of degradation

degree thanks to the weathering action, is necessary. Therefore, the involvement of an geologists is a logical and undoubtable step in a masonry survey.

The Prague urban conservation zone is rich for the monuments from natural stone. The use of natural stone was influenced by its resources and transport possibilities and technical development of its quarrying and processing. The sedimentary stones were widely used as a dimension stone of many monuments from Romanesque time to Baroque, whereas the magmatic stones, especially granites, have been used for these purposes in the architecture since 2nd half of 19th century. The main building stone of Romanesque time was predominantly opoka. Sandstones were mainly used as the dimension stone since Gothic period until the granitic stones were used instead. Another sedimentary stones, especially limestones, occurred in the Prague architecture in Gothic period, but its massive use together with marbles was mainly in Baroque. Due to a high demand for marble in this period, its resources were not sufficient and therefore artificial marble was widely used [1].

As any other building material, stones undergo to weathering processes and so are damaged. They lose their original qualitative properties, such as uniaxial compressive strength and durability. The presence of water in liquid state with dissolved chemical compounds is the most important factor controlling the durability of natural stone. For example, the ice and salt crystallization may cause the pressures from tens to hundreds MPa [2], what usually exceeds tensile strength of most stones. The relationship between frost and salt weathering is discussed by e.g., Williams and Robinson [3]. The damage rate depends on the salt combination applied in the salt weathering process. Crystallizing salts in stone pore space create a set of several processes acting together. Physical processes play the most important part [2], which may be accompanied with chemical processes and action of organisms [4]. This process may cause surface crumbling or delamination [2] and the tool traces are therefore damaged as well (see Figure 1).

Fig. 1 – Blistering of sandstone surface with the subsequent surface scaling with strongly damaged tool traces, St. Jacob's Church, Srbeč.

The clastic sedimentary stones are the most sensitive to weathering agents from the wide range of used building stone. The reason is the arrangement of its internal structure, especially the

abundant presence of interconnected pores. The way of their origin determines the character of their internal structure. The presence of water may also cause dissolution and leaching of binder and thus negatively influence the cohesion. To be able to better understand the behaviour of stone surface and traces on it during the time, we decided to monitor the chosen historical stone surface using the hyperspectral analysis.

Hyperspectral imaging

Hyperspectral imaging has been an area of active research and development in many different fields during past decades and its giant potential is getting more visible with technical development. Recently hyperspectral imaging data have started to be widely used among the public in a wide variety of applications. Different names were given to this field of study like hyperspectral imaging, imaging spectrometry, or imaging spectroscopy, but the output is similar – derive the set material's reflectance spectra in a given range. Unlike the multispectral sensor which operates in a relatively low number of wide spectral bands hyperspectral scanners give full information across the electromagnetic spectrum in given spectral range. This is done by collecting many (tens to hundreds) narrow, closely spaced spectral bands so that the resulting spectra appear to be continuous curves. Using these data one can enable the extraction of reflectance spectra at a pixel scale that can be directly compared with similar spectra measured in the field or in a laboratory. Although most hyperspectral sensors measure hundreds of wavelengths, it is not the number of measured wavelengths that define a sensor to be hyperspectral. It is rather the narrowness and contiguous nature of the measurements.

Soil weathering and alteration can be determined by various factors, where one can mention wind, sunlight and temperature as well as rain, snow, moisture and biological contamination. The first affects the stability of the rock matrix, while the second acts through chemical corrosion of the stone forming material. As we mentioned above, physical, chemical and biological agents act in co-association to deteriorate a stone [5]. Biodeterioration is a situation when biological material settles on a construction stone(s) of a structure and evolves there. In this case, we often deal with algae, bacteria, moss, lichens and fungi. This work is an example of how a stone affected by biodeterioration can be hyperspectraly analysed.

Biological contamination is very common in sandstone and it is often created by a layer of algae together with dust particles, soot, fungi fibres and bacteria. This coating creates a slime on its lower part that contain small stone particles. During frost circles and with changing water to ice stone particles that are covered by algae are crumbled. The crust prevents the stone from "breathing", plugs plasters pores and contributes to the disintegration of the masonry surface. Expansivity of such crust in its drying out and damping is different than the expansivity of material. Similar crumbling can be seen when cyanobacterium growth is visible [6]. Biological contamination of stone - its development, minimization and treatment methods are investigated by various authors worldwide, for more information see [7-14].

METHODS AND PROCEDURES

For the purpose of the survey a hyperspectral monitoring of processed stone surface was conducted which is negatively influenced by weathering action. We chose the stone block of the Křížovnické náměstí retaining masonry (Figure 2) which is dated back to 1848 [15]. Generally, this ashlar masonry is predominantly built form fine to middle grained sandstone which shows more or less surface degradation signs. The chosen stone block is of sufficient size and contains more degradation manifestations like presence of organisms (e.g. moss and lichen), signs of water freezing/thawing and also salt weathering action, as it is obvious in Figure 4. Moreover, the selection of this stone block is also very useful for studying and understanding a weathering processes synergy, which do not occur separately, but often together. Additionally, the studied stone block is

conveniently located near the Vltava River in the immediate vicinity of Charles Bridge and it is therefore influenced by its seasonal fluctuation.

Fig. 2 – The location of a selected sandstone block in Křížovnické náměstí retaining masonry.

Hyperspectral analysis

For the purpose of hyperspectral analysis, a unique portable hyperspectral imaging device consisting of a hyperspectral sensor, Pan&Tilt unit, tripod, illumination sources and a control unit was used. An A-series hyperspectral VNIR camera Hyperspec VNIR manufactured by Headwall Photonics Inc. [16] is used. Headwall Photonics' Hyperspec imaging spectrometer platform is built on a reflective concentric, f/2 optical design. The camera is lens-based, thus equipped with a C-Mount 35mm objective and 18mm long and 25/60um wide slit. The operational wavelength ranges between 400 to 1000 nm and the focal plane size is 1004 spatial and 810 spectral bands in this range. The setup (hyperspectral camera, Pan&Tilt unit and the illumination platform) has been placed on a strong tripod Callidus CINE 2000 to enable one to move the system and adjust the height of the camera. Special tripod head had to be created for the Pan&Tilt unit fitting. Control of the system is performed by the HDPU (Hyperspec Data Processing Unit) and using Hyperspec III. software developed by Headwall Photonics, Inc. Hyperspectral imaging data are commonly given in the form of a 3D data cube. The 3D data cube information resembles the reflectance spectrometer data – wavelength and a corresponding signal value. From this dataset, user can derive a spectral curve or to analyse and work with each band separately.

Data gaining and processing

In the second phase of the Czech Ministry of Culture project DG20P02OVV021 “Stone surface topography and its application in stone element restoration field” a historical sandstone sample was spectrally analysed in-situ to determine its biological contamination. For the specific object of interest temporal analysis is conducted. This paper shows preliminary results comparing summer (August 2021) and autumn (November 2021) results. The scanning distance of 2m (see Figure 3) ensures that the object of interest (Figure 4) is scanned in one file and gives a pixel size of approximately 4mm. Each dataset was collected with Zenith reflectance targets to ensure quality calibration and repeatability. ENVI 5.5 software was used for preprocessing and analysing the data.

Fig. 3 – Measuring setup.

Fig. 4 – Area of interest photograph.

Gained data has to be registered, resized and recomputed in order to compare results from various times. To monitor biological contamination of stone Normalized Difference Vegetation Index (NDVI) [17] was used to show the difference between summer and autumn vegetation over. NDVI is one of the oldest, most well-known, and most frequently used vegetation index. The combination of its normalized difference formulation and use of the highest absorption and reflectance regions of chlorophyll make it robust over a wide range of conditions. It can, however, saturate in dense vegetation conditions when leaf area index (LAI) becomes high. LAI is calculated as half the area of all leaves per unit area of ground. NDVI is defined by the equation:

$$NDVI = (NIR-RED) / (NIR+RED)$$

The value of this index ranges from -1 to 1. The common range for green vegetation is 0.2 to 0.8, the denser the vegetation the higher NDVI value. NDVI is one of the broadband greenness vegetation indeces included into the ENVI 5.5. software. These VIs are designed to provide a measure of the overall amount and quality of photosynthetic material in vegetation, which is essential

for understanding the state of vegetation for any purpose. Broadband greenness VIs compares reflectance measurements from the reflectance peak of vegetation in the near-infrared range to another measurement taken in the red range, where chlorophyll absorbs photons to store into energy through photosynthesis. Use of the near-infrared measurements, with much greater penetration depth through the canopy than red, allows sounding of the total amount of green vegetation in the column until the signal saturates at very high levels [18]. NDVI values are explained in Table 1.

Tab. 1 - NDVI value explanation table.

NDVI	INTERPRETATION	COLOR
-1,0 – 0,0	Bare rock	Red
0,0 - 0,2	Bare rock / almost absent density	Sienna
0,2 - 0,4	Low density	Yellow
0,4 - 0,6	Medium density	Dark green
0,6 - 0,8	High density	Green1
0,8 - 1,0	Very high density	Green2

RESULTS

Figures 5 and 7 show graphs with NDVI values and corresponding values with a scale step of 0,2. The first class (shown in red colour) covers negative NDVI values and therefore represents areas without any vegetation. Colours in resulting images (Figures 6 and 8) follow the graph legend. Mean spectral signatures of derived NDVI value classes are shown in Figure 9.

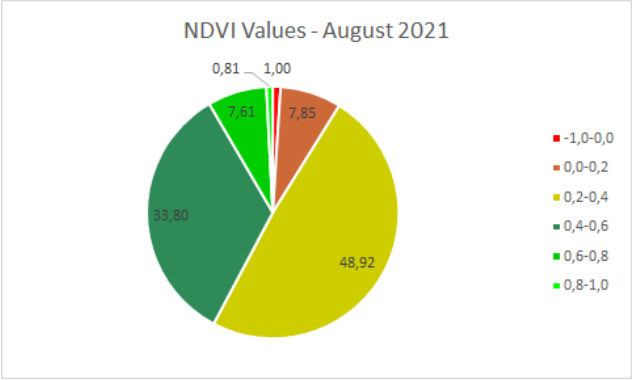

Fig. 5 - NDVI Values derived into 6 classes together with percentage of each class

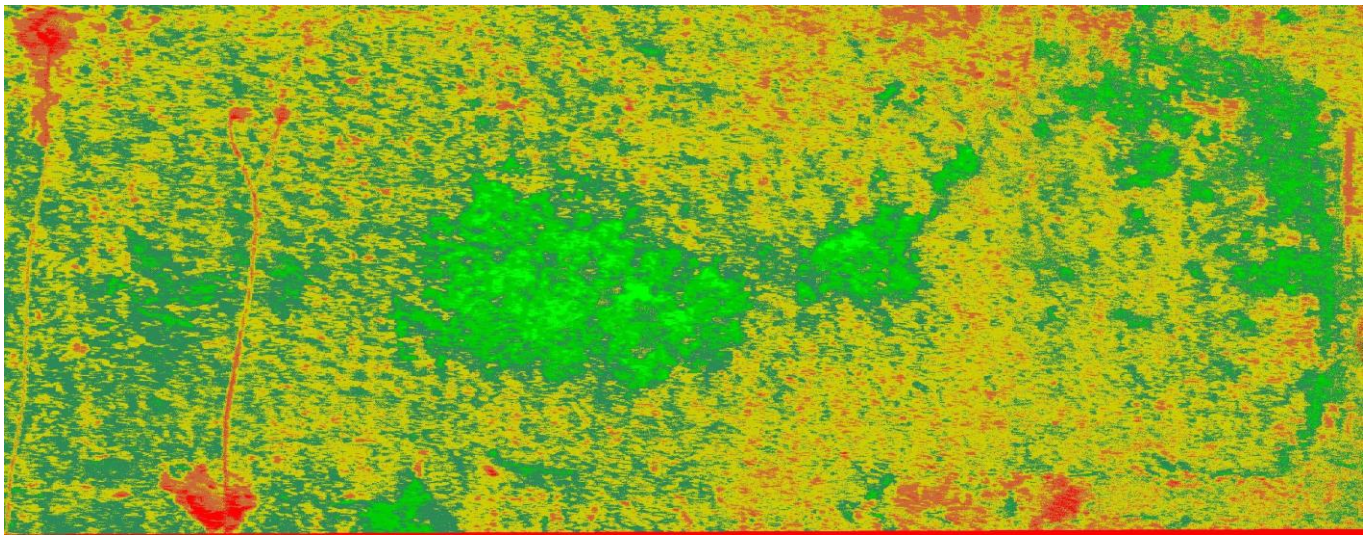

Fig. 6 – NDVI image with 6 classes, for legend see Figure GRAF August.

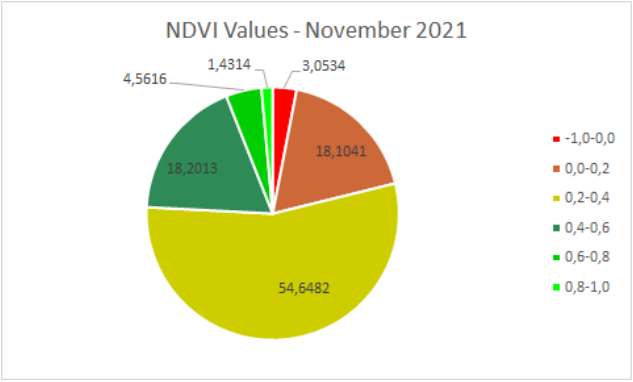

Fig. 7 – NDVI Values derived into 6 classes together with percentage of each class.

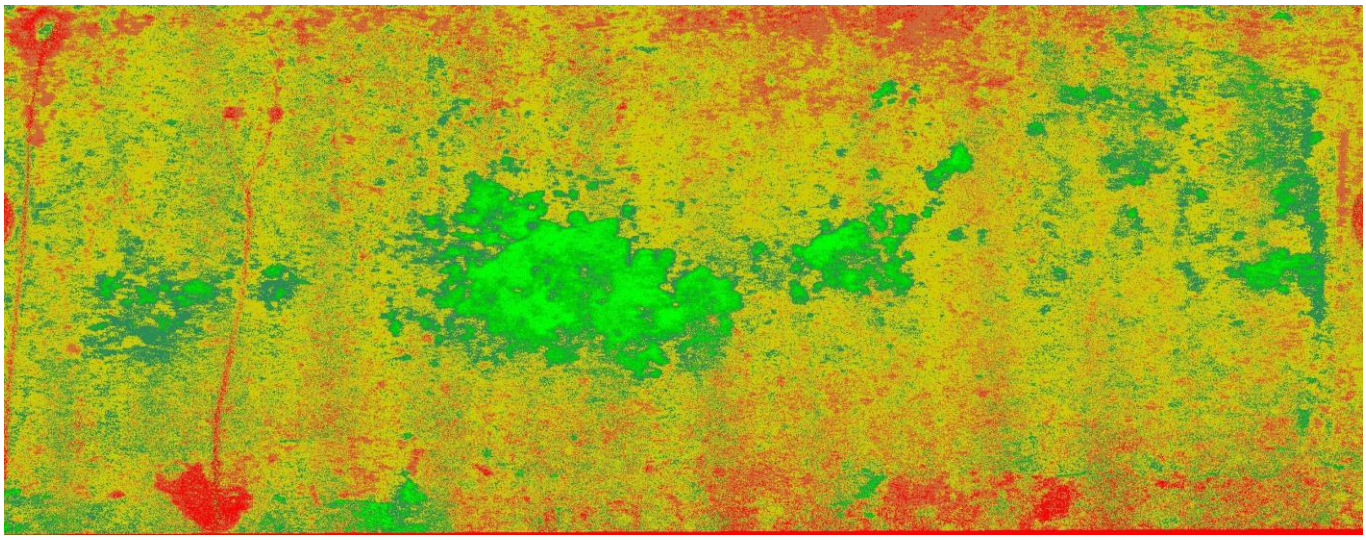

Fig. 8 – NDVI image with 6 classes, for legend see Figure GRAF November.

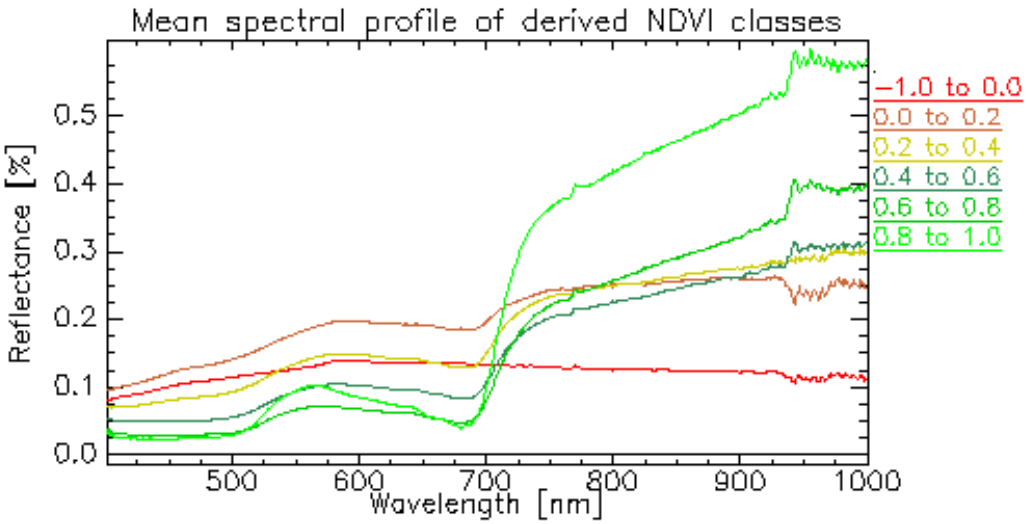

Fig. 9 - Mean spectral signatures of derived NDVI value classes.

CONCLUSION

A specific historical sandstone sample was chosen for a temporal analysis. Significant changes can be found when summer (August) and autumn (November) measurement were compared (Figures 6 and 8). The NDVI value changes between the measurements are summarized in Table 2.

Tab. 2: NDVI value change between November and August measurements.

Class NDVI value	Change [%]
-1,0-0,0	2,06
0,0-0,2	10,25
0,2-0,4	5,72
0,4-0,6	-15,60
0,6-0,8	-3,05
0,8-1,0	0,62

According to the authors assumption the negative value class (red) raised from 1 % to 3 % and class with values from 0 to 0,2 raised from 7,8 % to 18 % so more bare rock is visible in the autumn. Data show approximately 6 % more vegetation in the November image in the 0,2 to 0,4 class with represent low density vegetation that covers almost half of the area of interest. Medium density vegetation (NDVI Value 0,4 – 0,6) was decreased by 15,6 % and high-density vegetation (0,6 – 0,8) by more than 3 %. The increase of very high-density vegetation is very interested. We assume that this fact may be caused by growing homogeneity of moss towards winter season. The relationship of the moss leaves density and stress action is discussed by some authors. According to Malenovsky et al. [19], optimal growing conditions produce less dense and larger moss leaves, whereas worse growing conditions lead to smaller leaves with higher density.

Moss can hibernate, thanks to their possibilities to dry up, shut down, and go dormant until more suitable conditions return. Cell components of moss can remain intact even when no liquid remains in the cell. Moss leaves are usually only one cell thick, which enabling their rapid cooling

and dehydration. This process lowers the freezing point inside their cells and helps prevent internal crystal formation, which can damage the delicate cell walls [20].

Due to the nature of gained data there are many processing possibilities. With the project ongoing, they will be tested and final results will be published. Finally, the synergy of weathering processes will be also studied and evaluated, but the possibilities of laboratory analysis of stone samples is strongly influenced due to the inability of destructive sampling.

ACKNOWLEDGEMENT

This paper and corresponding research was conducted by the Czech Ministry of Culture project DG20P02OVV021 “Stone surface topography and its application in stone element restoration field”.

REFERENCES

[1] Březinová D., Bukovanská M., Dudková I., Rybařík V., Praha kamenná, Přírodní kameny v pražských stavbách a uměleckých dílech, Praha, 287 p., 1996.

[2] Goodman R., Introduction to rock mechanics, New York, 562 p., 1989.

[3] R.B.G. Williams, D.A. Robinson, Experimental frost weathering of sandstones by various combinations of salts, Earth Surface Processes and Landforms, 26 (2001) 811-818.

[4] A. Goudie, H. Viles, Salt weathering hazards, John Wiley & Sons Ltd., Chichester, 1997.

[5] WARSCHEID, Th. a J. BRAAMS. Biodeterioration of stone: a review. International Biodeterioration & Biodegradation [online]. 2000, 46(4), 343-368 [cit. 2020-08-18]. ISSN 09648305. Dostupné z: doi:10.1016/S0964-8305(00)00109-8

[6] Biologické napadení stavebních materiálů. Izolace.cz [online]. Praha: A.W.A.L. - PRO, s.r.o., 2006 [cit. 2020-08-18]. Dostupné z: https://www.izolace.cz/clanky/biologicke-napadeni-stavebnich-materialu/

[7] ADAN, Olf a Robert SAMSON. Fundamentals of Mold Growth in Indoor Environments and Strategies for Healthy Living. 1. Wageningen: Wageningen Academic Publishers, 2011. ISBN 978-90-8686-722-6.

[8] CANEVA, Giulia a Salvador ORNELLA. Biodeterioration of Stone. The Deterioration and Conservation of Stone: Notes from the International Venetian Courses on Stone Restoration. 1988, , 182-234.

[9] GRIFFIN, P.S., N. INDICTOR a R.J. KOESTLER. The Biodeterioration of Stone: a Review of Deterioration Mechanisms, Conservation Case Histories, and Treatment. International Biodeterioration [online]. 1991, 28(1), 187-207 [cit. 2020-08-18]. Dostupné z: doi:10.1016/0265-3036(91)90042-P

[10] MARTÍNEZ-MARTÍNEZ, Javier, David BENAVENTE, Miguel GOMEZ-HERAS, Luz MARCO-CASTAñO a M. GARCÍA-DEL-CURA. Non-linear decay of building stones during freeze–thaw weathering processes. Construction and Building Materials [online]. 2013, 38, 443-454 [cit. 2020-08-18]. ISSN 09500618. Dostupné z: doi:10.1016/j.conbuildmat.2012.07.059

[11] MCNAMARA, Christopher a Ralph MITCHELL. Microbial deterioration of historic stone. Frontiers in Ecology and the Environment [online]. 2005, 3(8), 445-451 [cit. 2020-08-18]. ISSN 1540-9295. Dostupné z: doi:10.1890/1540-9295(2005)003[0445:MDOHS]2.0.CO;2

[12] SCHEERER, Stefanie, Otto ORTEGA ‐ MORALES a Christine GAYLARDE. Chapter 5 Microbial Deterioration of Stone Monuments—An Updated Overview [online]. Elsevier, 2009, , 97-139 [cit. 2020-08-18]. Advances in Applied Microbiology. ISBN 9780123747884. Dostupné z: doi:10.1016/S0065-2164(08)00805-8

[13] SMITH, B.J., M. GOMEZ-HERAS a S. MCCABE. Understanding the decay of stone-built cultural heritage. Progress in Physical Geography: Earth and Environment [online]. 2008, 32(4), 439-461 [cit. 2020-08-18]. ISSN 0309-1333. Dostupné z: doi:10.1177/0309133308098119

[14] WELTON, , RYAN G, Simon CUTHBERT, Roger MCLEAN, Andrew HURSTHOUSE a John HUGES. A Preliminary Study of the Phycological Degradation of Natural Stone Masonry. Environmental Geochemistry and Health. 2003, 25(1), 139-45.

[15] PODLISKA J., SEMERÁD M. Nové poznatky o konstrukci Juditina mostu v Praze. *Staletá Praha*, 28(2), 2012, dostupné: http://www.staletapraha.cz/media/2012_2/clanky-cele/sp-2-2012-08-podliska-semerad.pdf

[16] Hyperspectral sensors. Headwall Photonics [online]. USA: Headwall Photonics, 2020 [cit. 2020-08-25]. Dostupné z: https://www.headwallphotonics.com/hyperspectral-sensors

[17] HUETE, A.R. a R.D. JACKSON. Soil and atmosphere influences on the spectra of partial canopies. *Remote Sensing of Environment* [online]. 1988, **25**(1), 89-105 [cit. 2021-12-17]. ISSN 00344257. Dostupné z: doi:10.1016/0034-4257(88)90043-0

[18] ENVI Classic. *ENVI Classic help* [online]. Harris Geospatial Solutions, 2019 [cit. 2021-12-17]. Dostupné z: file:///C:/Program%20Files/Harris/ENVI55/classic/help/ENVI3WHelp.htm#ENVI3WHome.htm%3FTocPath%3DGetting%2520Started%7C_____0

[19] MALENOVSKY Z., TURNBULL JD., LUCIEER A., ROBINSON SA. Antarctic moss stress assessment based on chlorophyll content and leaf density retrieved from imaging spectroscopy data. *New phytologist.* 2015, 208(2), 608-624, ISSN 0028-646X.

[20] ILLERBRUN K. Antifreeze and sunblock: How mosses survive an Alberta winter, 2021, available online: http://blog.abmi.ca/2021/11/29/antifreeze-and-sunblock-how-mosses-survive-an-alberta-winter/

CIVIL ENGINEERING JOURNAL

Article no. 59

THE CIVIL ENGINEERING JOURNAL 3-2021

INVESTIGATING THE BEHAVIOR OF BOUNDARY ELEMENTS IN STEEL SHEAR WALLS WITH DIFFERENT CONNECTIONS

Bi Ying

Zheng Zhou Sheng Da University Of Economics, Business & Management; Zhengzhou Henan, 451191 China, biyingsu@126.com

ABSTRACT

In the recent five decades, steel shear walls have been one of the most important systems in the construction and rehabilitation of many structures. The system has many advantages, including high strength and stiffness, high ductility, and excellent energy dissipation capacity. Steel shear walls are made and executed in different types. These include walls with and without stiffeners as well as composites. Recent research shows that they are a type of steel shear wall in which the infill plate is slightly away from the boundary members. In fact, there is no connection between the infill plate and one of the boundary members. Therefore, in this study, the behavior of traditional one-story-one-span steel shear walls with four different lengths was investigated numerically using ABAQUS software. For comparison, walls in which the sheet was attached only to a beam or column were examined. Obtained results from the study showed that the lateral bearing capacity of samples with free beam or free column is less than that of samples with full connection, on average 20%. Also, the strength of the samples with the free column is slightly higher than the samples with the free beam. In addition, boundary members, especially columns, are much less affected by forces in free-column specimens than in other specimens, decreasing economic costs.

KEYWORDS

Steel structures, Steel shear walls (SSWs), Inserting plate, Numerical analysis, ABAQUS software

INTRODUCTION

Previous research has shown several advantages for steel shear walls, including high stiffness and strength, good ductility, higher energy dissipation capacity, fast construction, and economic savings [1, 2]. The main factor of lateral load strength in a steel shear wall system is the infill plate. Steel shear walls in their traditional type have defects such as premature buckling of the plate. This phenomenon subsequently reduces the energy dissipation capacity of the system, which can also reduce ductility. A steel shear wall typically consists of a thin sheet of steel enclosed in boundary members, including beams and columns. Web-plates can also be with or without stiffeners depending on the design conditions. Steel shear walls resist lateral loads by creating diagonal tensile fields in the infill plate. In order to fully utilize the capacity of the plate, a diagonal tension field action must be uniformly formed in it. Achieving such a goal requires that the boundary elements, especially the columns, must have a very high bending stiffness [3, 4]. The use of very strong columns in terms of bending stiffness makes the design look uneconomical and heavy. To overcome this problem, a special type of steel shear wall has recently been proposed in which the plate is somewhat separated from the main columns and attached to a sub-column that can be weak and semi-strong. Ultimately, this reduces the size of the main column to an economical design. The first research in this field began in the numerical research performed by

Xue and Lu [5,6]. They found that using a steel shear wall in which the plate is attached only to the beam reduces the forces acting on the columns. To better understand the behavior of steel shear walls with partial connection, many researchers have conducted numerous experimental and numerical studies. Some of the research on the above topic is briefly presented. In 2008, Hoi and Park tested a new type of steel shear wall called a steel shear wall with a partial connection. The infill plate in this system was only connected to the beams, and the columns were free [7]. In order to compare the behavior of this sample, they examined a typical steel shear wall while maintaining the geometric conditions of the boundary elements and the mechanical conditions of the infill plate. The result of the experiments was that the samples had the same initial hardness, but the final strength of the sample with partial connection was less than the final strength of the sample with the full connection. The energy absorption of the sample with cross-linking was also reported to be about 65% of the energy absorption of the sample with the full connection**.** But, acting forces on the columns of the still shear wall (SSW) with partial connection was reduced considerably. In 2011, Guo et al. Examined steel shear walls in which infill plate was attached only to beams [8]. The results of these experiments showed that the studied systems have good ductility and excellent energy dissipation capacity. They also studied the effect of height-to-thickness and width-to-height ratios. Therefore, obtained results showed that these values significantly affected the hysteresis behavior of the system.

Validation

In this section, to validate the results of this research, firstly, two laboratory models were validated using ABAQUS finite element software. The first laboratory sample used in this study is related to the experiment performed by Choi and Park [9]. During this experiment, a 3-story single-bay 2D frame was subjected to lateral cyclic loading. It is worth mentioning that to apply plate buckling in this model, an initial imperfection was considered according to the first buckling mode. To investigate the behavior of this laboratory sample, a cyclic load was inserted into the last floor column once. Figure 1 shows the hysteresis curve of the laboratory model and the results obtained from the numerical simulation.

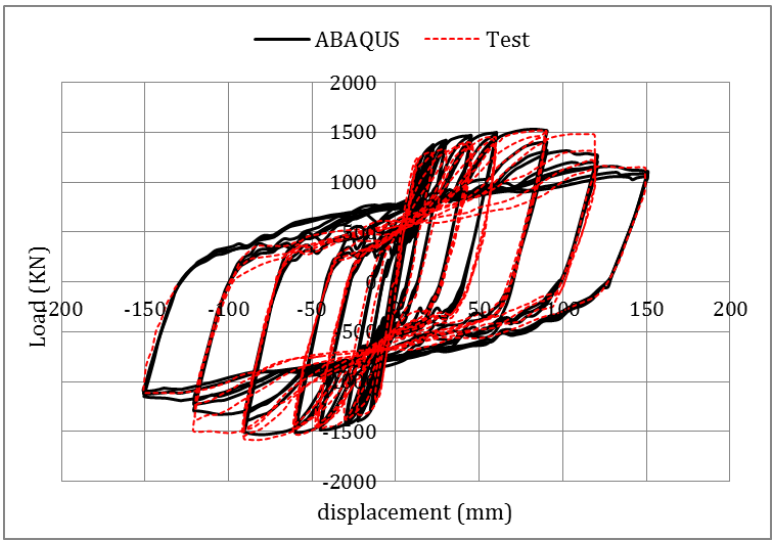

Fig. 1 - hysteresis curve of test and finite element of FSPW3 sample

The strength of the laboratory sample in the positive and negative directions of loading is 1500 and 1565 kN, respectively. On the other hand, the strength of the finite element model is 1529 and 1531 kN, respectively, in the positive and negative directions. Thus, the difference between the maximum strength of finite element and laboratory models for this sample in positive and negative directions is 1.9% and 2.3%, respectively. Therefore, ABAQUS software can predict

the behavior of this system well. Figure 2 and Figure 3 show the deformation of the laboratory specimen and the finite element model of this sample at the end of loading. According to Choi et al., In the test sample, the sample failure was primarily due to the suction of the column because of the post-buckling field of the plate on the first floor and finally, the failure of the column foot connection. As can be seen, the deformation of the finite element model and the laboratory model is very close to each other. In particular, the formation of plastic joints in the laboratory model is well reflected in the finite element model.

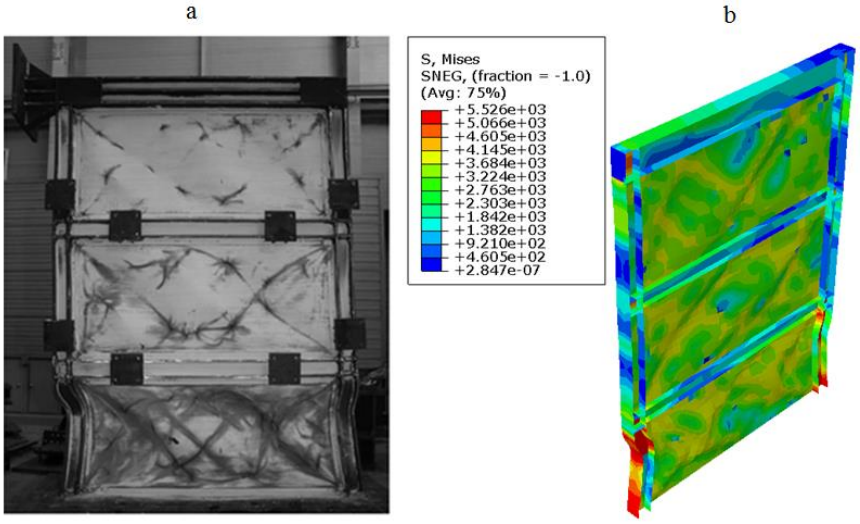

Fig. 2 - Deformation of test and finite element model

A: Experiment b: finite element

The next laboratory sample for validation is the experiment performed by Park et al. [10]. During this experiment, a 3-story single-bay frame was subjected to cyclic loading (see Figure 3).

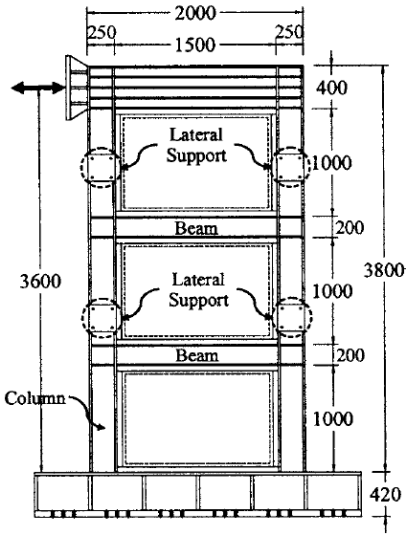

Fig. 3 - Schematic of laboratory sample [10]

Figure 4 shows the hysteresis curve of the laboratory model and the finite elements of the sample.

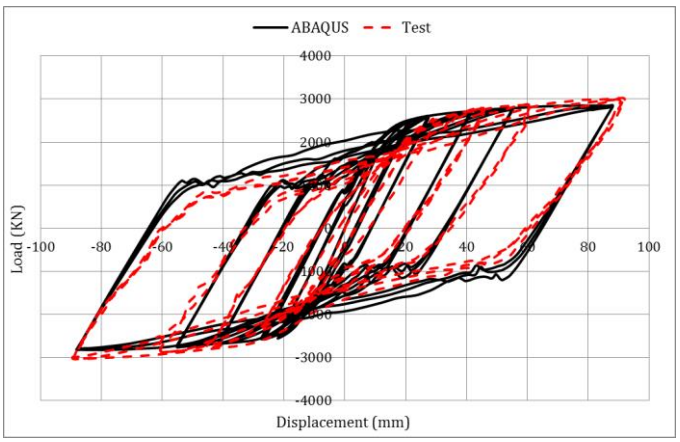

Fig .4 - hysteresis curve of the laboratory model and the finite elements

The strength of the laboratory sample in positive and negative directions is 2992 and 3021 kN, respectively. The strength of the finite element model in the positive and negative directions is 2847 and 2824 kN, respectively. Thus, the difference between the ultimate strength of finite element and laboratory models in the positive and negative directions of loading is 5% and 7%, respectively. In general, there is a good agreement between the hysteresis curve obtained from experimental and finite element modeling. Figure 5 shows the deformation of the laboratory sample and the finite element of SC6T at the end of loading. As can be seen, the deformation of the finite element model and the laboratory model is very close to each other. In particular, the formation of plastic hinges at the base column in the laboratory model is well reflected in the finite element model.

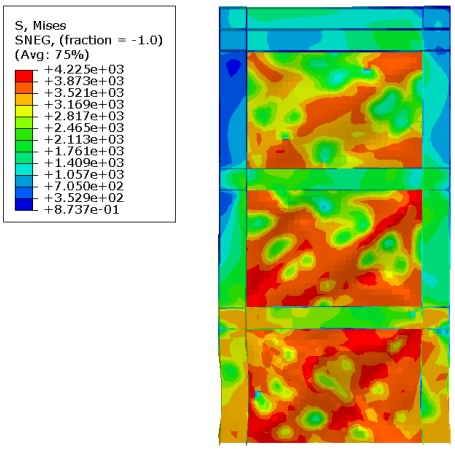

Fig .5 - Deformation of the SC6T sample in the end of loading

Fig .6 - yielding of the first floor column in the experiment [10]

Modelling and Method of Study

In this study, several samples of single-story-one-way conventional steel shear walls were first designed according to the LRFD method considering AISC341 Guideline No. 20 requirements [11]. Then, to study the behavior of steel plate shear walls connected to frame beam only, plate at designed SSW was separated from side columns and only connected to the overhead beam. It should be noted that the distance between plate edge and boundary columns was much selected to be very low. The geometrical dimensions and the mechanical properties of the boundary members and infill plates in both cases are the same. To model all boundary members and steel plates in ABAQUS software [12], the shell element (S4R) was used, 2a quadruple element with reduced integration. Each node of this element has 6 degrees of freedom, that is, 3 degrees of freedom of movement and 3 degrees of transitional freedom. In this research, by applying an initial imperfection according to the first buckling mode in the model, the possibility of infill plate buckling was provided. It also prevents off-screen deformation of the columns from preventing curvature on the page. Von Mises's yield level was also selected as the yield criterion. In predicting the desired behavior, nonlinear geometric and nonlinear effects of the material are also considered. For die sheets LYP100 steel with 100 MPa yield stress and for boundary members including beams and columns, St52 with 360 MPa yield stress was used.

To investigate the behavior of the samples, these samples were considered in 4 groups with different lengths. The axis to axis distance of the columns in groups A, B, C, and D is 4.5, 5.5, 6.5, and 7.5 m, respectively. Group D, with a length of 7.5 m, represents a wide steel shear wall. Also, the height of all samples was considered to be 3.2 m. The geometric characteristics of the studied samples in the present study are presented in Table 1.

Tab. 1 - Geometric characteristics of the samples studied in the present study

model	Width (m)	Height (m)	Plate thickness (mm)	beam	column
A	4.5	3.2	4	H 400-250-35-25	Box 370×370×35×35
B	5.5	3.2	4	H 400-250-35-25	Box 370×370×35×35
C	6.5	3.2	4	H 400-250-35-25	Box 370×370×35×35
D	7.5	3.2	4	H 400-250-35-25	Box 370×370×35×35

In this paper, by separating the connection of the plate to the beam or columns, their behavior under cyclic loads was investigated. As shown in Figure 7, the lateral load is applied to the column. The foot of the wall was attached to the ground. To simulate this in ABAQUS software, the transitional and rotational displacement of the lower points of the wall in three directions was prevented. To study the behavior of studied models, hysteresis analysis according to the SAC loading protocol was utilized. (Figure 8) [13]. In this study, the loading continued until the ultimate strength decreased by at least 20% compared to the maximum strength.

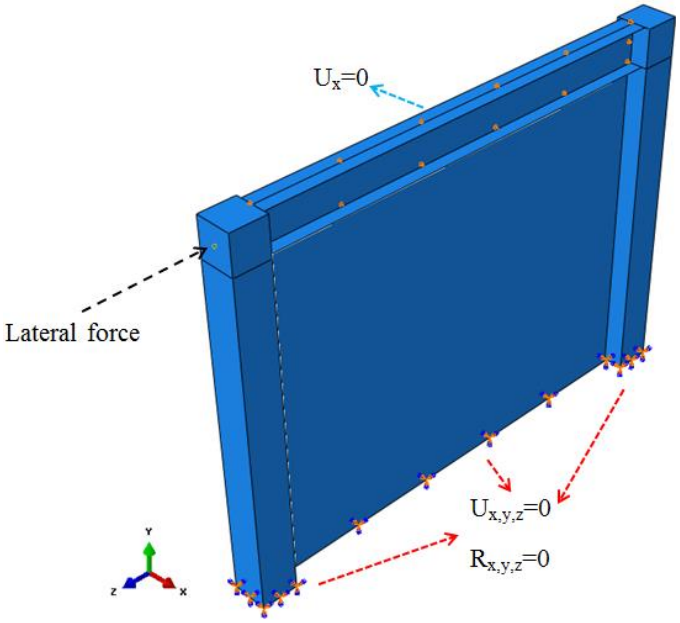

Fig. 7 - Boundary conditions of the studied samples

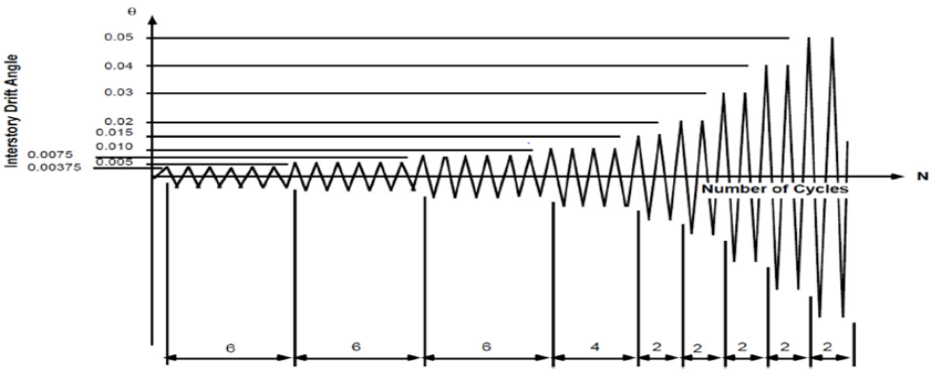

Fig. 8 - Loading protocol based on SAC [13]

In the following sections, the word „Full“ represents steel shear walls with full connection and the symbol "BF" refers to steel shear wall connected to frame column. Also, the symbol "CF" refers to the steel shear wall connected to the frame beam. For example, the CF model in group A is shown in Fig. 9. As can be seen, there is no connection between plate and columns in this model along column height, and the plate is connected to the beam. It should be noted that the web plate is attached to the boundary members, including the beam and column, using welding. In order to simulate this problem in ABAQUS software, the plates were tied to the boundary elements in the interaction module in ABAQUS.

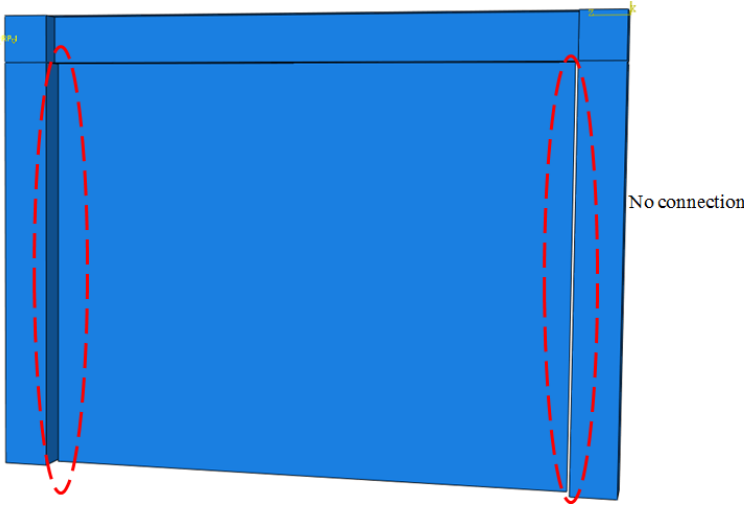

Fig. 9 - No connection between plate and columns in CF model

RESULTS

Shear capacity

Maximum shear capacity of the studied samples in different models is presented in Table 2.

Tab. 2 - Maximum shear capacity of the studied samples

Group	Full	CF	BF	The difference between the maximum strength of the CF sample and Full (%)	The difference between the maximum strength of the BF sample and Full (%)
A	4402.4	3429.9	3342.9	22.0	24.0
B	4593.9	3608.3	3433.2	21.4	25.2
C	4710.3	3711.1	3398.4	21.2	27.8
D	4884.0	3927.2	3563.7	19.5	27.0

According to Table 2, the strength of the Full samples in all groups is higher than the CF and BF samples. The difference between maximum strength of Full and CF samples in groups A, B, C, D, and E are 22.0, 21.4, 21.2, and 19.5%, respectively. It is noteworthy that with the increasing the width of the samples, differences between maximum strength of Full and CF samples slightly decreased. In addition, the difference between maximum strength of Full and BF samples in groups A, B, C, D, and E are 24.0, 25.2, 27.8, and 27.0%, respectively. It is noteworthy that the strength of the BF samples is 2.6, 5.1, 9.2, and 10.2% lower than the CF samples in groups A, B, C, and D, respectively. On the other hand, when the infill panel is only connected to beams, it has higher strength than the corresponding sample.

Beam behavior

In Figure 10, maximum bending moment of beam during lateral loading is shown.

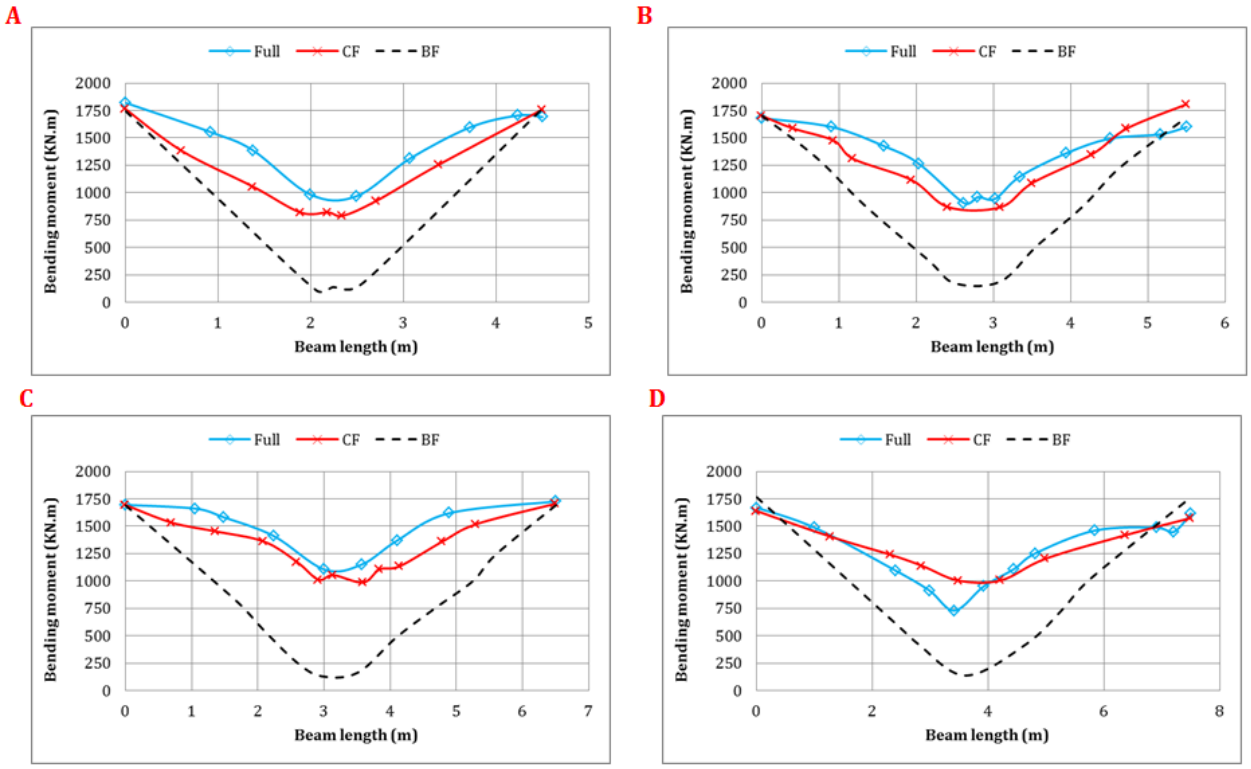

Fig. 10 - Comparison between the maximum bending moment of the beam during loading in different modes

As can be seen, the maximum bending moment occurred at both ends of the beam. Totally, the maximum bending moment at the end of the beam of Full, CF, and BF models are approximately equal. The bending moment of the beam in all sections of the beam length in the Full sample at groups A, B, and C is more than in other samples (except for the two ends). It is noteworthy that in the CF model in group D, the bending moment of the CF model is greater than that of the Full model. This highlights the importance of paying attention to the design of beams in wide steel shear walls in which the plate is attached only to the beam. Another point is that, in BF models, the beam has been subjected to the much less bending moment in different sections except the two ends than in the Full and CF models.

Column behavior

Investigating the axial force of the column

In Figure 11, the maximum axial force of the column is presented in different models.

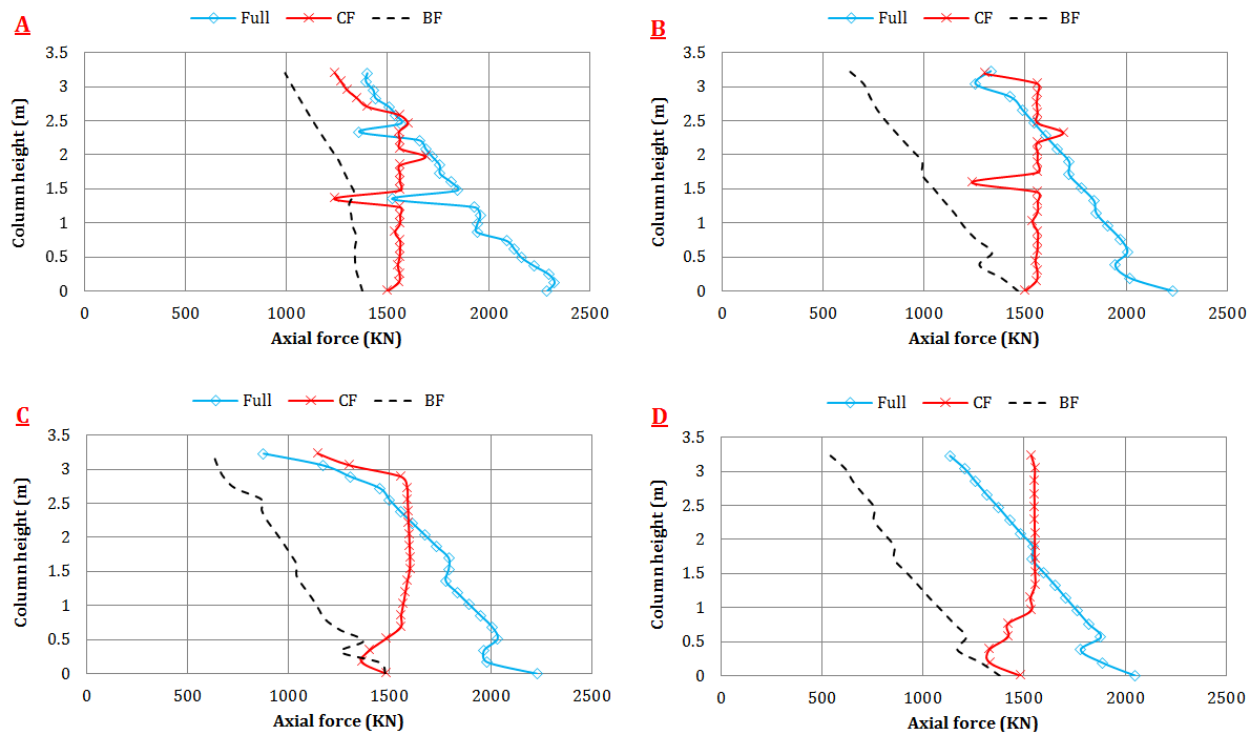

Fig. 11 - Comparison between the maximum axial force of column during loading in different modes

According to Figure11, the first thing to see is that the maximum axial force in the Full sample is greater than that of CF and BF samples. Another result is that in the full sample, the axial force at the foot of the column is maximum, and the axial force in the column is reduced by moving towards the beam ends. However, maximum axial force at the height of the column of the CF model did not occur at the foot of the column but happened in the upper parts. The noteworthy point in this section is that in the upper parts of the column, the maximum axial force was almost constant alongside the column height. The maximum axial force at the foot of the column for CF and BF samples is approximately equal. But in the upper sections, the maximum axial force of the BF model is lower than that of CF models. Table 3 presents the maximum values of the axial force of the column at the height of the column for different modes in studied groups.

Tab. 3 - Maximum values of column axial force at column height for different modes in different groups

Group	Full	CF	BF	difference between CF with full models (%)	difference between BF with full models (%)	difference between BF with CF models (%)
A	2327	2000	1928	14.05	17.14	3.6
B	2232	1688	1465	24.37	34.36	13.21
C	2229	1601	1478	28.17	33.69	7.68
D	2051	1555	1380	24.18	32.71	11.25

According to Table 3, it is clear that the difference between the maximum axial force acting on the column in the Full sample compared to the CF model in groups A, B, C, and D, are 14.06, 24.37, 28.17, and 24.18%, respectively. In addition, the difference between the maximum axial force acting on the column in the Full sample compared to the BF model in groups A, B, C, and D

are 17.15, 34.36, 33.7, and 32.7%, respectively. Also, the difference between the maximum axial force in the column in the CF model compared to the BF model in groups A, B, C, and D is 3.6, 13.2, 7.7, and 11.3%, respectively. Therefore, by increasing the width of the span, the difference between the axial forces of the column in the two modes CF and BF has been increased.

Investigating the shear force of the column

In Figure 12 the maximum shear force of the column is presented in different models.

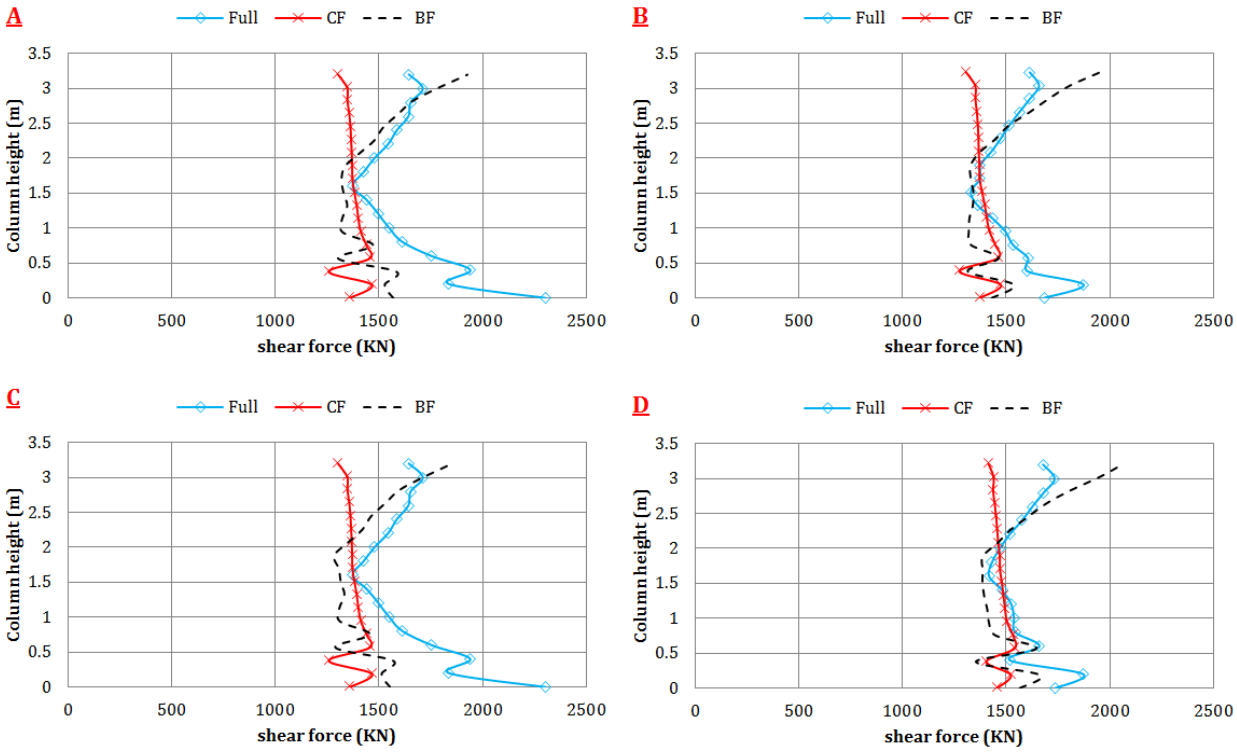

Fig. 12 - maximum shear force acting on the column in different models

According to Figure 12, the maximum shear force of the column in the cf sample is approximately equal along the column. Also, the value of column shear force in the CF sample in all groups is less than the Full and BF models. In groups A and C, the maximum shear force of the column along the height of the column for the full model is greater than the other two models. But in groups B and D, the maximum shear force of the column along the height of the column for the BF model is more than the other two models. Table 4 presents the maximum values of column shear force at column height for different models in studied groups.

Tab. 4 - Maximum values of column shear force along column height for different modes in different groups

Group	Full	CF	BF	difference between cf with full models (%)	difference between BF with Full models (%)	difference between BF with CF models (%)
A	2305	1466	1927	36.39	16.39	31.44
B	1874	1474	1953	21.34	4.21	32.49
C	2305	1466	1852	36.39	19.65	26.33

D	1872	1540	2063	17.73	10.20	33.96

As can be seen in Tab. 4, the difference between the maximum shear force acting on the column in the Full model compared to the cf model in groups A, B, C, and D are 36.39, 21.34, 39.36, and 17.73%, respectively. In addition, the difference between the maximum shear force acting on the column in the Full model compared to the BF model in groups A, B, C, and D is 16.39, 4.21, 19.65, and 10.2%, respectively. Also, the difference between the maximum shear force in the column in the CF model compared to the BF model in groups A, B, C, and D is 31.44, 32.49, 26.33, and 33.96%, respectively.

DEFORMATION

Deformation of models in group A is presented in Figure 13.

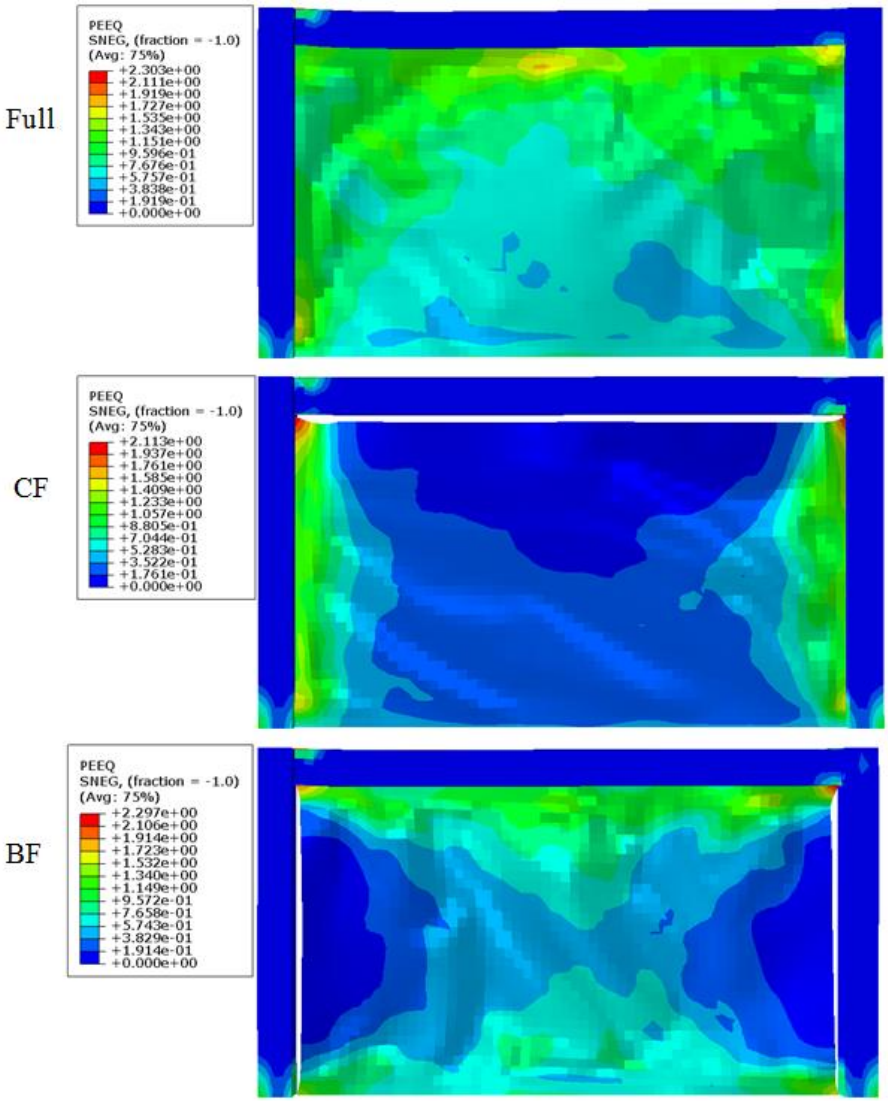

Fig. 13 - Equivalent plastic strain (PEEQ) contours of A group

CONCLUSION

In this study, the behavior of steel shear walls by connecting the infill plate to only one of the boundary members was investigated. In other words, the behavior of steel shear walls with different conditions of plate connection to boundary members was investigated. Therefore, four groups of steel shear walls with different lengths were considered, and then in these four groups, three different modes of plate connection to the boundary members were considered. In the first case, the plate was attached to the surrounding beams and columns, traditionally. In the second case, the plate was attached only to the beam, and in the third case, the plate was attached only to the columns. To investigate the behavior of the samples studied in this study, quasi-static analysis was used in accordance with the rules of the SAC loading protocol. The main obtained results from this study are as follows:

- ✓ When the plate is attached only to the beam, the strength of the steel shear wall in the samples of groups A, B, C, and D is 22.0, 21.4, 21.2, and 19.5% lower than the sample with full connection, respectively.
- ✓ When the plate is attached only to the columns, the strength of the steel shear wall in the samples of groups A, B, C, and D is 24.0, 25.2, 27.8, and 27.0% lower than the sample with full connection, respectively.
- ✓ The strength of the specimens with the connection of the plate only to the beam is higher than the specimens with the connection of the plate only to the columns. This difference is increased by increasing the width of the steel shear wall.
- ✓ The maximum bending moment of the beams in the studied samples in different groups with different plate connections to the boundary members are almost equal to each other. The maximum bending moment of the beams in the studied samples in different groups with different connections of the sheet to the boundary members are almost equal to each other. However, in beams in which the plate is attached only to the columns, the beam has a less bending moment in different sections except for the end of beams.
- ✓ The maximum axial force acting on columns in steel shear walls with Full connection is considerably higher than in BF and CF samples. The maximum axial force of columns in CF models is equal to or slightly less than that of BF models. The interesting point here is that the axial forces of the column in the CF samples are almost constant along the height of the column. While in other specimens, it decreased almost linearly with increasing column height.
- ✓ The shear force of the column in all groups in the BF sample is less than the full and CF samples. By comparing the shear force in Full and CF samples, it was found that no special relationship is established

REFERENCES

[1] P.A. Timler, C.E. Ventura, H. Prion, R. Anjam, Experimental and analytical studies of steel plate shear walls as applied to the design of tall buildings, The Structural Design of Tall and Special Buildings 7 (1998) 233–249.

[2] A. Astaneh-Asl, Seismic Behavior and Design of Steel Shear Walls, Steel Tips, Structural Steel Educational Council, Technical Information and Product Service, 2001.

[3] A. Jahanpour, J. Jön&TDREFS;sson, H. Moharrami, Seismic behavior of semi-supported steel shear walls, Journal of Constructional Steel Research 74 (2012) 118–133.

[4] A. Jahanpour, H. Moharrami, Evaluation of behavior of the secondary columns in semi-supported steel shear walls, Thin-Walled Structures 93 (2015) 94–101.

[5] M. Xue, L.W. Lu, Monotonic and cyclic behavior of in-filled steel shear panels, in: Proc. Seventeenth Czech and Slovak International Conf. on Steel Structures and Bridge, 1994.

[6] M. Xue, L.W. Lu, Influence of steel shear wall panels with surrounding frame members, in: Proc. SSRC Annual Technical Session, 1994.
[7] I. Choi and H. Park, CYCLIC TEST FOR FRAMED STEEL PLATE WALLS WITH VARIOUS INFILL PLATE DETAILS, the 14th World Conference on Earthquake Engineering
October 12-17, 2008, Beijing, China
[8] Lanhui Guo, Qin Rong, Xinbo Ma, and Sumei Zhang, Behavior of Steel Plate Shear Wall Connected to Frame Beams Only, International Journal of Steel Structures December 2011
[9] In-Rak Choi and Hong-Gun Park, Ductility and Energy Dissipation Capacity of Shear-Dominated Steel Plate Walls, J. Struct. Eng. 2008.134:1495-1507
[10] Hong-Gun Park; Jae-Hyuk Kwack; Sang-Woo Jeon; Won-Ki Kim; and In-Rak Choi, Framed Steel Plate Wall Behavior under Cyclic Lateral Loading, J. Struct. Eng. 2007.133:378-388
[11] Sabelli R, Bruneau M. Design guide 20: steel plate shear walls, American Institute of Steel Construction. Chicago, IL, USA 2007.
[12] ABAQUS Version 14.1. (2014). ABABUS user's manual, Hibbitt, Karlsson, and Sorenson Inc. (HKS), Pawtucket, R. I, USA
[13] H. Krawinkler, Loading histories for cyclic test in support of performance assessment of structural components, in: 3rd International Conference on Advances in Experimental Structural Engineering, San Francisco, 2009.

CIVIL ENGINEERING JOURNAL

Article no. 72

THE CIVIL ENGINEERING JOURNAL 4-2021

AVAILABILITY AND COMPARISON OF DATA FROM SENTINEL-1 SATELLITES IN AREAS OF INTEREST IN THE CZECH REPUBLIC AND SUDAN

Dominik Brétt[1,2]

1. *Czech Technical University in Prague, Faculty of Civil Engineering, Department of Geomatics, Prague, Thákurova 2077/7, 166 29, Czech Republic*
2. *Faculty of Environment, J. E. Purkyně University in Ústí nad Labem, Pasteurova 3632/15, 400 96 Ústí nad Labem, Czech Republic*

;dominik.brett@fsv.cvut.cz

ABSTRACT

The article is focused on the methodology of processing interferometric images and associated challenges with the processing. The article also contains useful links with explanations that can be used for processing data from the Sentinel-1 satellite. To emphasize the data limits of Sentinel-1, several areas of interest were chosen for comparison – in the home environment of the Czech Republic, the Bílina quarry area, and the Žatec area were selected. For subsequent comparison, arid areas with a rich history located in Sudan were selected. The colleagues of the author from the Faculty of The Environment of Jan Evangelista Purkyně University participate in expeditions there. Each of these locations is limited by different parameters – the areas in the Czech Republic are mainly limited by location because of occurring vegetation. Sudan's regions, on the other hand, are arid but are limited by insufficient coverage by capturing the Sentinel-1 satellite. To create digital height models from Sentinel-1 satellite data, it is necessary to search for data with sufficient coherence of images, and parameters of the amount of vegetation with a period between individual images play an important role. The areas were compared with each other and with the commonly available SRTM elevation model, both from a visual point of view – where digital height models and shaded surface models were created, as well as statistically using RMSE.

KEYWORDS

InSAR, Remote Sensing, Sentinel-1, GIS, RMSE

INTRODUCTION

Almost from the earliest days of mapmaking, people have tried to express elevation in these maps. They used, for example, drawn hills, hatching, and last but not least, contour lines [1]. Today's age of digital technology makes it possible to model the landscape in the form of digital elevation models. Various contact and non-contact data collection technologies are now commonly used to derive digital elevation models [2]. Non-contact data collection methods, such as photogrammetry and airborne laser scanning, allow the creation of very detailed digital terrain and surface models, but it is always necessary to send a vehicle equipped with the chosen type of sensor to the area of interest [3]. This is a limitation for the creation of digital terrain models in areas with limited accessibility. Here, there is an opportunity for the use of radar interferometry methods where a satellite is used as a carrier [4].

The Sentinel-1 mission is aimed at monitoring sea ice, ocean waters, the coastline, and polar regions, as well as monitoring the land itself, building in particular on successful Envisat and ERS-1 satellite missions. For Europe, their possible use in crisis management is especially important, mainly due to the availability of up-to-date data almost in real-time. Specific data utilization is

foreseen for flood or terrain deformations, which can be detected with millimeter accuracy with appropriate images using radar interferometry [1].

A major advantage of radar data, as opposed to optical data, is that it can be acquired when the sky is covered with clouds. This can be used, for example, to monitor current flood events caused by rainfall. Another area of application for Sentinel-1 data is the monitoring of the territory - e.g., forest mapping, monitoring of crops, or monitoring of the extent of snow cover. Similar information can also help predict floods or monitor the impact of climate change [5].

The use of Sentinel-1 data brings several general advantages - firstly, the data are freely downloadable on the official ESA site, and secondly, the mission Sentinel-1 provides almost real-time data of the whole World. The mission satellite is using synthetic aperture radar [6].

The objectives of this paper are aimed at understanding the processing, and the subsequent analysis of radar data from the Sentinel-1 mission. The satellites of this mission operate based on InSAR - interferometric radar with synthetic aperture. Digital elevation models of areas of interest were derived from the processed data, which were subsequently compared visually and statistically.

DATA AND METHODS

The creation of a digital elevation model (DEM) was not the main objective of the Sentinel-1 mission in comparison with SRTM, where generating the most complete high-resolution digital topographic database of Earth was the primary objective. The main objective of Sentinel-1 is designed to provide enhanced revisit frequency, coverage, timeliness, and reliability for operational services and applications requiring long time series and the constellation will cover the entire world's landmasses on a bi-weekly basis, sea-ice zones, Europe's coastal zones and shipping routes on a daily basis and open ocean continuously by wave images. It is not possible to apply this procedure of creating the DEM to the whole World, even if the data of the area are available. The process of DEM derivation is based on the InSAR data hardware-intensive and it is necessary to take into account long-lasting processes, especially for less powerful devices.

Area of interest

To derive a DEM from Sentinel-1 data, it is important to select a suitable area. Sentinel-1 works in band C, which in practice means that vegetation has a big influence on the quality of the model. Unfortunately, the beam cannot penetrate a layer of vegetation with its rays, and modeling, for example, within the rainforest environment is impossible from this data.

A total of four test areas were thus chosen – two areas in the Czech Republic and two areas in Sudan. Within the Czech Republic, areas with low vegetation were sought, thus the sites Bilina open-pit quarry and an area within the Zatec municipality were processed (see **Chyba! Nenalezen zdroj odkazů.**). These areas were selected because the vegetation cover is completely removed

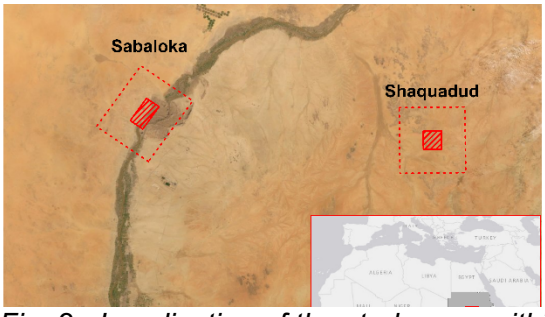

Fig. 2 - Localization of the study area within Sudan
Author: Dominik Brétt, 2021
Ortophoto: Esri, DigitalGlobe, GeoEye, i-cubed, USDA FSA, USGS, AEX, Getmapping, Aerogrid, IGN, IGP, swisstopo

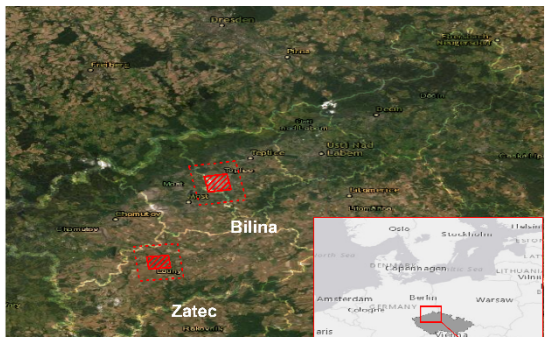

Fig. 1- Localization of the study area within Czechia
Author: Dominik Brétt, 2021
Ortophoto: Esri, DigitalGlobe, GeoEye, i-cubed, USDA FSA, USGS, AEX, Getmapping, Aerogrid, IGN, IGP, swisstopo

during opencast mining and the Zatecko region represents a typical Central European landscape with a low incidence of higher vegetation.

The sites in Sudan were chosen not only because of the desert nature of the landscape but also because, thanks to the cooperation on archaeological research with the Czech Institute of Egyptology, Faculty of Philosophy and Arts - Charles University in Prague and the Institute of Archaeology of the Czech Academy of Sciences, Prague [7, 8, 9], we have field-measured reference data to verify the quality of the resulting DEMs.

Principles of Radar and InSAR

The word "radar" originated from "radio detection and ranging". The device emits its electromagnetic radiation, these short and intense microwave signals are sent in a certain direction and part of the signal (so-called echo) is reflected from the objects. Radar systems can be located on the earth's surface, aircraft, and satellites and can create image recording. The Sentinel-1 satellite uses Synthetic Aperture Radar [10].

Synthetic Aperture Radar is a technically more complex device allowing acquisition of radar recordings. SAR carries a physically short antenna which transmits radiation that is reflected from the scanned surface. This procedure has a very narrow beam even at very large transverse distances from the carrier. To improve longitudinal spatial resolution, SAR uses Doppler's frequency shift. The signal recorded from the objects behind the carrier has a lower frequency. SAR then processes only the middle part of the beam – there is no shift in frequencies – and this significantly improves the longitudinal spatial resolution [11].

The device works with a combination of two or more radars and senses the topography of the terrain and its deformation from different angles. The resulting image has two parts of intensity and phase and both of these parts of the reflected beam [6]. The radar is mounted on the satellite with an antenna aimed at the Earth's surface in a plane perpendicular to the orbit – this is how it works in theory, but in practice, this is not entirely true to the rotation of the Earth around its axis. The antenna closes the angle with the ground normal (off-nadir angle) and in current systems, it is usually 34 in the range between 20° and 50°. Due to the curvature of the Earth's surface, the incidence angle, i.e., the angle at the point of impact of the signal between the Earth's normal and the direction from which the signal is coming, is greater than the angle of view. For simplicity, it should be assumed that the Earth is flat and therefore the angle of impact is equal to the angle of reflection [6].

The basic principle of this method is the beam transmitted from the radar, with reflecting surfaces at different distances showing different response times between sending and capturing the beam. At the same time, the method uses changes in the phase of reflected radiation and the difference between two images of the same territory. Due to the almost pure sine nature of the transmitted signal, the T response is equal to the change in phase Φ between the transmitted and the captured beam. The phase change is therefore proportional to the two-way beam distance divided by the wavelength of the radar [6].

Radar data is processed by multiple sensing of a single location for the composition of the final image, and georeferenced using the earth's reference ellipsoid (e.g., WGS 84). The data is available in three spatial resolutions (Full Resolution, High Resolution, Medium Resolution) [12].

Synthetic aperture radar (SAR) is a radar system for data collecting using microwave length for measuring the distance from the satellite. Microwave length provides features such as penetrating the cloudy atmosphere, through this wavelength, it also recognizes the soil moisture. Synthetic aperture radar works without an external source of light – it means it can collect data in the nighttime - so it belongs to the category of active sensors [13].

Synthetic aperture radars record reflections where they add a specific value to each point and it is possible to obtain a reflection of one point from multiple angles thanks to the different orbits of orbiting satellites. These points will differ in their phase and create a difference – interference. The phase can be a carrier of the height of a given location, and interferometry is then a method of

precise altitude measurement based on differences in the phase of two radar signals obtained from a different position [11].

The satellite is mounted with a radar with an antenna aimed at the Earth's surface in a plane perpendicular to orbit – this is how it works in theory, but in practice, this is not entirely true due to the rotation of the Earth around its own was. The antenna is closed by an angle with Earth's normal called an off-nadir angle and in current systems, it is usually in the range between 20° and 50°. Due to the curvature of the Earth's surface, the angle of impact (incidence angle), that is, the angle at the point of impact of the signal between the Earth's normal and the direction from which the signal is coming, is greater than the angle of view. For simplicity, it should be assumed that the Earth is flat and therefore the angle of impact is equal to the angle of reflection [6].

Freely according to [14] and [11], by processing images, it is possible to create an interferogram and from it is possible to determine the relative height differences of the individual elements of the image, which can be further converted to the altitude of the terrain to build a digital model of the terrain [1].

The basic geometry of radar images

The configuration of satellites has an important role in InSAR processing. The base configuration can lead to different results, and thus the user should understand the main ideas and concepts of SAR geometry. The distance between two satellites and the axis, which is perpendicular to the orbit, is called the perpendicular baseline [6]. The perpendicular baseline has a positive effect on altitude accuracy. The larger this parameter is, the higher the accuracy. At the same time, however, if the perpendicular base is too long, coherence decreases. A critical parameter is a perpendicular base. From this limit, the signal becomes decorrelated, and interferometric stripes cannot be generated [15]. Another critical parameter is the temporal baseline – time between two satellite images. If the temporal base is high, the slightest growth of vegetation – leaves on trees or growth of the lower floor – is reflected in the picture. All this leads to an increase in decorrelation and thus to a decrease in the coherence of the images [16].

Sentinel-1 data specifications

Single Look Complex (SLC) are data georeferenced based on information about the orbit and altitude at which the imaging satellite observes. Compared to GRD[1], it has a phase component that is suitable for interferometric processing [17]. The data is in a zero-Doppler orientation, where each row of pixels represents points along a line perpendicular to a sub-satellite path. SLC in Stripmap mode contains one frame for each shot for both polarizations. Interferometric Wide Swath mode, which has three frame bands, contains three images in simple polarization and six frames in dual-polarization. Extra Wide Swath mode consists of five 43 frame bars, five frames for simple polarization, and ten frames for dual-polarization [12].

Sentinel-1 data products are distributed in Standard Archive Format for Europe (SAFE), which was designed to archive and transmit ESA earth observation data while recommended for harmonizing data from all Copernicus satellites. SENTINEL-SAFE contains a folder with image data in binary data format and METADATA in XML format [5].

[1] Ground Range Detected – another data product of Sentinel-1 mission

The name of the data package itself contains a lot of information about the product, which can be demonstrated by the example of a single paired image from the Bílina quarry area:

S1B_IW_SLC__1SDV_20181228T165908_20181228T165935_014245_01A7C8_3 659

- S1B – satellite platform, mission identifier (Sentinel-1B)
- IW – operating mode (Interferometric Wide Swath Mode)
- SLC- product type (Single Look Complex)
- 1SDV – level of processing of the data, beam polarization (Level-1 product, Standard, dual polarisation VV+VH)
- 20181228T165908 – start date and time of acquisition (format YYYYMMDDTHHMMS)
- 20181228T165935 – end date and time of acquisition (format YYYYMMDDTHHMMS)
- 014245 – Orbit number
- 01A7C8 – Mission Identifier
- 3659 – Product Identifier

Software and data sources used for Sentinel-1 data processing

The processing of interferometric images is quite hardware-intensive and therefore it is recommended to process data on a powerful machine. The SNAP software was chosen for the processing of interferometric data. It is freely available software that offers tools for processing all Sentinel mission data even the Sentinel-1. A strong and active user community is also an advantage.

Before processing the data itself, it is important to install the *snaphu* unwrapping plugin. This plugin provides unwrapping the phase of the interferometric data, which is not supported in the software by default. The unwrapping plugin is located in the Tools Tab, in the Plugins section. In this section, the Available Plugins tab must be selected. The Plugin has to be active, this is done in the Tools tab in the Manage External Tools. After these steps, SNAP was ready to process interferometric data, which was subsequently opened using the Open Product button in the original ZIP folder.

Visualization and presentation of the results were carried out in the environment of the ArcGIS Pro software.

To select suitable data, a website from the Alaska Satellite Facility -Vertex tool [18](used, which, after selecting the data type and placing the polygon of areas of interest, searched for all data dealing with the selected area.

To find the correct paired image, another tool from the same institution was used, the Baseline Tool [18].

A portal from the European Space Agency [19] was used to obtain data. However, only 3 images can be downloaded at a time and only images under 2 years of age are available and older images must be requested.

There is an alternative for obtaining data for the Czech Republic, namely Collaborative Ground Segment, [20] which was created in cooperation with the CESNET association, the Czech Ministry of Transport, and the European Space Agency.

Before the actual image processing, the SNAPHU Unwrapping plug-in had to be installed in the SNAP software, which enabled the unwrapping of the phase.

Verification of the quality of the resulting data

Several datasets were used for the verification of the quality of the resulting DEMs. The SRTM (Shuttle Radar Topography Mission) was used for both test sites. The SRTM data were acquired on 22.11.2000 during the mission STS-99. It has started by launching two Endeavour satellites equipped with C-Band radar. This mission was under the protection of NASA and NGA and was launched to acquire radar data for the basis of the digital elevation model of the (almost) whole world. Elevation data offers worldwide coverage at a resolution of 1 arc-second (which is 30 meters in the

metric system) and provides open distribution of this high-resolution global data set [21]. Data for this article were obtained from the website EarthExplorer [22], which is managed by the United States Geological Survey.

The areas in the Czech Republic were further compared with LiDAR data. There is lidar data for the whole area of the Czech Republic – DMR 5G. It is the newest lidar observation of the Czech Office for Surveying, Mapping, and Cadastre and it contains coordinates X, Y, H, where H represents the altitude in the Balt elevation reference system after alignment (Bpv) with a total mean error of 0,18 m in exposed terrain and 0,3 m in forested areas. [23] Lidar data were obtained from web service ArcGIS Online.

The Root Mean Square Error (RMSE) is an advanced method for the determination of the accuracy of DEM. This method measures the variance of the frequency distribution of deviations between the two DEMs. The higher value of RMSE represents wider deviations between two datasets. The lower value of RMSE, the more accurate is the resulting model. The unit of RMSE is given by the input data.

RESULTS

Sentinel-1 data processing

After obtaining packages, data had to be in the zip folder and cannot be renamed or data would not be recognized by SNAP software. All the information that can be read from the name, as the date of observation, can be read by SNAP.

Orb Stack product was made as a result of S1-TOPS Coregistration with ESD. The purpose of this process is to shrink the examined territory and combine the data of input ZIP packages.

After coregistration, interferogram preparation was followed. As input data were used as output the results of the coregistration. This step is not important only for the whole workflow of processing radar data, but also in this step, the quality of the final output can be predicted. Interferogram acquires values from zero to one – the closer the value is to 1, the less noise the images contain and the image is, the more quality.

After those steps, there were a few defects in the output image of the interferogram and other phases. First, black lines which were showing individual paths of the satellites. Second, noise that could be filtered. Black lines showing paths of the satellites were removed by process TOPS Deburst. The overlay of the paths was chosen and it got rid of the black lines. With Goldstein Phase filtering, the noise was reduced. As the name of this function suggests, it influences only the phase, and coherence remains the same. After that, the Raster subset was created to quicken the next step of this workflow.

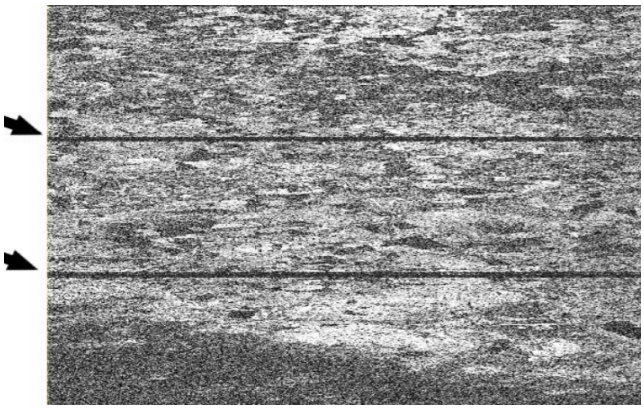

Fig. 3 – Black lines showing individual paths

At this moment, the plugin for the unwrapping phase was used and this step is the most challenging for the hardware.

For converting from radian units to absolute height was used function phase to elevation and the Range Doppler Terrain Correction was applied for geometric distortion and terrain correction. Output models were created with 15 m spatial resolution and were exported in the GeoTIFF format.

Software ArcGIS Pro was chosen for the next processing , where the digital elevation models were opened and then hillshaded models were created. In the hillshade tab there were inserted these parameters: azimuth 315, altitude 45. The key parameter was z-factor and the value 0.000015

was inserted. Every model was projected in WGS84 (which is based on degrees) and the height is given in meters.

The test data for the Czech Republic were acquired during the dormant season in the year 2018, due to the lowering decorrelation caused by vegetation cover during the summer. On the other hand, the selected areas were in the same data frame as the Ore Mountains are, and the results were not correlated as expected – even though the dormant season was present there is still vegetation cover such as grass or coniferous forests which are increasing the decorrelation.

The biggest limit in the Sudan areas was especially the temporary baseline, wherein at that time, only 12 days temporary baseline was found. Data was acquired also in the year 2018.

For result comparison of processed Sentinel-1 data were used data from SRTM. 22.11.2000, this mission has started by launching two satellites Endeavour with radar with C-Band on board. This mission was under the protection of NASA and NGA and was launched to acquire radar data for the basis of the digital elevation model of the (almost) whole world [21]. The quality of the resulting models was verified also statically using RMSE.

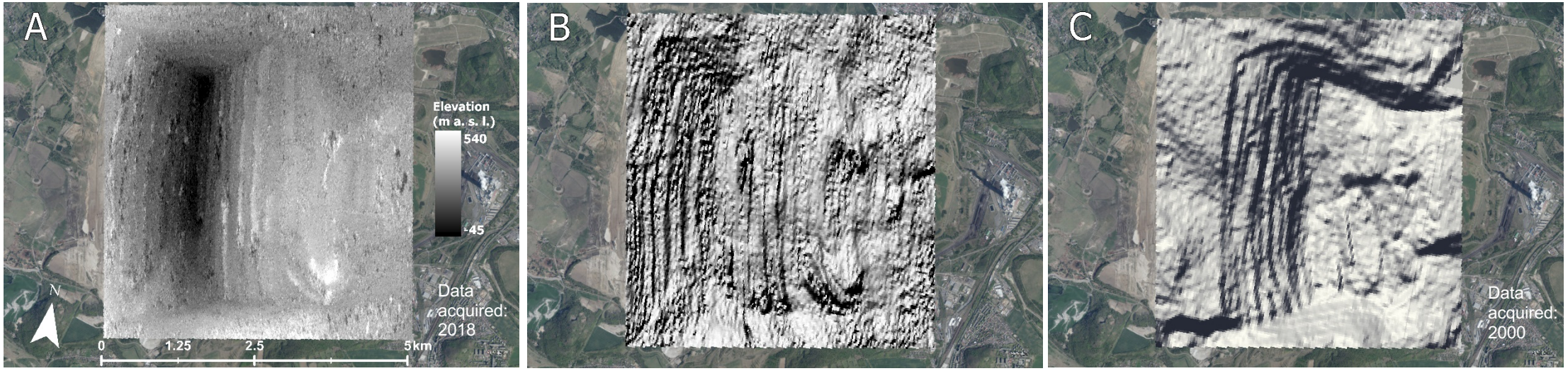

Fig. 4 - Resulting models of the Bílina quarry area, author: Dominik Brétt, 2021, orthophoto: ČÚZK

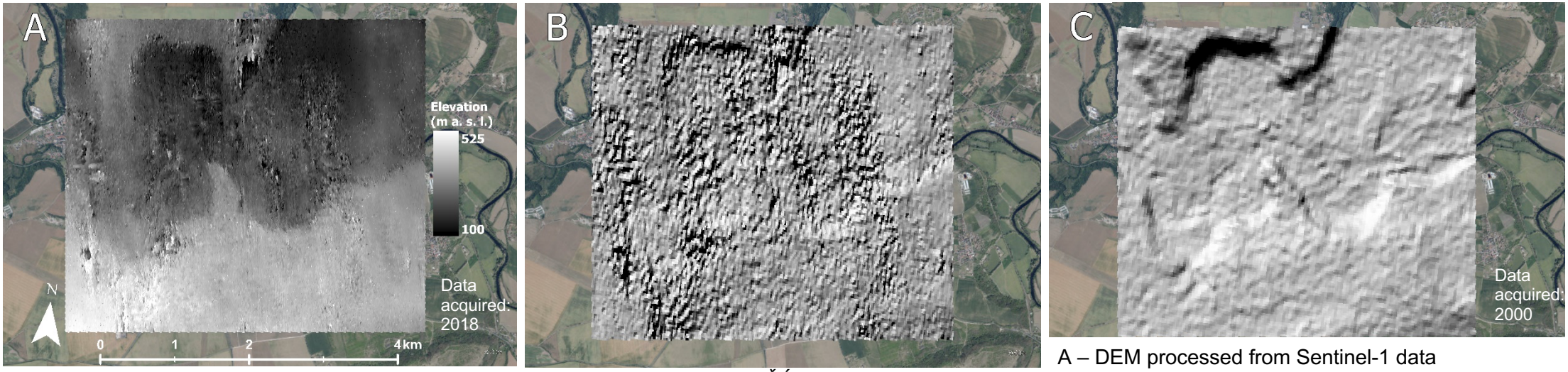

Fig. 5 - Resulting models of the Zatec area, author: Dominik Brétt, orthophoto: ČÚZK

A – DEM processed from Sentinel-1 data
B – Hillshaded model processed from Sentinel-1 DEM
C – Hillshaded model processed from SRTM

DOI 10.14311/CEJ.2021.04.0072

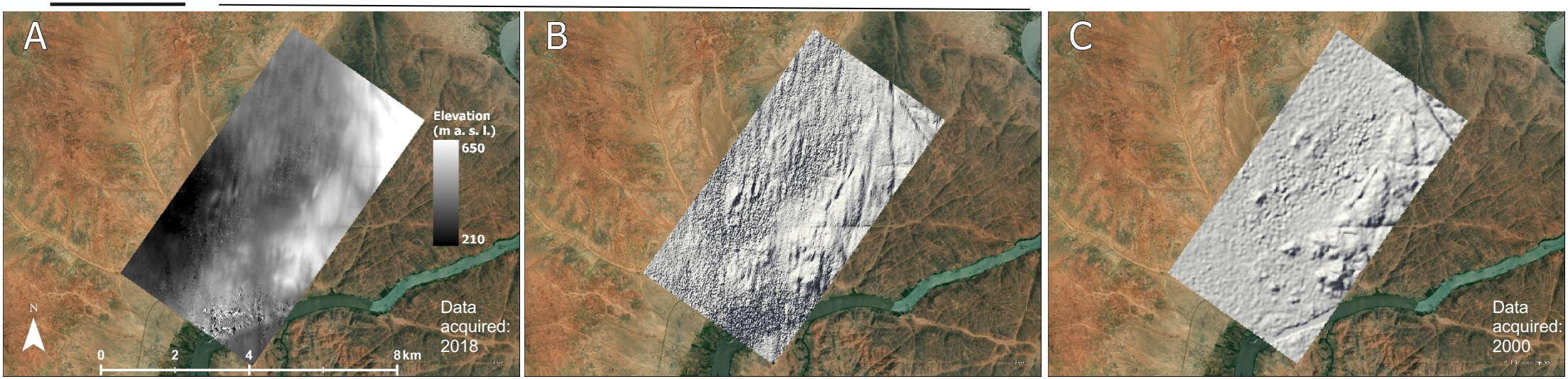

Fig. 6: Resulting models of the Sabaloka locality, author: Dominik Brétt, 2021, source: Esri, Maxar, Earthstar Geographics, USDA FSA, USGS, Aerogrid, IGN, IGP,

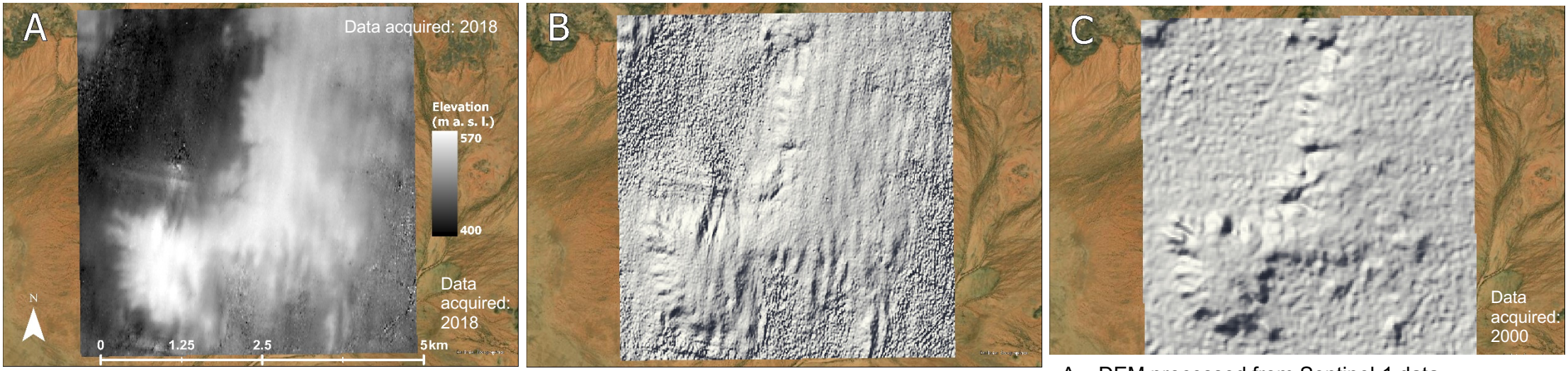

Fig. 7 - Resulting models of the Shaquadud localit, author: Dominik Brétt, 2021, source: Esri, Maxar, Earthstar Geographics, USDA FSA, USGS, Aerogrid, IGN, IGP, and the GIS User Community

A – DEM processed from Sentinel-1 data
B – Hillshaded model processed from Sentinel-1 DEM
C – Hillshaded model processed from SRTM

DOI 10.14311/CEJ.2021.04.0072

Accuracy of the produced DEMs

The quality of the resulting DEMs was checked using different data sources. The residuals in the Z coordinates were analyzed and the quality of the resulting models was verified also statically using RMSE. All four localities were compared with the SRTM data. Altogether in the first test comparison with the SRTM data, 25 points were set as the expected sufficient minimum sample size, and those points were randomly created and used for statistical analysis in each of the localities.

In Sudan, points were acquired by direct measurement. A total number of 45 points for the Sabaloka and 95 points for the Shaquadud locality were used. The sites in the Czech Republic were also compared to DMR 5G where another 100 points were tested. The results of the accuracy analysis are presented in Tab. 1.

Tab. 1: Results of the RMSE in meters

	Czech Republic		Sudan	
	Žatec (m)	**Quarry Bílina (m)**	**Sabaloka (m)**	**Shaquadud (m)**
Sentinel-1 and SRTM	25.7	104.2	26.9	10.8
Sentinel-1 and GCP	-	-	32.3	23.3
Sentinel-1 and Lidar	71.8	79.4	-	-

As regards the quality of the INSAR altitude model, according to the ESA Forum, the normal deviation of RMSE when compared to SRTM ranges from -75 meters to 75 meters and models have to fit within this certain error size. SRTM digital height models had a pixel resolution of about 30 meters, while digital height models from data Sentinel-1 15 meters.

The areas chosen in Sudan turned out better both visually and statistically. The RMSE value of Sudan's first Sabaloka area was 26.935 meters in comparison with SRTM and 32.338 meters in comparison with directed measurements. In the second area Shaquadud was RMSE value 10.839 meters and in comparison with direct measurements 23.339 meters.

The height data from the SRTM are from 2000 and in the Bílina quarry area, it is clear that there has been a development and process of mining and therefore the data could have been misleading since it was a comparison of heights 18 years later. The RMSE deviation when comparing interferometric data with SRTM was 104.169 meters. The RMSE of the Žatec area turned out better with a value of 25.723 meters. Compared to lidar data Žatec area did not meet the expectations and the RMSE value raised to almost 72 meters. Another test was made and the RMSE was compared between data from Sentinel-1 and SRTM, where the same 100 points were tested and the result was 68.03078. The DEM of the area of the quarry Bílina made from the Sentinel-1 data was also compared to DMR 5G. The data from DMR was acquired in the year 2013 so the data were closer to terrain to the Sentinel-1, which were acquired, in this case, in the year 2018. RMSE value of the quarry Bílina dropped in the second test with the lidar data from almost 105 meters to 79 meters.

Even though in the Czech Republic, areas were chosen in the period of the dormancy, the author did not succeed to find paired interferometric images that had comparable RMSE values to the Sudan areas and excessive occurrence of noise has harmed the quality of the shaded models and models display the terrain very roughly.

CONCLUSION

The results of digital elevation models processed from Sentinel-1 interferometric data were verified against a commonly available elevation model derived from the data of the satellites SRTM. The application of these models is especially suitable for areas that are poorly available for other and more accurate methods of obtaining elevation data. Models processed from Sentinel-1 data turned out much better for areas in Sudan, even though the time difference between individual images was 12 days compared to 3 days for areas in the Czech Republic. 25 testing points were insufficient amount for areas in the vegetated areas – in the Czech Republic.

Processing of the Sentinel-1 data is more complex and the user has to find suitable paired images – which take the most time during the processing itself when selecting a less suitable locality, especially with occurring vegetation. This is followed by pre-processing the images to create a digital model. In SRTM processing user has to choose suitable tiles with prepared DEM.

SRTM provides satellite data that is not as accurate as the direct measurement methods, and the RMSE value, when compared to Sentinel-1 data is therefore lower and appears to be of better quality. On the other hand, the data from GNSS instruments are very accurate and so the deviation when comparing the data is higher.

Satellite data can be useful for areas that are poorly accessible and more accurate methods cannot be used. Then the Sentinel data can provide 14-meter resolution and relatively accurate models for suitable areas (primarily arid areas).

The results of the digital elevation models processed from the Sentinel-1 interferometric data were verified with a commonly available elevation model acquired by the SRTM. The use of these models is especially suitable for areas that are poorly accessible to other alternative and more accurate methods of obtaining altitude data cannot be used. The Sentinel data can provide 14-meter resolution and relatively accurate models for suitable areas (primarily arid areas) that have a minimum of the surrounding vegetation which can also harm the quality of the models. It can be seen for the Sudan areas as the example of the arid areas and in comparison with the Czech areas.

ACKNOWLEDGEMENTS

This work was supported by Project Number: UJEP-SGS-2019-44-001-3 (Spatial data remote sensing methods as a tool for modeling and observing the environment) covered by student grant competition at UJEP - Jan Evangelista Purkyně University in Ústí nad Labem.

The reference data for test sites in Sabaloka, Sudan were supplied by the Czech Institute of Egyptology, Faculty of Philosophy and Arts - Charles University in Prague (L. Varadzinová) and the data for the site in Shaquadud, Sudan were supplied by the Institute of archaeology of the Czech academy of sciences, Prague (L. Varadzin).

REFERENCES

1. SONG, Dunjiang, Tianxiang YUE a Zhengping DU. DEM Construction from Contour Lines Based on Regional Optimum Control. In: *2010 Third International Joint Conference on Computational Science and Optimization* [online]. IEEE, 2010, 2010, s. 162-165 [cit. 2021-11-30]. ISBN 978-1-4244-6812-6. Available from: doi:10.1109/CSO.2010.87

2. JARIHANI, Abdollah A., John N. CALLOW, Tim R. MCVICAR, Thomas G. VAN NIEL a Joshua R. LARSEN. Satellite-derived Digital Elevation Model (DEM) selection, preparation and correction for hydrodynamic modelling in large, low-gradient and data-sparse catchments. *Journal*

of Hydrology [online]. 2015, 524, 489-506 [cit. 2021-11-30]. ISSN 00221694. Available from: doi:10.1016/j.jhydrol.2015.02.049

3. LAZNA, Tomas, et al. Cooperation between an Unmanned Aerial Vehicle and an Unmanned Ground Vehicle in Highly Accurate Localization of Gamma Radiation Hotspots. International Journal of Advanced Robotic Systems, Jan. 2018, doi:10.1177/1729881417750787.

4. MASSONNET, Didier. Satellite Radar Interferometry. *Scientific American*, vol. 276, no. 2, Scientific American, a division of Nature America, Inc., 1997, pp. 46–53, http://www.jstor.org/stable/24993607.

5. Collaborative Ground Segment - Czech Republic, Sentinel-1 – Datové specifikace [online]. [cit. 2020-03-08]. Available from: https://collgs.czechspaceportal.cz/sentinel-1-datove-specifikace/

6. FLETCHER, K. Sentinel-1: ESA's Radar Observatory Mission for GMES Operational Service. Noordwijk, Netherlands: ESA Communications, 2012. ISBN 978-92-9221-418-0.

7. LISÁ, Lenka, BAJER Aleš, PACINA Jan, McCOOL Jon-Paul, CÍLEK Václav, ROHOVEC Jan, MATOUŠKOVÁ Šárka, KALLISTOVA Anna a Zdeněk GOTTVALD. Prehistoric Dark Soils/Sediments of Central Sudan; Case Study From the Mesolithic Landscape at the Sixth Nile Cataract. CATENA. ISSN: 0341-8162

8. PACINA, Jan. Geodetic surveying as part of archaeological research in Sudan. Geoinformatics FCE CTU. 2015, 14(1): 47-63.

9. VARADZINOVÁ SUKOVÁ, Lenka, Ladislav VARADZIN, Aleš BAJER, Lenka LISÁ, Jan PACINA a Petr POKORNÝ. Tracing Post-depositional Processes at Mesolithic Occupation Sites in Central Sudan: View from the Site of Sphinx (SBK.W-60) at Jebel Sabaloka. Interdisciplinaria Archaeologica – Natural Sciences in Archaeology (IANSA). 2015, 6(2), 133-150. ISSN 1804-848X.

10. NATURAL RESOURCES CANADA. Fundamentals of Remote Sensing [online]. [cit. 2021-04-20]. Available from: https://www.nrcan.gc.ca/sites/www.nrcan.gc.ca/files/earthsciences/pdf/resource/tutor/fundam/pdf/fundamentals_e.pdf

11. DOBROVOLNÝ, Petr. Remote Sensing: Digital Image Processing (Dálkový průzkum Země: Digitální zpracování obrazu). Brno, 1998. ISBN 80-210-1812-7.

12. Remote Sensing: Digital Image Processing (Copernicus v České republice. Družice Sentinel) [online]. [cit. 2021-06-06]. Available from: http://copernicus.gov.cz/druzice-sentinel

13. BOURGEAU-CHAVEZ, Laura, Kevin RIORDAN, Richard POWELL, Nicolle MILLER a Mitch NOWELS. Improving wetland characterization with multisensor, multi- Improving wetland characterization with multi-sensor, multitemporal SAR and optical/infrared data fusion [online]. 2009 [cit. 2021-05- 05]. Available from: http://www.dx.doi.org/10.5772/46139

14. BRAUN, Andreas a Luis VECI. TOPS Interferometry Tutorial [online]. 2015 [cit. 2021-06-06]. Available from: http://step.esa.int/docs/tutorials/S1TBX%20TOPSAR%20Interferometry%20with%20Sentinel-1%20Tutorial_v2.pdf

15. ROTT, Helmut. Advances in interferometric synthetic aperture radar (InSAR) in earth system science, Institute of meteorology and geophysics. Institute of meteorology and geophysics: University of Innsbruck, 2009.

16. GUPTA, Ravi P. Remote Sensing Geology. 2. New York: Springer, 2003. ISBN 978-3-642-07741-8.

17. ESA SENTINEL ONLINE. Sentinel Overview [online]. [cit. 2021-04-08]. Available from: https://sentinel.esa.int/web/sentinel/missions/

18. *Alaska Satellite Facility* – [online]. [cit. 2021-06-06]. Available from: https://search.asf.alaska.edu/#/

19. Copernicus Open Access Hub [online]. [cit. 2020-03-08]. Available from: https://scihub.copernicus.eu/dhus/#/home

20. Collaborative Ground Segment - Czech Republic [online]. [cit. 2021-06-06]. Available from: https://dhr1.cesnet.cz/#/home

21. U.S. GEOLOGICALSURVEY. USGS EROS Archive - Digital Elevation - Shuttle Radar Topography Mission (SRTM) 1 Arc-Second Global [online]. [cit. 2021-06-15]. Available from: https://www.usgs.gov/centers/eros/science/usgs-eros-archive-digital-elevation-shuttle-radar-topography-mission-srtm-1-arc?qt-science_center_objects=0#qt-science_center_objects

22. SRTM image courtesy of the U.S. Geological Survey. Available from: https://earthexplorer.usgs.gov/

23. Czech Office for Surveying and Cadastre: Digital model of the relief of the Czech Republic 5th generation (DMR 5G)(Český úřad zeměměřičský a katastrální: Digitální model reliéfu České republiky 5. generace (DMR 5G)) [online]. [cit. 2021-10-15]. Available from: https://geoportal.cuzk.cz/(S(z5hdhew0ycnv515y22ujq0a1))/Default.aspx?mode=TextMeta&side=vyskopis&metadataID=CZ-CUZK-DMR5G-V&head_tab=sekce-02-gp&menu=302

CIVIL ENGINEERING JOURNAL

Article no. 73

THE CIVIL ENGINEERING JOURNAL 4-2021

REMOTE SENSING DATA IN MUNICIPAL GOVERNMENT

Jaroslav Nýdrle[1,2]

1. *CTU in Prague, Faculty of Civil Engineering, Department of Geomatics, Prague, Thákurova 7, Czech Republic, jaroslav.nydrle@fsv.cvut.cz*
2. *Jan Evangelista Purkyně University in Ústí nad Labem, Faculty of Environment, Department of Geoinformatics, Ústí nad Labem, Pasteurova 3632/15, Czech Republic*

ABSTRACT

This article focuses on the issue of using data obtained through remote sensing methods in the administrative district of the municipality with extended powers of Liberec (the Czech Republic). The first part of the article discusses the question of using Earth remote sensing data for city agendas in general. Then, it presents a questionnaire, created for evaluating the needs of the Liberec municipality. This questionnaire, focusing on the use of remotely sensed data, was created on the basis of a review of relevant literature. Based on the results of the questionnaire, thefollowing spatial information requirements were chosen to be addressed: land surface temperature map - LST (Landsat 8), vegetation index - NDVI (Sentinel 2, Planet Scope), normalized difference water index - NDWI, NDWI 2 (Sentinel 2), normalized difference built-up index - NDBI (Sentinel 2). All data obtained during the creation of this study have become part of the database of the Urban Planning and GIS Department and are available to employees of the City of Liberec.

KEYWORDS

Satellite, Landsat 8, Planet Scope, Sentinel 2, Remote sensing, LST, NDVI, NDWI, NDBI

INTRODUCTION

Literature Review

Satellite data are a type of remotely sensed data [1]. The main advantage of satellite data over other types of remotely sensed data, is the ability to swipe a large area in a fairly high spatial resolution (for example, Sentinel1: up to 5 m / pixel, Sentinel 2: 10 m / pixel), another advantage is the frequency of data acquisitionin our latitudes (Sentinel 2A, 2B – once every 5 days) [2]. Satellite data is also very often extended by so-called spectral bands, which are called multispectral data. Information about the specific reflectivity curve of the monitored material on planet Earth allows one to extract various types of information from multispectral data (for example water, greenery, rocks) [3].

To date, Landsat has extended operations to 8 satellites, including Landsat 9, launched in September 2021. (The seeming contradiction in numbers is due to the fact that although they have launched 9 satellites Landsat 6 was destroyed at launch.) These satellites, propelled to orbit by the USS NASA and the USGS, supply data to the satellite data archive. Data from these satellites are freely available after registration and are frequently used for purposes of research. Their use is enhanced by the use of time series and the resulting possibility of analyzing changes in the landscape over time. S. Ahmadi et al, for example, use Landsat 4, Landsat 5 (data from 2001, 2008) and Landsat 8 (data from 2018) in their study to study drought [1]. Based on a combination of spectral bands, they calculate, amongst others, the NDVI vegetation index, which monitorsdrought successfully using data from different years.

J. P. Mondejar and A. F. Tongco have used Landsat 8 data to obtain spatial information about the location of watercourses and water bodies [4]. They have proven that thesemethods are suitable

DOI 10.14311/CEJ.2021.04.0073

for surface water mapping. The most usable zone for exploring water bodies, in their view, is NIR, as it captures the largest difference in reflectance values between water and solid earth structures (it has better results in this respect than NDWI and MNDWI water indices). Therefore, Mondejar and Tongco's study has confirmed that remote sensing can extract or define bodies of water very quickly, repeatedly and accurately [4]. A problem may, however, arise when attempting to map small watercourses in wooded areas. In such cases, it is advisable to supplementthe mapping with a digital model of relief, or a temperature map created using the TIRS (thermal infrared sensor) of the Landsat 8 band (assuming a different temperature of water and its surroundings).

Further, Marcof and Statescu have used Landsat 8 data to examine the relationships between LST (Earth surface temperature), NDBI (standardized building index) and NDVI (vegetation index) [3]. The results of this work have confirmed a strong linear relationship between LST and NDBI, which suggests that in urban areas the surface temperature depends on the materials used (generally throughout the territory of land use and related landscape cover). The relationship between LST and NDVI, however, has been found to vary by season.

Other freely available satellite data is accessible through the European Union's Copernicus program. Here, we focus only on Sentinel-2 data. The Sentinel-2 mission is designed to collect data suitable for research on landscape use and for mapping changes in the landscape (according to the Copernicus program's Czech website). This is multispectral data composed of thirteen bands. Wong, M.F. F. et al. have based their research on Sentinel-2 data to calculatethe NDVI in the Pearl Delta region. Their article compares the resulting layer of filtered vegetation with high-resolution data from Google Maps RGB [5]. The data correlation reaches 0.97, confirming thehigh quality of Sentinel-2 data.

J. Radax et al. compare the usability of Landsat 8 and Sentinel-2 data in mappinglandscape usage [6]. The authors acknowledge the better spatial resolution of the Sentinel-2 sensor compared to Landsat-8 and conclude that Sentinel-2 data is already usable for mapping small watercourses with a width of about 5 m and strips of vegetation in the city. At the same time, they add that it would be appropriate to modify or supplement certain zones in the event of another similarmission, and also conclude that the progressively more detailed spatial resolution and subsequent interpretation of data has been moving the boundaries of the research and understanding of naturalprocesses. Kaplan G. et al. has also discussed the mapping of heat islands through the use of satellite data [7].

Other operators that provide multispectral satellite data include, for example, Planet Labs Inc.'s satellite system that includes the following satellite groups: Planet Scope (175 Dove satellites), RapidEye (5 satellites), Skysat (13 satellites). Planet Labs Inc. data. grant free use of data for study purposes, and it was, indeed, possible to obtain a limited amount of data from their satellites. Other commercial projects working for the acquisition of satellite multispectral data are DigitalGlobe (WorldView, Ikonos, QuickBird, Geoeye-1); AIRBUS Defence and Space (Pléiades, SPOT). This data, however, is understandably used to a lesser extent in science than data freely available (Landsat, Sentinel).

Satellite data has significant information power in terms of longer-term earth observation by the same (data archives) or very similar methods (sensors). In fact, in scientific studies, a combination of different satellite data is very frequently used. An example of the use of satellite data archives and the combination of imagery from different satellites is, for example, the work of MacLachlan, A. et al., which explores urbanization and the growth of the city of Perth in Australia through images from Landsat satellites (Landsat 5 TM, Landsat 7 ETM+, Landsat 8 OLI) [2]. The authors of the study have calculated that the spatial range of the city of Perth increased by 45 %(320 sq km) between 1990 and 2015.

The Context of the Research

This article discusses the possibilities of using remotely sensed data in city administration, and, in particular, public administration. The discussed research was originally executed for the Municipality of Liberec (the Czech Republic). Up to this point, the Municipality of Liberec tended to use remotely sensed data only to a limited extent. Among the data previously used were orthophotos

of the Czech Surveying Office as well as those of the State Administration of Land Surveying and Cadastre, available through the WMS service. Other data used by city workers were in the form of orthophotospurchased to order (also via WMS). Figure 1 shows the location of the area.

The city of Liberec has access to data on watercourses and water bodies through the use of Digital Base of Water Management Data, and small watercourses have also been mapped as part of the processing of the Territorial Landscape Study of Liberec Municipality's Administrative District with Extended Powers. Ä possible use of the satellite method, similarly to those outlined above, can be thus seen in refiningand, if possible, supplementing existing databases with missing watercourses and water areas.

This is especially so since the city of Liberec, before the present research, did not have such interpreted data, yet this type of data could be a suitable source of complementary information aiding the activities and work ofthe Department of Greenery and Public Space Administration to plan the planting and maintenanceof existing greenery. This issue is also related to so-called urban heat islands (UHI), whose scientificmapping with clear and understandably visualized results in Liberec is also lacking.

The reason Sentinel-2 data is usable for the city of Liberec is that the city does not yet have a green passport. At the same time, the detail of data thus accessible does not provide a high enough resolution to create a green passport. Nevertheless, using this data could at least serve as abasis for mapping and monitoring the development of vegetation in the city.

RESEARCH AIMS

The aim of this article is thus to assess the possibility of using remotely sensed data on the territory under the auspices of the Municipality of Liberec. The statutory city of Liberec is a city with extended powers and therefore also manages the surrounding municipalities in some agendas (e.g. environmental protection, spatial planning), therefore the focus of research is not only the city of Liberec, but also the surrounding municipalities (28 municipalities altogether including that of the city of Liberec itself.

Based on the processing of the above survey of the possibilities of using remotely sensed data, a questionnaire was prepared on the use of spatial data and on the potential information needs of the municipality's various departments and organizations (this latter aspect was formulated in a general manner, since many workers have had no idea what remote sensing is). The results of the questionnaire were then used to select the appropriate remote sensing data for earth analysis. The main aim of the research was to confirm the applicability of DPZ data in the working environment of the administrative district of the municipality. A selection of data from satellites would be thus used to fulfill the identified needs of city workers and urban organizations.

One of the main challenges of the research was presented by the implementation of the resulting layers in the strategic documents of the city of Liberec (Adaptation of the City of Liberec to climate change, Manual of public space of the city of Liberec), which are still in the process of creation or finalization.

DATA AND RESEARCH METHODS

Area of interest

The research area is defined by the administrative district of the municipality with extended powers Liberec (SO ORP Liberec). Liberec City Hall (because it is a municipality with extended powers) is in charge of the data for all 28 municipalities. Figure 1 visualizes the administered area of SO ORP Liberec in the context of the Liberec region and indicates its location within Europe. SO ORP Liberec is located in the north of the Czech Republic and borders the northern part of The Federal Republic of Germany and the Republic of Poland.

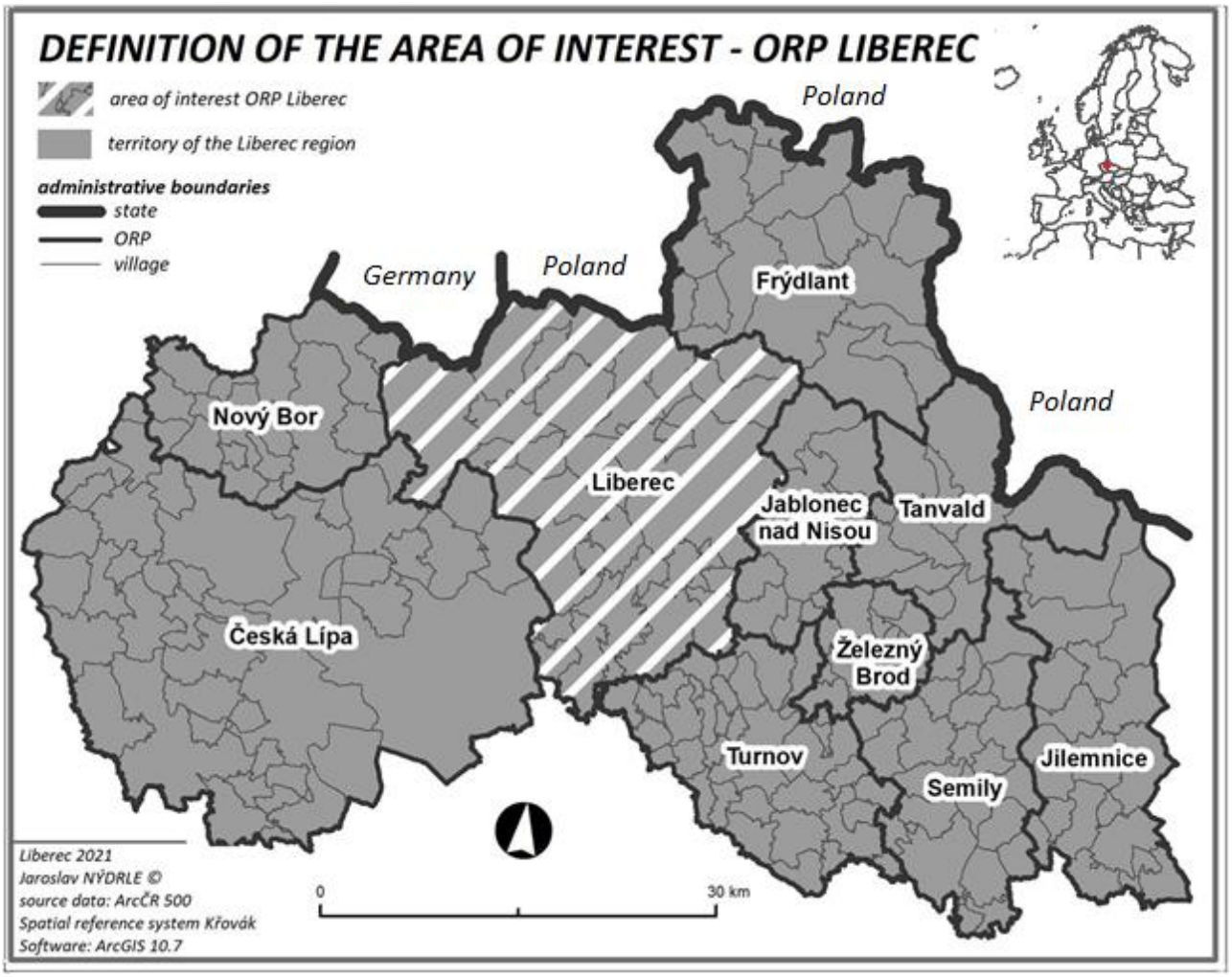

Fig. 1 – Definition of the area of interest – ORP Liberec

Questionnaire

As part of the questionnaire survey, all heads of individual departments of the City of Liberec (Department of Tourism, Culture and Sports; Department of Transport; Department of ecology and public space; Department of Economics; City Architecture Office; Mayor's Office Department; Control and Internal Audit Department; Property Management Department; Legal Department and public procurement; Department of Education and Social Affairs; Department of Building Authority; Department of Social Welfare; Department of Administration and Trade; Public Property Management Department; Department of Strategic Development and Subsidies; Spatial Planning Department; Department of Home Affairs; Department of the Environment) and selected contributory organizations that are likely to use spatial data (Liberec IT services; Urban forests Liberec) were asked to fill in a questionnaire. The questions in this questionnaire were previously consulted with the staff of the UAP and GIS departments.

As part of the questionnaire survey, 18 departments of the City of Liberec and 2 contributory organizations (Liberec IT services; Urban forests Liberec) were contacted. Thanks to the support of the Secretary of the City of Liberec, we managed to obtain a 100% feedback on the questionnaires. Of the 20 subjects surveyed, 75% of the respondents use spatial data, which is exactly 15 respondents (heads of individual departments consulted the answers with their subordinates). On the contrary, 25 % of the answers were negative, i.e. 5 respondents (subjects) do not use spatial

data. We can therefore say that spatial data are widely used at the City of Liberec and municipal organizations and there is great potential for further development.

Satellite imagery

With the aid of the questionnaire survey, key information needs were selected, which were then matched with the possibilities of using the available data, as identified above on the basis of the literature. In this manner, freely available satellite data from the US Landsat program (specifically data from the Landsat satellite 8 – 30 meters / pixel), as well as from the European satellite program Copernicus (consistently data from the sentinel 2 – 10 meters / pixel), became the main source of data.

In addition, as a result of a successful correspondence with the American company Planet and my inclusion in their Science Program Education and Research, images ofPlanet Scope satellites that scan the earth's surface at a frequency of 5.5 days above the same place could be obtained. Planet Scope's data is 3 m pixel in resolution and has a multispectral spectral resolution (RGB + NIR = 4 band), thanks to the nearby infrared band, the Planet Scope satellites (represented by 175Dove satellites) could be used to analyze vegetation and the combination of bands in the grid calculator could create an NDVI index.

In terms of supplementary data available for the territory of the SO ORP Liberec, relevant data from any Landsat mission (1-9) is worth mentioning, as well as that of the European program Copernicus Sentinel 1, Sentinel 3, Sentinel 5P. What makes these information sources especially valuable for Liberec city workers is the fact that this additional data is available at all times and, if necessary, their availability is ensured at a moment’s notice, i.e. a smooth download from the hub of the European Copernicus program. Landsat 8, Sentinel 2 and Planet Scope satellite data were thus also used in this work.

The main reason for using a single data set instead of data from longer time span sprung from the specific requests made by the Municipality of Liberec. They requested the most up-to-date data available since they intended to use them as the basis for creating such documents as the city’s green passport, public space manual, or the layer of surface waters. Thus, the latest momentary data was favored over an average calculated from a wider sample of data. As a result, the latest available images with no cloud cover were used (e.g. in the case of temperatures on a hot summer day).

In addition, in the case of surface temperature, the research was aimed only at mapping thermal islands, and thus it was appropriate to use the latest usable image of the hottest summer day without cloud cover. The use of an average value could have led to biased results due to a range of factors (e.g. construction work, changes in the use of land).

Related Works

In their 1974 study, Rouse, J. et al., used the Normalized Difference vegetation index (NDVI) for the first time on Landsat 1 satellite data [8]. Rouse J. was the director of the Earth Remote Sensing Center at Texas A&M University at the time. The NDVI vegetation index is still widely used in the basic form, but also in other modifications.

The NDBI constructionindex was first used in 2003 in the work "Using the normalized index of difference created in the automatic mapping of urban areas from TM images" [9]. Currently, for example, Macarof, P. et al. work on comparing NDVI and NDBI as a factor in defining heat islands in cities [3]. Kaplan G. at al. use the same data processing method for the extraction of thermal islands information (LST – land surface temperature) in Skopje (case study 2013 - 2017) [7]. They alsonormalize the data to the NDVI vegetation index. In their 2017 work, Macarof P. and Statescu F. compare the relationship between the surface temperature of Landsat 8 in comparison with the NDVIvegetation index and the NDBI construction index [3].

The normalized index of water content on the Earth's surface has two variants reported in the literature [10]. The first variant is: NDWI = (Xgreen - Xnir) / (Xgreen + Xnir). In this form, satellites with

anear infrared band (NIR) are usable (Landsat 8, Sentinel 2 and Planet Scope). The index of water content on the Earth's surface was used, for example, in 1996 by McFeeters S. K. in his work in defining the layer of uncovered water bodies [10]. Hafizi, H. et al. use NDWI to obtain an NDWI surface moisture layer, from which a layer of water surfaces can be obtained by categorization and conversion to a vector in their work:"Evaluation of approaches to the extraction of water bodies based on objects using Landsat-8 images" [11]. The fact that the NDWI index is still used in 2020 confirms that the index is still current and scientifically relevant.

Analyzed indices

Based on the sources discussed above, it is possible to conclude that the relationship between LST and NDBI (normalized difference built-up index) is a strong linear relationship. When examining the relationship between the vegetation index and surface temperature, it was found that the relationship is very dependent on the season. It can therefore be argued that the NDBI construction index is a fairly accurate indicator of the effects of urban heat islands in the city.

For the purposes of mapping of water surfaces, a normalized index of water content based on Sentinel 2 data (10 meters / pixel) was used for data processing for the entire SO ORP, because it has sufficient spatialresolution for regional planning (Planet Scope data - 3 meters / pixel is more suitable for the analysis of the city of Liberec).

Sentinel 2 is a multispectral satellite of the European program Copernicus. For comparison, a layer of Landsat 8 satellite data was made using the same methodological procedure. The resulting data would be available as a source material for the Department of the Environment. A new phenomenon of territorial analytical data is (after the amendment to the Building Act, which has been in force since 1 January 2018) phenomenon No. 46A - surface water used for bathing. As a first step in determining said areas, it is convenient to analyze the Sentinel 2 data to obtain an NDWI surface moisture layer, from which a layer of water surfaces can be obtained by categorization and conversion to a vector.

The construction index can be calculated by raster algebra in any GIS program environment fromthe data of the Landsat 8 satellite or the Sentinel 2 satellite. In the previous chapter, it was confirmed that a larger scale is a better option for the needs of the city of Liberec. It is true that the identification ofbuildings using the Build-up index would be possible using Landsat 8, where a resolution of 30 meters / pixel can also distinguish most buildings, but since data from Sentinel 2 with a resolution of10 meters / pixel is also available, they are naturally preferable for the user.

Build-up Index (NDBI), or construction index is a usable form of data for the Office of Architecture of the City of Liberec, or for the Department of Spatial Planning (rather as overview data, otherwise they have more detailed data from the spatial planning process, but those are sometimes out of date and this provides further potential for use). Alternatively, it is possible to consider the use of the methodology in the planned update of the map Land use / Land cover (Territorial study of the landscape SO ORP Liberec).

The NDBI construction index was calculated from Sentinel 2 satellite data. It was important, as always, to select suitable data, which could not contain more than 10% cloud cover (ideally none) and had to cover the entire territory. The calculation of the NDBI index in the raster calculator looks like this NDBI = SWIR (band 11) - NIR (Band 8) / SWIR (band 11) + NIR (band 8).

NDVI works on the principle of vegetation display based on the difference between the near infrared and red bands. It is calculated according to the relation: NDVI = (NIR - RED) / (NIR + RED). The physiological state (higher chlorophyll content) of green plants absorbs red light (RED). The cellular structure of vegetation, on the other hand, reflects the NIR (near infrared spectrum). The data are again processed using raster algebra in the ArcGIS program environment.

Processing software

In the processing of satellite multispectral data (Landsat 8, Sentinel 2, Planet Scope), raster algebra tools were used. The analyses were carried out in ArcGIS 10.8. Other GIS software can also

be used. The reason I chose ArcGIS 10.8 is that it is user friendly. Raster algebra allows for the calculation of indices (NDVI, NDWI, LST). The calculated indices represent the mathematical ratio of bands from the data of a particular satellite.

RESULTS

Map of Surface Temperature and Delimitation of Heat Islands in the Administrative District of the Municipality with Extended Scope of Liberec

The data from the Landsat 8 satellite is multispectral data with Thermal Infrared Sensor (TIRS). The data has the aforementioned TIRS band, which allows the processor to extract surface temperature information using a raster algebra. We are here limited by the frequency of Landsat 8's overflight, which is every 16 days. Current weather conditions (especially cloud cover) further limit its use.

Tab. 1 - Area of individual surface temperature categories, data source: calculated from Landsat 8

Area of individual surface temperature categories	
[°C]	*[km^2]*
less than 26	8.15
26.1 – 28	145.31
28.1 – 30	168.2
30.1 – 32	138.53
32.1 – 34	84.24
34.1 – 36	28.87
36.1 and over (maximum 44.5)	5.15
Area SO ORP Liberec (total)	578.45

DOI 10.14311/CEJ.2021.04.0073

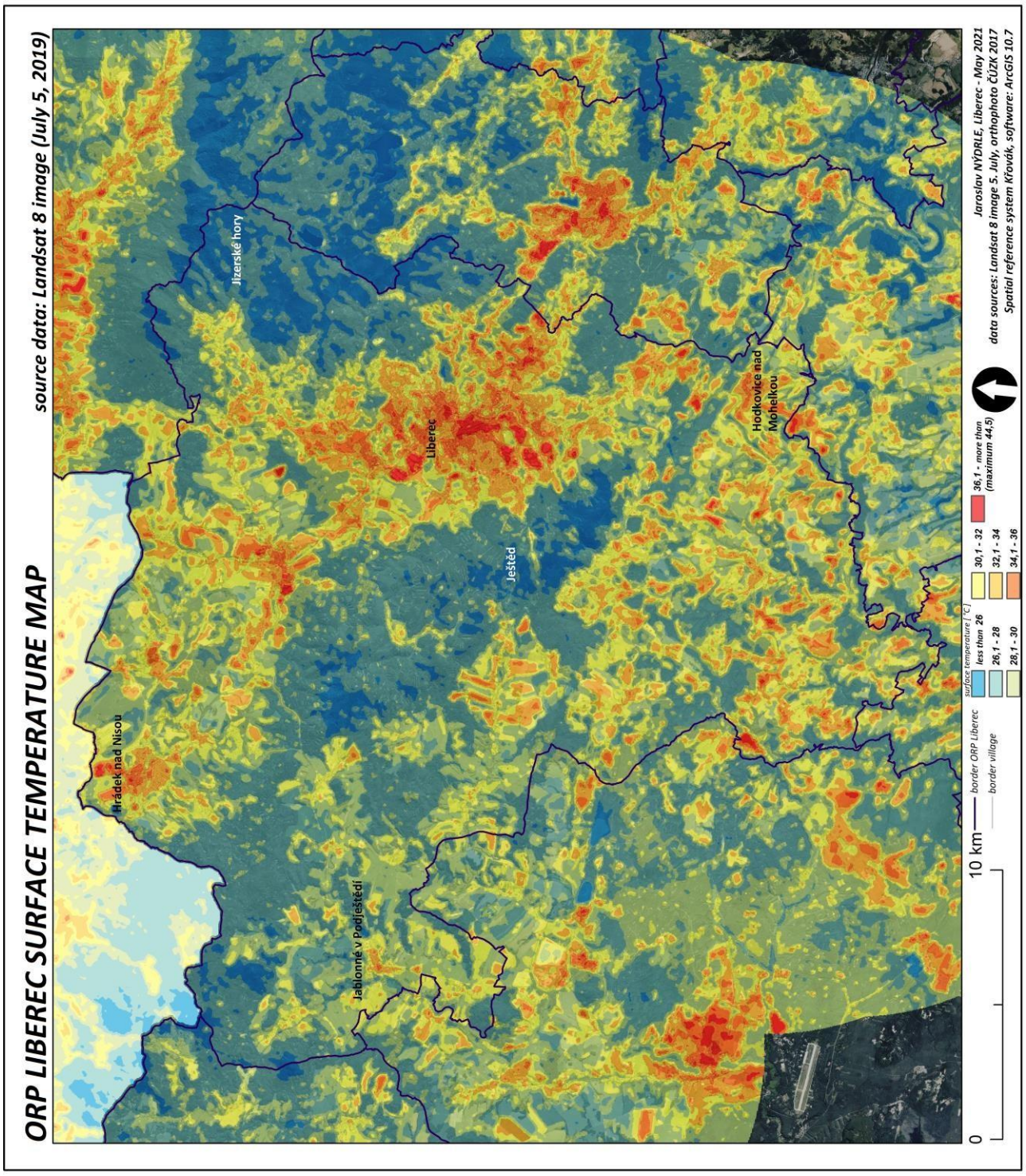

Fig. 2 – ORP Liberec land surface temperature map, data source: Landsat 8 image 5 July 2019

The image from 5 July 2019 was selected for the delimitation of the heat islands, when the highest surface temperature was identified (high temperature difference in the area of the entire image - high amplitude). Figure 2 visualizes a map of the surface temperature of SO ORP Liberec from 5 July 2019. The data was categorized into 7 intervals, so that the boundaries of heat islands in municipalities are more clearly defined. The map shows that the thermal islands are almost identical in boundaries to the buildings and built-up areas. By interpreting the map, we find that the heat islands in the Administrative District of the municipality with extended powers of Liberec are the

built-up centers of municipalities (localities of the warmest category 36.1 and more with a peak of 44.5 °C). Other areas that are in the intervals of 34.1 – 36 °C and 32.1 – 34 °C are localities with exposed substrate, burned meadows, areas with arable land, and roads. Other categories 30, 1 – 32 °C and 28.1 – 30 °C are represented from the point of view of land use by meadows and places with small vegetation. The coldest two categories 26.1 – 28 °C and less than 26 °C are represented by forests and water bodies. The most extensive localities with low temperatures are the Ještěd-Kozákov ridge (Karlov Beech Forest) and the foothills of the Jizera Mountains (Jizera Mountains Beech Forest).Areas are shown in Table 1.

From the information obtained, it is clear that the surface temperature is a reflection of land use. This fact is a guide for us in planning adaptation as well as mitigation measures in city centers. The current trend of implementing greenery, water features, retention reservoirs, dry polders, but also the revitalization of watercourses and generally a return to a near-natural state, is important for mitigating the effects of climate change in urban centers. However, it is also important to deal with large soil blocks, which we should supplement with drawbridges, woods and retention reservoirs and thus reduce their area and reduce the surface temperature there as well (places will be more suitable for animal life and biodiversity will increase).

Map of the Standardized Water Index of the Administrative District of the Municipality with Extended Powers of Liberec

In Figure 3 visualizations of water content on the Earth's surface in SO ORP Liberec can be seen.There is a comparison of results from Sentinel 2 - 10 meters / pixel and Landsat 8 - 20 meters / pixel(Sentinel 2 image from June 30, 2019 and image from Landsat 8 satellite from July 5, 2019). In the section at the bottom left, where the Harcov Reservoir can be seen, the importance of raster resolution is clearly demonstrable in the extraction of spatial information. From the Sentinel 2 satellite (10 meters / pixel) we can obtain a relatively accurate estimate of the water surface boundary. In contrast, in the image from Landsat 8 (30 meters / pixel) we can obtain a defined water area only very approximately. In the cut-out on the right we can see the Harcov Reservoir again. The data were created by raster algebra from the bands of the Landsat 8 satellite. The resulting raster is based on a Landsat resolution of 8 - 30 meters / pixel. Landsat 8 is therefore more suitable for regional planning or survey analysis. In contrast, Sentinel 2 with 10 meters is sufficient (it is also possible to use Planet Scope, but the detail of the defined water areas is sufficient). From the obtained data visualized in Figure 3, it is apparent that the calculation of NDWI according to this algorithm does not completely display surface moisture. NDWI in the variant with NIR and GREEN band is suitablefor obtaining a layer with water surfaces.

DOI 10.14311/CEJ.2021.04.0073

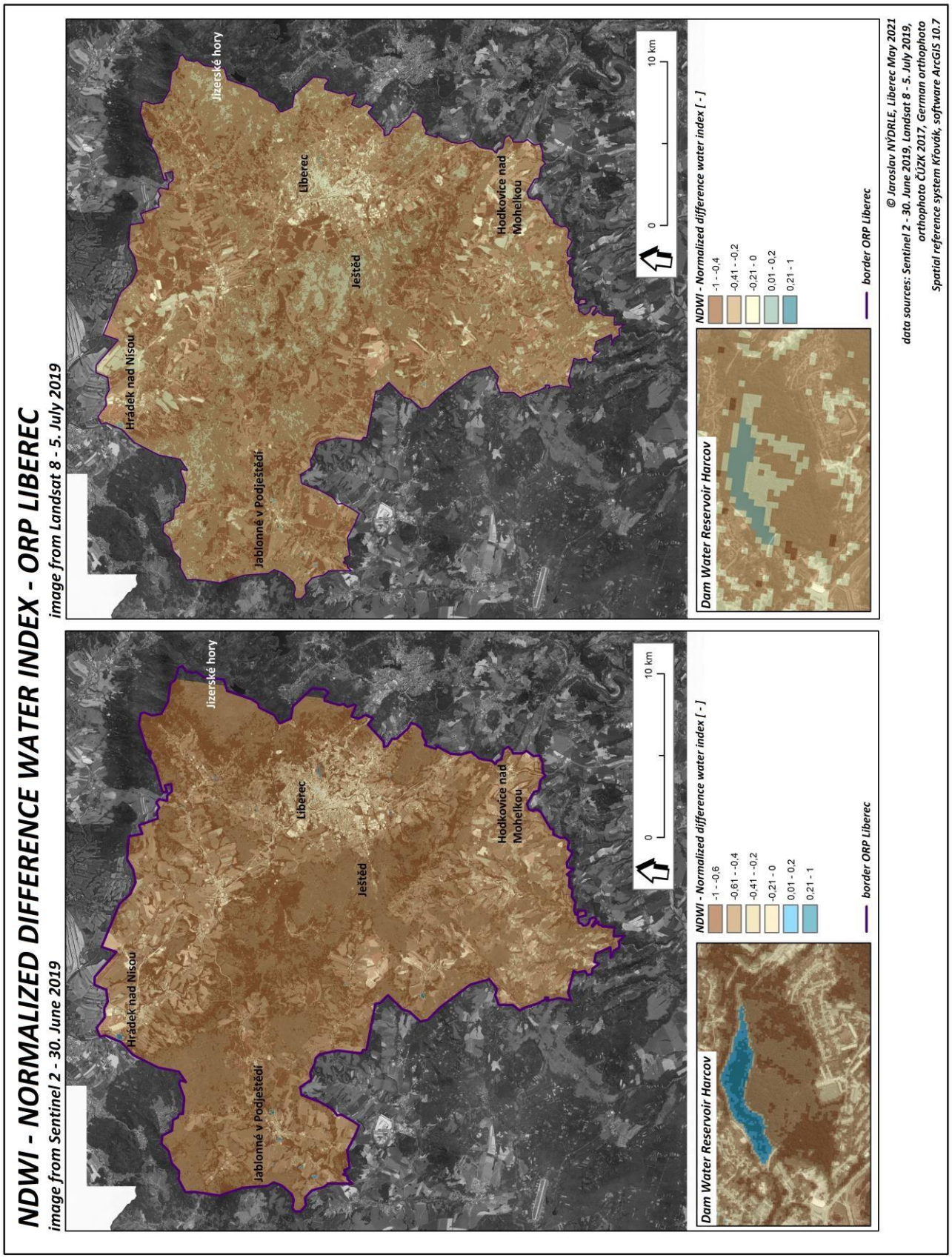

Fig. 3 – NDWI – Normalized difference water index – ORP Liberec, source data: Sentinel 2 - 30. June 2019, Landsat 8 - 5 July 2019.

DOI 10.14311/CEJ.2021.04.0073

Map of the Normalized Build-Up Index (NDBI) of a Municipality with Extended Powers in Liberec

Figure 4 visualizes the construction index data from images from the Sentinel 2 satellite from 5 June 2016 and from 30 June 2019. The NDBI construction index is a tool that allows for the visualization of the growth of urban development. However, it is more important in places where we do not have better data (Sentinel 2 - 10 meters pixel). In our case, the city has an overview of the construction within the spatial planning process. The potential is in detecting illegal structures (at a time when there will be a better resolution of the new satellite and the process will be automated). From the cut-outs around the Train Station in Liberec, it is clear that the resulting data do not differ significantly. In the peripheral parts of the city, the color is increasing (growth of buildings). The analysis is based on a similar value of the area without vegetation (arable land) as the area with buildings, which is its limit.

The city of Liberec has more accurate data on the location of individual buildings within the spatial planning process (Cadastre of Real Estate of the Czech Republic, RÚIAN - register of territorial identification, addresses and real estate, Land use / land cover mapping), but there is a problem with their timeliness (and also with illegal buildings). If the algorithm for extracting data from multispectral remote sensing data (in the future hyperspectral data) could be improved, this process (inspections of illegal structures) could be performed regularly by automatic inspection using (for example) a difference assembly with approved and unapproved structures. This would be a great contribution to the process of controlling illegal construction, which is objectively happening in the area today. The way in the right direction will also be to increase the spatial resolution of the satellites (SkySat satellites already paid today - 0.8 meters / pixel).

DOI 10.14311/CEJ.2021.04.0073

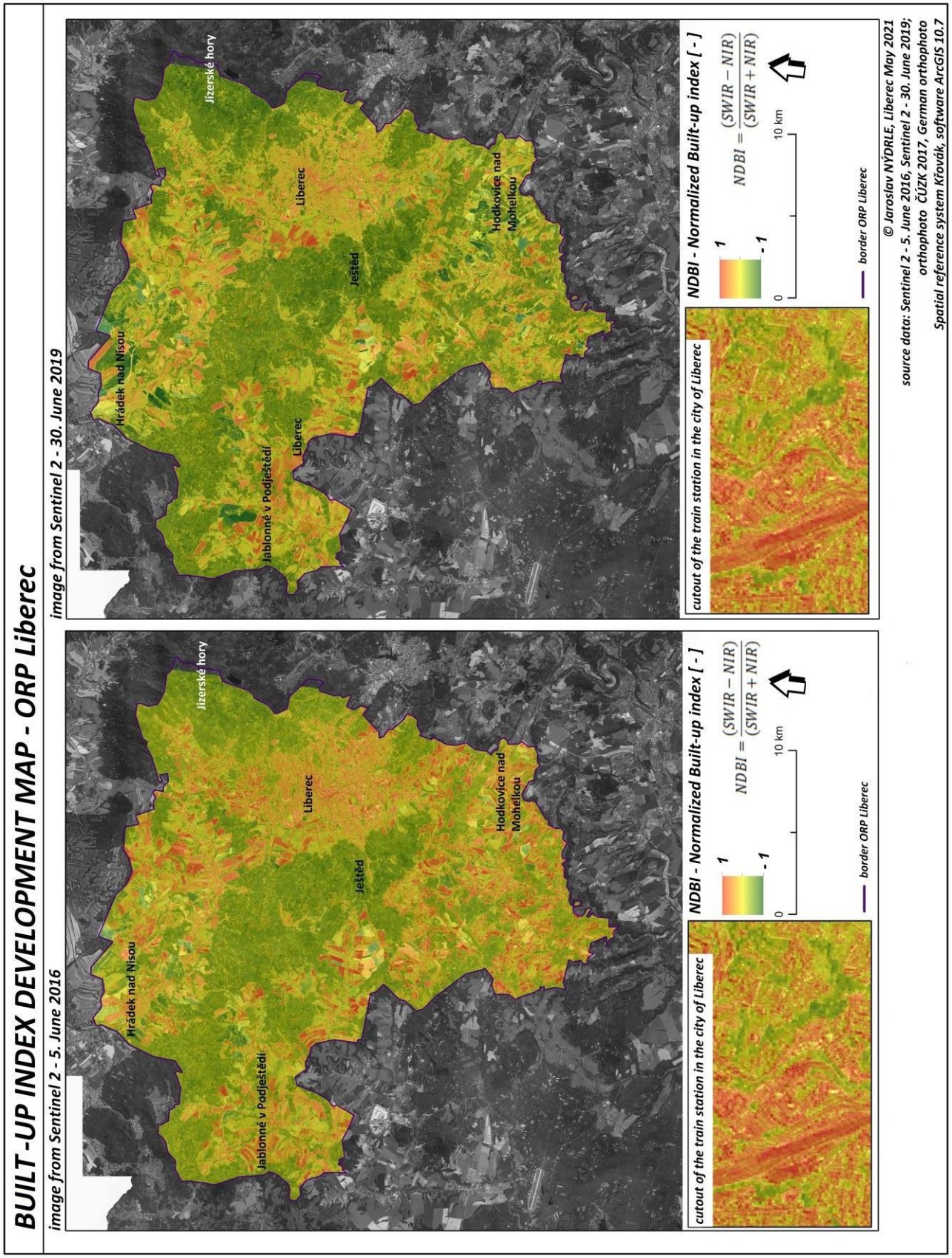

Fig. 4 – Built-up index development map – ORP Liberec, source data: Sentinel 2 – 5. June 2016, Sentinel 2 – 30 June 2019

Map of the Normalized Vegetation Index (NDVI) of a Municipality with Extended Powers in Liberec

The data accessible for this research project has the necessary bands for the calculation in the following resolutions: Landsat 8 (30 meters / pixel); Sentinel 2 (10 meters / pixel) and Planet Scope (3 meters / pixel). For the most current situation, as a basis for mapping greenery for the purposes of green passport in the city of Liberec, the most detailed possible Planet Scope data would be used, and the obtained results would be available to the Department of Ecology and Public Space in Green Management in Liberec, green mapping (for green passport), the Office of Architecture of Liberec as a basis for the Public Space Manual of Liberec and also for the UAP and GIS Department as part of the Adaptation Strategy to change the climate of the city of Liberec.

Because the green passport's development was handled by the Department of Ecology and Public Space in the spring / summer 2020 period, the most recent image of the Planet Scope satellite from May 2020 was selected. Planet Scope is represented by several satellites (Dove) that scan the Earth's surface parallel to each other at one time, it is thus necessary to create a raster mosaic for the needs of analysis and then to analyze the data. Processing the data acquired from Planet Scope is therefore more time consuming, mainly as a result of the higher resolution. Visualization of the obtained NDVI vegetation index details in Figure 5.

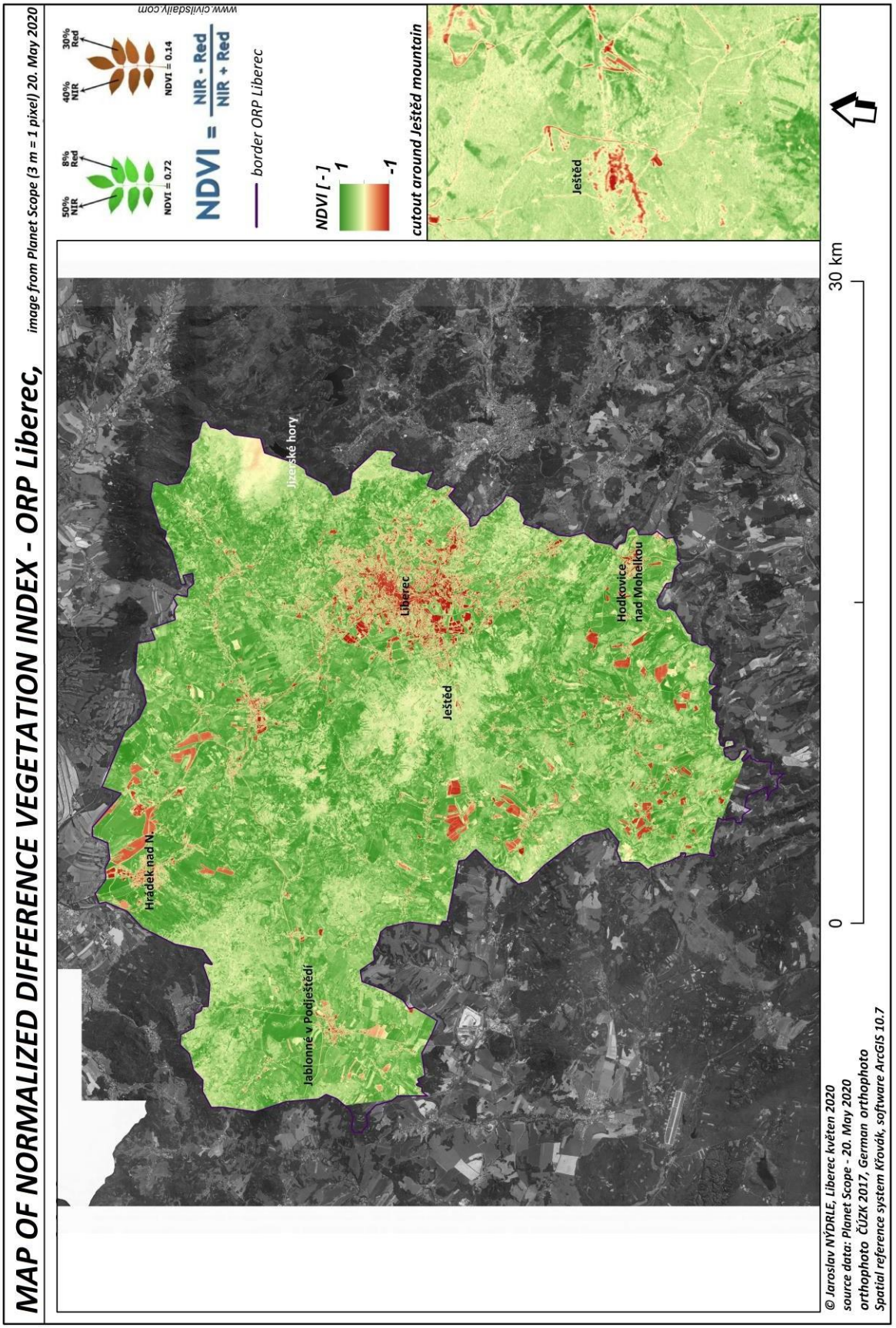

Fig. 5 – Map of normalized difference vegetation index – ORP Liberec, source data: Planet Scope

DISCUSSION

From the available data of the Landsat 8 satellite, surface temperature maps for the city of Liberec were prepared using raster algebra in the ArcGIS program environment. The data were processed for the entire area of interest of SO ORP Liberec (28 municipalities). The method of obtaining surface temperature information was applied to the data. The image from 5 July 2019 was selected for the identification of heat islands, because it has large differences (high amplitude) in temperature between the urban environment and close to nature. The image was classified into 7 temperature categories, of which the highest 36 ° C - and more (maximum 44.5 ° C) represents the city centers with the highest temperature (industrial zones, squares, parking lots - places with the lowest percentage of vegetation). The hypothesis in the introduction of the article was the assumption that the warmest places will be just the mentioned type (paved surfaces, parking lots, etc.). In this way, the areas of the heat islands were defined. In the second category, the areas of 34.1 - 36 ° C, are less urbanized places in the centers, which already contain greenery and water features, but in minimal form. Other categories are simply used in a state closer to a natural state (places with arable land or exposed substrate also show a high temperature). Areas of individual categories were also calculated, the sum of which is in accordance with the area of SO ORP Liberec (578.4 km^2). The same method of obtaining information on thesurface temperature of the Earth is used by Kaplan, G. et al. in their work from 2018, where they apply the methodology to the city of Skopje (examination of the surface temperature of the city in theyears 2013 - 2017) [4]. All data became part of the data warehouse of the UAP and GIS Department.

The potential of surface temperature data may be seen in the possibility of using a thermal sensor ona UAV (drone) in problem areas in city centers, but also in natural areas where it is necessary to identify the problem. Processing the surface temperature map from Landsat 8 data can serve as a tool for identifying problem areas that can be further mapped via UAV with a higher thermal imager resolution (Landsat 8 - 30 meters / pixel; UAV thermal imager 0.5 - 2 meters / pixel - v depending on the flight altitude).

Multispectral data from the Sentinel 2 satellite with a spatial resolution of 10 meters / pixel were used to calculate the NDWI water index in the variant reported in the literature as follows: NDWI = (Xgreen - Xnir) / (Xgreen + Xnir). The resulting raster (created using raster algebra) was classified and converted to a vector. A category containing water bodies was selected from the vector and exportedto a separate layer. In this way, the data applicable to the territorial analytical data (46A - marking of the phenomenon in the official geodatabase) surface water bathing phenomenon were generated. It is worth mentioning that data from the Planet Scope satellite with ahigher resolution (3 meters / pixel) can also be used for this index. The NDWI index in the variant with GREEN and NIR band was used by S. K. McFeeters already in 1996 in his work in defining thelayer of uncovered water areas [10].

The potential of multispectral data in satellite images can be generally seen in increasing their resolution and flight frequency (as well as in improving image interpretation methods). In the future also in the 5G network and the "world internet". In the case of usability of the image (cloudless conditions), it could be possible to immediately apply remote sensing methods using scripts and, thanks to automated interpretation, to immediately know information about the state of the earth's surface. All this will be usable in case of sudden changes, disasters managements, calamities, etc.

The normalized difference built-up index(NDBI) was interpreted using raster algebra based on the multispectral data from the Sentinel 2 satellite. NDBI highlights urban areas where shortwave infrared(SWIR) reflectivity is usually higher than near infrared (NIR) areas. The construction index was developed for use with the Landsat TM 5 and 4 bands. However, the index works with all multispectral data that contains the SWIR and NIR bands. The NDBI construction index was first used in 2003 in the work "Using the normalized index of difference created in the automatic mapping of urban areas from TM images" Zha, Y. et al. [9].

The last multispectral data analyzed are again images of the Sentinel 2 satellite for the purpose of analyzing the physiological state of vegetation. The index works with RED and NIR bands. The index relationship is as follows: NDVI = (NIR - RED) / (NIR + RED). The normalized difference

vegetation index (NDVI) is a graphical indicator usable over Earth remote sensing data that can be used to assess whether objects on the Earth's surface contain vegetation in physiologically good condition. In the literature, the NDVI index was first used by Rouse, J. W. et al.already in 1974 (Monitoring of vegetation systems in large plains using ERTS) [8]. The index is used inthe basic modification and in various others to this day. Thanks to technological development, this index can also be used with data in a more detailed resolution (Planet Scope 3 meters / pixel). PlanetScope data were used to analyze the current state of vegetation in the city of Liberec for the purposesof its mapping.

CONCLUSION

Based on the needs (questionnaire survey and consultations with employees) of employees of the City of Liberec and contributory organizations, various usable data were captured and processed on the territory of SO ORP Liberec. The aim of the work was to prove the usability of data from remote sensing in the state administration, which was proven because all the resulting data became part of the database of UAP and GIS departments and are used by Liberec City staff and contributory organizations.

The acquired data on surface temperature has served as a basis of the city's adaptation strategy for climate change and in public space manual. The data gained for the purposes of calculating vegetation indices have been used both for the same manual and for the city's green passport. The obtained water index data have been used to ascertain the location and area of water surfaces. These pieces of information have then been incorporated into the city's urban planning documentation. Other municipalities, both in the Czech Republic and abroad, can use the methodology described in this article for their own local agendas.

ACKNOWLEDGEMENTS

This work was supported by Project Number: UJEP-SGS-2019-44-001-3 (Spatial data remote sensing methods as a tool for modeling and observing the environment) covered by student grant competition at UJEP - Jan Evangelista Purkyně University in Ústí nad Labem.

REFERENCES

[1] AHMADI, S., Azarnivand, H., Khosravi, H., Dehghan, P., Behrang Manesh, M., 2019. Assessment the effect of drought and land use change on vegetation using Landsat data. Desert(2008-0875) 24, 23–31.

[2] MACLACHLAN, A., Biggs, E., Roberts, G., Boruff, B., 2017. Urban Growth Dynamics in Perth, Western Australia: Using Applied Remote Sensing for Sustainable Future Planning. Land 6,9. https://doi.org/10.3390/land6010009

[3] MARCOF P., Statescu F., 2017. Comparasion of NDBI and NDVI as Indicators of SurfaceUrban Heat Island Effect in Landsat 8 Imagery: A Case Study of Iasi. Present Environment and Sustainable Development 141. https://doi.org/10.1515/pesd-2017-0032

[4] MONDEJAR, J. P., Tongco, A. F., 2019. Near infrared band of Landsat 8 as water index: a case study around Cordova and Lapu-Lapu City, Cebu, Philippines. SustainableEnvironment Research 1. https://doi.org/10.1186/s42834-019-0016-5

[5] WONG, M.M.F., Fung, J.C.H., Yeung, P.P.S., 2019. High-resolution calculation of the urban vegetation fraction in the Pearl River Delta from the Sentinel-2 NDVI for urban climate model parameterization. Geosci. Lett. 6, 2. https://doi.org/10.1186/s40562-019-0132-4

[6] RADOUX, J., Chomé, G., Jacques, D.C., Waldner, F., Bellemans, N., Matton, N., Lamarche, C., d'Andrimont, R., Defourny, P., 2016. Sentinel-2's Potential for Sub-Pixel LandscapeFeature Detection. Remote Sensing 8, 488.

[7] KAPLAN, G., Avdan, U., Avdan, Z.Y., 2018. Urban Heat Island Analysis Using the Landsat8 Satellite Data: A Case Study in Skopje, Macedonia. Proceedings 2, 358. https://doi.org/10.3390/ecrs-2-05171

[8] ROUSE, J.W, Haas, R.H., Scheel, J.A., and Deering, D.W. (1974) 'Monitoring VegetationSystems

in the Great Plains with ERTS.' Proceedings, 3rd Earth Resource Technology Satellite (ERTS) Symposium, vol. 1, p. 48-62.
[9] ZHA, Y., J. Gao a S. Ni. "Using the normalized index of difference created in the automaticmapping of urban areas from TM images." International Journal of Remote Sensing 24, no. 3 (2003): 583-594.
[10] McFEETERS, S. K., (1996) The use of the Normalized Difference Water Index (NDWI) in the delineation of open water features, International Journal of Remote Sensing, 17:7, 1425-1432,DOI: 10.1080/0143116960894871
[11] HAFIZI, H., KALKAN, K. Evaluation of Object-Based Water Body Extraction ApproachesUsing Landsat-8 Imagery. Journal of Aeronautics [online]. 2020, 13(1), 81-89 [cit. 2020-07-01]. ISSN 13040448. Available from: http://search.ebscohost.com/login.aspx?direct=true&db=a9h&an=141501455&scope=site